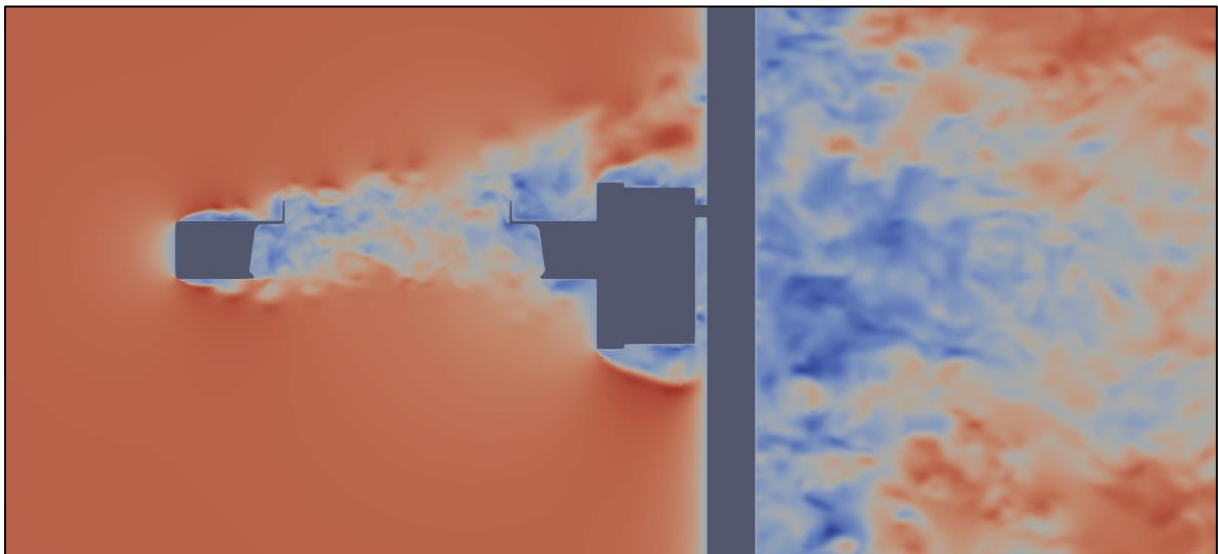


Ph.D. Program in Civil, Chemical and Environmental Engineering
Curriculum in Fluid Dynamics and Environmental Engineering



Department of Civil, Chemical and Environmental Engineering
Polytechnic School, University of Genoa, Italy.



Bluff-body aerodynamics and transfer functions for non-catching precipitation measurement instruments.

Enrico Chinchella

BLUFF-BODY AERODYNAMICS AND
TRANSFER FUNCTIONS FOR NON-CATCHING
PRECIPITATION MEASUREMENT INSTRUMENTS.

BY

ENRICO CHINCHELLA

*Dissertation discussed in partial fulfilment of
the requirements for the Degree of*

DOCTOR OF PHILOSOPHY

*Civil, Chemical and Environmental Engineering
curriculum in Fluid Dynamics and Environmental Engineering,
Department of Civil, Chemical and Environmental Engineering, University of Genoa, Italy*



April, 2023

Adviser:

Prof. Luca G. Lanza – Dep. of Civil, Chemical and Environmental Engineering, University of Genova

External Reviewers:

Prof. Mareile A. Wolff – Department of Physics, Norwegian University of Life Sciences (NMBU)

Prof. Michael L. Larsen – Department of Physics and Astronomy, College of Charleston

Examination Committee:

Prof. Carlo V. Camporeale – Dep. of Environment, Land and Infrastructure Engineering, Politecnico di Torino

Prof. Marco E. Colombini – Dep. of Civil, Chemical and Environmental Engineering, University of Genova

Prof. Davide Laera – Dep. of Mechanics, Mathematics and Management, Politecnico di Bari

Prof. Marco Mancini – Dep. of Civil and Environmental Engineering, Politecnico di Milano

Ph.D. program in Civil, Chemical and Environmental Engineering

Curriculum in Fluid Dynamics and Environmental Engineering

Cycle XXXV

ABSTRACT

Starting from the old and trivial technique of using a graduated cylinder to collect and manually measure precipitation, numerous advances were made for in-situ precipitation gauges. After decades of scarce innovation, a new family of in-situ precipitation gauges was developed. They are called Non-Catching Gauges (NCG) since they can measure precipitation and its microphysical and dynamic characteristics without the need to collect hydrometeors.

The attention that NCGs are gathering today is quite notable, even if they represent only a small fraction of the total precipitation gauges deployed. Their use in the field is bound to continuously grow in time, due to several advantages, discussed in this work, that such instruments present over more traditional ones.

However, their major disadvantage is their increased complexity, the effects of which are highlighted by the literature through evidence of calibration and correction issues. Various field intercomparison experiments showed the evidence of significant biases in NCGs measurements. The goal of this work is to investigate two main sources of bias, producing the largest impact on precipitation measurements.

The first source of bias evaluated in this work is due to instrument calibration. Several attempts at developing a calibration procedure are presented both in the scientific literature and from the manufacturers. Nevertheless, those methods are hardly traceable to international standards and, in most cases, lack a suitable reference measure to compare against the instrumental output. In this work, a fully traceable calibration procedure is proposed, in analogy with the one already existing for catching type gauges. This requires drops of known diameter and fall velocity to be released over the instrument sensing area.

For this reason, the Calibrated Rainfall Generator (CRG) is developed, able to release single drops on demand and measure them independently just before they reach the instrument sensing area. Detachment of drops is obtained by using an electrostatic system, while the measure of their diameter and fall velocity is performed by means of a photogrammetric approach.

The Thies Laser Precipitation Monitor (LPM) was tested using the CRG considering two different output telegrams. The first one provides the raw measure of each drop sensed by the instrument while the second one provides the Particle Size and fall Velocity Distribution (PSVD) matrix. Both telegrams show a tendency to underestimate the drop diameter that increases with decreasing the drop size, while errors in the fall velocity measurements have a less definite trend. Furthermore, tests also show a large standard deviation of the measurements, significantly higher than the one of the reference measurements.

The underestimation of drop size and fall velocity is also reflected into the RI measurements provided by the instrument, with a resulting underestimation that decreases with increasing the precipitation intensity. The difference between the two telegrams considered is large and may only be explained by differences in the instrument internal processing for the two telegrams.

The second instrument tested using the CRG is the Biral VPF-750, a light scatter gauge. Results show a tendency to underestimate both the drop diameter and fall velocity. In the first case, the error decreases with increasing the drops size, similarly to the Thies LPM. However, the error in the fall velocity is considerably higher and instead increases with increasing the drop sizes. In terms of Rainfall Intensity (RI),

the instrument shows a strong underestimation that, due to the opposite trend observed for drop diameter and fall velocity, is almost constant with the precipitation intensity.

Both instruments show significant biases, corroborated by field intercomparison results from the literature, that is often larger than 10% for the investigated variables. This means that both gauges cannot be classified according to the guidelines proposed in this work for the development of a standard calibration procedure, derived from those already existing for CGs.

The second source of bias is wind, a well-established source of environmental error for traditional Catching-type Gauges (CG) but also affecting NCGs. The wind-induced bias is investigated using a numerical approach, combining Computational Fluid Dynamics (CFD) and Lagrangian Particle Tracking (LPT) models. Two different CFD models were tested, the first providing a time-independent steady state solution, while the other is fully time-dependent. Both were compared against wind tunnel results, showing a good agreement with the experimental data, and proving their ability to capture the complex aerodynamic response of instruments when impacted by the wind.

The Thies Laser Precipitation Monitor (LPM) is first chosen as a test instrument, being representative of the typical NCGs that are currently deployed in the field. CFD simulations show that wind direction is the primary factor determining the aerodynamic disturbance close to the instrument sensing area. Similar results were found for the OTT Parsivel², that is another widely diffused NCG. For wind flow parallel to the laser beam, strong disturbance close to the gauge sensing area is observed. Meanwhile, wind coming perpendicular to the laser beam produces minimal flow disturbance.

The wind-induced bias is also investigated for the Vaisala WXT-520, an impact disdrometer. This gauge is smaller and has a more regular shape if compared to the optical disdrometers, but its measuring principle is based on the detection of the drop kinetic energy, while the size and fall velocity are indirectly obtained. CFD simulations show limited disturbance close to the sensing area of the instrument and a negligible dependency on the wind direction (due to a more radially symmetric geometry). The instrument body further provides minimal shielding of the sensing area. Strong updraft however occurs upstream of the instrument for all wind directions, significantly affecting the fall velocity of the smaller and lighter drops.

Using these results, three different LPT models are also tested. The first is an uncoupled model based on the time-independent CFD results and is used to evaluate the instrument performance for all wind speeds and directions considered. The other two models, due to their high computational requirements, are applied only to a selected number of combinations of wind speed and direction for the Thies LPM. Results show a good agreement and allow concluding that the significant increase in computational burden of the latter two models does not significantly improve the accuracy of the results. However, the one-way coupled model highlights the role of turbulence, that may have a significant impact on the instrumental performance when strong recirculation is present near its sensing area. In the case of the two other gauges, only the uncoupled LPT model in combination with the time-independent CFD model is used, this being the best compromise between numerical accuracy and computational cost. Results of the LPT model are presented in terms of variation in the retrieval of precipitation microphysical properties, Catch Ratios (CR), Collection Efficiency (CE) and Radar Retrieval Efficiency (RRE).

For the three gauges considered, it is shown that smaller hydrometeors fall velocity close to the instrument sensing area is strongly affected by wind and is – in general – reduced. A significant wind-induced bias is also evident in the Drop Size Distribution (DSD) measured by the gauges. Optical gauges may report a significant lower number of small hydrometeors even at moderate wind speed. Due to the gauge body partially shielding the sensing area. Impact gauge DSD is also strongly influenced by wind, since hydrometeors with high kinetic energy are sensed as having a large diameter. The DSD is therefore shifted towards larger diameters and the instrument tends to overestimate the number of hydrometeors of all sizes. This suggests that the different shapes of the DSD function reported in the field by different instruments may be due, at least partially, to wind-induced biases.

In terms of integral precipitation characteristics, the wind direction is the primary factor in determining the performance of optical gauges in windy conditions. For wind parallel to the laser beam, the instrument senses less and less precipitation with increasing the wind speed, with no hydrometeors even reaching the sensing area in some configurations. On the other hand, when the wind is perpendicular to the laser beam, the instrument performs similarly for all wind speeds, with CR and CE values close to one and only a moderate amount of overcatch being observed at high wind speed. Only for the OTT Parsivel² a non negligible overcatch is also evident for wind coming at a 45° angle with respect to the beam direction.

For the Vaisala WXT-520 the Kinetic Catch Ratio (KCR) and Kinetic Collection Efficiency (KCE) are defined as substitutes for the CR and CE. At low wind speed, the KCR is below unity, due to the reduction in fall velocity produced by the updraft. However, with increasing wind speed, the kinetic energy of hydrometeors carried by wind increases considerably, overcoming the reduction caused by the updraft close to the gauge. For this reason, KCR values becomes much higher than unity, especially for small size hydrometeors. The increase in kinetic energy is reflected into increased KCE values, that are close to unity at low wind speed, but rapidly grow with increasing the wind speed. Wind direction has instead very limited influence on the measurements.

In terms of RRE, optical gauges present limited bias for all combinations of wind speed and direction, except for the highest wind speed and flow parallel to the laser beam. This is because a large portion of the radar reflectivity factor (dBZ) is due to medium and large size hydrometeors, that are less influenced by wind. In the case of the impact disdrometer instead, RRE behaves very similarly to the CE, with values that increases with increasing wind speed. This is due to the shift toward larger diameters noted in the DSD that occurs when hydrometeors kinetic energy is increased by wind.

INDEX

1 INTRODUCTION.....	5
1.1 In-situ measurement of atmospheric precipitation.....	5
1.2 Innovation and recent advances	7
1.3 Evidence of calibration and correction issues	8
2 MICROPHYSICAL CHARACTERISTICS OF PRECIPITATION.....	12
2.1 Particle size distribution.....	13
2.2 Drop shape and crystal types	15
2.3 Terminal velocity	17
3 IN-SITU PRECIPITATION MEASUREMENT INSTRUMENTS	20
3.1 Catching instruments.....	20
3.1.1 Tipping bucket precipitation gauges	20
3.1.2 Weighing precipitation gauges.....	21
3.1.3 Drop counter gauges	22
3.1.4 Thermodynamic gauges	22
3.2 Non-catching instruments	23
3.2.1 Optical precipitation gauges.....	23
3.2.1.1 <i>Optical transmission</i>	24
3.2.1.2 <i>Optical scattering</i>	25
3.2.1.3 <i>Optical imaging</i>	27
3.2.2 Impact precipitation gauges	29
3.2.2.1 <i>Electro-acoustic devices</i>	29
3.2.2.1 <i>Displacement devices</i>	30
3.2.3 Radar precipitation gauges.....	30
3.3 Opportunistic sensors	33
3.3.1 Measures from telecommunication antennas	33
3.3.2 Measures from surveillance cameras	34
3.3.3 Measures from car automatic wiper sensors	35
4 MEASUREMENT ACCURACY AND INSTRUMENTAL SOURCES OF BIAS	37
4.1 Calibration of non-catching instruments.....	37
4.2 Proposed procedure for traceable calibration.....	43
4.3 Development and characterization of a laboratory rain drop generator	49
4.3.1 The drop releasing head	49
4.3.2 The photogrammetric verification system	52
4.3.3 The motorized alignment gantry	55

4.3.4	Characterization of the CRG	57
4.4	Application to sample NCGs	60
4.4.1	The Thies Laser Precipitation Monitor	60
4.4.2	The Biral VPF-750	61
4.4.3	Laboratory calibration results	62
4.4.3.1	<i>Results for telegram 3</i>	64
4.4.3.2	<i>Results for telegram 4</i>	68
4.4.3.3	<i>Biral VPF-750 results</i>	73
4.5	Discussion	78
5	BLUFF-BODY AERODYNAMICS AND TRANSFER FUNCTIONS FOR NCGS .81	
5.1	The exposure problem	81
5.2	Hardware solution: the wind shield	83
5.3	Numerical simulation and transfer functions	85
5.3.1	Computational Fluid-dynamics (URANS and LES)	86
5.3.1.1	<i>Time-independent simulation</i>	88
5.3.1.2	<i>The time-dependent approach</i>	93
5.3.1.3	<i>Meshing requirements</i>	96
5.3.2	Lagrangian Particle Tracking	97
5.3.3	Drag coefficient	100
5.4	Wind-tunnel measurements	101
5.4.1	Probe measurements	102
5.4.2	Particle image velocimetry	102
5.4.3	Experimental campaign in the DICCA wind tunnel	103
6	SYNTHESIS OF TRANSFER FUNCTIONS FOR CGS	105
6.1	Meshing and fluid dynamic setup	106
6.2	CFD simulation results	107
6.3	Particle trajectories	113
6.4	Overall catch ratio	118
6.5	Transfer function for A sample precipitation climatology	125
7	CFD RESULTS AND VALIDATION FOR SAMPLE NCGS	129
7.1	OTT Parsivel²	129
7.2	Vaisala WXT-520	130
7.3	Meshing and fluid dynamic setup	131
7.3.1	Thies LPM time independent approach	131
7.3.2	Thies LPM time dependent approach	133

7.3.3	OTT Parsivel2	135
7.3.4	Vaisala WXT-520	137
7.4	CFD simulation results	139
7.4.1	Thies LPM time independent approach	139
7.4.2	Thies LPM time dependent approach	145
7.4.3	OTT Parsivel ² time independent approach.....	149
7.4.4	Vaisala WXT-520 time-independent approach.....	154
7.5	Wind tunnel testing and validation	158
7.5.1	Validation of the time independent model for the Thies LPM	159
7.5.2	Reynolds number dependency	164
7.5.3	WT comparison against the time dependent model for the Thies LPM....	165
7.5.4	Validation of the time independent model for the Vaisala WXT-520	166
7.5.5	Discussion	171
8	LPT RESULTS AND CATCH RATIOS	172
8.1	LPT model setup	172
8.1.1	LPT simulation setup for the Thies LPM.....	172
8.1.2	LPT simulation setup for the OTT Parsivel ²	174
8.1.3	LPT simulation setup for the Vaisala WXT-520	175
8.2	visualization OF PARTICLE TRAJECTORIES.....	176
8.2.1	Hydrometeor trajectories near the Thies LPM.....	176
8.3.2.1	<i>Time-independent uncoupled LPT simulation.....</i>	<i>177</i>
8.3.2.2	<i>Time-dependent uncoupled simulation.....</i>	<i>179</i>
8.3.2.3	<i>Time-dependent one-way coupled simulation</i>	<i>180</i>
8.2.2	Hydrometeor trajectories near the OTT Parsivel ²	181
8.2.3	Hydrometeor trajectories near the Vaisala WXT-520.....	184
8.3	Catch ratios	186
8.3.1	Catch ratios for the Thies LPM.....	186
8.4.1.1	<i>Catch ratios from the time-independent uncoupled LPT model.....</i>	<i>186</i>
8.4.1.2	<i>Catch ratios from the time-dependent uncoupled LPT model.....</i>	<i>190</i>
8.4.1.3	<i>Catch ratios from the time-dependent one-way coupled LPT model</i>	<i>191</i>
8.3.2	Catch ratios for the OTT Parsivel ²	191
8.3.3	Catch ratios for the Vaisala WXT-520.....	194
9	IMPACT ON PRECIPITATION MEASUREMENTS	198
9.1	Wind induced bias on the PSVD.....	198
9.1.1	Fall velocity.....	198
9.1.1.1	<i>Fall velocity bias for the Thies LPM</i>	<i>198</i>
9.1.1.2	<i>Fall velocity bias for the OTT Parsivel²</i>	<i>199</i>
9.1.1.3	<i>Fall velocity bias for the Vaisala WXT-520</i>	<i>201</i>

9.1.2 Drop size distribution	201
9.1.3.1 DSD bias for the Thies LPM.....	202
9.1.3.2 DSD bias for the OTT Parsivel ²	203
9.1.3.3 DSD bias for the Vaisala WXT-520.....	203
9.2 The collection efficiency.....	204
9.2.1 The collection efficiency of the Thies LPM.....	205
9.2.2 The collection efficiency of the OTT Parsivel ²	208
9.2.3 The kinetic collection efficiency of the Vaisala WXT-520.....	210
9.3 Radar reflectivity factor	213
9.3.1 Radar retrieval efficiency for the Thies LPM	214
9.3.2 Radar retrieval efficiency for the OTT Parsivel ²	217
9.3.3 Radar retrieval efficiency for the Vaisala WXT-520	219
9.4 Discussion.....	222
10 CONCLUSIONS.....	224
11 REFERENCES	226

1 INTRODUCTION

Precipitation is a key component of the hydrological cycle and has a direct impact on numerous aspects of society, like drinkable water availability, agriculture, transportation, energy production, flooding events and much more aspects of everyday life. It is therefore evident that a precise and meticulous measure of precipitation is a priority of human society. Examples of systematic measurements of precipitation dating back to almost 800 years ago can be found in China and evidence of previous attempts – more than two thousand years old – can be found in other parts of the globe, meaning that precipitation measurement is something that is directly correlated with the development of society itself.

The first modern measurement of rainfall is usually attributed to Benedetto Castelli, an Italian monk, that in a letter to Galileo in 1639 wrote: *“I took a glass formed like a cylinder, about a palm high, and half a palm broad [12 centimetres diameter]; and having put in it water sufficient to cover the bottom of the glass, I noted diligently the mark of the height of the water in the glass, and afterwards exposed to open weather, to receive the rain water, which fell into it; and I let it stand for the space of an hour; and having observed that in that time the water was risen in the vessel the height of the following line [about 10 millimetres long to represent the depth]. I considered that if I had exposed the same rain such other vessel equal to that, the water would have risen in them according to that measure”*. In the following centuries numerous technological advancements followed, with the creation of several mechanical (first) and electrical (later) gauges capable of automatically recording precipitation events over long periods of time (Strangeways I., 2010).

1.1 IN-SITU MEASUREMENT OF ATMOSPHERIC PRECIPITATION

In the Guide to Meteorological Instruments and Methods of Observation (WMO, 2021) published by the World Meteorological Organization (WMO), precipitation is defined as *“the liquid or solid products of the condensation of water vapour falling from clouds, in the form of rain, drizzle, snow, snow grains, snow pellets, hail and ice pellets; or falling from clear air in the form of diamond dust”*. The total amount of precipitation which reaches the ground in a stated period is expressed in terms of the vertical depth of water (or water equivalent in the case of solid forms) to which it would cover a horizontal projection of the Earth’s surface. The measurement unit of precipitation amount is therefore linear depth, usually in millimetres (volume/area), or kg m^{-2} (mass/area). Less than 0.1 mm (or 0.2 mm depending on the resolution used) is generally referred to as trace precipitation. The common observation times are hourly, three-hourly, and daily, for synoptic, climatological, and hydrological purposes, respectively.

Precipitation intensity is defined as the amount of precipitation collected per unit time interval and can be derived from the measurement of precipitation amount using an ordinary precipitation gauge. In that sense, precipitation intensity is a secondary parameter, derived from the primary parameter precipitation amount. However, precipitation intensity can also be directly measured as the flow of the captured water, the accretion of collected water as a function of time or using some optical principles. Various techniques for determining precipitation amount are based on these direct intensity measurements after integrating the

measured intensity over a certain time interval. The measurement unit of Rainfall Intensity (RI) is linear depth per hour, usually expressed in millimetres per hour (mm h^{-1}). Rainfall intensity is normally measured or derived at a one-minute time resolution due to its high variability from minute to minute. For some purposes, such as the design and management of urban drainage systems, forecasting and mitigation of flash floods, transport safety measures, and in general most of the applications where rainfall data are sought in real time, such a fine temporal resolution is required to measure high rainfall rates over short periods.

Precipitation varies considerably in both space and time; it is erratic in nature and intermittent even during a single precipitation event. The precipitation process is made of an ensemble of a wide variety of hydrometeors, each of them reaching the ground with its own size, shape, density and fall velocity, resulting from the complex atmospheric processes of nucleation, accretion, melting and interactions between the hydrometeors (see e.g., Wang, 2013). The microphysical characteristics of precipitation therefore depend on the generating weather phenomenon and climate at any specific location (temperature, humidity, etc.).

Typical instruments used for measuring precipitation are also very sensitive to exposure, and in particular to wind, especially for solid precipitation, which is more susceptible to wind effect than liquid precipitation due to the lower density of hydrometeors. Precipitation is, therefore, among the most challenging environmental measurements, and accurate evaluation of the amount of water that would ultimately land on a well-defined portion of the ground surface in undisturbed conditions is a difficult task. This is the aim of the so-called in-situ measurements at the ground, with the measurement instrument located precisely where the information is sought, at a single location immersed in the precipitation process. Precipitation gauges (or rain gauges if only liquid precipitation is measured) are the most adopted measurement instruments.

Precipitation measurements from in-situ instruments are still the primary source of data also for areal analysis (e.g., catchment hydrology), although each gauge is representative of a limited area in space, the size of which is a function of the length of the accumulation period, the physiographic homogeneity of the region, local topography, and the precipitation-producing process (WMO, 2021). Therefore, techniques for areal measurement like weather radar and, more recently, satellite borne sensors are also often used to quantify the spatial distribution of precipitation from a remote sensing perspective, with the sensor generally located far from the precipitation process. The information is inferred from the observed modifications of other physical quantities due to their interference with the precipitation process (e.g., active/passive microwave reflectivity, infrared temperature, etc.).

In-situ precipitation gauges, however, provide the only direct measurement of precipitation at the ground and are usually referred to as the ground truth. Remote sensing techniques for extensive observations (essentially weather radar, aircraft and satellite borne radiometers) still require the use of in-situ measurements for calibration and validation purposes. Following Michaelides et al. (2009), “*measurements at the ground have been proved indispensable, despite advances in several areas of remotely sensing of precipitation. Ground truth seems to be inseparable from any study on precipitation. A better understanding of the behaviour of precipitation on the ground with direct measurements can lead to more effective estimations by using other methodologies*”. In principle, a suitable integration of all three sources of areal precipitation data into national precipitation networks (automatic gauges, radar, and satellite sensors) can

be assumed to provide sufficiently accurate areal precipitation estimates on an operational basis for a wide range of users.

All methods for measuring precipitation should aim to obtain a sample that is representative of the true amount falling over the area which the measurement is intended to represent, whether on the synoptic scale, mesoscale or microscale. The choice of the siting of the measurement instrument is, therefore, important. For a discussion of the effects of the siting, see Sevruk and Zahlavova (1994) and the siting classification standard EN-19289:2014 developed by WMO. The location of precipitation stations within the area of interest is important, because the number and locations of the gauge stations determine how well the measurements represent the actual amount of precipitation falling in the area. The effects on the wind field of the immediate surroundings of the site can also have a significant impact and give rise to local excesses and deficiencies in precipitation measurements. In general, objects should not be closer to the gauge than twice their height above the gauge orifice. Sites on a slope or the roof of a building should be avoided. Sites selected for measuring snowfall and/or snow cover should be in areas sheltered as much as possible from the wind. The best sites are often found in clearings within forests or orchards, among trees, in scrub or shrub forests, or where other objects act as an effective windbreak for winds from all directions.

1.2 INNOVATION AND RECENT ADVANCES

Starting from the old and trivial technique of using a graduated cylinder to collect and manually measure precipitation, numerous advances were made for in-situ precipitation gauges. The need for continuous measurements over a long period of time, allowing for automatic recording of data with limited user intervention, prompted the development of precipitation gauges using several different measuring principles. The first and for a long time unique family of precipitation gauges is constituted by the so-called catching-type instruments. They collect precipitation inside a reservoir to measure the water volume or weight. Catching-type Gauges, hereinafter CGs, due to their simple functioning principles and relative low cost, are widely diffused and are still being deployed in the field by National Meteorological and Hydrological Services (NMHS) and other similar organizations. Yet they present two major drawbacks: the frequent maintenance required (usually to prevent clogging of the funnel used to collect precipitation or to periodically empty the instrument reservoir), and the limited amount of information provided, in general limited to the precipitation amount and/or intensity.

Recently, after decades of scarce innovation, a new family of in-situ precipitation gauges was developed. They are called Non-Catching Gauges, hereinafter NCGs, since they can measure the microphysical and dynamic characteristics of single or multiple hydrometeors while these cross a given section, or a volume, of the atmosphere (or directly impact the sensor) by employing optical, acoustic, and microwave principles. These gauges experienced a considerable growth in market share, with a significant increase in interest from NMHSs (Cauteruccio et al., 2021b). They differ from traditional CGs because the collection of precipitation inside a reservoir is no longer needed and, usually, a contactless approach is used. Another fundamental difference between CGs and NCGs is the wider range of information they can provide, which, due to the more complex measuring principles adopted, is not limited to precipitation amount and intensity, but also includes, for example, visibility, present weather, and the size and fall velocity of each hydrometeor (therefore they are also called “disdrometers”).

NMHSs and other organizations in charge of the management of monitoring observation networks over large regions, increasingly look at such kind of instruments as a potential improvement over the more traditional CGs (typically tipping bucket and weighing gauges), notwithstanding the higher lifecycle cost. The reasons are their potential in reducing the maintenance burden (by eliminating any moving part or containers to be periodically emptied and serviced), the high temporal resolution, the large number of parameters provided, and their suitability to be part of a fully automated monitoring network. Drawbacks can be easily identified in the higher complexity of the exploited technology, so that the capability of the user to correctly manipulate, maintain and calibrate the instrument may be limited.

1.3 EVIDENCE OF CALIBRATION AND CORRECTION ISSUES

Due to the focus they gathered from researchers, NMHSs, and similar organizations, several attempts to compare measurements from CGs and NCGs are available in literature, generally in the form of field intercomparisons. One of the most detailed and comprehensive is the WMO field intercomparison of rainfall intensity gauges (Vuerich et al., 2009), a collaboration between WMO and the Italian Meteorological Service that took place in the experimental site of Vigna di Valle (IT), as a follow up of the WMO Laboratory Intercomparison of Rainfall Intensity Gauges (Lanza et al., 2005). The focus of that work was to compare the performance of in-situ rainfall intensity instruments using different measuring principles, with special consideration given to high rainfall intensities. Further objectives were to offer advice on improvements of instruments and precipitation measurements.

The intercomparison hosted 25 different rainfall intensity gauges, the majority of which were CGs comprising tipping-bucket gauges, weighing gauges and one water level gauge. NCGs were represented by optical and impact disdrometers, one optical/capacitive gauge and one microwave radar. Measurements from those instruments installed in the field were compared against a four-folded reference pit gauge, with reference instrument installed inside a specifically designed pit, with their collecting area positioned at ground level so that the influence of wind on measurements was minimized (Lanza & Vuerich, 2009).

While the CGs were calibrated at the University of Genoa before starting the intercomparison, NCGs were calibrated by the manufacturers in the absence of any standard calibration procedure. Therefore, factory calibration reports and information about calibration methods as provided by manufacturers were the only sources of information available on the achievable accuracy of these instruments. Results of the field campaign showed that the accordance with the reference measurements was, on average, lower for the NCGs than in the case of traditional CGs. Depending on the measuring principle adopted by the instrument and on the precipitation intensity itself, significant under- or over-estimation was observed. Also, most of those instruments presented a nonlinear behaviour coupled with a larger spread of the data if compared with CGs. That work therefore highlighted the need to improve calibration methods of the NCGs for one-minute Rainfall Intensity (RI) measurements.

Similar conclusions were independently reached in a previous work published by Lanzinger et al. (2006) where three identical NCGs (Thies Laser Precipitation Monitor – LPM) (Thies, 2011), were tested against a reference CG positioned in a pit. Results showed a low agreement between the three NCGs and the reference, with the tendency of overestimating precipitation intensity, especially in the higher range. Low

agreement between measurements was also shown by comparing the three NCGs against themselves, with differences in the total precipitation amount provided at the end of the intercomparison campaign summing up to 20% higher if compared against the reference and more than 10% if compared against one another.

In the work of de Moraes Frasson et al. (2011) four Thies LPM optical disdrometers and three Vaisala WXT-510 impact disdrometers were compared against reference tipping bucket gauges. The total precipitation amount reported by the instruments over the long period show a strong difference between the three types of precipitation gauges, with the disdrometers significantly overestimating the precipitation amount. The bias between NCGs and the reference tipping bucket was shown to increase with the precipitation intensity.

During this work, an evaluation of beam uniformity for the Thies LPM was also performed, with the intent of reducing the measurement bias arising from the difference in beam power density across the sensing area. A correction was proposed using Montecarlo simulations to evaluate the influence of beam uniformity for each instrument. This approach reduced the spread between the Thies LPMs measurements but did not significantly reduce the bias between them and the reference. This suggested that factors other than beam power density control the measurement bias.

Another intercomparison, more focused on the additional data that is usually provided by NCGs, between a Dual Beam Spectropluviometer (DBS) (Delahaye et al., 2006), a two-dimensional video disdrometer (2DVD) (Kruger & Krajewski, 2002) and an optical PM Tech Parsivel disdrometer (Löffler-Mang & Joss, 2000), was presented by Krajewski et al. (2006). Instruments were installed in a small airfield and compared between themselves and against a reference CG installed in close proximity. The authors noted that differences between NCGs were higher than expected and not justified by the spatial variability of precipitation due to the small size area of the test site. Differences were especially noted in the distribution of the size and fall velocity of hydrometeors, with some instrument (like the PM Tech Parsivel) consistently reporting a higher number of small hydrometeors and fall velocities that were far from long established velocity-diameter relationships (Gunn & Kinzer, 1948). It was also noted that accordance in the number of hydrometeors sensed in the ranges of both small ($< 1\text{mm}$) and large ($> 3\text{ mm}$) diameter was poor for both the 2DVD and the DBS.

A similar intercomparison is presented in the work of Tokai et al. (2013), where an impact-type Joss–Waldvogel disdrometer, an improved version of the 2DVD, and the OTT Parsivel were compared. In terms of precipitation amount, the NCGs produced results closer to the reference CG but still showed a tendency to overestimate or underestimate rainfall rates that increased with the precipitation intensity. It was also noted that the OTT Parsivel tended to overestimate the number of large drops if compared with the 2DVD, especially for high rainfall rates. An improved version of the OTT Parsivel disdrometer, called Parsivel², was tested in the work of Tokay et al. (2014) reporting a significant improvement in performance if compared with the previous version, yet reporting some anomalies on the measured fall velocity (possibly due to software issues that required the manufacturer intervention).

An almost identical conclusion is reached in the work of Sarkar et al. (2015), where a Joss–Waldvogel impact disdrometer, a Thies LPM and a Metek Micro Rain Radar (MRR) were compared against each other in a tropical region, during the monsoon season. Results showed that the three NCGs were able to provide

consistent results only for rainfall rates below 30 mm h⁻¹ and presented strong differences for higher intensities.

A radar disdrometer was tested in the work of Caracciolo et al. (2005) by comparing the results of the newly developed Pludix radar disdrometer against the Joss–Waldvogel impact disdrometer and the 2DVD in two different sites, Ferrara in Italy, and Cabauw in the Netherlands. Consistently with the experiments reported above, results showed not negligible differences in both the rainfall amount (compared against reference CGs) and the drop size distribution for diameters in both the small and very large ranges.

A recent intercomparison of optical disdrometers is presented in the work of Johansen et al. (2020), where two Campbell Scientific PWS100, one Thies LPM and one first generation OTT Parsivel were tested against some reference CGs. Although the work was mostly focused on evaluating the kinetic energy flux of precipitation for soil erosion evaluation purposes yet results in terms of rainfall amount and drops sizes and fall velocities were presented, showing a tendency of the NCGs under test to underestimate precipitation and discrepancies on the reported fall velocities that was in general underestimated for large diameter drops (above 1mm) and overestimated for the smaller ones.

Regarding solid precipitation, NCGs were included in the recent WMO SPICE (Solid Precipitation InterComparison Experiment) and compared with CGs in a reference shielded configuration (the DFIR – Double Fence Intercomparison Reference) at various test sites (Nitu et al., 2018). The study was inconclusive on these instruments and recommended that further research is undertaken to better understand the behaviour of non-contact type measurement instruments, especially working with the raw data (drop size and fall speed distribution) and exploiting the full capacity of such devices to provide additional information than the precipitation accumulation (precipitation type, SYNOP and METAR codes, etc.). Field tests at SPICE reference sites have been continued in that sense after the official end of the project (Smith et al., 2020) to enhance the knowledge on the operational use of non-catching type instruments in winter conditions. For example, results from the Formigal site, located in a mountainous region in Spain, highlighted the tendency of optical disdrometers (Thies LPM and OTT Parsivel2) to strongly overestimate precipitation amount (up to 100%) under windy conditions, which persists even for instruments installed inside the wind shield as a reference installation.

Further important sources of information about solid precipitation measurement using NCGs are the field campaigns held during the Global Precipitation Measurement Cold-season Precipitation Experiment (GPM-GCPEX) (Skofronick-Jackson et al., 2015) and the Olympic Mountains Experiment (OLYMPEX) (Houze et al., 2017). Both these NASA sponsored intercomparisons that were conducted respectively near Egbert, Ontario, Canada in January-February 2012 and in the Olympic Peninsula of Washington State in 2015/2016, aimed to study the physical characteristics and microwave radiative properties of the column of hydrometeors in cold season precipitation events, with the intent of improving knowledge about satellite based solid precipitation measurement. Limited information about the measurement bias of NCGs for these intercomparisons is available since those instruments were mostly employed as the ground truth and were then compared against radar and satellite measurements. Yet some bias, already highlighted in previously presented works, were observed, like a noticeable difference between the Parsivel and 2DVD measurements and a significant bias of NCGs with respect to the reference CGs (Höschen et al., 2013).

It is worth noting that in the context of the literature presented above, it is often unclear if the CGs used as reference were properly calibrated against instrumental error, that could have had a very strong impact on the results.

Also, in the case of reference CGs placed inside the DFIR/DFAR (Automatic Double Fence Reference) wind shield for solid precipitation measurement, a residual wind-induced bias is still present due to the geometry of the shield and construction issues (see e.g., Thériault et al., 2015).

It is evident that NCGs are the subject of increasing attention from the scientific community because they can have a significant impact on several fields tied to the study of precipitation and are often used in critical applications like airport management. Yet, it is also abundantly clear that before such gauges can express their maximum potential, further research is needed, especially on evaluating the bias of the various types of measurements they provide. The goal of the present work is to improve the overall knowledge available on NCGs, in terms of the biases that affects them. In this thesis procedures for the evaluation of both the instrumental bias and the wind induced bias are developed and some applications of such methods are presented. Regarding the first form of bias, it was shown to be relevant by several intercomparisons, that highlighted sizeable differences both between different NCGs and the reference or even between different specimen of the same NCG. This is mostly due to the complexity required to properly calibrate one such gauge to a traceable standard, since the actual precipitation microphysical properties must be reproduced. Furthermore, the lack of common guidelines and calibration procedures makes evaluating instrument performances challenging for the user and may introduce gross errors when comparing measurements from different gauges. Regarding the latter, wind is a well-known source of bias, that affects all precipitation gauges that was thoroughly evaluated for CGs and may be even more relevant for NCGs for which it was however rarely investigated. This is because NCGs usually present much more complex shapes and measure not only the total volume collected but several microphysical properties of precipitation, that may be also affected by wind. Since NCGs are often used for research applications and ground reference for satellite or radar measurements, understanding and correcting the biases that affects such gauges is a necessary step to improve our overall capability of measuring precipitation. Furthermore, these new methods and information may also spur manufacturer to improve existing gauges, providing newer and better performing alternatives to the users.

2 MICROPHYSICAL CHARACTERISTICS OF PRECIPITATION

Precipitation can be described using several different parameters, that can be divided in two categories, microphysical characteristics, describing the properties of each individual hydrometeor, and integral characteristics, describing the overall precipitation process.

Microphysical characteristics of hydrometeors are, for example, their diameter, shape, density and fall velocity. Usually, one method used to characterize precipitation events is to provide the associated Particle Size Distribution (PSD) or, in the case of liquid precipitation only, the Drop Size Distribution (DSD). The PSD, usually indicated with $N(D)$ and expressed in $[L^{-3} L^{-1}]$, provides the number of particles (liquid or solid) per unit volume of air and per unit size interval having a volume equal to the sphere of diameter comprised between D and $D + dD$. If the fall velocity of hydrometeors is also associated with each corresponding diameter, the Particle Size and fall Velocity Distribution (PSVD) is obtained.

More often, integral quantities are provided to describe the precipitation event. Those are for example the precipitation amount, the precipitation intensity or radar reflectivity, that are obtained by integrating the microphysical properties like the DSD. The most common is precipitation intensity $[mm\ h^{-1}]$ (usually indicated as Snowfall Intensity, SI, for solid and Rainfall Intensity, RI, for liquid precipitation), that is an integral parameter obtained as the third-order weighted moment of the drop size distribution $N(D)$, when the drop terminal velocity w_T $[m\ s^{-1}]$ is used as the weight of each individual drop, as follows (see e.g., Ulbrich 1983; Nespor and Sevruk, 1998):

$$RI = C_c \int_{D_{min}}^{D_{max}} N(D) V(D) w_T(D) dD \quad 2.1$$

where $C_c = 3.6 \cdot 10^6$ $[mm\ h^{-1}\ m^{-1}\ s]$ is the numerical factor for the conversion of the rate of rainfall from $[m\ s^{-1}]$ to $[mm\ h^{-1}]$; $N(D)$ $[m^{-3}\ m^{-1}]$ is the number of drops per unit volume of air and unit drop size interval, with the equivalent diameter D $[m]$ ($D_{min} \leq D \leq D_{max}$); $V(D) = \pi D^3/6$ $[m^3]$ is the drop volume; and $w_T(D)$ $[m\ s^{-1}]$ is the drop terminal velocity.

Another integral characteristic of precipitation that is often sought from NCGs measurements is radar reflectivity factor (Z), that is obtained from Equation 2.2.

$$Z = \int_{D_{min}}^{D_{max}} N(D) D^6 dD \quad 2.2$$

It is defined as the integral of the sixth-order weighted moment of the drop size distribution within a control volume divided by the control volume itself, that in the case of Equation 2.2 is $1\ m^3$.

Radar reflectivity factor is the primary variable used by weather radar and it is directly proportional to the intensity of the radar signal that is reflected by the hydrometeors in the air. It is computed under the hypothesis that Rayleigh approximation holds true, meaning that drops are considered as dielectric spheres that are small in respect the signal wavelength. Under these hypotheses it can also be correlated to the precipitation intensity. Its measurement unit is $[mm^6 m^{-3}]$ and, since its value can change drastically, is more often expressed in logarithmic unit (dBZ), as shown by equation 2.3.

$$dBZ = 10 \log \left(\frac{Z}{1 mm^6 m^{-3}} \right)$$

2.3

The following sections are published in (Lanza et al. 2021).

2.1 PARTICLE SIZE DISTRIBUTION

The PSD is usually depicted in a $(d, N(D))$ semi-logarithmic plot. A universal formulation that can describe in a straightforward way the high variability of PSDs in nature, influenced by the regional and seasonal climatology and processes governing the formation of hydrometeors in the atmosphere, is not available. Information about the PSD comes from observations and is therefore subject to uncertainties that are rarely quantified. Two formulations for the PSD are commonly used in the literature, the Exponential (Marshall and Palmer, 1948) and the Gamma (Ulbrich, 1983) distributions. By fitting experimental observations obtained using dyed filter paper Marshall and Palmer (1948) provided the exponential form of the PSD as follows:

$$N(D) = N_0 e^{-\Lambda d}$$

2.4

where N_0 and Λ are two suitable parameters, with $N_0 [L^{-1} L^{-3}]$ the intercept and $\Lambda [L^{-1}]$ the slope of the linear form of this curve in a semi-log plot. Marshall and Palmer, for a widespread mid-latitude rain, found a constant value $N_0 = 8000 [mm^{-1} m^{-3}]$ and a relationship for Λ , as a function of the rainfall intensity (RI), as reported in Equation 2.5.

$$\Lambda = 41 RI^{-0.21} [cm^{-1}]$$

2.5

This distribution is valid for stratiform precipitations and has the tendency to overestimate the concentration of small drops (typically under 0.5 mm). Indeed, these droplets cannot fall if there is upward wind and tend to evaporate when they enter non-saturated air. Integration of this distribution between 0.5 and 6 mm for a rainfall rate of e.g., 5 mm h⁻¹ gives a total concentration of drops of 6.4x10⁻⁴ [cm⁻³]. This

means that there are typically between 100 and 1000 drops/m³ during stratiform rain, corresponding to an approximate distance between drops of 20 cm and 10 cm. Waldvogel (1974), by measuring the distribution of raindrops with an electro-acoustic device (see functioning description in section 3.2.2) and by means of a radar reflectivity analysis, for different types of precipitation (showers, thunderstorms and widespread rain), showed that the parameter N_0 is not constant and can change abruptly because it is a function of the convection activity in the clouds. He called this phenomenon “The N_0 jump”. Radar measurements indicated that the N_0 jump occurred when one of the mesoscale convective areas moved in or out the region above the station, which means that the situation changed from uniform (widespread rain) to convective (shower or thunderstorm) or vice versa. For very small drop diameters (below 1 mm) the $N(D)$ values decrease with decreasing particle diameter, therefore, a downward concavity of the PSD is obtained. Currently, it is not clear whether this characteristic is ascribable to the limitation of the measuring instruments to detect very small particles, or it is physically based. Moreover, some disdrometers, especially radars, provide higher $N(D)$ values for small diameters causing an upward concavity in the distribution. Ulbrich (1983) proposed the Gamma distribution in the form:

$$N(D) = N_0 d D^\mu e^{-\Lambda d}$$

2.6

where the exponent μ is the shape parameter and can have positive or negative values and the intercept N_0 is in [mm^{-1- μ} m⁻³], D in [mm], when $N(D)$ is expressed in [mm⁻¹ m⁻³].

Ulbrich summarized experimental observations reported by other authors including Mueller (1965), Caton (1966) and Blanchard (1953). In the work of Mueller, a variety of rainfall types including continuous rain, showers and thunderstorms were observed and for all of them the observed PSDs are concave downward. When fitted with the gamma formulation these PSDs would have $\mu > 0$. Almost all Caton's PSDs are similar to those reported by Mueller and can be described by a Gamma distribution with $\mu > 0$. Differently, orographic precipitation, as observed by Blanchard, is characterized by many small size drops. This type of precipitation events can be described by a Gamma distribution with $\mu < 0$. In addition, Ulbrich conducted a theoretical analysis with the aim to describe the modification of the distribution from the exponential form to a concave shape. The author affirmed that the variation in N_0 is independent from the variation of Λ while a direct relationship between N_0 and μ exists in the form:

$$N_0 = 6 * 10^4 e^{3.2\mu} [\text{cm}^{-1-\mu} \text{m}^{-3}]$$

2.7

The work of Caracciolo et al. (2008) is based on rain events measured in the Italian territory by employing radar and two different types of disdrometers (Joss-Waldvogel and Pludix) with a sampling time of one minute. Each 1-minute PSD value was classified into one out of six categories, based on the measured liquid precipitation intensity (RI). Two examples of the average observed PSD data collected in

Florence (Italy) obtained by the Joss-Waldvogel and Pludix disdrometers are reported in Figure 2.1, where the minimum diameter observed by the Pludix is 1 mm while the Joss-Waldvogel also reports data for $D < 1$ mm. It is useful to observe that, for the same region and precipitation rate category, different PSD were obtained by the two instruments, especially in the case of higher precipitation intensity, also showing an opposite trend for hydrometeors of $D < 2$ mm.

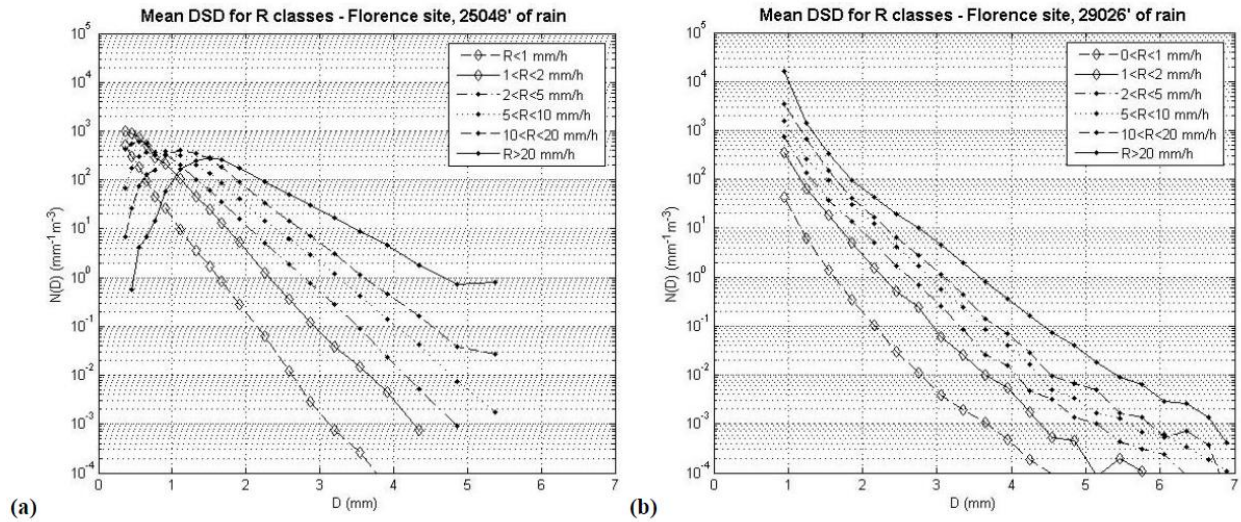


Figure 2.1: Average observed PSDs for the Florence database collected in Florence (Italy): Joss-Waldvogel disdrometer (a) and Pludix disdrometer (b), for six rainfall rate categories as reported by Caracciolo et al. (2008).

As for solid precipitation, in the work of Houze et al. (1979) the parameters of the Marshall-Palmer distribution (Equation 2.4) were derived as a function of the air temperature from measurements in frontal clouds obtained using an optical particle spectrometer. The temperature (T) at flight altitude during the probe measurements ranged from -42 °C to $+6$ °C. Results showed that both N_0 and Λ decrease with increasing (T) and a sudden “jump” of the Λ value occurred for (T) > 0 °C when aggregated snow particles melt to much smaller and faster falling drops.

2.2 DROP SHAPE AND CRYSTAL TYPES

Some measurement principles exploited by non-catching type gauges detect the dimension of the horizontal axis of the drop to calculate its volume. Small drops, up to 1 mm in diameter, are almost perfectly spherical. Larger drops are flattened by the dynamical pressure applied by the air. Different theories exist to model the shape of the drops as a function of their equivalent diameter (diameter of a sphere with an equal volume). The result of one of these theories is presented in Figure 2.2 (from Beard and Chuang, 1987). The drop surface can be represented by following equation developed by Pruppacher and Pitter, 1971) as a function of the equivalent radius a_o , the deformation coefficient c_n and the polar angle from the

forward stagnation point θ . The c_n values are listed in the two mentioned works as a function of drop size.

$$r = a_o(1 - c_n \cos(\theta n))$$

2.8

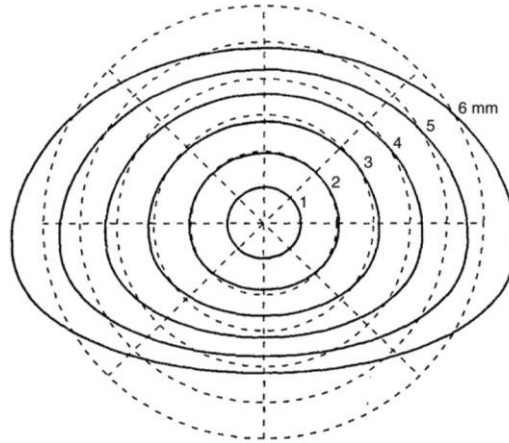


Figure 2.2: Shape of falling drops as a function of their equivalent diameter (from Beard and Chuang, 1987). Small drops up to 1 mm are almost perfectly spherical while larger ones quickly assume their typical oblate shape.

Some theories, such as the model of Pruppacher and Pitter (1971), predict a recurved base (a small dent present at the base of the drop) for large drops. Further to this equilibrium shape, vibrations appear in falling drops. These oscillations are typically at a frequency of a few tens of Hz or an oscillation period of a few tens of milliseconds (Szakall et al., 2009). The balance among the forces of surface tension, hydrostatic pressure, and aerodynamic pressure from airflow around the drop determines the shape and the terminal fall velocity of hydrometeors. Green (1975), using a simple hydrostatic model, represented rain drops as oblate spheroids with axis ratios determined by the balance of surface tension and hydrostatic forces. Pruppacher and Beard (1970), by means of wind tunnel experiments, found that the raindrop shape can be defined in terms of the axial ratio (b/a) between the vertical (b) and the horizontal axis (a). For raindrops with the equivolumetric drop diameter d between 1 mm and 9 mm they obtained the following empirical equation:

$$\frac{b}{a} = 1.03 - 0.062 d$$

2.9

while for $D < 1$ mm the axial ratio is $b/a = 1$.

Beard and Chuang (1987), introducing the contribution of the aerodynamic pressure in the equilibrium condition, provided a model able to explain the drop shape with its characteristic flattened base that increases with drop size and, for drops having a diameter between 2 mm and 6 mm, can be expressed in terms of the following polynomial:

$$\frac{b}{a} = 1.0048 + 5.7 \cdot 10^{-4}D - 2.628 \cdot 10^{-2}D^2 + 3.682 \cdot 10^{-3}D^3 - 1.677 \cdot 10^{-4}D^4$$

2.10

Model results of Beard and Chuang (1987) were consistent with the experiments of Chandrasekar et al. (1988) and by Bringi et al. (1998), which employed aircrafts to study the shape of raindrops in natural rainfall.

Contrary to raindrops, snow crystals present an incredible variety of shapes and sizes, that makes categorizing them a complex endeavour. Several attempts to classify crystal shapes spanning over a long period of time were made, the most used classification was proposed by Magono and Lee (1966), that classified natural snow crystals into 80 categories based on their shape. Their classification scheme is widely used by scientists to describe snow crystal shapes. However, it was based mainly on observations in Japan and did not include several types of snow crystals that are observed only in Arctic and Antarctic regions. Several works tried to improve that classification scheme, the last of which, proposed by Kikuchi et al. (2013), included observations of particles from middle latitudes to polar regions since 1968. It is called global classification and it consists of three levels: general, intermediate, and elementary. The general level has 8 categories, the intermediate level has 39 categories, and the elementary level has 121 categories.

2.3 TERMINAL VELOCITY

Since drops fall from a high altitude, they reach the ground with their terminal velocity. The terminal velocity, w_T , is defined as the maximum velocity attainable by an object as it falls through a fluid. This condition is reached when the sum of the drag force and the buoyancy force is equal to the downward force of gravity acting on the object. In these conditions the motion of the object is no more accelerated. As reported in various literature works where hydrometeor trajectories are modelled (see e.g., Nešpor and Sevruc, 1999; Thériault et al., 2012, 2015; Colli et al. 2016b) the motion of a falling particle in the atmosphere is described by the following equation:

$$\rho_p V_p \mathbf{a}_p = -\frac{1}{2} C_D A_p \rho_a (\mathbf{v}_p - \mathbf{v}_a) |\mathbf{v}_p - \mathbf{v}_a| + V_p (\rho_a - \rho_p) \mathbf{g}$$

2.11

where \mathbf{a}_p is the particle acceleration, \mathbf{v}_a and \mathbf{v}_p are the velocity vectors of the air and the particle, \mathbf{g} is the gravity acceleration, C_D is the drag coefficient, A_p is the particle cross section area and ρ_a and ρ_p are the density of the air and the particle. Equation 2.11 is written assuming the positive orientation of the z axis upward and the velocity and acceleration components are positive in the positive direction of the related axes. The quantity $\mathbf{v}_p - \mathbf{v}_a$ is the relative particle-to-air velocity. The vertical component of Equation 2.11 becomes:

$$a_{pz} = -\frac{1}{2} C_D A_p \frac{\rho_a}{\rho_p V_p} (w_p - w_a) |\mathbf{v}_p - \mathbf{v}_a| + \frac{(\rho_p - \rho_a)}{\rho_p} g \quad 2.12$$

where the gravity acceleration (g) assumes the negative value of -9.81 m s^{-2} . When a generic drop falls in a stagnant air, its terminal velocity can be obtained from Equation 2.12 as:

$$w_T = \left[\frac{2V_p(\rho_p - \rho_a)g}{C_D A_p \rho_a} \right]^{1/2} \quad 2.13$$

The drag coefficient (C_D) is a dimensionless quantity used to represent the resistance of an object in motion in a fluid, such as air or water and associated with the cross-sectional area of the object (A_p). The estimation of the drag coefficient is not easy. In the literature, different experiments were carried out with the objective to identify a relationship between the drag coefficient and the particle dimension and/or its terminal velocity for hydrometeors falling through the atmosphere (see e.g., Gunn and Kinzer, 1949; Beard, 1976). Semi-empirical relationships are also often used for rain and for different frozen hydrometeors (hail and snow), like the one, developed for raindrops, present in the work of Atlas et al. (1973) that is shown in Equation 2.11, where d is in mm, and w_T is in m s^{-1} .

$$w_T(d) = 9.65 - 10.3e^{-0.6D} \quad 2.14$$

The same principle applies to solid precipitation, with the caveat that, due to the variety of naturally occurring shapes of snowfall crystals, each one characterized by its own drag coefficient (see e.g. Tagliavini et al., 2021), a unique relationship between hydrometeors diameter and fall velocity is difficult to achieve. In the work of Rasmussen et al. (1999) observed data from the Marshall Snowfall Test Site, near Boulder (Colorado), of the National Center for Atmospheric Research, were classified in a large number of crystal types (e.g., dendrites, hexagonal plates, lump graupels, etc.) and aggregated in two macro categories: “dry” and “wet” snow. In that work, the volume V_p , the cross-section area A_p , density ρ_p and terminal velocity w_T of each type of snowflake are parametrized with a power law curve as a function of the equivalent particle diameter D :

$$Y(D) = a_Y D^{b_Y} \quad 2.15$$

where Y assumes the nomenclature of the volume V_p , the cross-section area A_p , density ρ_p and terminal velocity w_T while a_Y and b_Y are the parameters associated to each type of snowflake.

In Table 2.1, as an example, the values of the power law parameters for dry and wet snow as provided by Rasmussen et al. (1999) are reported. When the particle diameter is expressed in centimetres the following parameters provide w_T in $[m\ s^{-1}]$, V_p in $[cm^3]$, A_p in $[cm^2]$, and ρ_p in $[g\ cm^{-3}]$.

Table 2.1: Parameters a_V and b_V of Equation 2.15, from Rasmussen et al (1999), for the computation of the snowflake terminal velocity w_T , volume V_p , cross-section area A_p and density ρ_p

Crystal type	a_{w_T}	b_{w_T}	a_{V_p}	b_{V_p}	a_{A_p}	b_{A_p}	a_{ρ_p}	b_{ρ_p}
Dry snow	107	0.2	$\pi/6$	3	$\pi/4$	2	0.017	-1
Wet snow	214	0.2	$\pi/6$	3	$\pi/4$	2	0.072	-1

Several examples of drops falling both significantly faster and significantly slower than their terminal velocity are available in the literature, for example in the work of Montero et al. (2009), where this fact is first presented or, for example, in the more recent works of Larsen et al. (2014) and Chatterjee et al. (2022). Such drops are usually called sub-terminal if they fall at less than 70% of their w_T while they are called super-terminal if they fall at over 130% of their w_T . Furthermore, it was also shown that the percentage of sub-terminal and super-terminal drops in a precipitation event is strongly influence both by the precipitation intensity and the local climatology. This phenomenon of drops far from their terminal velocity is still quite an active field of research, and several explanations for such behaviour are provided, of which fragmentation and aggregation of drops is the primary suspect that is proposed by most of the literature. However, in this context it is not possible to exclude that such readings are, at least partially, due to instrumental biases, caused to calibration issues or wind. Therefore, with the intent of evaluating biases in the most general way possible, in this work it is considered for all hydrometeors that their fall velocity in the undisturbed flow is equal to their terminal one.

3 IN-SITU PRECIPITATION MEASUREMENT INSTRUMENTS

The development of highly accurate precipitation gauges for both liquid and solid precipitation is an increasingly relevant and pressing requirement in the environmental sciences and their applications (Lanza and Stagi, 2008). These instruments are divided into two major groups, catching and non-catching, depending on the necessity to collect or to not collect precipitation for measuring it. Gauges that fall in either group can also be divided in several other categories depending on their specific measuring principle. The following chapter presents a brief overview of the measuring principles, employed in the field, for in-situ precipitation measurement, using common precipitation gauges present on the market, as an example.

3.1 CATCHING INSTRUMENTS

Catching type precipitation gauges, as the name implies, measure precipitation by collecting it inside a reservoir, they are usually characterized by a radially symmetrical shape, that can vary considerably depending on the specific measuring principle.

3.1.1 Tipping bucket precipitation gauges

Nowadays, the backbone of all precipitation measurements networks is composed of tipping bucket rain gauges, that first originate in the ninetieth century and with limited improvements are still being used to measure rain, snow depth and the associated precipitation intensity. The reasons for such extensive use of this kind of instruments are their relative ease of maintenance and limited production costs. They use a simple operating principle, based on a metallic or plastic twin bucket balance to measure the incoming water. A funnel collects and conveys the precipitation water, by means of a nozzle, alternately in the two compartments of the tipping bucket. Once the bucket currently positioned under the nozzle is filled up to a certain point, a shift in the balance of the system occurs, producing a tip that empties the current bucket and positions the other one under the nozzle. Older gauges used a mechanical system to register the tipping of the bucket, while modern instruments use an electric system, based on a magnet, that triggers a reed relay during the movement of the bucket itself; the electrical signal is then recorded by a data logger.

Tipping bucket gauges usually have cylindrical shape (see e.g. Figure 3.1a), that are optimal for minimizing cost, but with the increasing awareness of the wind effect on the collection performance, new precipitation gauges characterized by more aerodynamic shapes (see e.g. Figure 3.1b), based on observations in the field, have been recently developed. Thanks to the automatic emptying principle, that allows water to be released outside the instrument body through dedicated apertures, these instruments do not require periodic emptying by an operator, however the presence of moving parts and of a collecting funnel requires periodic maintenance to avoid clogging and ensure a correct functioning of the system.



Figure 3.1: Example photos of tipping bucket rain gauges, CAE PG10 with a traditional cylinder shape (a) and EML SBS500 with an aerodynamic, inverted conical, shape (b).

3.1.2 Weighing precipitation gauges

Another, conceptually very simple, measuring principle for quantifying the collected precipitation is to weight the water volume. A weighing gauge consists of a metal or plastic bucket, where liquid and solid precipitation is collected. The weight of the container, together with the collected water, is measured by employing different type of sensors (balance, load cell, or vibrating wire load sensors). This type of gauges is widely used to measure solid precipitation because they do not require the snow to be melted before taking the measurement.

In the absence of an automatic emptying system, the dimensions of the container are usually larger than for other instruments, and this leads to a typical “chimney” shape with an increased section area at the bottom (see e.g. Figure 3.2a). The large capacity of the bucket has the objective of minimizing the emptying operation, which is manually performed in many cases. Some instruments use an automatic emptying principle based on a syphon, that has however the disadvantage of producing a loss of data during the emptying process.

Recently, a small size automatically emptying weighing gauge has been developed, integrating a load cell in a tipping bucket system (see Figure 3.2b). The balance measures the weight of the water collected alternately in the two compartments (conveyed through a funnel and a nozzle). Like in a traditional tipping bucket gauge, the water is released outwards by the tipping movement and then the empty compartment is placed under the nozzle to be filled and weighted. This automatic emptying principle leads to a reduction in the size of the instrument and ensures that the amount of weighted water is small and constant, therefore increasing the resolution of the gauge. However, the presence of moving parts, typical of tipping bucket rain gauges, requires additional maintenance operation.

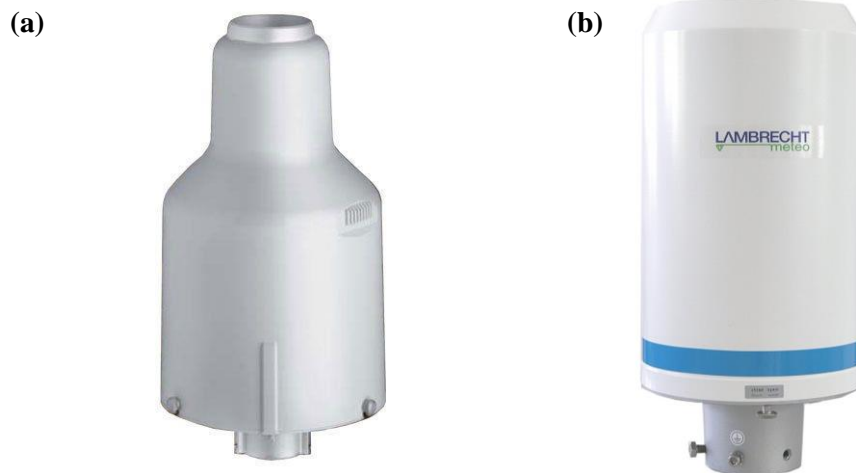


Figure 3.2: Example photos of weighing type rain gauges: the OTT Pluvio2 with its traditional chimney shape (a), and the Lambrecht Rain[e]H3 with a simpler cylindrical shape due to its automatic emptying mechanism (b).

3.1.3 Drop counter gauges

Drop counters gauges are a less-known family of catching-type gauges, consisting of a funnel to collect precipitation and to convey the rainwater towards a calibrated nozzle, which starts dispensing droplets within an internal chamber before releasing them outside of the instrument. An optical sensor is located below the nozzle and detects the passage of each falling drop. By assuming a constant volume for the calibrated droplets, the rainfall intensity can be derived from the drop release frequency. The resolution of a drop counting gauge depends on the size of the droplets generated by the nozzle, in the order of 0.005 mm of precipitation depth, and is suitable for the measurement of light precipitation. However, an operational limit of this type of instruments is given by the rainfall intensity at which the water flux from the nozzle starts to be continuous or irregular, then the measured frequency abruptly decreases, and large inaccuracies occur. A stand-alone installation is therefore discouraged, and a co-located rain gauge is required to avoid large underestimation of severe rainfall intensity.

3.1.4 Thermodynamic gauges

The thermodynamic gauge is an innovative type of instrument recently developed to measure light to medium liquid and especially solid precipitation rate (Rasmussen et al., 2011). The system consists of two heated identical aluminium plates, one facing upward that collects the precipitation, and the other facing downwards to serve as a reference (see Figure 3.3). This type of gauge can hardly be classified between catching and non-catching type gauges because it has neither a funnel nor a container but nevertheless collects the precipitation on the surface of the top plate by means of rings a few millimetres high. The lower plate is insulated from the top plate and is only affected by wind and ambient temperature and not by precipitation.

The two plates are heated to nearly identical constant temperatures (above 75 °C) which is hot enough to melt, in a few seconds, large snowflakes. The plates are maintained at a constant temperature during wind and precipitation conditions by either increasing or decreasing the supplied power. During

precipitation the top plate cools because of melting and evaporation of the hydrometeors, and the difference between the power required to heat the top and bottom plates is proportional to the precipitation rate.

The two plates are usually located at a height of 2 m above the ground. The diameter of the plate is large enough to permit collection of falling rain or snow particles and small enough that the power demand during heavy precipitation events and high wind speeds is not too high. To convert the power difference to liquid equivalent rate, a theoretical conversion factor is calculated by assuming that 100% of the heat of vaporization/sublimation from the precipitation is transferred to the instrument. The conversion factor is based on the surface area of the plate, the heat capacity of water, the density of water, and the latent heat of sublimation and evaporation. The shape of the instrument body is designed with the objective of minimizing the wind-induced undercatch (Rasmussen et al., 2011) that is, however, not negligible and was quantified in a recent study (Cauteruccio et al., 2021c). This instrument provides precipitation measurements every minute and can accurately measure rainfall rates up to 50 mm h^{-1} (WMO, 2018).

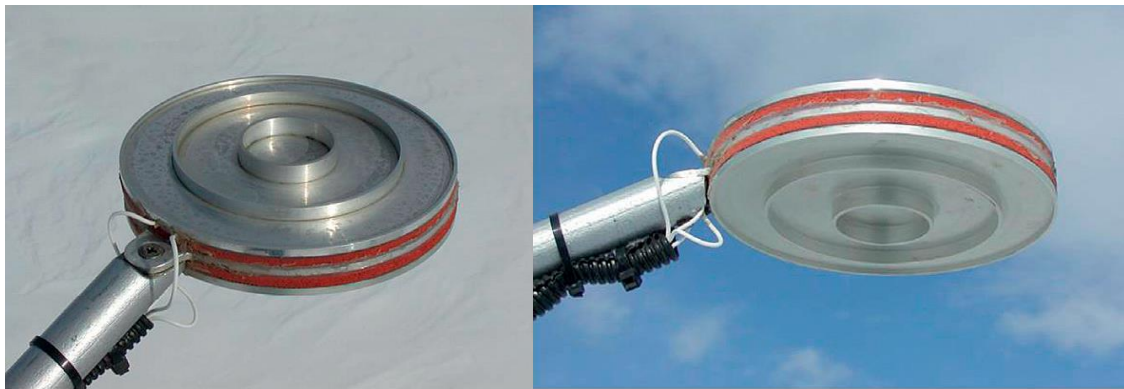


Figure 3.3: Example photos of the thermodynamic gauge from Rasmussen et al. 2011. Rings in the two plates are used to avoid precipitation sliding off the gauge in windy conditions.

3.2 NON-CATCHING INSTRUMENTS

The initial manual measurement methods for the study of the hydrometeor's characteristics evolved due to advances in technology and electronics. Nowadays different techniques are involved in the determination of liquid/solid particle characteristics, like devices to measure the displacement and mechanical energy caused by raindrops/graupels hitting a surface, optical imaging to measure the velocity, diameter and shape of the drops hitting a diaphragm and optical detection, whereby the size, shape, velocity, and diameter of hydrometeors are measured while they cross a light or laser beam, etc.

3.2.1 Optical precipitation gauges

Optical disdrometers use visible or infrared (IR) light to detect hydrometeors. They are equipped with IR or visible light emitters/transmitters that illuminate a volume of the atmosphere and with optical sensors to detect the light emitted from the transmitter. The illuminated measuring volume is usually defined by the shape of the lens and the relative position between the transmitter and the receiver. When hydrometeors cross the sensing volume, the light changes its intensity and scatters in various directions. This variation is

detected by the sensor allowing the physical properties of the particle (e.g., the diameter and the falling speed) to be derived. A simple schematic of the optical principle and configuration is shown in Figure 3.4.

Three physical configurations for optical gauges are commonly adopted. In the first case, here called optical transmission, the receiver is in front of the transmitter and captures the direct beam of light so that, when hydrometeors intersect the beam, light is partially obstructed and its intensity at the receiver is lowered. In the second case, here called optical scattering, the receiver is not located in front of the transmitter but at a given angle. In the absence of any obstruction, the signal at the receiver is very low, while when hydrometeors cross the measurement volume the light is scattered in various directions including the one of the receivers, therefore increasing the signal amplitude. The last type of instruments is based on optical imaging technology, with the instrument capturing images of the passing hydrometeors that can be further processed to obtain their physical properties.

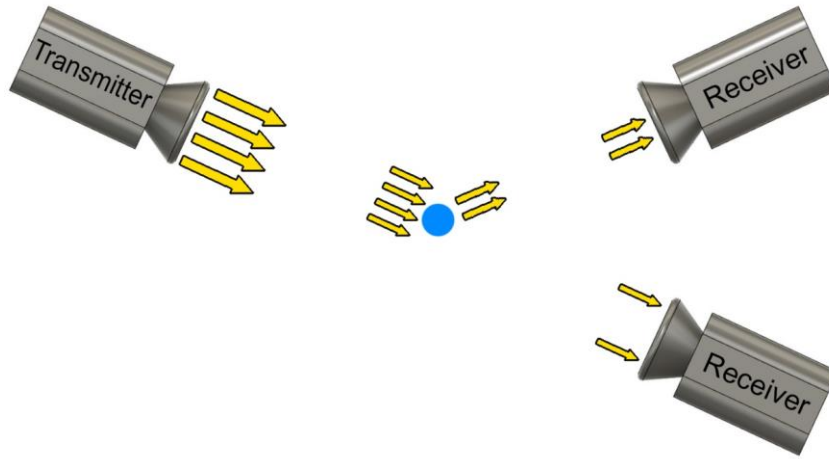


Figure 3.4: Schematic of the optical principle and configuration (from Lanza et al., 2021). The transmitter provide a coherent light beam, that can be aimed at the receiver (for gauges that measure beam extinction) or away from it (for gauges that measure the backscattered light).

3.2.1.1 Optical transmission

Instruments based on optical transmission are composed of a light source (typically an infrared light emitting diode, IR-LED) producing a homogeneous light beam, and a receiver (typically a photodiode). The light sheet has a width of few cm, a length of a few tens of cm, and a thickness on the order of 1 mm, resulting in an analysed volume of a few cm³, an example of which is shown in Figure 3.5.

When no hydrometeors are present within the measuring volume, the intensity of the light measured by the receiver is the maximum admissible one and corresponds to the reference level. When a rain droplet or ice particle crosses the analysed volume, it casts a shadow over the detector, and the measured voltage is reduced. The amplitude of the voltage drop is proportional to the surface of the shadow, while the duration of the shadow depends on the velocity of the falling particle. Based on such information, the sensor derives the fall velocity and the size of each hydrometeor.

The measured particles are classified by the sensor in various pre-defined classes by coupling the particle fall velocity with their measured diameter. Measurements are flagged and discarded by the instruments if the measured fall velocity of the hydrometeor is far from its theoretical value. This fact can occur when objects different from precipitation are detected, such as insects, leaves, etc. From these measurements the PSD is also calculated. The precipitation rate is derived by integrating over a short interval (typically on the order of one minute). When measurements are integrated over larger intervals the total amount of precipitation can be calculated.



Figure 3.5: Scheme of the measuring principle for an optical transmission NCG, using the Thies Laser Precipitation Monitor (LPM) as an example. Green coloured is the light sheet that is used to sense hydrometeors in flight.

3.2.1.2 Optical scattering

When light encounters a falling hydrometeor, part of the light intensity is scattered in various directions, depending on the wavelength of the emitted light and the size of the particle. For infrared light and typical drop sizes (0.1–6 mm), the angle of maximum diffraction is around 45° . This principle is used by optical scattering instruments to detect hydrometeors in the atmosphere and derive the associated precipitation rate.

A light source (typically IR-LED) emits a cone of light. A photodetector is placed at an angle of 45° with the source. The intersection of the light source and the cone of vision of the photodetector defines the analysed volume (typically, a few hundreds of cm^3). Instead of a cone of light, the source can also be a light sheet to decrease the analysed volume (down to a few cm^3) and increase the resolution. Since the scattered intensity is low, it is important to use a source with a sharp bandwidth and a filter in front of the detector to measure only the wavelengths emitted by the source. A lock-in can also be used to increase the accuracy, with a light source being modulated at a certain frequency, and the electrical signal being analysed at that frequency.

In undisturbed conditions, when no particles occupy the analysed volume, the signal measured by the photodetector is very low because the direction of the light differs from that of its cone of vision. When a particle travels through the measuring volume, the light is scattered in different directions and is partly detected by the photodetector, which records a peak in the signal. The amplitude of the peak is proportional to the droplet size; hence it is possible to obtain the PSD, therefore, the total precipitation and precipitation rate. From the characteristic frequency of the emitted signal, the returned signal is filtered to obtain only the components related to the falling hydrometeors. The small particles in suspension instead induce a base level of this characteristic frequency that can be linked to the visibility. A simple scheme of the measuring principle is shown in Figure 3.6.

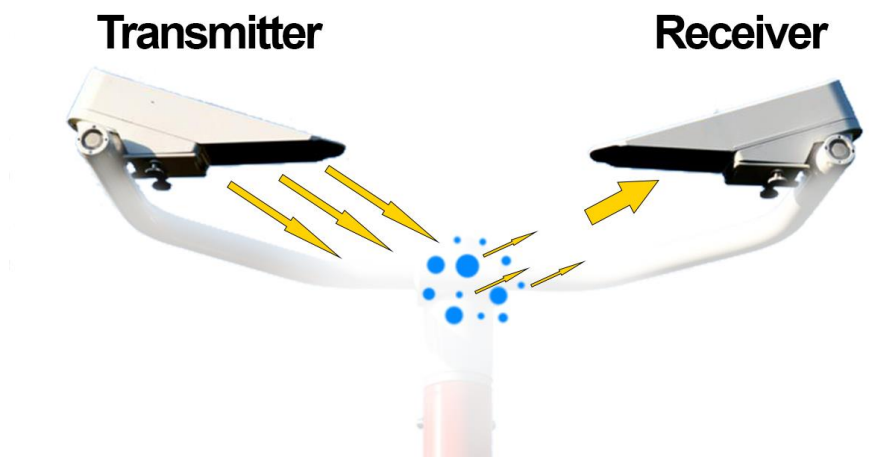


Figure 3.6: Scheme of an optical scattering sensor and measuring principle (from Lanza et al., 2021). The light cone produced by the transmitter head is scattered by the hydrometeors and the is then sensed by the receiver head.

Recently developed instruments are equipped with two receivers, usually positioned as shown in Figure 3.7. One of the detectors identifies the forward scatter radiation and it is usually located between 39° - 51° , meanwhile the other detector identifies the backward scattered radiation (107° - 119°). The second receiver improves considerably the performance of these instruments because it allows to discriminate between liquid and solid precipitation by combining the two signals. The ratio between the back- and forward-scattered signals allows to estimate visibility and to discriminate between different types of precipitation due to snow and other frozen hydrometeors having a much higher proportion of back scattered light when compared to rain.

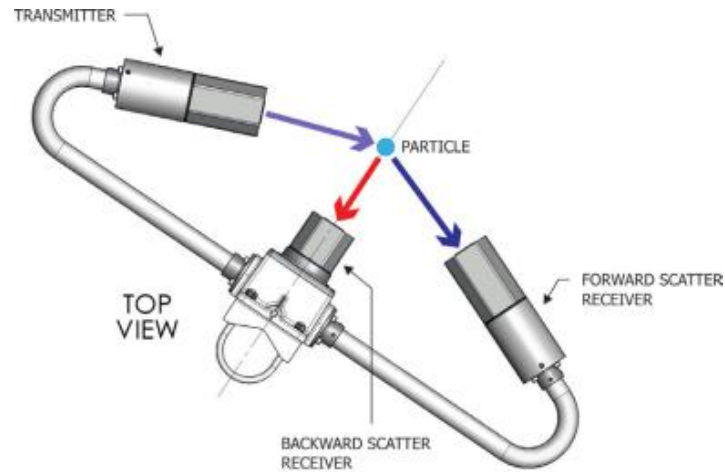


Figure 3.7: Schematic of the optical sensor with two receivers to detect the forward and backward scatter (from Biral Ltd., brochure on visibility and present weather sensor for aviation). Measures of the ratio between forward and back scattered light allow to differentiate liquid from solid precipitation.

3.2.1.3 Optical imaging

These gauges use a Charge-Coupled Device (CCD) or Complementary Metal–Oxide–Semiconductor (CMOS) photographic sensor, operating in the visible band of the light spectrum, to capture an image of each single hydrometeor that crosses the sensing volume. Two different types of sensors can be used, line-scan and total image sensors. The first is composed by a single line of pixels that can be read at high frequency; the image is therefore obtained after pre-processing and assembling of the consecutive slices. These sensors are commonly used by the industry for high-speed machine vision operations and can reach high spatial and temporal resolutions.

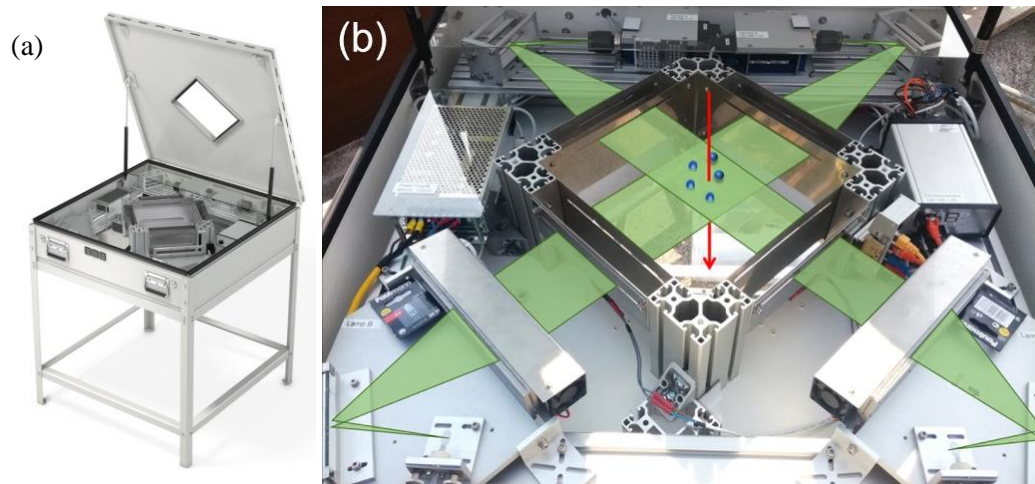


Figure 3.8: (a), image of the 2D Video Disdrometer (photo from Joanneum Research website) and (b) scheme of the measuring principle from Fehlmann et al. (2020). The gauges use two light sources (in green) that illuminate two line-scan sensor that capture images of the drops in flight.

Total image sensors are instead composed of a two-dimensional array of pixels and capture still pictures of the hydrometeors, the data obtained is directly usable without pre-processing but usually have lower spatial and temporal resolution. The line-scan camera is employed e.g., by the two-dimensional video disdrometer (2DVD), manufactured by Joanneum Research at The Institute for Applied Systems Technology in Graz, Austria. Inside the gauge, a visible light source generates a light sheet that is projected onto a line-scan camera, as shown in Figure 3.8 (right panel). The 2DVD uses two orthogonal light sheets and two synchronized cameras. The light sheets are quite bright and particles falling through them cast shadows on the photodetectors. The resulting signals are compared against a threshold to determine if a pixel is lit or obscured. The combination of bright light and video thresholding renders the raindrops opaque and makes the 2DVD insensitive to ambient light.

The two orthogonal projections provide, in principle, three-dimensional raindrop shape information and can limit the shadowing effect that can happen when two hydrometeors cross the beam exactly at the same time. Shape information allows computation of the drop volume and equivalent drop diameter, as well as the oblateness. The light sheets are spaced about 6 mm apart and the 2DVD software matches particle shadows in the upper light sheet with particle shadows in the lower sheet. By measuring the time needed for a particle to traverse the distance between the two light sheets, it is possible to obtain its vertical velocity. The 632 photodetectors are read out at a rate $f = 55.5$ kHz, creating slices of the image projection, and with this information it is possible to reconstruct the shape of the hydrometeor using the same principle of a flatbed scanner.



Figure 3.9: Image of the HOD disdrometer (from Testik and Rahman, 2016). An high speed camera (right-hand side) is used to capture images of the drops that cross its sensing area (centre), that are illuminated by a LED source (left-hand side)

Another optical imaging gauge is the High-speed Optical Disdrometer (HOD), illustrated in Figure 3.9. In this case, however, the instrument uses a total image sensor. The main components of the HOD are a high-speed CCD camera, a LED light with a diffuser, and a digital fibre-optic sensing unit. The camera and the light are installed at a distance of 160 cm, and the sensor is installed between the camera and the light source, with the camera focal plane centred 60 cm away from the camera. The sensor installed in the HOD captures raindrop images at 1000 frames per second with a resolution of 1024 x 1024 pixels. The measurement volume is defined by the vertical size of the camera view frame (70 mm) and the horizontal sensing area, which is defined by the sensor beam width (5.25 mm centred around the focal plane) and the transverse size of the camera view frame (70 mm). This configuration corresponds to a measurement volume of 25.73 cm³. The images are recorded only when there is a raindrop within the measurement volume by utilizing a sensor-based camera triggering system.

3.2.2 Impact precipitation gauges

These instruments exploit the kinetic energy of the falling droplets when impacting the exposed surface of the gauge. A plastic or metal membrane is used at the measurement surface to sense the impact of single precipitation particles. In some systems, the mechanical movement of the membrane is transduced into an electrical signal by an attached moving magnet/coil system. In other solutions, the amplitude and the frequency spectrum of vibrations generated by precipitation particles hitting the membrane are detected and analysed to determine the particles size and numerosity. Impact methods are therewith suitable to determine the particle frequency (drops s⁻¹ m⁻¹), the rain rate (mm h⁻¹) and the drop size distribution over a given time window. Both acoustic and displacement disdrometers are devoted to measuring liquid precipitation, since energy is directly related to the mass and density of the water droplets. Snowflakes and hailstones, for example, have completely different impacts on the sensor surface, and may lead to underestimation or overestimation of precipitation.

3.2.2.1 *Electro-acoustic devices*

In electro-acoustic devices, the falling precipitation particles (raindrops or graupels) impact a target or sensor cover made by metal or plastic (Figure 3.10). The amplitude of the pulse produced by the impact is assumed to be a function of the vertical momentum of the particle and thus of its mass and terminal velocity. The pulse can be detected either by an electrical force transducer, e.g., piezoelectric (Salmi, 2005, 2011; Förster, 2004), mechanically attached or linked to the sensor cover, or transmitted through a media to a microphone (Kinnel, 1972). The electrical transducer produces an output voltage that is a measure of the impact force (change of momentum over time) and thus the volume of the drop and the impact duration, that is the impact velocity. Knowing the area of the sensor cover and the time window, the rain rate and the accumulated precipitation can be calculated. To distinguish between rain drops and graupels, the characteristics of the waveform can be used, as ice and water produce very different waveforms. With assumptions on the hydrometeor velocity and density, its kinetic energy may be derived (Löffler-Mang, 2011).

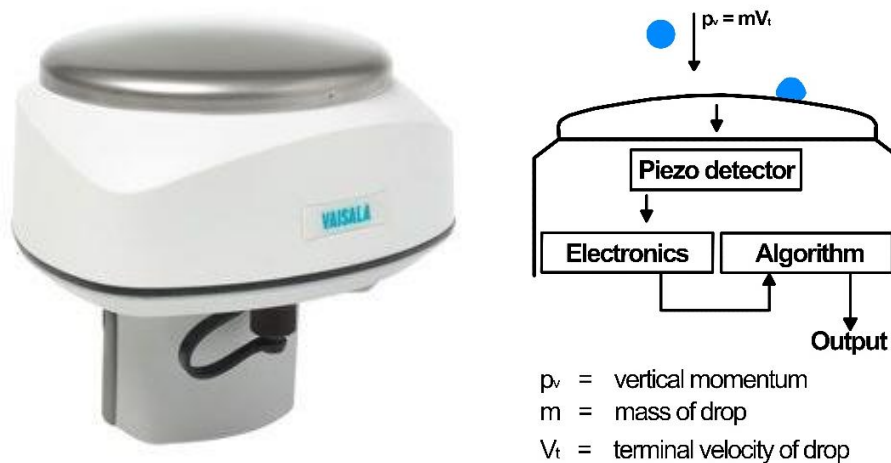


Figure 3.10: Image of the Vaisala electro-acoustic impact disdrometer and its functioning scheme (from Salmi, 2005). The metallic cap is the sensing area of the gauge, the impacts of drops are converted to an electric signal by a piezo element, the signal is then processed by the on-board electronics.

3.2.2.1 Displacement devices

In displacement disdrometers, the sensor cover is displaced when impacted by the falling precipitation particle. A magnet, moving in a coil, is mechanically attached to the cover and translates via magnetic induction the energy generated by the impact to an electrical pulse (voltage), as shown in Figure 3.11. Analogously to the electro-acoustic devices, the electrical signal is a measure of the impact force, which is used to calculate the volume of the drop and the principle for determining the rain rate and the accumulated precipitation is similar. As the instrument contains moveable parts it may require regular maintenance.



Figure 3.11: Image of the Joss-Waldvogel displacement impact disdrometer and its functioning scheme (from Kathiravelu, 2016). Drops impacting the top of the gauge displace a lightweight plastic cone, movement is converted into an electrical signal by means of magnetic induction.

3.2.3 Radar precipitation gauges

In-situ precipitation measurement instruments employing microwave sensors, also called microwave or radar disdrometers, are low-power, small-size Doppler radars, vertically looking (without scanning

capabilities) that exploit the Doppler effect due to falling drops to derive the spectrum of precipitating particle size. Continuous Wave (CW) radars use different antennas to transmit and receive the microwave signal, while Frequency-Modulated Continuous-Wave (FMCW) radars are also available and able to measure height-resolved drop size distributions (Löffler-Mang et al., 1999). Radar disdrometers operate by measuring the power of the backscattered signal and its Doppler shift to estimate the size of hydrometeors passing nearby, as described by Sheppard (1990) and Prodi et al. (2000). A falling drop, moving vertically towards the instrument, produces a return signal when entering the measurement volume. The return power (P_r) can be expressed as (Sheppard, 1990):

$$P_r = \frac{P_t \cdot L_w \cdot G_t(R1) \cdot G_r(R2) \cdot \lambda^2 \cdot \sigma}{64\pi^3 |R1|^2 |R2|^2}$$

3.1

where P_t is the transmitted power, L_w is the transmission loss due to wetting of the radomes, $R1$ and $R2$ are the distances between the emitting antenna and the falling drop, and between the drop and the receiving antenna, respectively (Figure 3.12), $G_t(R1)$ and $G_r(R2)$ are the antennas respective gains, λ is the emitted frequency and σ is the scattering cross-section. The Doppler shift (f_d) is a function of the velocity vector (\mathbf{v}) of the object when crossing the equi-phase surfaces having $R1 + R2 = \text{constant}$, and can be obtained using Equation 3.2, as a function of the phase shift gradient ($\nabla\varphi$) with the phase shift (φ) calculated from Equation 3.3.

$$f_d = \nabla\varphi \cdot \frac{\mathbf{v}}{2\pi}$$

3.2

$$\varphi = 2\pi \frac{|R1| + |R2|}{\lambda}$$

3.3

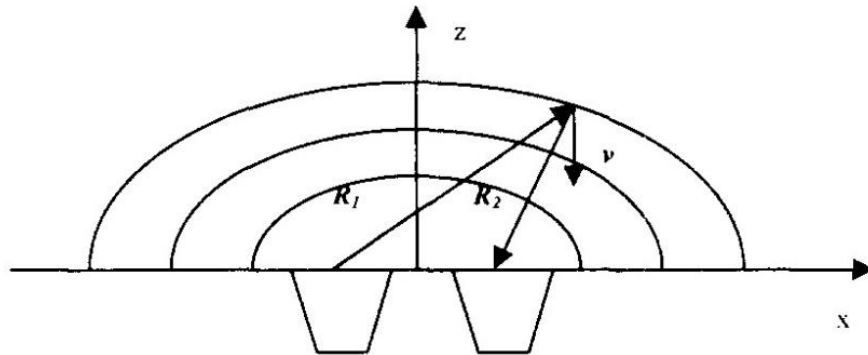


Figure 3.12: Configuration of the emitting (left) and receiving (right) antennas (from Prodi et al., 2000). Equi-phase surfaces are constructed considering the points having equal path length between the emitting and receiving antennas.

For a single drop, the return power depends on the backscattered signal that is a function of the scattering cross-section σ and the drop diameter. From measurements of the return power alone, depending on the instrument operating frequency, it may not be possible to uniquely determine the hydrometeor diameter because of Mie scattering that can occur for larger drops (Raubert and Nesbitt, 2018). The phase shift, on the other hand, is a function of the particle velocity, that is directly related to its diameter if the drop falls at terminal velocity. Semi-empirical relationships are used for rain and for different frozen hydrometeors (hail and snow), like the one proposed by Atlas et al. (1973), formulated for raindrops. During a precipitation event, the return signal is composed by the sum of the contribution of each drop and is usually collected in one-minute segments, that are then processed using Fourier transform to evaluate their spectrum. For the signal analysis, natural rain is considered as a superposition of monodisperse events, so that the spectral intensity of the return signal ($S(f)$) is:

$$S(f) = \int_{d_{min}}^{d_{max}} N(d)V(d)\bar{S}(d,f)dd$$

3.4

where $\bar{S}(d,f)$ is the volume-averaged Doppler power density and $V(d)$ is the measuring volume. The number of drops in the measurement volume can be obtained once the value of $\bar{S}(d,f)$ is known, at least in a discrete form. Evaluation of $\bar{S}(d,f)$ can be achieved using laboratory measurements of monodisperse drops (Prodi et al., 2000) or from numerical simulation once all the antenna parameters are known. A more in depth and detailed explanation can be found in the work of Sheppard (1990).

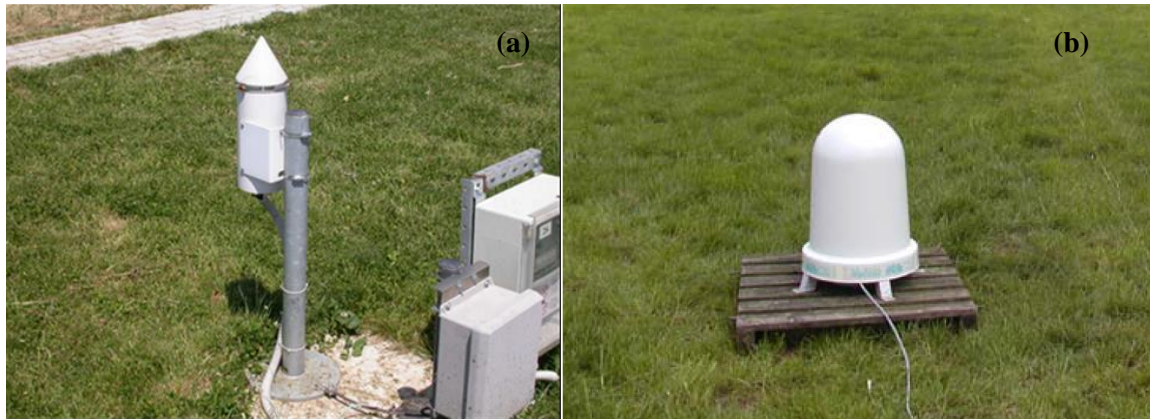


Figure 3.13: Microwave precipitation gauges: LCR PVK ATTEX (a) (from Cauteruccio et al., 2021b) and Pludix (b) (from Caracciolo et al. 2006).

Different models of microwave disdrometers have been developed (Figure 3.13), but the measuring principle of these gauges remains unchanged. During field intercomparison and testing, multiple instruments were compared against other disdrometers (optical or impact) and more traditional catching type gauges, showing sufficient agreement on the cumulated event precipitation but low agreement on

rainfall intensity, especially for heavy precipitation events and measurements at one-minute time resolution (Prodi et al., 2000; Caracciolo et al., 2006; Vuerich et al., 2009).

One limitation of this instrument is that the terminal velocity of the falling drops is calculated using a model that does not consider the presence of wind. Due to the position near the ground of these instruments it is acceptable to assume that the vertical component of wind is negligible, but the effect of the horizontal component of wind on radar measurements still has to be investigated (Caracciolo et al., 2006). Because the doppler shift depends on the hydrometeor velocity component in the direction of the antennas, a horizontal component of velocity can modify the doppler shift and consequently the instrument assumption on the diameter. This problem is usually limited by the manufacturer by shaping the antennas emission into a narrow cone.

Another critical aspect is related to the evaluation of $\bar{S}(d,f)$ when obtained from laboratory calibration. In this case it is imperative that all the released drops achieve terminal velocity before entering the sensing volume, because an accelerating drop generates a backscattered signal that differs both in frequency and amplitude from the one generated by a drop falling at terminal velocity.

3.3 OPPORTUNISTIC SENSORS

The term “opportunistic sensors” indicates a class of precipitation detecting devices, that were not developed with the intent of measuring precipitation rate/amount and usually serve a completely different purpose but, due to their working principle or physical characteristic, can be exploited as precipitation gauges. These sensors are usually largely diffused, especially in the urban environment, to perform their intended duty and, if exploited for precipitation detection/measurement, can constitute an extremely fine network, capable of providing precious information to support existing precipitation measurement networks, that are instead less densely available on the territory due to their elevated cost. In general, measurements obtained from opportunistic sensors are less reliable than those from traditional gauges and are still affected by significant uncertainties, yet the sheer amount of information that can be obtained from them outweighs these shortcomings for some specific application.

3.3.1 Measures from telecommunication antennas

The fact that for microwaves near the 1 cm wavelength, attenuation due to rainfall is almost linearly related to rainfall rate is known since a long time (Ryde, 1946), the major limitation in the development of such method for precipitation measurement being due to the high cost of such communication links. However, in a world where people and devices are increasingly globally connected, cellular communication networks using such frequencies, are now indispensable and virtually ubiquitous. Wireless communication between cell phones is possible via microwave antennas installed on roofs of buildings or on dedicated communication towers and electromagnetic signals exchanged between such antennas, that is, among telephone towers, are attenuated by rainfall along their propagation paths. It became therefore viable the use of such infrastructure for the opportunistic measurement of precipitation. As rainfall patterns change in time and space, so do the strengths of these attenuations. The relationship between the rain intensity RI (in

mm h⁻¹) and the attenuation of a microwave wireless signal A traveling in the atmosphere is relatively simple:

$$A = aRl^b$$

3.5

where A is in dB, l is the path length (in km) of the link. Furthermore a , b are constants, depending on the frequency and the polarization of the signal, as well as on the drop size distribution (DSD) of the rain, which is considered as typical to an area. This relation is a simplified model of complex physical relations (Atlas & Ulbrich, 1977) which has empirically been found to be a good approximation for the rain-induced signal's attenuation, for microwave frequencies and for links of length of about 0.5–20 km.

The temporal dynamics of these signal losses can be monitored relatively easily and converted into path-average rain rates (Leijnse et al., 2008; Messer et al., 2006). As such, any so-called microwave backhaul link can potentially be used as a path-average rain gauge. The rapid growth of the number of microwave links used globally for cellular communication therefore provides an enormous potential for improved continental-scale precipitation monitoring and prediction. Furthermore, this approach is not limited to cellular communication signal, but other types of communication networks can be exploited to, like satellite links (see e.g., Giannetti & Reggiani, 2021). However, challenges still remain, due to the complexity of the algorithms for rainfall retrieval and rainfall mapping (due to the nature of the retrieved data that is not punctual), the need to evaluate other factors that can produce attenuation in the signal and the necessity to access real time telemetry data of such network, that are not always available. A more in-depth discussion on the subject is available in the work of Uijlenhoet et al. (2018).

3.3.2 Measures from surveillance cameras

The density of closed-circuit television (CCTV) surveillance cameras is high in many urban areas. Compared to other crowdsourcing modalities, visual data (i.e., images or videos) from such surveillance cameras contains more information, are easier to work with and in most cases are readily available (Guo et al., 2017). Digital pictures and videos are strongly affected by weather conditions, including precipitation. In fact, the rainfall produces local variations in the pixel's intensity value of raster images depending on raindrops characteristics (shape, size, velocity, density), camera parameters (exposure time, F-number, depth of field, etc.) and environment settings (scene brightness, background, etc.).

Rainfall intensity can be quantified by separating rain streaks from the rain-free background in the images or videos. The rain streak is the visual appearance of a falling raindrop perceived by cameras owing to the persistence of vision. The motion blur due to exposure time causes falling raindrops to appear as streaks in the image. After Garg and Nayar's (2005) pioneering work on the photometry of rain streaks, developing effective and efficient algorithms for recognizing rain streaks from images and videos has been an appealing topic in the field of image processing.

However, the mainstream research in the field of computer vision and image processing has focused on removing rain streaks and even streak-like noises from images. In most cases, achieving a “clean” image is the goal. On the other hand, vision-based rainfall gauging is a considerably more difficult task because false positive identifications (i.e., misidentifying random noises as raindrops) must be avoided to accurately identify rain streaks. In the last years several attempts on improving current algorithms for precipitation detections were published in literature from several authors, both using traditional algorithms (see e.g., Jiang et al. 2019) and machine learning (see e.g. Notarangelo et al. 2021).

3.3.3 Measures from car automatic wiper sensors

With development in the automotive industry and the ever-increasing effort toward safer vehicles, sensors capable of detecting precipitation and use that information to automatically actuate the windshield wiper were eventually added to vehicles (see e.g., Ucar et al., 2001). Nowadays the number of cars equipped with such sensor is steadily increasing and it is easy to predict that this trend will continue forward. A considerable amount of effort is also focused on improving these sensors to be more precise and reliable (see e.g., Gormet et al., 2009).

While the idea behind these sensors for automotive applications is not particularly new (Masahiro, 1984), their use for a quantitative measure of precipitation is (La Barbera & Lanza, 2015). In the work of Haberlandt & Sester (2010), it was shown how a large number of precipitation measurements taken by not particularly precise gauges, that are however quite densely distributed over a large area, could significantly improve rainfall estimation, especially if used in combination with traditional, higher precision, precipitation measurement networks.

A very simple idea to evaluate precipitation using cars is proposed in the work of Rabiei et al. (2013) where the windshield wiper activation frequency is used as sole variable. The major drawback is that the system is tied to the number and frequency set by the manufacturer or rely on the user intervention, meaning that is prone to false reading and limited in the range of measure. A much complex but also less prone to errors approach is to use the signal from the rain sensor installed in the car or to add a specifically designed sensor to the windshield (Kim et al., 2017).

The measuring principles behind such sensor is usually optical, based on the scattering effect that the water droplets on the windshield produces. A LED, positioned inside the vehicle and placed, with the addition of suitable optics, on the windshield emits light in a narrow infrared (IR) band. An IR receiver positioned close to the emitting LED and coupled with optics, then picks up the emitted IR light. Because the IR beam is forced to travel inside the windshield glass, that had a boundary, the amount of light that is scattered depends on the refraction angle, that can be computed using Snell’s law. When no water is present on the windshield, the boundary interface is between glass and air, producing an internal refraction, that directs all the light toward the IR sensor, on the other hand, if water is present on the surface the refraction angle changes and a part or all the light (depending on the amount of water present) is diverted away from the receiving sensor. A simple scheme of the functioning principle is shown in Figure 3.14.

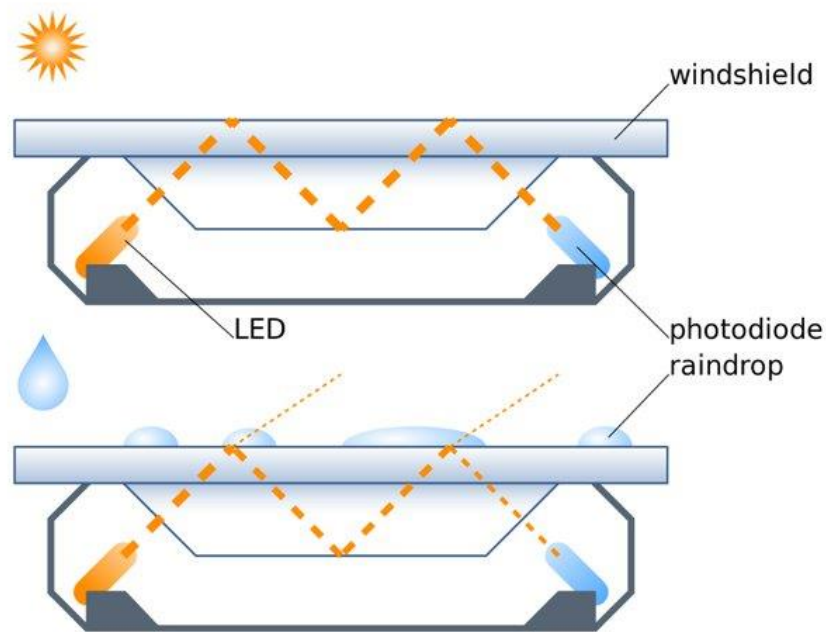


Figure 3.14: A schematic example of the functional principle of a drop detection system typically used in the automotive industry (from Puppenbenutzer, 2009). The infrared light is reflected internally toward the photodiode when the windshield is dry, however the presence of water makes part of the light is diverted away, reducing the power sensed by the photodiode.

Current research efforts are focused on the evaluation of a suitable postprocessing algorithm for the receiver signal, that can be used to obtain the precipitation amount. Several factors need to be taken into account, for example the car speed, the angle at which the windshield is positioned, the passage of the windshield wiper and the potential effect of outside lighting.

4 MEASUREMENT ACCURACY AND INSTRUMENTAL SOURCES OF BIAS

Instrumental biases are due to manufacturing tolerances and/or the operational characteristics of the measuring principle employed by the instrument. All instruments are affected, with a potentially strong impact on the measurement accuracy. However, being systematic in nature, this bias can be minimised by means of instrument calibration. The instrumental bias was extensively studied in the literature for CGs (see e.g., Colli et al., 2014) and standardized procedures are available to calibrate instruments to a common standard (EN-17277). Calibration is achieved by providing a known, constant flux of water to the gauge, which does not differentiate between individual drops but collects precipitation in a reservoir, thus measuring the cumulative water volume over the target time interval.

NCGs detect the microphysical and dynamic characteristics of individual or multiple hydrometeors that interact with their sensing area, thus instrument calibration requires that individual water drops of a known size, shape and fall velocity are generated for use as a reference. Calibrating NCGs is therefore considerably more difficult than for CGs. No widely agreed calibration procedure, nor any documentary standard exists so far within national or international institutions. NCGs are generally calibrated by the manufacturers using internal procedures developed for the specific technology employed and limited information is generally provided to the users.

Various methods for calibrating NCGs were presented in the literature, either using simple water drop generators or by dropping calibrated media through the sensing area/volume of the instrument under test (see Lanza et al., 2021, for a review). A common limitation of the available methods is that, due to the complexity of releasing very small drops on demand, relatively large drops are used, above 2 or 3 mm in diameter. Large drops are, however, quite scarce in natural precipitation, accounting for a limited fraction of the total precipitation volume. Therefore, calibration of NCGs should also include drops in the lower size range, below 2 mm in diameter, which accounts for about 99% to 97% of the total number of drops, and 85% to 62% of the total water volume (see Cauteruccio and Lanza, 2020).

4.1 CALIBRATION OF NON-CATCHING INSTRUMENTS

Information about the calibration procedure adopted by manufacturers is usually undisclosed, but in some cases, like for Vaisala Inc. (Tuukka, 2015), a calibration procedure for NCGs is described, at least in a simplified form. In the Vaisala calibration laboratory, they developed a rainfall generator (Figure 4.1a) that can be positioned above the instrument. A “dripper tank” (Figure 4.1b) is raised 14 m over the instrument and drops of fixed diameter are released continuously on to a screen just under the tank. The idea is that the constant size drops, after hitting the grid, are broken in smaller drops of random size that would reproduce a realistic precipitation event. This is however doubtful, since the DSD of real-world events is of the exponential or gamma type, while a random breaking of water drops would be close to a Gaussian distribution.

Just above the gauge under test, an optical instrument measures the incoming precipitation and is used as a reference. The precipitation intensities can be varied by increasing or decreasing the flow to the “dripper tank” and different PSD are generated by changing the distance between the tank and the

redistribution screen. The optical reference is composed of two laser emitters that produce two different sheets of light and two sensors that measure the received intensity. Assuming that only one drop crosses the light beam at the same time, the drop dimension is obtained by the reduction in the laser beam intensity while the time that the particle needs to cross both sheets is used to calculate velocity. Finally, all the released drops are collected under the instrument and a weight scale is used to obtain the cumulated water amount.

This approach has the advantage of producing drops that fall almost at terminal velocity. On the other hand, because of the method used for generating drops, it is not possible to freely choose the drop crossing position with respect to the sensing area, that would allow for example to assess the effect of the non-uniformity of the beam for laser precipitation gauges. Also, the physical principle used for checking the generated drop in flight is very similar to that used by some of the instruments that could be calibrated and presents the same limitations and shortcomings, being not the ideal reference for calibration purposes.

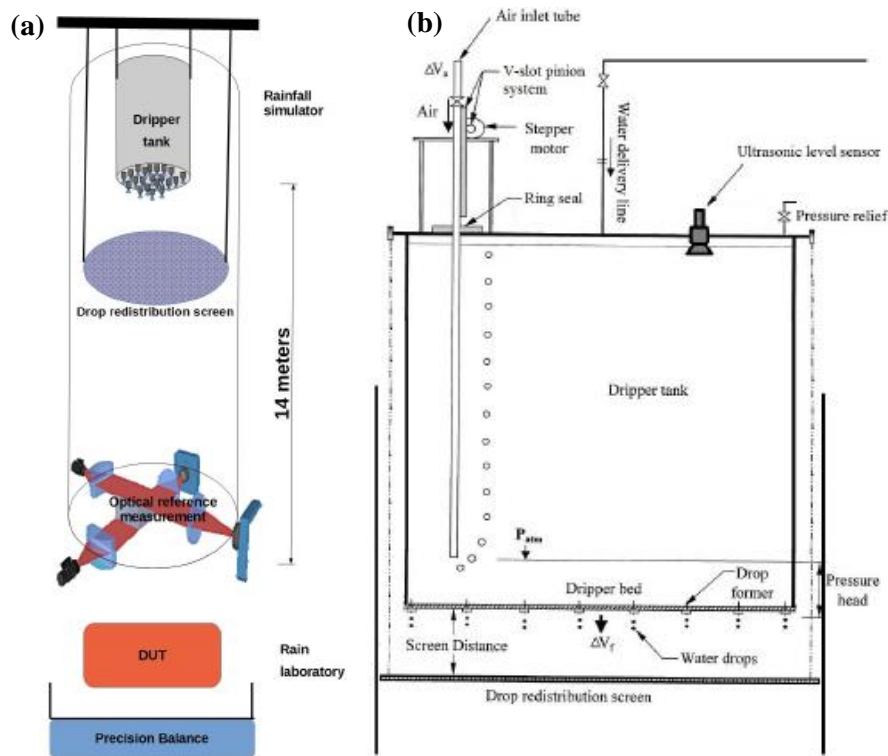


Figure 4.1: Schematics of the Vaisala calibration tower (Tuukka, 2015) with the “dripper tank” as a drop generator (left panel) and a sketch of the whole setup (right panel), where DUT indicates the Disdrometer Under Test.

The calibration procedure used by the manufacturer is known also for the Thies LPM (Lanzinger et al., 2006), an optical disdrometer. The factory calibration comprises the determination of the geometrical shape and size of the laser light sheet and a calibration of the drop volume measurement. The characteristics of the light sheet such as beam width and alignment are exactly measured by using an optical beam analyser. For the volume calibration, an automated calibration bench is used. It consists of a precision dispensing pump with an accuracy of 0.3 % and a drop generator that is mounted on a 2D positioning system. Uniform

drops with a diameter of about 3 mm are released through the light sheet at 15 equally distributed positions. At each position, 30 drops are released. Based on the repeatability of the disdrometer measurements at any fixed position, the uniformity of the drop diameters can be estimated to 2 %.

The calibration process is carried out in two steps, allowing to assess the deviation of the mean volume from the reference. After the first run, the device is adjusted by setting appropriate calibration parameters. In a second run, the adjustment is checked. The manufacturer obtained a maximum allowed tolerance of 2.2 %. This is the estimation of the uncertainty for the volume measurements under laboratory conditions provided that a large number of drops fall in equally distributed positions through the light sheet. It does not apply to the volume measurement of a single drop. This procedure is based on the specific characteristics of the targeted instrument and allows controlling the position of each released drop. However, the drop diameter and velocity are not preliminarily measured, independently on the instrument under tests, therefore no reference is available, and it is unclear if drops are released from a sufficiently high elevation to approach terminal velocity. Finally, only one drop diameter is investigated, so that differences could arise when different drop diameters are measured.

When information about the manufacturer calibration is not available, the only source of information is the scientific literature. For example, in the work of de Moraes Frasson et al. (2011) a different approach for calibrating the Thies LPM is proposed. In their procedure, the diameter of a calibrated metallic sphere is repeatedly measured by the disdrometer and then contrasted to its nominal diameter. They developed a device to deploy metallic spheres of 2 mm, 3 mm, 4 mm, 5 mm, and 6 mm in diameter on approximately the same position of the disdrometer laser sheet (Figure 4.2). The device consists of a reservoir for the spheres, ending in a tunnel that leads them to the loading rod. The loading rod has a set of grooves, each one matching the size of the sphere currently being used. When the groove is aligned to the reservoir, it allows one sphere to be loaded. The loaded sphere is deployed when the loading rod is moved to the release position and the loaded groove is aligned with an opening at the bottom of the calibration device.

The calibration device has two supports that adjust to the disdrometer's frame and align the centre of the device's outlet with the centre of the laser beam. The release height of the spheres is chosen to provide the spheres with enough height to achieve a velocity of approximately 1 m s^{-1} at the height of the beam. The steel spheres had their diameter checked with a calliper, and the authors found no deviations from their nominal diameter to a tenth of a millimetre. For this reason, they assumed that the nominal diameter is the real diameter of the sphere, which allowed them to refer to the difference between disdrometer measurement and nominal diameter as a measurement error. The average error for each instrument is an indication of the bias in the diameter measurement, while the standard deviation of the error will characterize the uncertainty of the diameter measurement. This procedure is extremely simple, but the use of metallic spheres is only compatible with some types of non-catching gauges, like the optical ones. Also, the fall velocity of the spheres is not considered, meaning that only one of the two parameters measured by disdrometers can be calibrated.

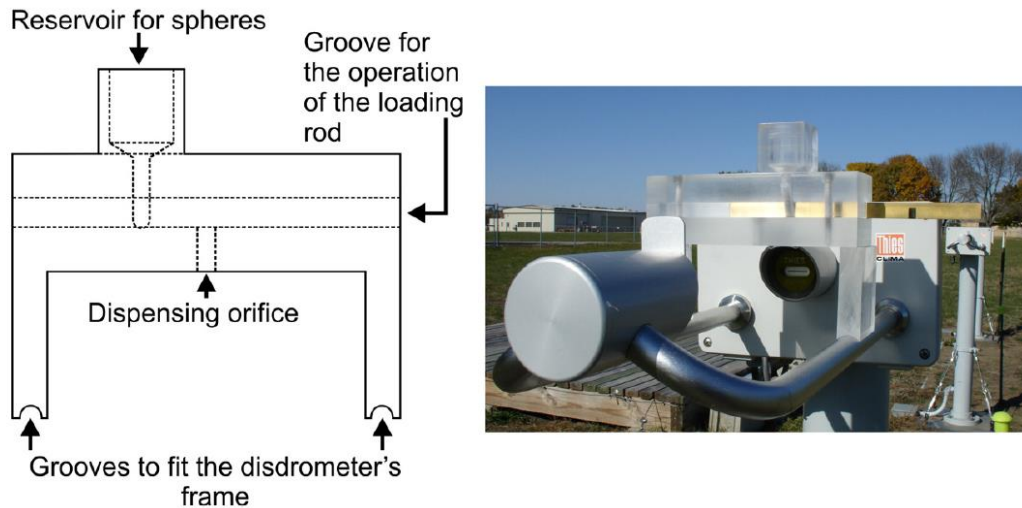


Figure 4.2: Calibration apparatus scheme (left panel) and operational use (right panel) for the Thies LPM disdrometer (from de Moraes Frasson et al., 2011). Metallic spheres are released by the movement of the operating rod over different portion of the light sheet.

In the work of Testick and Rahman (2016), different laboratory experiments were designed to evaluate the measurement accuracy of the High-speed Optical Disdrometer (HOD) and its performance in a controlled environment. The laboratory tests involved experiments with high-precision spherical calibration lenses and free-falling water drops of known sizes. In the first set of laboratory tests spherical lenses with diameters of 0.5 mm, 1 mm, 3 mm, and 5 mm with a diameter tolerance of $62.5 \mu\text{m}$ were adopted. Spherical lenses were made of two different materials, fused silica, and sapphire, with refractive indices of 1.46 and 1.77, respectively. These tests provided information on the overall measurement errors, including both hardware- and software-related errors, and within the simplified hypothesis of spherical object. Results showed that the maximum percentage error in the measurement of the diameter decreases with increasing the diameter and the maximum deviation is about 11 % for the sphere with diameter 0.5 mm.

The second set of laboratory tests was carried out with free-falling water drops of various size generated using needles attached to a constant-head tank as shown in Figure 4.3. The constant-head tank was used, while fixing the needle to generate drops with nearly the same size throughout the test. The average equivalent drop diameter was derived based on the total volume released in each test. Larger drops, compared with the spherical lens, were released with diameter between 2.0 mm and 5.0 mm. Water drops were released at 60 cm above the measurement volume. Each released drop triggers the HOD, and 10 images of the same water drop are captured. The error in the measurement was derived and expressed in terms of total volume; the generated water drops were collected in a graduated cylinder, and the total volume of the collected water was measured and compared with the total volume of the drops measured by the HOD. The measure of the total volume within the graduated cylinder is affected by an error of about 0.5 ml. These tests provided a maximum percentage error in HOD measurements of 9.2 % in terms of water volume. This procedure is similar to the previous one and presents similar shortcomings both in terms of the lack of a reference measure for drops diameter and velocity and of the limited applicability to some types of instruments only.

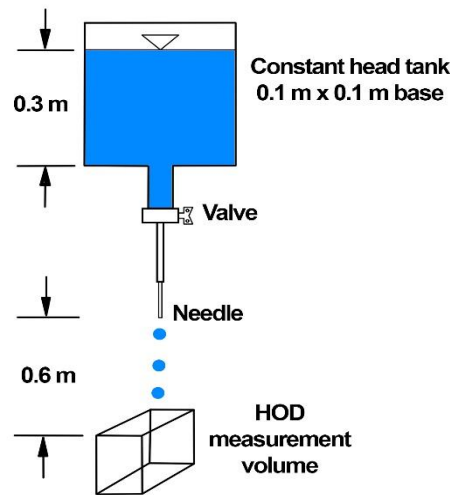


Figure 4.3: Scheme of the laboratory setup used to calibrate the HOD (from Testick & Rahman, 2016). A constant head tank with a fixed needle is used to generate drops with nearly the same size, that are then released over the instrument sensing area.

From the work of Licznar et al. (2008), information is obtained about the calibration procedure of impact disdrometers as used by the Institute of Fundamental Technological Research of the Polish Academy of Sciences (IPPT PAN). The instrument output was recorded for several single waterdrops with different known volumes and fall velocities. The drops were free-falling in still air conditions after being released at different elevations. Their velocities just before the impact were measured using a high-speed digital video camera (Figure 4.4), at 25 cm above the sensing plate of the DBI impactometer. The interval between the camera frames was set to 0.8 ms, and the exposure time was set to 0.2 ms. The waterdrops were generated through a thin silicon pipe (adapted from a medical intravenous infuser kit manufactured by Polfa Lublin SA) ending with the medical needle of selected diameter. The different diameters of the needles controlled the waterdrop size. An Ascor syringe pump, type “Ap 12”, was used to supply distilled water to the pipe at a constant rate. The regulated outflow rate of the pump controlled the frequency of waterdrop release.

The diameter of the falling drops was measured directly from the pictures taken by the camera with fixed setting. As a reference, a picture of a square-grid paper sheet (with a grid size of 1 mm x 1 mm), placed along the falling route of the waterdrops, was used. The reference-grid picture was taken at the same camera setting as for the rest of the experiment. As an independent verification of the drop diameters, they were also weighted with accurate laboratory scales. The DBI impactometer was tested for single drops falling from three different elevations: 2.34 m, 11.68 m, and 26.00 m. Tests for the 2.34 m falling height were conducted in the laboratory room in steady air conditions. The test runs for the two other elevations were performed in the interior staircase of the IPPT PAN building. The air temperature measurements made on different floors showed only small variations from 21.0 °C to 22.3 °C, while the airflow velocities were below 0.08 m s⁻¹.

Preliminary tests of the DBI impactometer revealed that its output depends not only on the waterdrop diameter and impact velocity but also on the distance between the drop landing position and the centre of the sensing plate. This procedure can produce drops of different size falling at their terminal velocity and employs an independent measure of both drops diameter and velocity. One limitation is the elevated cost of high-resolution high-speed video cameras and the lack of an automated procedure to be used to calibrate a large number of instruments.

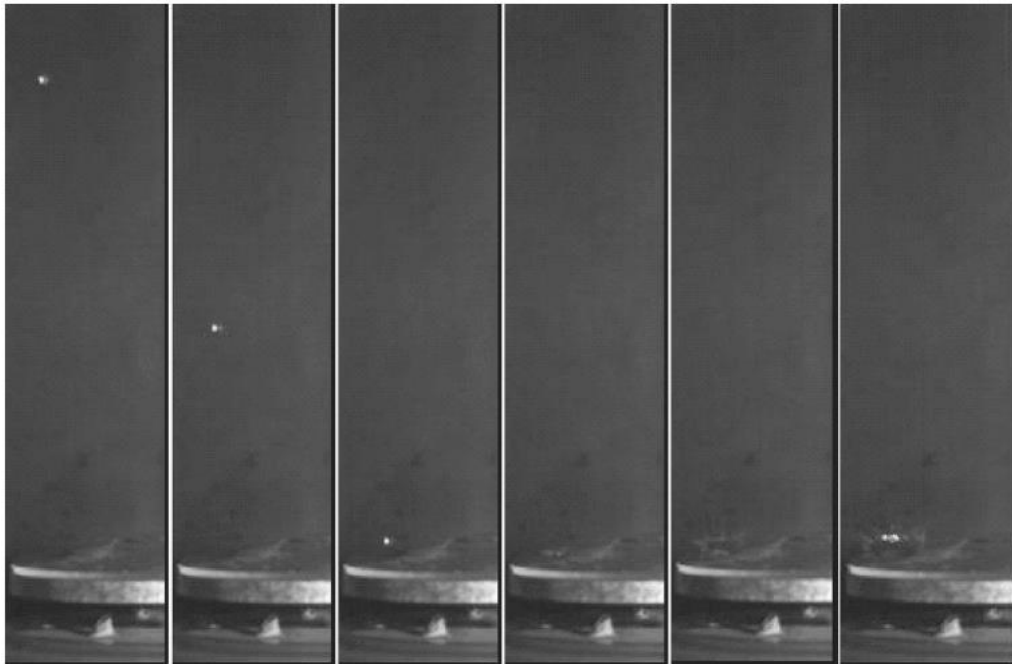


Figure 4.4: Images captured by the high-speed camera used to estimate the drop velocity just before the impact (from Licznar et al., 2008).

Another calibration procedure found in the literature for impact disdrometers is based on the numerical minimization of a function, conceptually similar to an adaptive digital filter. The strategy behind this technique is to use a tipping bucket rain gauge or another reference gauge to provide the data to optimize a set of adaptive coefficients. An error surface is defined as the sum of the square of the differences between the disdrometer cumulated volume and the reference cumulated volume. The calibration function is obtained with a series of iterative steps in which the coefficients are obtained by minimizing the error surface (Kourtellis, 2005). This approach is based on real precipitation events, meaning that it is influenced by the environmental conditions at the test location, and requires a large amount of time to calibrate each instrument. The most important drawback is the use of a tipping bucket rain gauge, which measures neither the diameter nor the velocity of hydrometeors, and its adoption as a reference for the calibration of a disdrometer is rather questionable.

To assess the performance of impact disdrometers in measuring hail, a peculiar calibration method has been proposed by Löffler-Mang et al. (2011). The hail precipitation event was reproduced in laboratory using a specifically designed hail gun, and spheres made of ice or frozen fruit juice, to resemble more spongy ice.

After thoroughly searching the scientific literature, the most recurring idea for testing the performance or calibrating disdrometers seems that of using plastic or metal spheres of a known diameter, released over the sensing area of the instrument. This solution is adopted because of its simplicity and repeatability, and examples of this method can be found in Grossklaus et al. (1998), Löffler-Mang et al. (2011), Kruger et al. (2002). In one case, following the same basic idea, small pieces of Styrofoam (Figure 4.5) were used, instead of spheres, to better simulate snowflakes (Bernauer et al., 2015). The use of water drops is limited and, in most cases, only drops of relatively large diameters are used. As discussed before, the use of solid media as a substitute for water drops is less than ideal and should be avoided, because it cannot reproduce neither the peculiar shape of falling drops nor their terminal velocity.



Figure 4.5: Image of the Styrofoam particles used by Bernauer et al. (2015) to simulate solid precipitation.

4.2 PROPOSED PROCEDURE FOR TRACEABLE CALIBRATION

The literature analysis shows that, although numerous attempts were made and various approaches were tested, no fully traceable calibration procedure, that can be used for most of the NCGs on the market, is currently available. To address this problem, a calibration procedure is proposed below, developed from the experience gained during the Joint Research Project “EMPIR 18NRM03 - INCIPIT *Calibration and accuracy of non-catching instruments to measure liquid/solid atmospheric precipitation*” (Merlone et al., 2022).

Some instruments (disdrometers) provide independent drop size and fall velocity output information for each individual detected drop, and these two parameters are used first for calibration. Then the integral value of the rainfall intensity, as determined by Equation (2.1), is used as well to compare with the associated instrument output. For instruments providing the rainfall intensity as the only output (therefore assuming a theoretical relationship between the drop diameter and its terminal velocity), or providing no output information for individual drops, such an integral parameter can be used alone for calibration.

Raw data are used for calibration of each instrument, intending as raw data the dimensional (size) and kinematic (fall velocity) information about each individual drop. Derived variables, such as kinetic energy

(KE) and precipitation intensity (RI), will be used for calibration only in case raw data are not provided as an output of the instrument. The role of any filtering or interpretation software that is not open (e.g., proprietary software, undisclosed procedures), nor released for the purpose of the testing, must be included in the calibration results.

Calibration of non-catching precipitation measuring instruments must be performed by generating a controlled set of water drops and letting them fall from a sufficient height over the sensing area (or volume) of the instrument under test. The drop size and fall velocity must be determined by means of an extensive characterisation of the adopted drop generator and their uncertainty assessed and traced back to the international system of units (Baire et al., 2022). When triggered by the generated drops, the reading of the instrument must be recorded and compared with the known drop characteristics.

Water drops of at least three different diameters in the range 0.5 mm – 6 mm must be generated (it is advisable to generate five different diameters, including those at the limits of the above range). The release height above the sensing area of the instrument under test must be such that at least 50% of the terminal velocity is achieved when the drop reaches the sensing area (or volume) of the instrument (this requirement means that at least 0.063 m are used for a drop with diameter 0.5 mm and at least 2.1 m for a drop with diameter 6 mm, see Table 4.1 for further reference). It is recommended that the size and fall velocity of each generated drop are measured immediately before or after they reach the instrument under test by means of an independent measurement method (gravimetric, photogrammetric, etc.).

Drops should be released in different positions over the sensing area (or volume) of the instrument under test, to cover both the central and peripheral measurement regions (a minimum of 5-6 different positions is recommended, depending on the instrument geometry). Enough drops should be released to allow statistical significance of the results (at least 30 drops per each position) and the mean and coefficient of variation of each set of drops will be used to assess the performance of the instrument under test.

Table 4.1: Required fall height to achieve 50% of the terminal velocity starting from near-zero velocity for drops of a given equivolumetric spherical diameter.

Equivalent drop diameter [mm]	Fall height [m] to reach 50 % of w_T	Equivalent drop diameter [mm]	Fall height [m] to reach 50 % of w_T
0.50	0.063	1.50	0.442
0.55	0.077	2.00	0.629
0.60	0.091	2.50	0.816
0.65	0.107	3.00	1.002
0.70	0.123	3.50	1.187
0.75	0.141	4.00	1.371
0.80	0.159	4.50	1.554
0.85	0.179	5.00	1.737
0.90	0.199	5.50	1.919
0.95	0.220	6.00	2.101
1.00	0.242		

A test report will be produced to include the results of the calibration procedure. Results will first be reported in the form of a summary table including, per each test, the drop nominal diameter, D [mm], the mean and standard deviation of the actual equivolumetric diameter, D_{eqv} [mm], and the mean and standard deviation of the actual fall velocity, w_{act} [$m\ s^{-1}$]. In the same table, the readings of the instrument under test will be summarised, by reporting the mean and standard deviation of the measured drop diameter, D_m [mm], and the mean and standard deviation of the measured fall velocity. An example of the proposed Table is provided below.

Table 4.2: Sample table for reporting calibration results

N.	Nominal drop diameter (mm)	Drop diameter avg. (mm)	Drop diameter std. dev. (mm)	Fall velocity avg. ($m\ s^{-1}$)	Fall velocity std. dev. ($m\ s^{-1}$)	Meas. diameter avg. (mm)	Meas. diameter std. dev. (mm)	Meas. velocity avg. ($m\ s^{-1}$)	Meas. velocity std. dev. ($m\ s^{-1}$)
1	D_1	μ_{Deqv}	σ_{Deqv}	μ_{wact}	σ_{wact}	μ_{Dm}	σ_{Dm}	μ_{wm}	σ_{wm}
2	D_2
3	D_3
4	D_4
5	D_5

Normalized values of the sample statistics of the measured drop diameter and fall velocity (with μ_{Deqv} and μ_{wact} , respectively) can be provided instead of the absolute values.

It is recommended to provide a box-plot graphical representation of the same data in two separate graphs, one obtained by plotting the non-parametric distribution of the measured drop diameter data from each test against the average actual diameter, and a second one obtained by plotting the non-parametric distribution of the measured fall velocity data from each test against the average actual fall velocity.

It is recommended to fit the average measured drop data against the reference values using a suitable mathematical expression, whose form and parameters must be explicitly included in the test report.

For consistency with the established classification of catching type gauges (see EN17277:2019), the acceptability range of the test results is here defined in terms of rainfall intensity. Indeed, irrespectively of the actual output of the instrument under test, reading or calculation of the rainfall intensity value at the time resolution of at least one minute (and even lower) is always possible for non-catching precipitation measuring instruments.

By neglecting the effect of the interaction between contiguous or contemporary drops on the measurement, thanks to the low density of the liquid phase in natural rainfall, synthetic rainfall events can be constructed by sampling the DSD at each relevant rainfall intensity value. An exponential mathematical form can be assumed for the DSD, according to Marshall and Palmer (1948), as follows:

$$N(D) = N_0 \exp(-\Lambda D)$$

4.1

with N_0 ($\text{mm}^{-1} \text{ m}^{-3}$) and Λ (mm^{-1}) the scale and slope parameters, expressed as a function of the rainfall intensity RI (mm h^{-1}) as (Cauteruccio & Lanza, 2020):

$$N_0(RI) = 835.91 \cdot RI^{0.8942}$$

4.2

$$\Lambda(RI) = 3.2863 \cdot RI^{-0.0760}$$

4.3

Although in natural precipitation events the rainfall intensity derives from a combination of numerous drops of various size and fall velocity, according to a continuous drop size distribution, Equation 2.1 is also applicable to a set of monodisperse rainfall components like the ones produced in the laboratory by the raindrop generators described below. By replacing the integral operator with the sum of a discrete number of individual components, separated by a given interval $\Delta D_{i.eqv}$, we obtain:

$$RI_{ref} = C_c \sum_{D_{min}}^{D_{max}} N(D_{i.eqv}) \Delta D_{i.eqv} \cdot V(D_{i.eqv}) \cdot w_{act}(D_{i.eqv})$$

4.4

with the same terminology used above and being RI_{ref} a reconstructed target event, $D_{i.eqv}$ the i -th equivolumetric diameter chosen for the discretisation of the target event, $\Delta D_{i.eqv}$ the interval between two consecutive diameters, and w_{act} the actual fall velocity of the released drop obtained from Equation 2.11. Furthermore $C_c = 3.6 \cdot 10^6$ [$\text{mm h}^{-1} \text{ m}^{-1} \text{ s}$] is the numerical factor for the conversion of the rate of rainfall from [m s^{-1}] to [mm h^{-1}].

The target rain event is obtained as follows. Per each investigated (nominal) diameter D_i , a set of at least 30 drops is generated and released above the instrument under test. The resulting target rainfall intensity RI_{ref} is calculated using Equation 4.4 with the mean diameter of the generated drops and their mean fall velocity (see Figure 4.6).

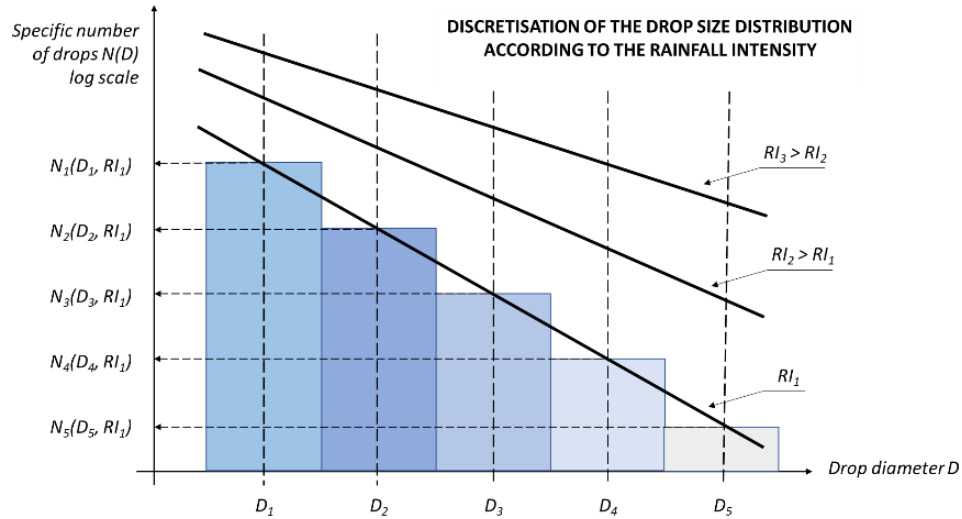


Figure 4.6: Method for the discretization of the drop size distribution as a function of the rainfall intensity used to calculate the target rain event.

Analogously, a measured rain event RI_{meas} can be reconstructed using Equation 4.4 based on the output measurements obtained from the instrument under test. Therefore, the mean measured drop size and fall velocity can be used in Equation 4.5, to obtain:

$$RI_{meas} = C_c \sum_{D_{min}}^{D_{max}} N(D_{i.eqv}) \Delta D_{eqv} \cdot V(D_{i.m}) \cdot w_m(D_{i.m})$$

4.5

with all symbols already defined above.

From the measured and the target rain event, the percentage relative deviation is calculated as:

$$e_{rel}[\%] = \frac{RI_{meas} - RI_{ref}}{RI_{ref}} \cdot 100$$

4.6

Performance requirements are met when the percentage relative deviation is within the limits required for the various classes defined in the existing EN17277:2019, already available for CGs. More precisely, attributing a class to an instrument within a given range of rain intensity values can be performed according to the following limits:

- Class A: Class A precipitation measuring instruments have percentage relative deviations within $\pm 3\%$ against the reference rainfall intensity.
- Class B: Class B precipitation measuring instruments have percentage relative deviations within $\pm 5\%$ against the reference rainfall intensity.

Class C: Class C precipitation measuring instruments have percentage relative deviations within $\pm 10\%$ against the reference rainfall intensity.

If a precipitation measuring instrument has a percentage relative deviation greater than $\pm 10\%$ in measuring the reference rainfall intensity, then it cannot be classified according to the proposed standard.

Results can first be reported in the form of a summary table including, per each target rainfall intensity value, the percentage relative deviation between the measured and target values. It is recommended that a graphical presentation of the same data is also provided, and the errors are fitted against the measured rain intensity using a suitable mathematical expression, whose form and parameters must be explicitly included in the test report.

Classification of a precipitation measuring instrument can be limited to a reduced measurement range with respect to the entire operational range of the instrument (instruments can have different classes for different measuring ranges). For example, Class B can be attributed between 2 and 50 mm·h⁻¹, while Class A is attributed for higher rainfall rates.

The data used in the calibration and to attribute a given class to the instrument will be “precipitation intensity” (or similarly named) and obtained as the output from the instrument. If any other quantity provided by the instrument is not consistent with this, then it must be declared. For example, a possible additional quantity “rainfall depth” (or similarly named) must be consistent with the time interval of the measured precipitation intensity except for a reasonable numerical approximation of the data.

When NCGs are used as disdrometers only, calculation of the accuracy of the rainfall intensity variable may not be necessary. In that case, the accuracy of the DSD measurements can be directly assessed by using the data reported in Table 4.2. In the absence of any pre-existing knowledge about the traceable calibration of disdrometers, it is recommended that the percentage relative deviations in the measurement of the drop size and fall velocity are used and calculated as:

$$e_{rel.d}[\%] = \frac{\mu_{dm} - \mu_{deqv}}{\mu_{deqv}} \cdot 100 \quad 4.7$$

$$e_{rel.w}[\%] = \frac{\mu_{wm} - \mu_{wact}}{\mu_{wact}} \cdot 100 \quad 4.8$$

The accuracy of the instrument for each single parameter is evaluated, separately, through estimates of sample statistics that are indicative of trueness and repeatability of consecutive measurements. The interval containing 80 % of the percentage relative deviations can be evaluated in the form:

$$R = \{q_{10}^e, q_{90}^e\} \quad 4.9$$

where:

q_{10}^e is the 10° percentile of the percentage relative deviation;

q_{90}^e is the 90° percentile of the percentage relative deviation.

Deviations can be assumed to have a Gaussian-like distribution and the interval can be expressed as:

$$R = \{\mu_{rel.d} + k \cdot \sigma_{rel.d}, \mu_{rel.d} - k \cdot \sigma_{rel.d}\} \quad 4.10$$

$$R = \{\mu_{rel.w} + k \cdot \sigma_{rel.w}, \mu_{rel.w} - k \cdot \sigma_{rel.w}\} \quad 4.11$$

where:

- k is the numeric constant depending on the probability distribution of the deviations (in case of the Gaussian distribution, k is approximately equal to 1,28);
- $\sigma_{rel.d}, \sigma_{rel.w}$ are the standard deviations of the percentage relative deviation of the drop size and fall velocity (indicating the repeatability of the measurement);
- $\mu_{rel.d}, \mu_{rel.w}$ are the expected values of the percentage relative deviation of the drop size and fall velocity (indicating the trueness of the measurement);

Performance requirements are met when the average value and the 10° and 90° percentiles (i.e., 80 % of all recorded values) of the percentage relative deviation are within 5%.

4.3 DEVELOPMENT AND CHARACTERIZATION OF A LABORATORY RAIN DROP GENERATOR

To satisfy the need for reliably releasing on demand water drops of different diameters and independently verifying their diameter and fall velocity, a bespoke Calibrated Rainfall Generator (CRG) was developed in the present thesis work at the University of Genova as part of the activities of the INCIPIT project, where it was proposed as a suitable calibration method (Merlone et al., 2022; Baire et al., 2022). It is composed of three main functional components, the Drop Releasing Head (DRH), the Photogrammetric Verification System (PVS) and the Motorized Alignment Gantry (MAG). It was developed to be flexible, with ample use of off the shelf components and 3D-printed parts that allowed to produce a relatively low-cost system that could be adopted by even small organizations with the intent of calibrating NCGs.

4.3.1 The drop releasing head

The drop releasing head is capable of releasing on demand water drops of different sizes. It is composed of two high-precision syringe pumps and an electrostatic detachment system.

The two pumps were designed to be light-weight and with a high precision in delivering the desired amount of water. Both pumps are based around a hollow-shaft stepper motor, while the other major components are 3D-printed. Water is contained inside a commonly available plastic syringe, with a nominal capacity of 1 ml for the smaller pump and 20 ml for the larger pump. A threaded rod – inserted through the hollow shaft of the motor – is used to push on the syringe plunger creating the water flow. Motion of the

threaded rod is granted by threaded nuts (two for the smaller pump and one for the larger one) that are attached to the motor shaft. Attached to the other end of the threaded rod is an anti-rotation system, that runs on small ball bearings. This approach ensures that the rotation of the motor is completely converted into linear motion thanks to the sloped surface of the thread.

Contrary to other more common designs where the motor shaft is not in-line with the syringe axis, the pump body is here subject to axial forces only, without requiring gears or pulleys to transfer motion between the motor and the piston, allowing for a lightweight and compact design, and considerably improving the stiffness of the system while maintaining tighter tolerances. For the 1 ml syringe, the plunger diameter is 4.5 mm and a M2.5 threaded rod is used, allowing for a dispensed volume resolution of 0.016 μl . Meanwhile, for the 20 ml syringe the plunger diameter is 20 mm and a M3 rod is used, resulting in a dispensed volume resolution of 0.393 μl . The stepper motors are operated by means of an Arduino microcontroller with DRV8825 stepper drivers. An over-travel safety is implemented by embedding two end-stop switches in the pump body that are actuated by the anti-rotation system once the plunger end-of-travel is reached. In Figure 4.7, cross-sections of both pumps are presented, where all previously described components are visible. It is worth noting, in the smaller pump, the presence of a secondary nut that can be used to control the amount of clearance between the threaded rod and the primary nut, eliminating backlash.

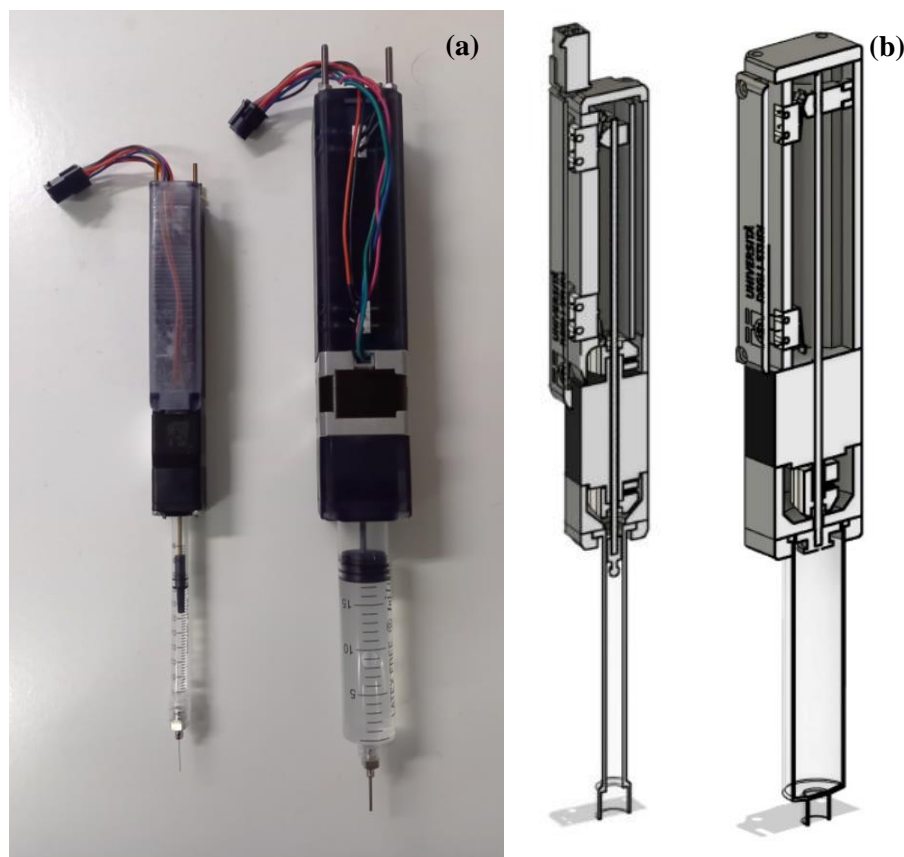


Figure 4.7: Image of the two syringe pumps that compose the DRH (a) and the cross-section of the two pumps (b).

The second major component of the DRH is the electrostatic detachment system. It is primarily composed by a 5V to 5kV DC-DC converter that is used to detach the drops. It is housed inside a sealed plastic box positioned behind the pumps. Other than the converter, inside the box a normally closed 5000V capable relay is also present. Its control pins are connected in parallel to the low voltage side of the DC-DC converter, while its high voltage side connects the two high voltage side terminals of the converter to a 1 MOhm resistor. This ensures that no residual charge (due to capacitors inside the DC-DC converter) can remain in the system while it is powered off. Two cables provide the 5V input current to the box, that can be switched on or off at will, while other four cables get out of the box, the two negative ends are connected to each syringe needle while the two positive ends are connected to a metallic ring below the nozzle. The metallic ring is positioned by a 3D-printed arm, designed to precisely align it with respect to the syringe nozzle, by moving it in the three directions using alignment screws. To ensure safe operations all cable insulation is rated for 6kV, and the ones connected to the high voltage side are further shielded by 1mm thick PTFE tubing. In Figure (4.8) an image of the electrostatic detachment system with the alignment arm is shown.

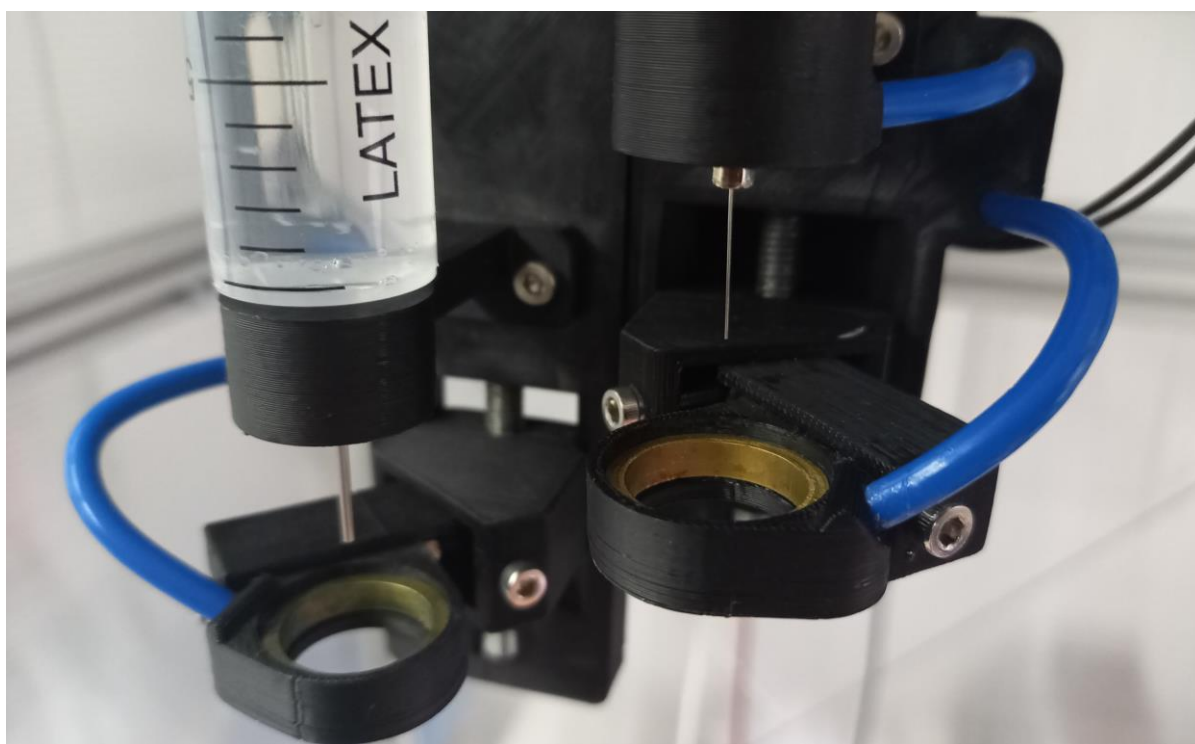


Figure 4.8: Image of the electrostatic detachment system with the supporting arm and the high voltage leads isolated with PTFE tubing (in blue). Both the needle and the metallic ring are clearly visible for both pumps.

The chosen pump can displace the amount of water volume necessary to produce a drop of the requested diameter, that will remain attached to the end of the needle. Then power to the electrostatic release system is switched on, the relay (that is normally closed) will open, allowing a potential difference to be produced between the needle and the metallic ring below it. The water drop is negatively charged and thus strongly attracted by the metallic ring that is instead positively charged. Once this additional force is applied, the

previous equilibrium is broken, and the drop is forcibly detached from the needle. Power is immediately turned off, allowing the drop to freely fall.

4.3.2 The photogrammetric verification system

To achieve fully traceable calibration, once the drop is released and in flight, its diameter and fall velocity must be independently assessed before it reaches the instrument sensing area. The measure should be contactless and should not affect the drop trajectory. A photogrammetric approach was chosen, thanks to its flexibility, compactness, and ease of use. The PVS is based on a Sony a6100 mirrorless camera, equipped with a 24mpx APS-C CMOS sensor. A Sony SEL 30 f3.5 macro lens, capable of a 1:1 reproduction ratio, is attached to the camera. This setup is ideal for taking high resolution pictures of very small objects, with a maximum spatial resolution (in the case of 1:1 reproduction ratio) of $3.89 \mu\text{m}$.

Further to the camera, two compact speedlights are used to illuminate the falling drop. A specifically designed diffuser is attached to the camera lens, to provide optimal illumination of the drop, and to highlight its contour on a black background. The diffuser is composed of a translucent plastic, that helps directing the speedlights beam, covered by an opaque layer to minimize light spillage. The whole setup, including the supports to align the camera and the speedlights, is 3D-printed. A photograph of the setup is shown in Figure 4.9(a) while on the right-hand side (Figure 4.9b) a cross section of the diffuser is shown.

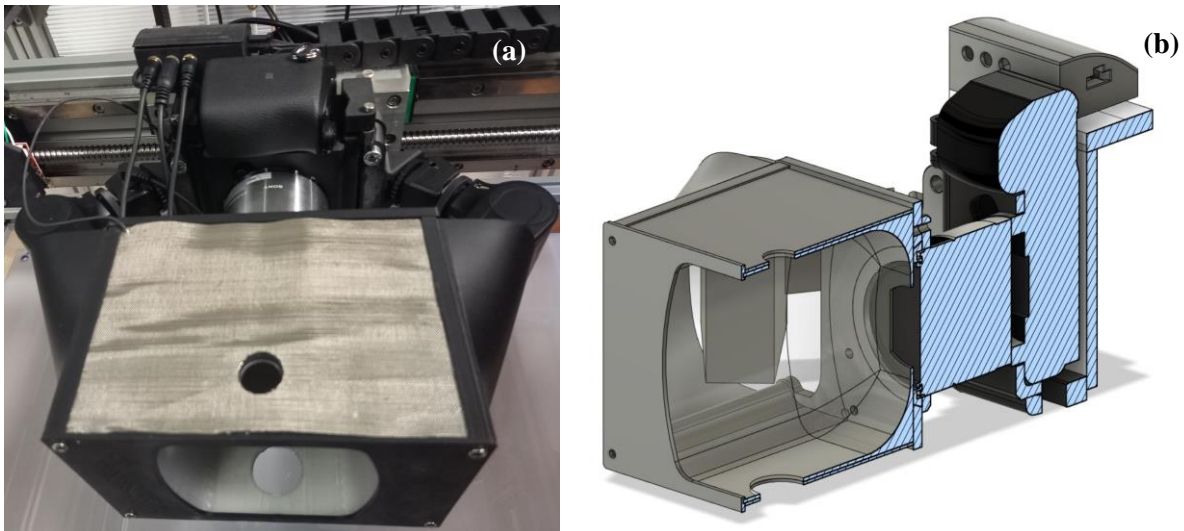


Figure 4.9: Image of the PVS, clearly visible is the diffuser that is used to light the drops in flight (a). Cross-section of the PVS, including the camera and the diffuser (b).

The PVS is synchronized with the release of the drop, a delay is set so that the camera shutter is opened just before the drop enters the camera field of view. While the camera shutter is open, three flashes of light are emitted by the speedlights with a 4.2 ms interval so that the image of the drop is impressed three times on the camera sensor. An example of the pictures obtained by the PVS for different drop diameters is shown in Figure 4.10.

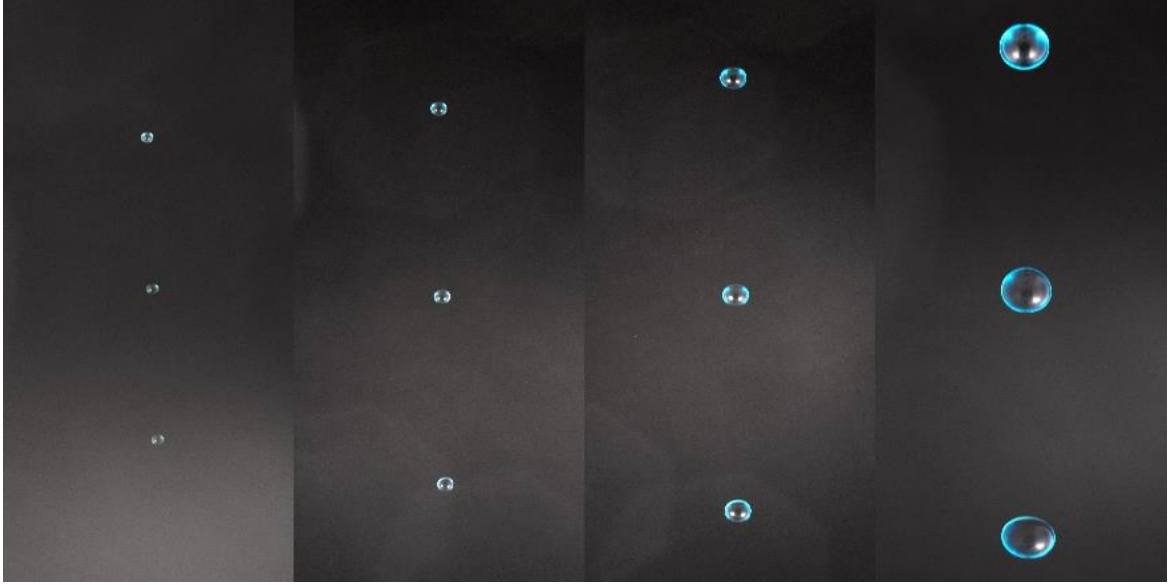


Figure 4.10: example of the images obtained from the PVS, from left to right the drop size is: 0.75, 1, 2 and 3.5 mm. During preliminary testing water was dyed to improve visibility of drops.

Those images constitute the reference measure for the calibration, both in terms of drop size and fall velocity. To extract the required information, a photogrammetric approach is used. This can be done using the collinearity equation, that can be written as:

$$X = X_0 + (Z - Z_0) \frac{r_{11}(\xi - \xi_0) + r_{12}(\eta - \eta_0) - r_{13}F}{r_{31}(\xi - \xi_0) + r_{32}(\eta - \eta_0) - r_{33}F} \quad 4.12$$

$$Y = Y_0 + (Z - Z_0) \frac{r_{21}(\xi - \xi_0) + r_{22}(\eta - \eta_0) - r_{23}F}{r_{31}(\xi - \xi_0) + r_{32}(\eta - \eta_0) - r_{33}F} \quad 4.13$$

where X, Y and Z are the coordinates of the generic position in the chosen Reference System (RS), X_0, Y_0 and Z_0 are the coordinates of the projection centre in the RS, while ξ and η are the coordinates of the positions in the image RS and ξ_0 and η_0 are the coordinates of the projection centre in the camera RS. Symbol \mathbf{r} denotes the rotation matrix and F is the camera focal length. Since this is a peculiar case, the origin of the reference system can be chosen arbitrarily, and the rotation matrix \mathbf{r} is equal to the identity matrix because the hydrometeor trajectory is fully contained in a plane parallel to the camera sensor. Under these very specific conditions, the collinearity equations can be simplified to:

$$X = X_0 + (Z - Z_0) \frac{(\xi - \xi_0)}{F} \quad 4.14$$

$$Y = Y_0 + (Z - Z_0) \frac{(\eta - \eta_0)}{F} \quad 4.15$$

For the evaluation of the drop size and fall velocity, only the computation of distances is required. Therefore, by using Equations 4.14 and 4.15, the distance d between two arbitrary positions on the image can be written as:

$$d = \sqrt{\left(\frac{Z - Z_0}{F}\right)^2 [(\xi_2 - \xi_1)^2 + (\eta_2 - \eta_1)^2]} = \frac{Z - Z_0}{F} d_{image} \quad 4.16$$

By choosing a reference system for Equation 4.16 so that $\frac{Z - Z_0}{F} = \frac{Sd - C}{F}$, where Sd is the shooting distance, the distance between two positions in the image becomes:

$$d = \frac{Sd - F}{F} d_{image} \quad 4.17$$

The shooting distance in the PVS is maintained constant and the focal length is a physical characteristic of the lens used, therefore the term $\frac{Sd - F}{F}$ becomes a constant of the problem that can be obtained once the focal length of the camera and the shooting distance are known. The value of this term can also be verified by photographing a graduated scale of known size.

Post processing of the images is automatically performed, using a machine vision algorithm implemented in MATLAB. The code detects the contours of the drop thanks to the high contrast that is generated by the combination of the diffuser and a black background. Once the contour of the drops is known, the area, maximum and minimum diameters, and the centre of mass of the drop can be easily computed. The fall velocity is also easily obtained since the time interval between flashes is known and can also be directly measured by means of a photodiode.

In Figure (4.11), a sample captured image is shown (left-hand panel) while the same picture after software processing is presented in the right-hand panel to show the drop area (highlighted in blue), the equivolumetric circular shape of the drop (D1–D3, in red), and the travelled distances (L1 and L2). The red circle plotted over each drop has a diameter equal to the computed one and its origin is positioned in the centre of mass estimated by the software.

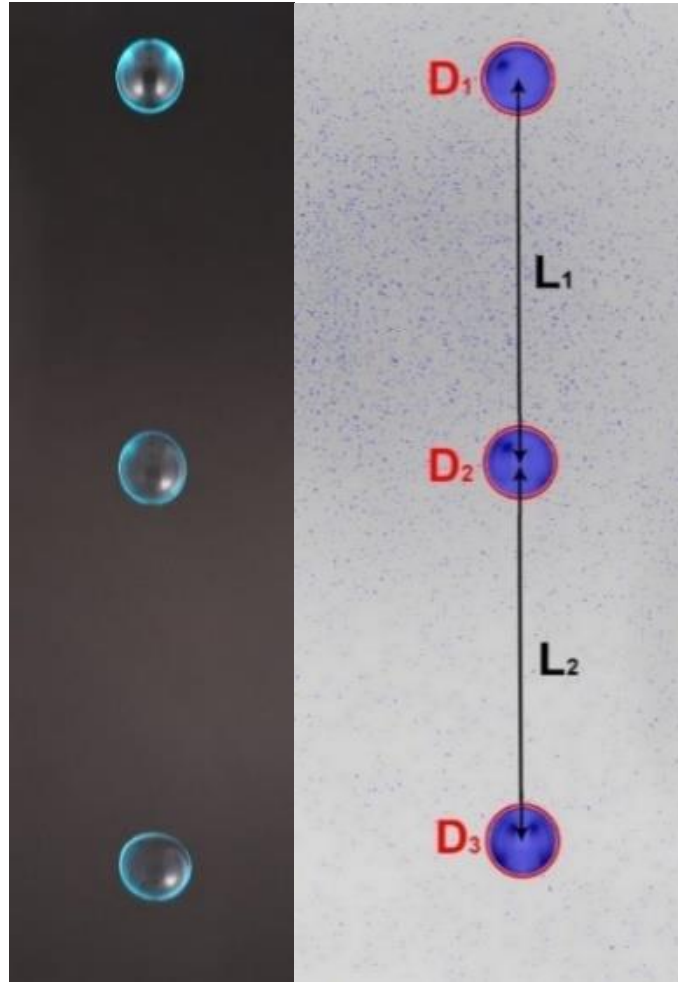


Figure 4.11: sample image of a single drop in flight as released by the DGH and captured by the PVS (left-hand side). In the right-hand panel the same image, after software post-processing, is reported.

This method allows for rapid and efficient processing of a large number of photographs. A considerable advantage of the presence of the PVS is that, since the actual size and velocity of each single drop are measured, the strict repeatability of the drop characteristics is a much less relevant issue. In fact, the measured diameter of each drop rather than the nominal one is used for comparison with the instrument output. Analogously, the knowledge of the fall velocity of each drop avoids resorting to theoretical formulations and the need to adopt very tall supporting structures to achieve the terminal velocity for the largest drops.

4.3.3 The motorized alignment gantry

Both the DRH and the PVS must be maintained in place and aligned with each other and to the instrument under test. This is necessary to ensure that the drop, once released, follows a trajectory that crosses the focal plane of the camera and then reaches the instrument sensing area at the chosen location. Automatic alignment of the two components is ensured by the MAG, that is composed of two identical aluminium frames housing the DRH and the PVS. The frame has a C shape and is constructed using aluminium extrusions. On the two parallel sides of the frame, linear rails are installed and allow a transversal gantry to

move in one direction. On the moving gantry another set of linear rails is used to allow movement of a supporting plate, where the DRH or the PVS is mounted, along the other direction. Both the gantry and the supporting plate are maintained in position and moved using ball-screws, each one connected to a stepper motor by means of toothed belts with a 2:1 reduction ratio. In Figure 4.12 an image of one of the frames is shown.

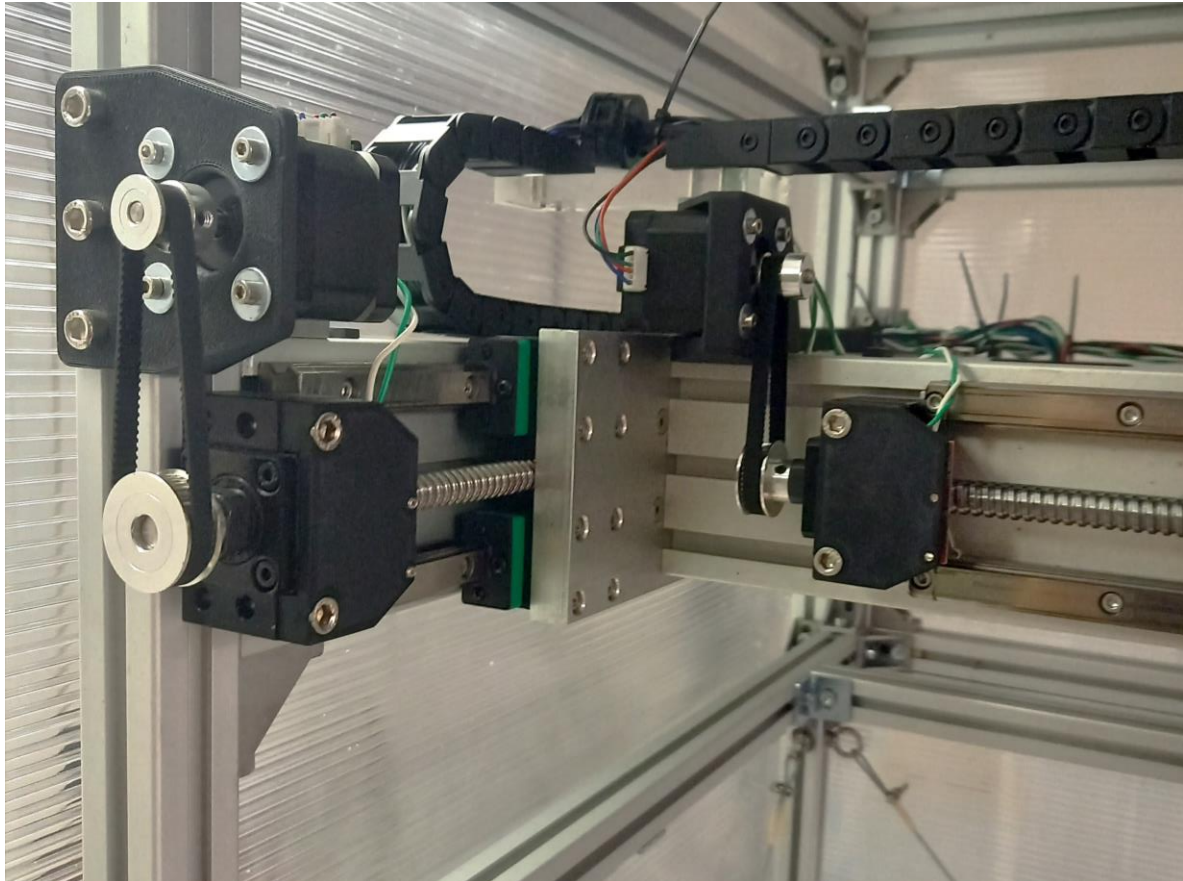


Figure 4.12: Image of the MAG frame, the motors are connected to the lead screws using a timing belt with a 2:1 reduction ratio. The linear rails supporting both the gantry and the supporting plate are visible. In the background the drag chain that contains all the electrical connections.

All the stepper motors are controlled by an Arduino board and the frames are equipped with end stops, to ensure protection against overtravel. Electrical connections between the frame and the DRH or the PVS are ensured by flexible cable chains. The system is capable of a high level of repeatability of the positioning and has a movement resolution of 0.01 mm. In Figure 4.13 the supporting structure for the two frames is shown. Plastic panels are used to shield against air gusts, so that the trajectory of the drop is not disturbed by external factors.



Figure 4.13: Image of the structure that is used to support the two fames, lightweight plastic panels are used to provide shielding for the released drops.

4.3.4 Characterization of the CRG

To assess the performance of the CRG in terms of the generated drops size, several tests were performed by releasing drops of nominal size between 1 and 5.5 mm. Depending on the size, 50 to 180 drops were released (for $D = 5.5\text{mm}$ and 1.0mm , respectively) from a height of 1.20 m above the centre of the measurement plane of the camera. Each released drop was photographed by the PVS and the images interpreted using the automatic post-processing algorithm. As a validation of drop size measurements, for each test, the total volume of samples of each diameter was weighted by means of a precision balance having a resolution of 0.001 g. Oil was poured inside the container placed on the scale to avoid evaporation during the tests. Results are summarized in Table 4.3 in terms of average drop diameter obtained from the PVS and the scale, together with the percentage error between them. Because no independent measure of the drop fall velocity is available, numerical results are used to compare against the PVS results both in terms of vertical velocity after a 1.2m fall and of the percentage of terminal velocity reached by the drop.

Table 4.3: Results of the tests expressed as average diameter for both the PVS and scale measurements.

N° drops	Nominal D [mm]	PVS avg. D [mm]	Std. dev. D [mm]	Scale avg. D [mm]	Std. dev. D [mm]	Error [%]
50	5.5	5.017	0.356	4.98	0.052	0.78
100	5	4.398	0.190	4.40	0.111	0.03
100	4	3.584	0.112	3.66	0.043	-2.04
100	3	2.803	0.082	2.80	0.027	0.14
110	2	2.066	0.067	2.04	0.004	-0.87
180	1	1.013	0.060	0.97	0.052	4.23

Table 4.4: Results of the tests expressed as average diameter for both the PVS and scale measurements.

N° drops	Nominal D [mm]	Avg. w [m s^{-1}]	Std. dev. w [m s^{-1}]	Theoretical w [m s^{-1}]	Fraction of w_t [%]
50	5.5	4.42	0.520	4.598	42.376
100	5	4.48	0.069	4.560	45.099
100	4	4.22	0.281	4.488	49.637
100	3	4.25	0.104	4.376	55.602
110	2	4.00	0.086	4.185	63.810
180	1	3.13	0.100	3.339	85.054

Drops released with the larger pump (5.5 to 3 mm) tend to have a diameter below the expected one (about 10%) while drops released with the smaller pump (2 and 1 mm) are close to nominal. This could be due to the different volume resolution of the two pumps. Also, larger drops tend to leave a small amount of water still attached to the syringe needle when detached by the electrostatic release system, and this can be easily corrected by increasing the volume produced by the pump accordingly. The average diameter obtained with the PVS is in very good accordance with the one obtained from the scale, with an average difference always below 5%, and below 1% for most diameters. Standard deviations are quite low for both the PVS and the scale, indicating a good repeatability of the drop generation and release.

Fall velocities, shown in Table 4.4, are slightly lower than the ones computed numerically, yet are still in good accordance. Observing the terminal velocity reached by the drops, except for the 1 mm drops, larger drops are far from their terminal velocity. Drops failing to approach the aerodynamic equilibrium during the flight, i.e., their terminal fall velocity, present oblate sections due to significant oscillations in their shape, which may render the hypothesis of axial symmetry not completely accurate.

To be used as reference, it is necessary that the approach used is, from a metrological standpoint, fully traceable to international standards. The photogrammetric method here described is used to compute drop

diameter and fall velocity, therefore it must be ensured that it is traceable to the international standards of length and time. Regarding time, the time interval used to compute velocity, is obtained as a differential measure using the internal clock of the acquisition system that monitors the output of a photodiode. As for length measurements, three parameters are influential: the pixel physical size (pixel pitch, Pp), the lens focal length (F) and the shooting distance (Sd). The sensor pixel pitch is provided by the manufacturer of the camera with high accuracy. The lens focal length can be measured and certified in optical laboratories. The shooting distance is directly measured on the device once assembled. The equivalent length of one pixel in the captured image (Ip) is obtained as:

$$Ip = \frac{(Sd - F)}{F} \cdot Pp$$

4.18

The uncertainty associated with the definition of F and Pp is assumed as negligible compared to the uncertainty of Sd , and the latter is mainly determined by the drop releasing mechanism. It was calculated from the observed drop positions in several images, assuming that the uncertainty of the drop position is isotropic. The resulting standard deviation for the shooting distance Sd ranges between 1.87 and 0.67 mm when the drop size is between 1.5 and 5 mm, respectively. These values lead to an uncertainty between $\pm 2.4 \times 10^{-3}$ mm and $\pm 8.7 \times 10^{-3}$ mm for Ip , depending on the drop size. The uncertainty on the photogrammetric determination of the drop size has a resulting maximum value equal to 0.016 mm when the drop size is equal to 1.5 mm.

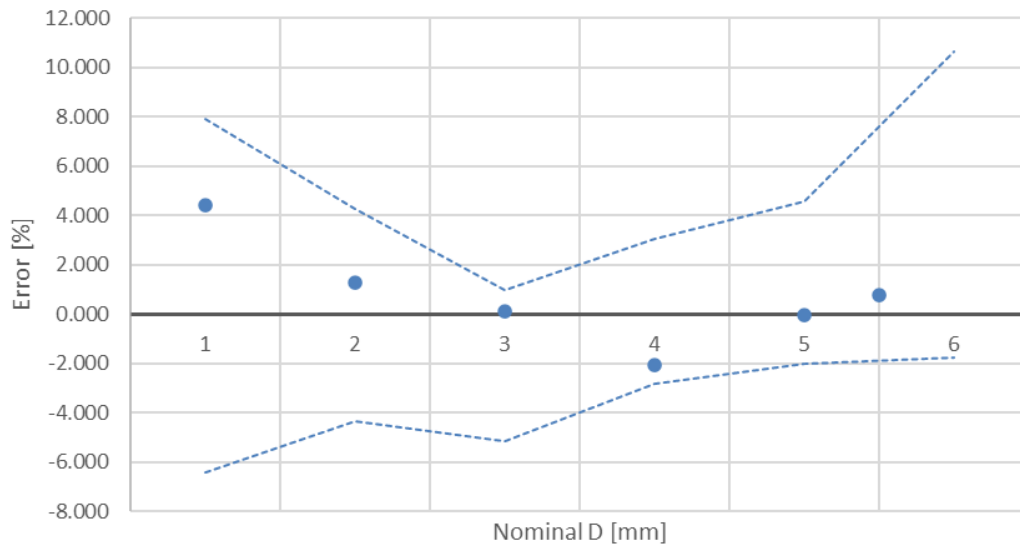


Figure 4.14: Percentage error of the PVS results compared against the scale measurements, the confidence interval of PVS results is shown by the dashed lines.

From the data presented in Table 4.3 the percentage error of the PVS (using the scale diameter as a reference) is plotted in Figure 4.14, together with the associated confidence interval (dashed lines). The

scale measurements are always inside the confidence interval of the PVS, meaning that the latter is a suitable reference for measuring the size of falling drops used for calibrating NCGs.

4.4 APPLICATION TO SAMPLE NCGS

The proposed calibration procedure is here applied, as an example of the CRG capabilities, on two NCGs employing different measuring principles. The instruments are commonly deployed in the field and these tests can provide insights on the performance that can be expected when measuring both integral and microphysical properties of liquid precipitation.

4.4.1 The Thies Laser Precipitation Monitor

The Thies LPM is an optical NCGs that uses the optical transmission principle to detect hydrometeors in flight. As shown in Figure 4.15, the instrument body is composed of a prismatic housing for the circuitry boards, with attached the light emitting head and two supporting arms. Located at the end of the two arms, and aligned with the emitting head, is the receiving sensor.

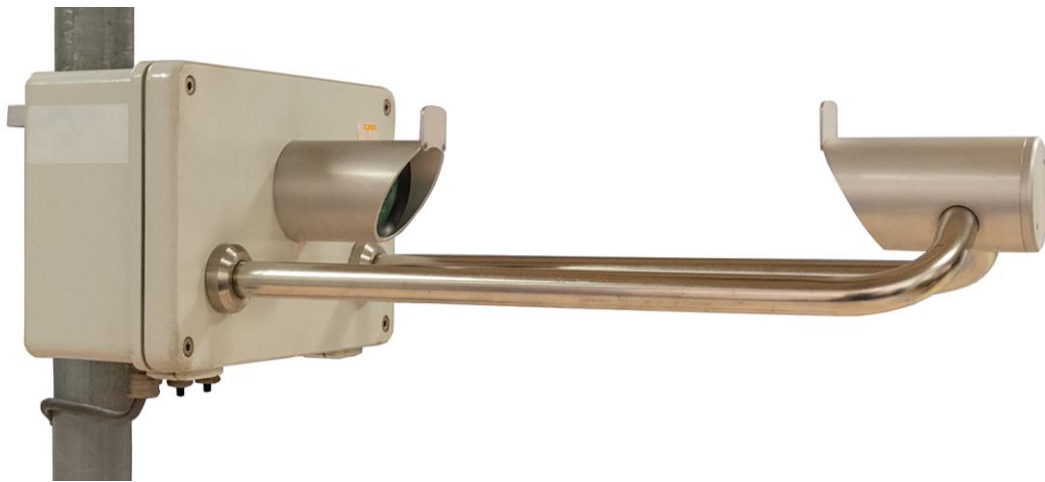


Figure 4.15: The Thies LPM (Thies, 2011), with the emitting head (attached to the circuitry box on the left-hand side) and the receiving head (attached to the supporting arms on the right-hand side).

The instrument uses an infrared (785 nm) laser diode, coupled with suitable optics, to produce an infrared light sheet 228 mm long and 20 mm wide with a thickness of 0.75 mm. The laser emission is maintained at a constant frequency of 173 kHz and a low-pass filter is used to minimize interference from the ambient light. A photodiode in the receiving head is then used to convert the laser beam power into an electric signal. When each single hydrometeor crosses the beam, the receiver will detect a reduction in the laser power and therefore a reduction in the electric signal. The diameter of the detected particle is calculated as a function of the voltage drop, while its fall velocity is obtained from the duration of the voltage reduction.

The combined values of the diameter and fall velocity at one-minute resolution are used to define the precipitation type (drizzle, rain, snow, soft hail, hail, and mixed precipitation), and to derive the precipitation intensity. Velocity is also used to automatically discard false readings produced by objects

like insects or falling leaves that may cross the beam. The system cannot differentiate between multiple hydrometeors simultaneously crossing the laser beam; therefore, these may be interpreted as a single particle of a larger diameter or be discarded by the instrument software, leading to an overestimation or underestimation of the total water volume. Another similar, but opposite, error is due to hydrometeors crossing the beam near its edges, blocking the laser beam only partially, which are detected as smaller particles leading to some underestimation of the water volume.

Note that installation instructions from the manufacturer (Thies, 2011) indicate that the orientation of the instrument in the field should be with the main symmetry axis aligned with the North direction, and the receiving end toward the equator (to minimize the effect of direct sunlight on the sensor), meaning that it is not possible to orientate the instrument according to the prevalent wind direction at the installation site.

4.4.2 The Biral VPF-750

The Biral VPF-750 is an optical NCGs that uses light scattering principles to detect hydrometeors in flight. As shown in Figure 4.16, the instrument body is composed of a cylindric housing for the circuitry boards, with attached the back scatter receiver head. At both sides, two supporting arms hold the sensor heads, one for the emitter and the other for the forward scatter receiver. The instrument can be further equipped with a humidity sensor, an ambient light sensor and/or temperature sensor.



Figure 4.16: The Biral VPF-750 (Biral, 2022), with its two receiving heads (one attached to the cylindrical circuitry box and one on the supporting arm to the left of the image) and the emitting head (attached to the supporting arm on the right-hand side).

The instrument uses an infrared (850 nm) IRED diode, coupled with suitable optics, to produce an infrared light cone that is projected outward, not aimed at any of the receivers. The IR light emission is maintained at a constant frequency of 2 kHz and a low-pass filter is used to minimize interference from the ambient light. Once hydrometeors cross the light beam, a certain amount of light is scattered towards the two receiver heads. A photodiode is then used to convert the light power into an electric signal by the detector and amplifier chain, and to generate an AC signal (due to the emitter frequency modulation) whose amplitude is proportionally to the size of the particle and whose duration is inversely proportional to its velocity.

The ratio between the back and forward scattered light and the combined values of the diameter and fall velocity at one-minute resolution are then used to define the precipitation type (drizzle, rain, snow, soft hail, hail, and mixed precipitation), and to derive the precipitation intensity. Velocity may also be used to automatically discard false readings produced by objects like insects or falling leaves that may cross the sensing volume. This system can differentiate between multiple hydrometeors simultaneously crossing its sensing volume.

Note that, like in the case of other optical gauges, installation instructions from the manufacturer (Biral, 2022) indicate that the orientation of the instrument in the field should take into account the presence of reflecting surfaces and care should be taken in avoiding direct sunlight entering the field of view of the receiving sensors. This means that it is not possible to orientate the instrument according to the prevailing wind direction at the installation site.

4.4.3 Laboratory calibration results

For laboratory calibration, both the Thies LPM and the Biral VPF-750 were placed below the PVS, inside the supporting structure, attached to a short metal pole. The instrument under testing, inside the CRG, is surrounded by plastic panels on three sides, to limit the air movement inside the enclosure, while one side is maintained open to allow access to it. Measurements were obtained by connecting the instruments to a pc using the serial RS485 communication protocol. For the Thies LPM two of the several outputs, called telegrams, that are available from the instrument were used, meanwhile the Biral VPF-750 provides only one output suitable for calibration purposes.

It was found that both instruments are affected by the flash of the speedlights. The Thies LPM tends to produce false readings when exposed to light flashes, that are roughly proportional to the intensity of light received by the gauge. The receiver sensor of the Biral VPF-750, instead, is quickly saturated by the speedlight flashes and, for a brief period following each flash, cannot sense any incoming hydrometeor. Shielding against light was therefore implemented using blackened material that completely blocks light, yet allows drops to pass through two small holes, one at the top and one at the bottom. An example of the light shielding setup for the Thies LPM is shown in Figure 4.17, a very similar setup was used for the Biral VPF-750. Before starting the calibration procedure, the light shielding of both gauges was thoroughly tested to ensure that no residual interference due to the speedlights was present that could interfere with the results.

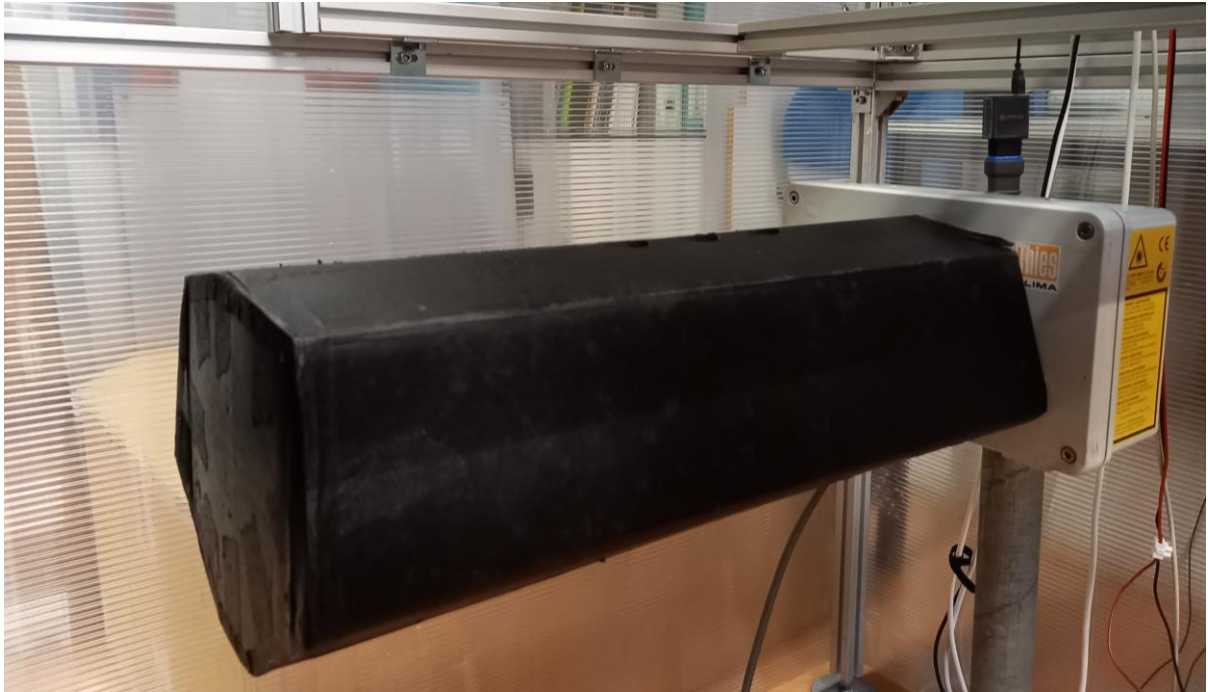


Figure 4.17: Image of the experimental setup used; the instrument, with the shielding, is visible under the PVS and inside the supporting structure. Both at the top and bottom a small hole is present to allow drops reaching the instrument sensing area.

Tests were performed for six different drop sizes, in the case of the Thies LPM being 0.6, 1, 2, 3, 4 and 5 mm in diameter, released singularly or in sequences of five and ten drops, investigating a total of at least 50 drops for each diameter and for each telegram considered. For the Biral VPF-750, a different choice of diameters was made, due to the bin size of the PSVD matrix provided by the instrument being skewed toward the smaller ones. Tests were performed for drops of 0.75, 1, 1.5, 2, 3 and 4 mm in diameter, by releasing at least 50 drops for each size. Smaller drops of 0.6 mm in diameter were also tested, but it was observed that the instrument is not capable of reliably detecting such small drops, reporting only between half and one third of the total released drops, even when the speedlights were turned off.

Each drop was visually checked, making sure that it did in fact cross the instrument sensing area and was correctly photographed by the PVS. Proper alignment, camera timing and focus were also thoroughly checked before each test. All images obtained were then post-processed as explained in section 4.3.2, by extracting both the diameter and fall velocity information.

Of the two telegrams tested for the Thies LPM, the first, called Telegram 3 in the instrument user manual, provides the raw measurement of each drop that crosses the instrument sensing area. Every time a drop crosses the IR beam, its size and fall velocity, as registered by the instrument, are sent to the PC through the serial channel. This telegram is not viable for field installation but is ideal for calibration purposes since direct comparison between PVS and instrumental results are possible. Telegram 3 also provides the values of both diameter and velocity in two different versions: the first is obtained by assuming the drop as spherical, while the second considers the typical “hamburger” shape of the drop. The latter is used in the following chapter since it is used by the instrument to operationally compute rainfall intensity and the PSVD

matrix. The second telegram here considered, is called Telegram 4 in the instrument user manual, and is a viable option for field measurements, providing the PSVD matrix alongside several other parameters like rainfall intensity, METAR and SYNOP codes, temperature, etc.

The Biral VPF-750 instead, does not provide raw data regarding the individual hydrometeors crossing its sensing volume (like the telegram 3 of the Thies LPM), but only provides the PSVD matrix, computed using a moving window of 5 minutes. This output information was therefore the one used for laboratory testing.

The telegrams that provide the PSVD matrix do not allow direct comparison between drops and images since the detection time stamp of individual drops is not provided. This could be overcome by releasing one drop at a time, but at the cost of considerably increasing the time required for calibration. Except for the Thies LPM telegram 3, each drop sensed by the gauge was characterized by considering the average value of the bin in which it was placed, both in term of size and velocity. The average drop diameter from each test was then compared against the average of the corresponding reference values provided by the PVS.

4.4.3.1 Results for telegram 3

Calibration results are presented here following the procedure proposed in section 4.2 above. Table 4.5 contains the summary of the results, in terms of average values and standard deviation of both the instrument measurements and the PVS reference information.

Table 4.5: Results of the calibration for the Thies LPM using data from telegram 3.

N.	Nominal drop diameter (mm)	Drop diameter avg. (mm)	Drop diameter std. dev. (mm)	Fall velocity avg. (m s ⁻¹)	Fall velocity std. dev. (m s ⁻¹)	Meas. diameter avg. (mm)	Meas. diameter std. dev. (mm)	Meas. velocity avg. (m s ⁻¹)	Meas. velocity std. dev. (m s ⁻¹)
1	0.6	0.55	0.06	2.10	0.18	0.64	0.04	2.22	0.33
2	1	0.93	0.08	3.30	0.18	1.06	0.02	3.19	0.06
3	2	2.05	0.11	4.19	0.26	2.10	0.02	4.03	0.07
4	3	2.57	0.08	4.16	0.21	2.76	0.09	4.27	0.11
5	4	3.49	0.30	4.12	0.38	3.80	0.11	4.24	0.07
6	5	4.44	0.19	4.50	0.29	4.70	0.13	4.56	0.06

Table 4.5 shows that the CRG produced drops that are slightly larger than nominal for diameters up to 2 mm but become smaller for the larger diameters. The standard deviation for the CRG is low, both for the drop diameter and the fall velocity, meaning that drops were released with good repeatability.

The instrument under test shows a tendency to underestimate both the drop size and the fall velocity, presenting also standard deviation values that are, in general, higher than the reference. Computing the error

according to Equation 4.6, for both the drop diameter and the fall velocity, the boxplots presented in Figures 4.18 and 4.19 are obtained.

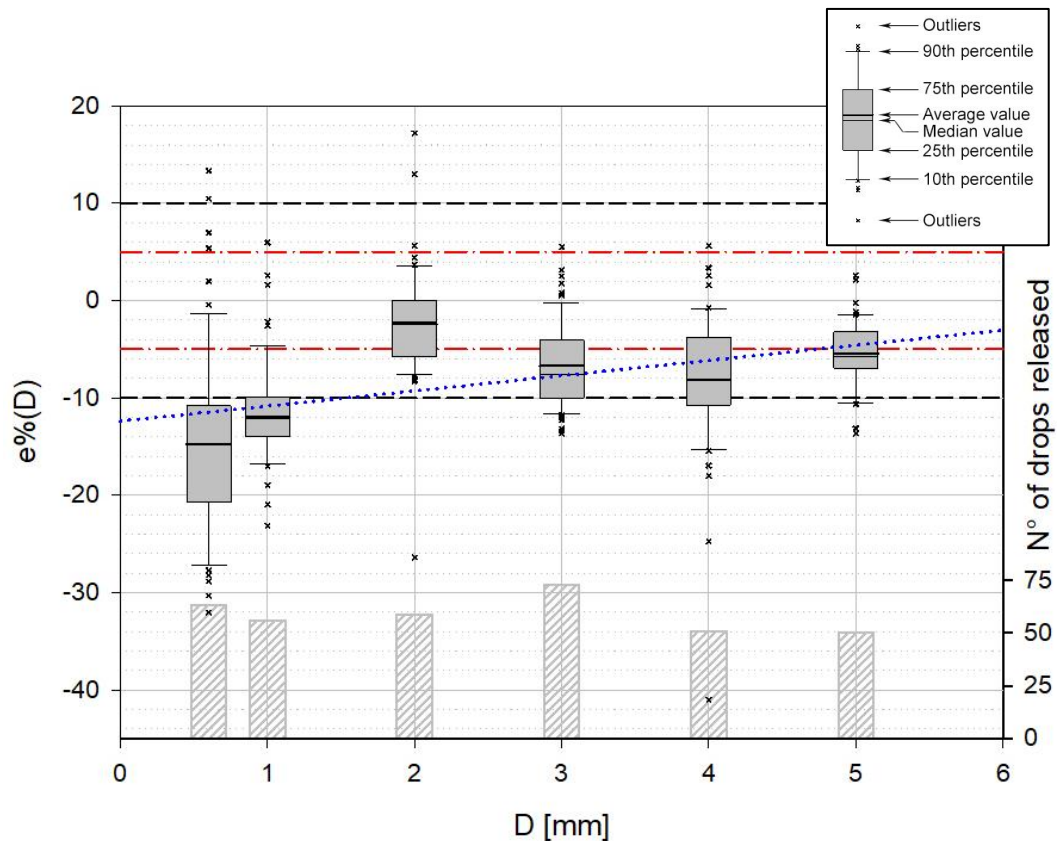


Figure 4.18: Non-parametric distribution of the drop diameter error for the Thies LPM telegram 3: the central line indicates the median, the bottom and top edges are the 25th and 75th percentiles, respectively, while the whiskers are the 10th and 90th percentiles. Each outlier is plotted individually and denoted by the 'x' symbol. The blue dotted line is the best-fit linear trend of the average values. Bars at the bottom indicates the number of drops released for each test.

Figure 4.18 shows the instrumental error on drop size. A general underestimation of the drop size emerges, with the smallest drops being, on average, underestimated by about 15%, while drops with diameters between 2 and 5 mm show errors between 5 and 10 %. The error tends to decrease with increasing the drop size, with the test performed at 2 mm showing the best results. The dispersion of the results is similar for all diameters, except for the smallest one showing a higher value. A linear trend can be fitted to the data, whose parameters are shown in Table 4.6.

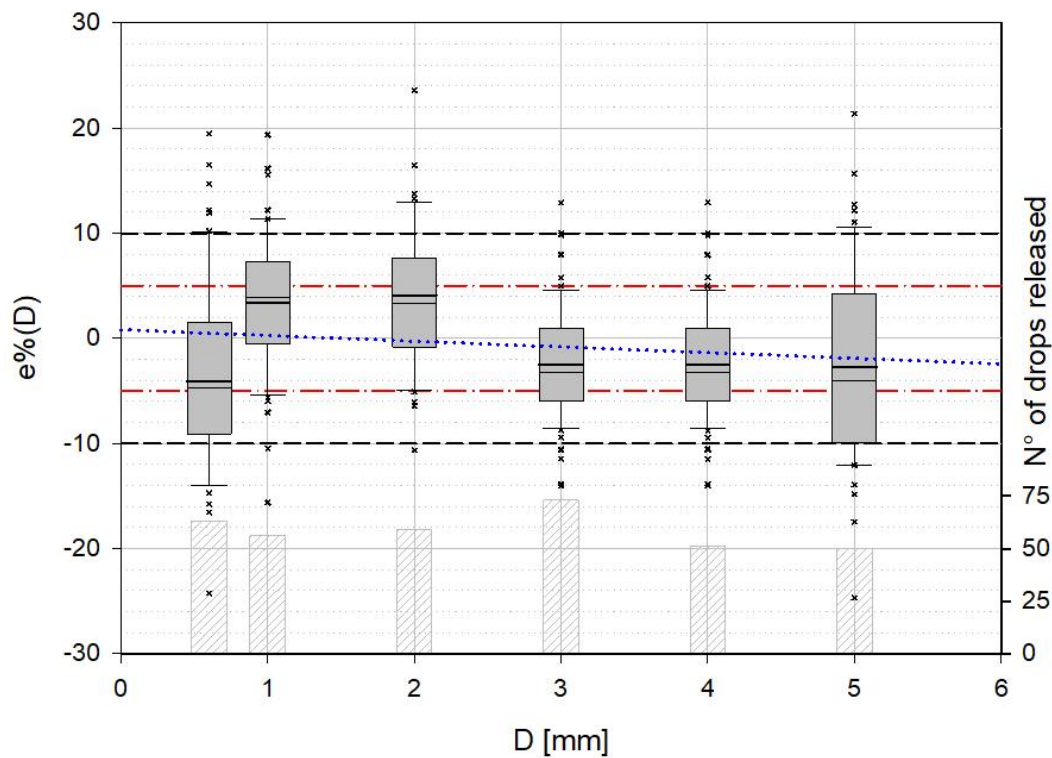


Figure 4.19: Non-parametric distribution of the fall velocity error for the Thies LPM telegram 3: the central line indicates the median, the bottom and top edges are the 25th and 75th percentiles, respectively, while the whiskers are the 10th and 90th percentiles. Each outlier is plotted individually and denoted by the 'x' symbol. The blue dotted line is the best-fit linear trend of the average values. Bars at the bottom indicates the number of drops released for each test.

Note in Figure 4.19, where the instrumental error on the fall velocity is shown, that the average error is between +5% and -5%, meaning that the instrument provides, on average, more accurate measurements of the fall velocity than of the drop size. A strong variability in the results is however evident, with extremes that range between -25% and +20%, both for small and large diameters. Data dispersion is about constant throughout diameters, with only a limited increase for the smallest and largest ones. Again, a linear trend can be fitted to the data, whose parameters are also presented in Table 4.6.

Table 4.6: Parameters of the linear fit for the average error of both the drop size and fall velocity.

$e\%(D) = a \cdot D + c$		a	c
	Drop size	1.56	-12.40
	Fall velocity	-0.54	0.79

Using Equations 4.4 and 4.5, the error on the rainfall intensity can be estimated, considering e.g., six events of increasing intensity (from 1 mm h⁻¹ to 500 mm h⁻¹). From the measured and the target results, the

percentage relative deviation is computed as shown in Equation 4.6 and results are graphically presented in Figure 4.20.

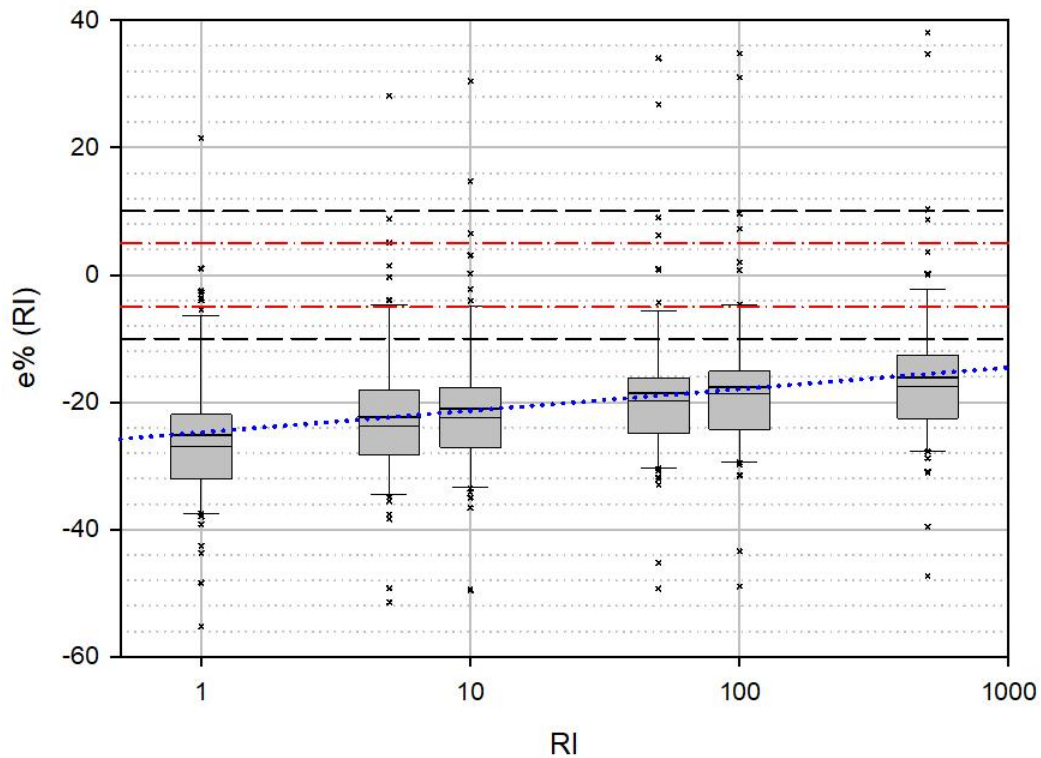


Figure 4.20: Non-parametric distribution of the rainfall intensity retrieval error computed from the calibration results for the Thies LPM telegram 3: the central line indicates the median, the bottom and top edges are the 25th and 75th percentiles, respectively, while the whiskers are the 10th and 90th percentiles. Each outlier is plotted individually and denoted by the 'x' symbol. The blue dotted line is the best-fit linear trend of the average values. Red and black dashed lines show the 5% and 10% limits respectively.

The instrument shows a considerable underestimation of precipitation intensity that, for light events, can reach almost 30% and decreases to 15% for higher intensity events. Various outliers are also evident. Results can be fitted using a logarithmic curve as shown in Equation 4.19.

$$e\% = 1.4775 \ln(RI) - 24.746$$

4.19

Following the limits proposed in chapter 4.2 for the percentage relative deviation defined in the existing EN17277:2019, already available for catching type gauges, it is concluded that since the Thies LPM under test has a percentage relative deviation greater than $\pm 10\%$ in measuring the reference rainfall intensity, it cannot be classified according to that standard.

In Table 4.7, the average error and the 10^o and 90^o percentiles (i.e., the values encompassing 80 % of all recorded values) for both drop size and fall velocity are presented. As shown in Figure 4.21 (a) for the drop

size, only the average error for the 2 mm test falls inside the 5% limit, while larger diameters remain inside the 10% limit and smaller diameters fall outside the 10% mark. In Figure 4.21 (b), the average error for the fall velocities is inside the 5% limit for all diameters, but the same is not true for both the 10° and 90° percentiles, which in some cases fall even outside of the 10% mark. Since values are outside the maximum percentage relative deviation of 5%, the instrument cannot be classified according to the proposed standard even if used only as a disdrometer.

Table 4.7: Average value, 10° and 90° percentiles for the measurement error on the drop size and fall velocity for the Thies LPM.

D_{nom}	Q10 (D)	Avg. e% (D)	Q90 (D)	Q10 (W)	Avg. e% (W)	Q90 (W)
0.6	-0.45	-14.80	-29.15	9.97	-4.10	-18.18
1	-2.04	-12.10	-22.16	11.43	3.37	-4.68
2	4.93	-2.42	-9.77	13.74	4.09	-5.57
3	-2.01	-7.16	-12.31	3.80	-2.91	-9.61
4	1.24	-8.14	-17.53	9.28	-2.74	-14.76
5	-0.95	-5.44	-9.93	6.01	-1.40	-8.82

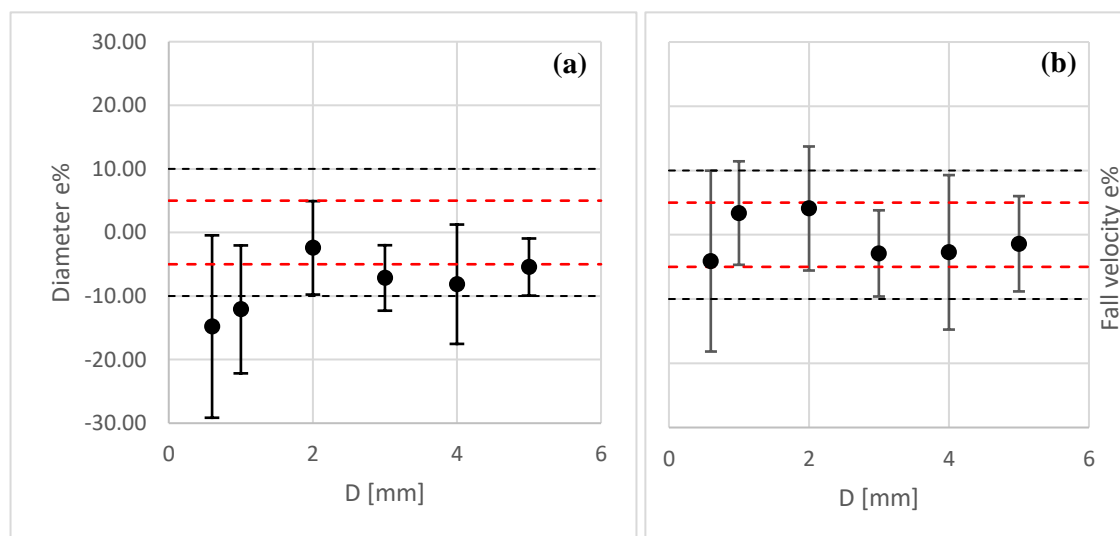


Figure 4.21: Average error (black dots), 10° (upper dash) and 90° (lower dash) percentiles for the drop size (a) and fall velocity (b); red and black dashed lines represent the 5% and 10% limits, respectively.

4.4.3.2 Results for telegram 4

Table 4.8 shows the results obtained from telegram 4, where the instrument is configured as it would be in the field, under typical measurement conditions. This setting introduces a quantization error in the instrumental results, since the gauge categorises drops in predetermined bins, but also provides a better insight on the performance that could be expected in operational conditions.

Table 4.8: Results of the calibration for the Thies LPM using the output telegram 4.

N.	Nominal drop diameter (mm)	Drop diameter avg. (mm)	Drop diameter std. dev. (mm)	Fall velocity avg. (m s ⁻¹)	Fall velocity std. dev. (m s ⁻¹)	Meas. diameter avg. (mm)	Meas. diameter std. dev. (mm)	Meas. velocity avg. (m s ⁻¹)	Meas. velocity std. dev. (m s ⁻¹)
1	0.6	0.44	0.00	2.12	0.14	0.68	0.03	2.28	0.08
2	1	0.69	0.09	3.47	0.26	1.14	0.03	3.30	0.10
3	2	1.84	0.03	3.80	0.00	2.15	0.04	4.13	0.09
4	3	2.25	0.00	3.91	0.21	2.71	0.07	4.21	0.08
5	4	3.24	0.26	4.16	0.34	3.87	0.18	4.30	0.09
6	5	4.18	0.32	4.45	0.54	4.63	0.24	4.45	0.09

Table 4.8 shows similar performance of the CRG than in the previous test in producing drops close to the intended nominal diameter. For the telegram 4, the tendency to underestimate both the drop size and fall velocity observed in the previous test increases considerably for the drop size. The standard deviation of instrumental results is affected by the quantization operated by the gauge, with values that are equal to zero if all drops fall into the same bin. PVS results, unaffected by quantization, remain similar to the ones obtained for telegram 3 both for the drop size and fall velocity. After computing the error, the non-parametric distribution presented in Figures 4.22 and 4.23 is obtained.

Figure 4.22 shows the instrumental error on the drop size. Even in this case a general underestimation of the drop size is evident, with the smaller drops presenting a larger underestimation than before. Errors spans between -25% and -45% for the smaller drops, while diameters between 2 and 5 mm present errors between -10% and -20%, which is close to the results obtained for telegram 3. A general decreasing trend of the error with increasing the drop size emerges, with the 5 mm test showing the best results in this case. A linear fit can be used to represent the trend, whose parameters are presented in Table 4.9.

Considering Figure 4.23, where the instrumental error on the fall velocity is shown, an underestimation between -5% and -10% is observed, except for the 1 mm test where a relevant overestimation is present. Still, the instrument provides more accurate measurements of the fall velocity than of the drop size, although with strong variability in the results, with extremes ranging between -15% and +25%, both for small and large diameters. Again, a linear fit is shown, whose parameters are presented in Table 4.9.

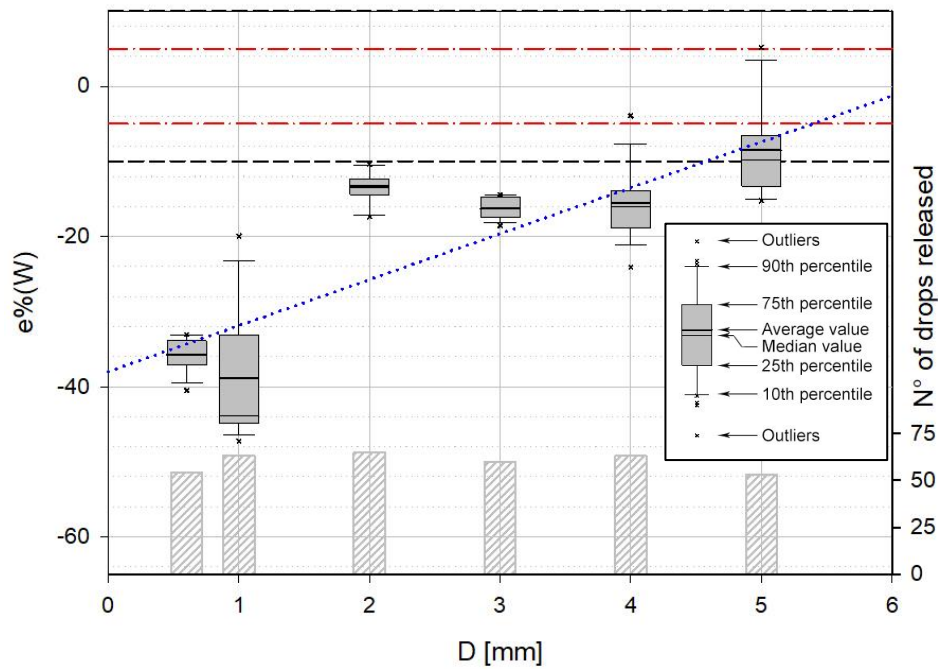


Figure 4.22: Non-parametric distribution of the drop diameter error for the Thies LPM telegram 4: the central line indicates the median, the bottom and top edges are the 25th and 75th percentiles, respectively, while the whiskers are the 10th and 90th percentiles. Each outlier is plotted individually and denoted by the 'x' symbol. The blue dotted line is the best-fit linear trend of the average values. Bars at the bottom indicates the number of drops released for each test.

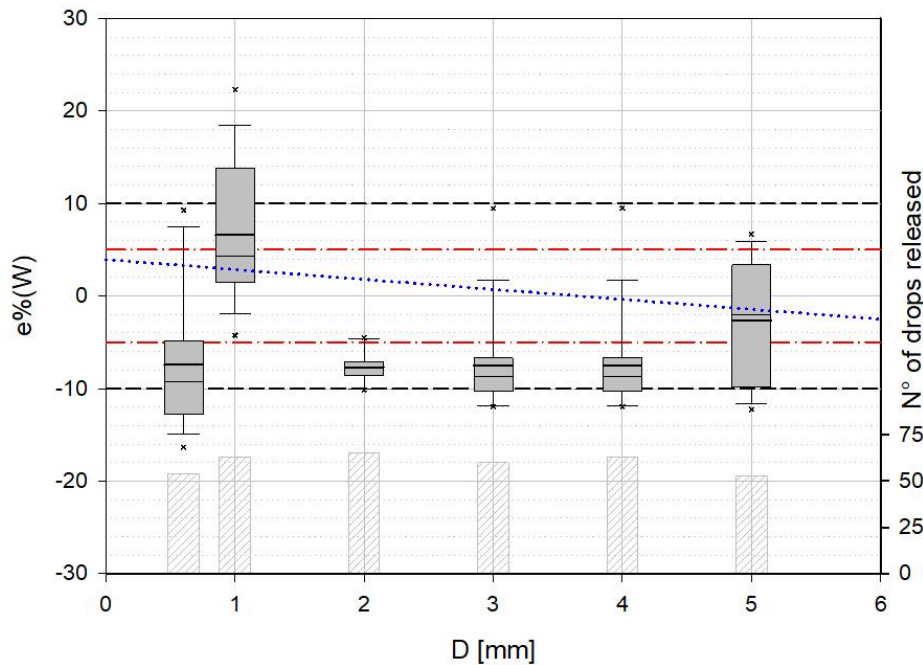


Figure 4.23: Non-parametric distribution of the fall velocity error for the Thies LPM telegram 4: the central line indicates the median, the bottom and top edges are the 25th and 75th percentiles, respectively, while the whiskers are the 10th and 90th percentiles. Each outlier is plotted individually and denoted by the 'x' symbol. The blue dotted line is the best-fit linear trend of the average values. Bars at the bottom indicates the number of drops released for each test.

line is the best-fit linear trend of the average values. Bars at the bottom indicates the number of drops released for each test.

Both diameter and fall velocity results show some dispersion, which is lower for mid-range diameters while it is considerably higher for both the smaller (0.6 and 1 mm) and larger (5 mm) diameters. Since the PVS results show a limited variance for those tests and these results cannot entirely be attributed to quantization error, this phenomenon may be ascribable to some environmental effect, possibly temperature and humidity, on the instrument performance.

Table 4.9: Parameter of the linear fit for the average error of both the drop size and fall velocity.

$e\%(D) = a \cdot D + c$		a	c
	Drop size	6.120	-38.006
	Fall velocity	0.235	3.929

Using Equations 4.4 and 4.5, the error is once again expressed in terms of rainfall intensity, considering six events of increasing intensity. From the measured and target rain data, the percentage relative deviation is computed, and the results are presented in Figure 4.24.

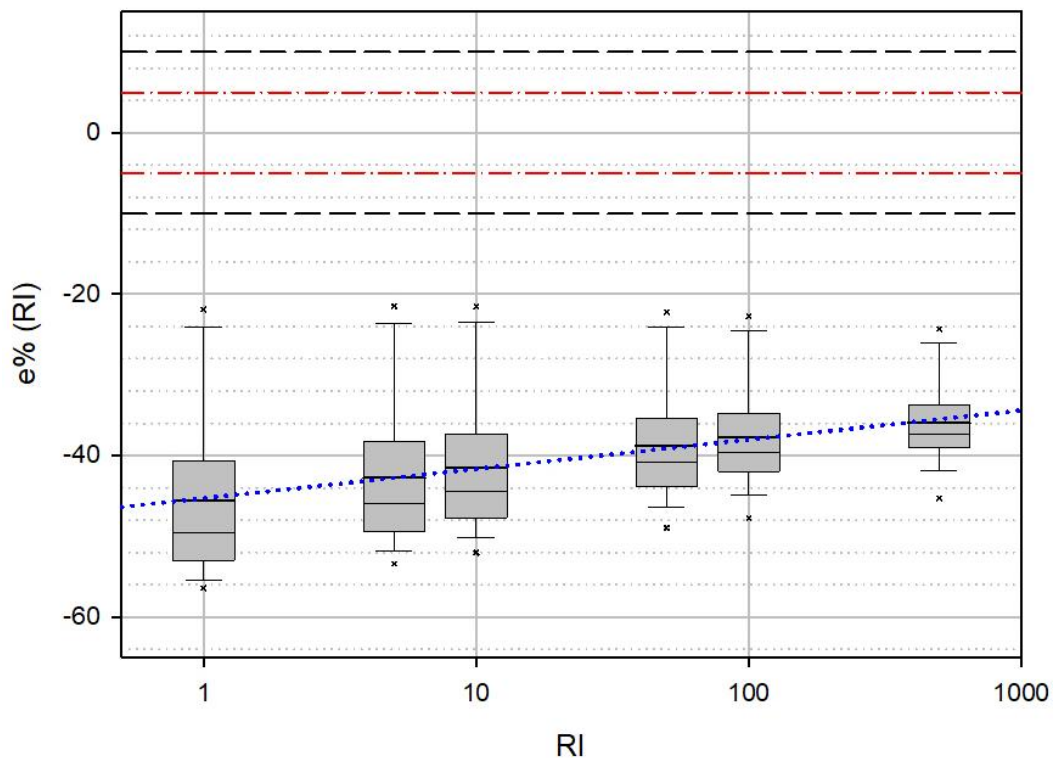


Figure 4.24: Non-parametric distribution of the rainfall intensity retrieval error computed from the calibration results for the Thies LPM telegram 4: the central line indicates the median, the bottom and top edges are the 25th

and 75th percentiles, respectively, while the whiskers are the 10th and 90th percentiles. Each outlier is plotted individually and denoted by the 'x' symbol. The blue dotted line is the best-fit linear trend of the average values. Red and black dashed lines show the 5% and 10% limits respectively.

The instrument behaviour is consistent with the previous case, but the underestimation of precipitation intensity further increases and, reaches about 50% for light rain events, while it decreases to 35% for the high intensity events. Results can be fitted using a logarithmic function as shown in Equation 4.20.

$$e\% = 1.5768 \ln(RI) - 45.298$$

4.20

As observed in the case of telegram 3, for telegram 4 the instrument performance exceeds the limits proposed in section 4.3. Therefore it can be concluded that the Thies LPM under test cannot be classified according to the proposed standard also when using telegram 4.

Likewise, in Table 4.10, the mean error and the 10° and 90° percentiles for both the drop size and fall velocity are presented. As shown in Figure 4.25 (a) for the drop size, the mean errors far exceed the 5% limit and only for the largest diameters remains within 10%. In Figure 4.25 (b), the mean error for the fall velocity is shown to be within the 5% limit for the two largest diameters, while it remains within 10% for the other diameters. Since the observed deviations, like in the previous case, are significantly above the maximum percentage relative deviation of 5%, the instrument cannot be classified according to the proposed standard, even if used only as a disdrometer.

Table 4.10: Average, 10° and 90° percentiles of the relative percentage error on the drop size and fall velocity for the Thies LPM.

D _{nom}	Q10 (D)	Avg. e% (D)	Q90 (D)	Q10 (W)	Avg. e% (W)	Q90 (W)
0.6	-32.97	-35.71	-38.46	9.97	2.35	-16.52
1	-28.47	-39.59	-50.70	11.43	14.92	-4.31
2	-11.60	-14.36	-17.12	13.74	-5.91	-10.23
3	-15.08	-16.86	-18.65	3.80	-0.31	-13.55
4	-10.45	-16.44	-22.43	9.28	5.36	-11.84
5	-2.13	-9.60	-17.08	6.01	14.79	-14.57

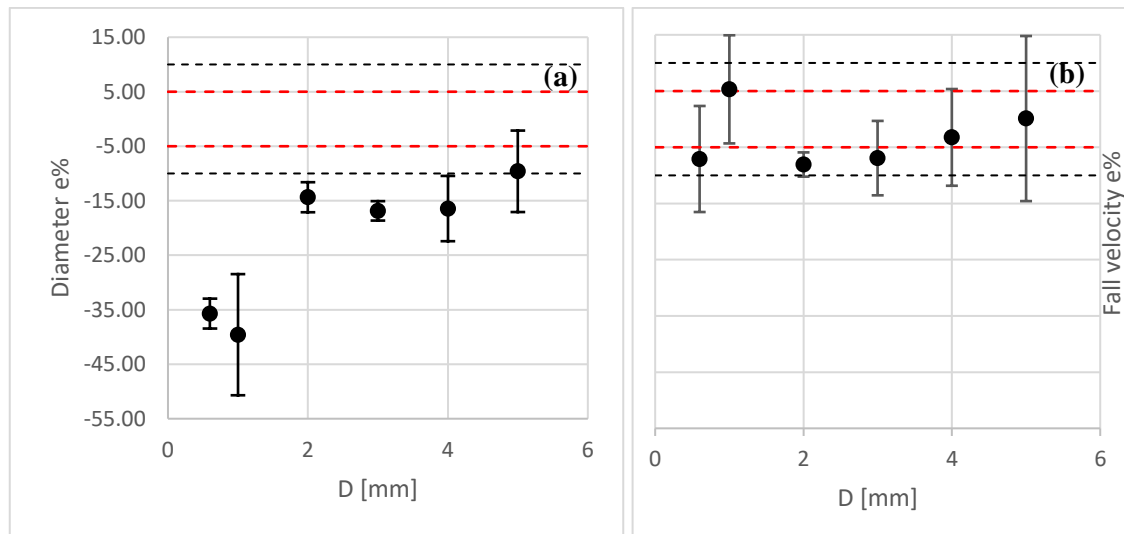


Figure 4.25: Mean percentage relative error (black dots), and 10° (upper dashed line) and 90° (lower dashed line) percentiles for the drop size (a) and fall velocity (b); red dashed lines represent the $\pm 5\%$ limits, while the black ones represent the $\pm 10\%$ limits.

4.4.3.3 Biral VPF-750 results

The Biral VPF-750 provides only the PVSD matrix as a viable output for calibration and is therefore treated similarly to the Thies LPM for telegram 4. A summary of the results is presented in terms of average values and standard deviations in table 4.11.

Table 4.11: Results of the calibration for the Biral VPF-750.

N.	Nominal drop diameter (mm)	Drop diameter avg. (mm)	Drop diameter std. dev. (mm)	Fall velocity avg. (m s^{-1})	Fall velocity std. dev. (m s^{-1})	Meas. diameter avg. (mm)	Meas. diameter std. dev. (mm)	Meas. velocity avg. (m s^{-1})	Meas. velocity std. dev. (m s^{-1})
1	0.75	0.64	0.06	2.23	0.66	0.77	0.03	2.54	0.10
2	1	0.97	0.04	2.70	0.40	1.10	0.03	3.29	0.04
3	1.5	1.53	0.10	3.23	0.38	1.67	0.03	3.77	0.08
4	2	1.78	0.12	3.06	0.38	2.14	0.03	4.11	0.05
5	3	2.50	0.13	3.30	0.41	2.71	0.03	4.19	0.04
6	4	3.41	0.31	3.14	0.49	3.86	0.04	4.33	0.07

Table 4.11 confirms, for diameters equal to 0.75 mm and 1.5 mm that were not released in the previous tests, the behaviour of the CRG in producing slightly larger drops for a nominal diameter less than 2 mm. Larger drops are instead slightly smaller than their nominal diameter.

The Biral VPF-750 shows values of both the average drop diameter and fall velocity that are lower than the reference ones, obtained from the PVS. In terms of standard deviation, the instrument shows much higher values, especially for the fall velocity. This can be, at least partially, attributed to the binning operated by the instrument when building the PSVD matrix, that for some combination of drop size and fall velocity is quite coarse. The percentage error between the instrument measurement and the reference is computed for both the drop diameter and the fall velocity, and results are presented in terms of the non-parametric distribution shown in Figures 4.26 and 4.27.

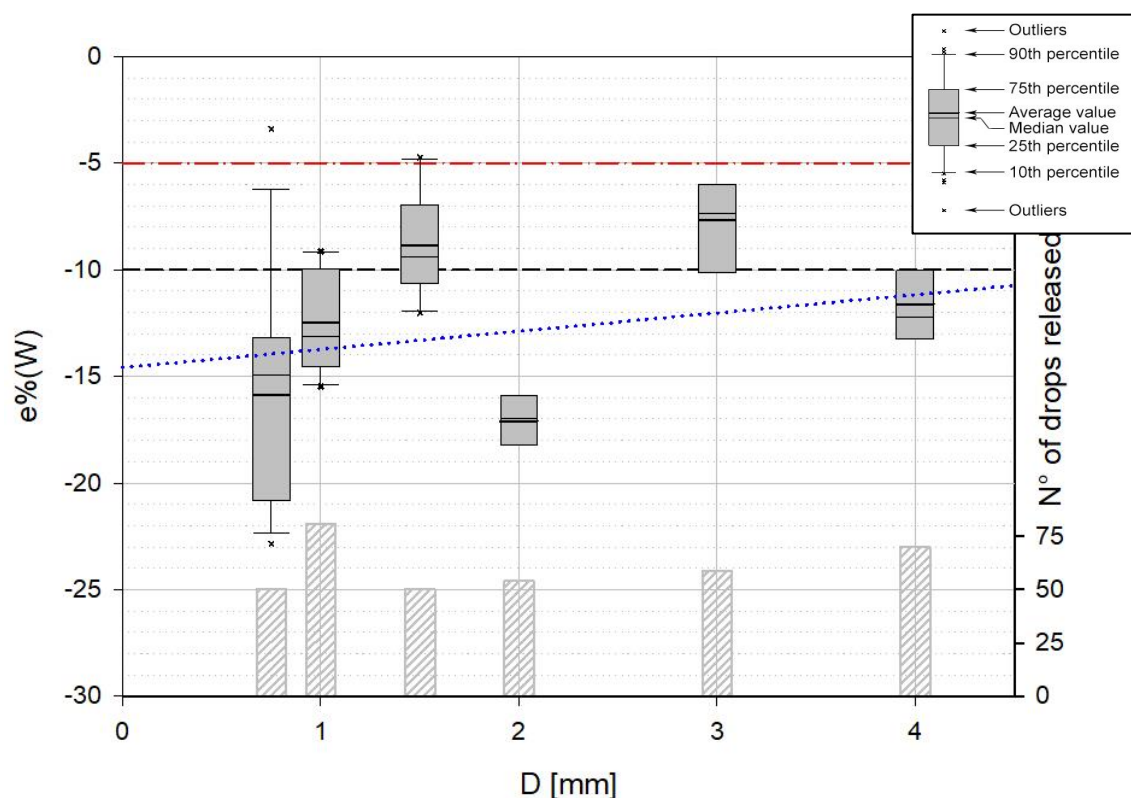


Figure 4.26: Non-parametric distribution of the drop diameter error for the Biral VPF-750. The central line of each box indicates the median, while the bottom and top edges indicate the 25th and 75th percentiles, respectively. The whiskers indicate the 10th and 90th percentiles, while outliers are plotted individually using the small crosses. The black dashed line indicates the linear best-fit of the average values.

Image 4.27 shows the instrumental error on the drop size. A general underestimation is evident, with maximum values of up to -25%, while the error is generally between -5% and -15%. The linear fit of the results, the parameters of which are shown in Table 4.12, shows a trend of decreasing error with increasing the drop size, although a larger error is observed for drops with a nominal diameter of 2 mm. Since detailed checking of both the PVS results and instrumental measurements did not show any inconsistency, this error may be attributable to environmental factors that were not considered in this work like e.g., the air temperature and humidity.

Considering Figure 4.27, where the instrumental error on the drop velocity is shown, an opposite trend is observed, whose parameters are also shown in Table 4.12. In fact, the calculated error tends to increase with increasing the drop size and the drop velocity is underestimated to as much as -25% for any drop size equal or larger than 2 mm. Instead, small drops present lower errors but a much higher dispersion, that for the smallest drop may even result in some overestimation. The average error is however between -10% and -20%.

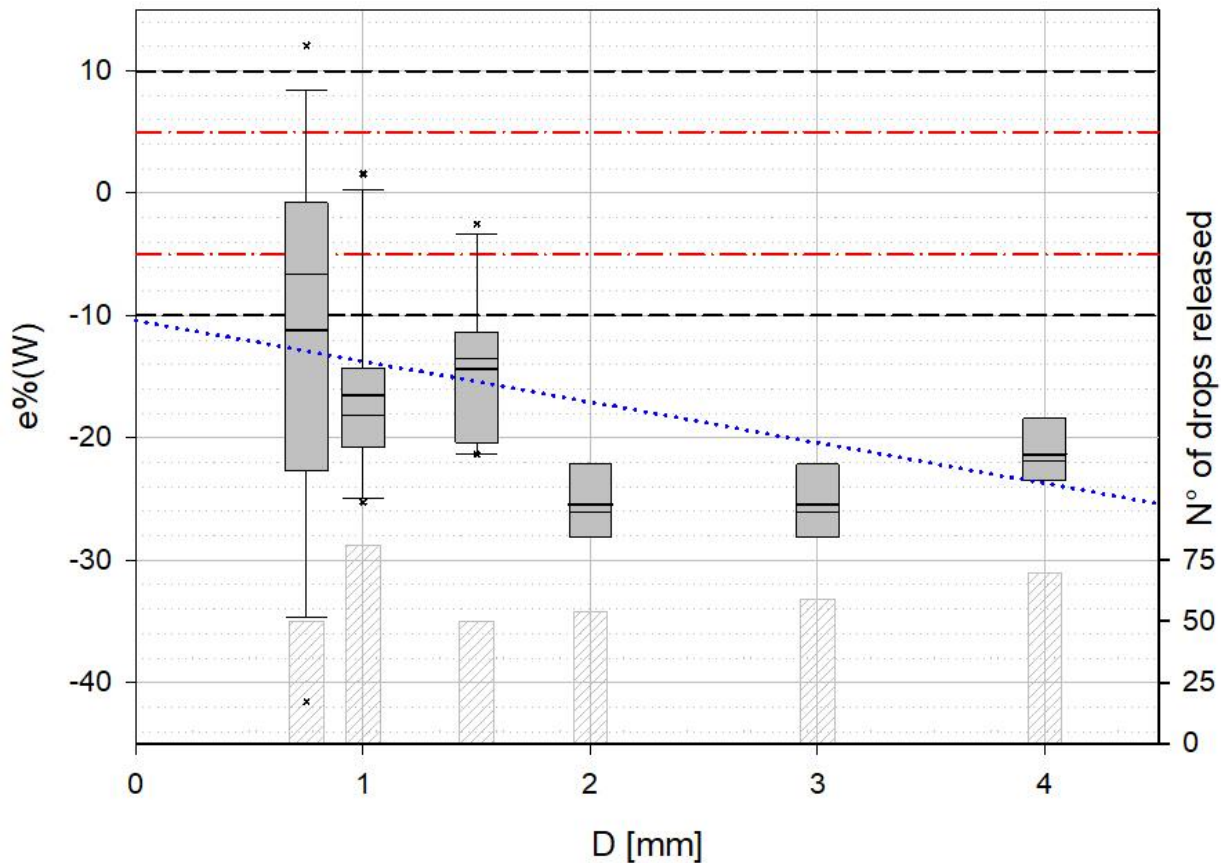


Figure 4.27: Non-parametric distribution of the error on the fall velocity for the Biral VPF-750. The central line within each box indicates the median, while the bottom and top edges indicate the 25th and 75th percentiles, respectively. The whiskers indicate the 10th and 90th percentiles, while outliers are plotted individually using the small crosses. The black dashed line indicates the linear best-fit of the average values.

The average errors for both the drop size and fall velocity are similar and, even if with opposite trends, it is concluded that the instrument provides about the same performance in measuring both precipitation microphysical characteristics. A large dispersion is evident in both cases for any drop size below 2 mm, meaning that the instrument receiving sensors may not be sensitive enough for such small hydrometeors when only one drop is present in the sensing volume. This fact is corroborated by the lack of detection for drops having a diameter equal to 0.6 mm.

Table 4.12: Parameter of the linear best-fit for the average error of both the drop size and fall velocity

$e\%(D) = a \cdot D + c$		a	c
	Drop size	1.141	-14.60
	Fall velocity	-4.437	-10.42

Using Equations 4.4 and 4.5 the error can be expressed as a function of the rainfall intensity, considering six events of increasing RI. From the measured and the target rain results the percentage relative deviation is computed, and results are presented in Figure 4.28.

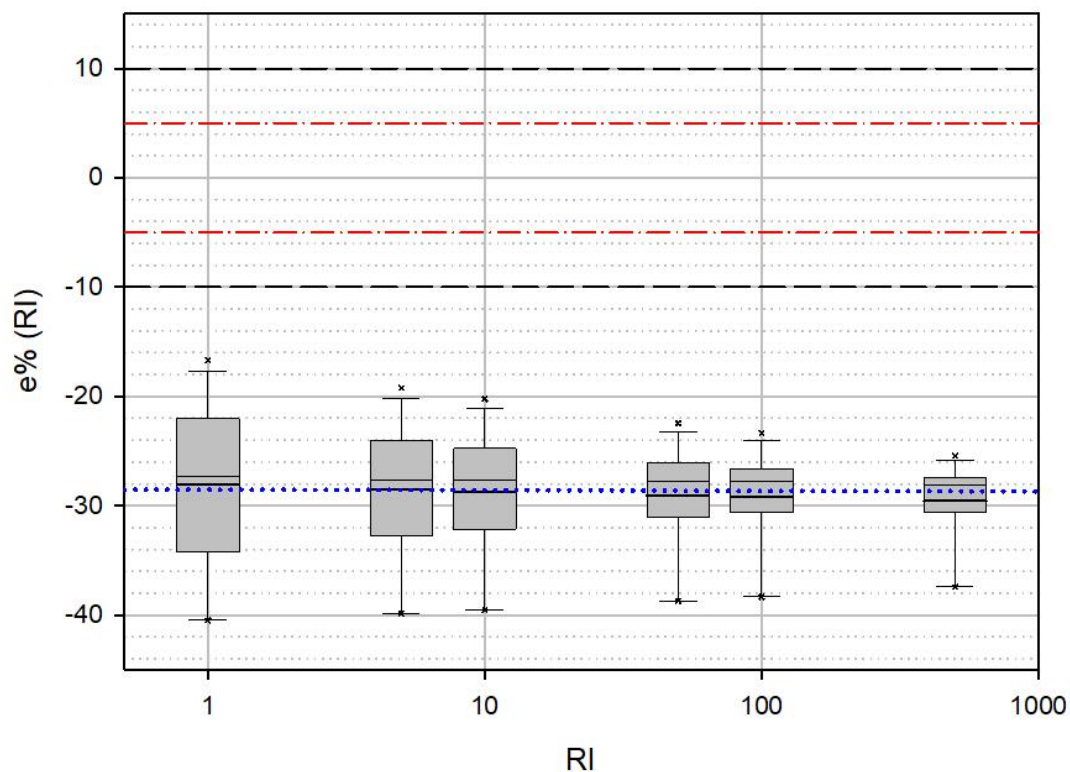


Figure 4.28: Non-parametric distribution of the rainfall intensity retrieval error computed from the calibration results for the Biral VPF-750: the central line indicates the median, the bottom and top edges are the 25th and 75th percentiles, respectively, while the whiskers are the 10th and 90th percentiles. Each outlier is plotted individually and denoted by the 'x' symbol. The blue dotted line is the best-fit linear trend of the average values. Red and black dashed lines show the 5% and 10% limits respectively.

The two opposite trends noted above on the individual drop size and fall velocity measurement errors make the instrument performance almost independent on RI. The Biral VPF-750 underestimate precipitation intensity by as much as about -30%, on average, with the error that remains almost constant over the whole RI range considered. The dispersion decreases with increasing RI, since the contribution of larger hydrometeors becomes more and more substantial. Results can be fitted using a logarithmic function as shown in Equation 4.21.

$$e\% = -0.026 \ln(RI) - 28.525$$

4.21

The performance of the Biral VPF-750 are largely outside of the limits proposed in section 4.3 and, even applying a correction to the results, both the 10th and 90th percentiles would remain outside of those limits. It is concluded that the Biral VPF-750 under test cannot be classified according to this proposed standard.

In Table 4.13, the average value and the 10° and 90° percentiles (i.e., 80 % of all recorded values) of the error for both the drop size and fall velocity are presented. As also shown in Figure 4.29 (a), for the drop size the average error always falls outside the -5% limit and only two diameters barely remain inside the -10% limit. In Figure 4.29 (b), the average error for the fall velocity is always below the -10% mark. Since values are outside the maximum percentage relative deviation of 5%, the instrument cannot be classified according to the proposed standard, even if used only as a disdrometer.

Table 4.13: Results in terms of average value, 10° and 90° percentiles of the measurement error for the Biral VPF-750.

D _{nom}	Q10 (D)	Avg. e% (D)	Q90 (D)	Q10 (W)	Avg. e% (W)	Q90 (W)
0.6	-8.97	-15.89	-22.80	7.07	-11.23	-29.52
1	-9.50	-12.47	-15.43	-7.04	-16.54	-26.04
2	-5.88	-8.85	-11.83	-7.06	-14.35	-21.64
3	-14.40	-17.09	-19.78	-21.49	-25.47	-29.45
4	-4.70	-7.70	-10.70	-17.82	-21.35	-24.88
5	-8.08	-11.61	-15.14	-23.80	-27.95	-32.09

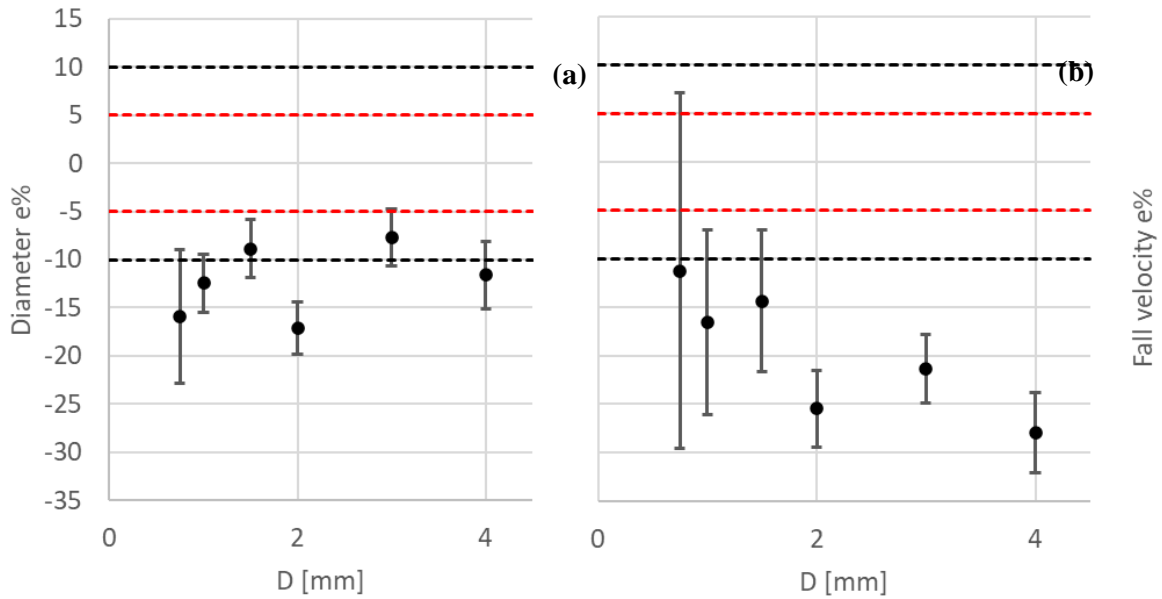


Figure 4.29: Average error (black dot) and the 10th (upper dash) and 90th (lower dash) percentiles on the measurement error for the drop size (a) and fall velocity (b). Red dashed lines represent the $\pm 5\%$ limits while black lines represent the $\pm 10\%$ limits.

4.5 DISCUSSION

The CRG showed good performances and was capable to release a wide range of drop diameters maintaining good repeatability both in terms of the generated drop size and fall velocity. It can be concluded that the CRG developed in this work is suitable for the laboratory calibration of NCGs.

Regarding the gauge performance, the fact that both instruments were affected by light flashes may arise the question of the influence that fulminations or in general light pollution has on the measurement in the field. Further experiments, to be conducted in operating conditions, are necessary before quantitative information can be provided about this potential source of bias.

Variability in the instrumental results is quite large, with standard deviations that in some cases are one order of magnitude higher than the standard deviation showed by the CRG. This suggests that the NCGs tested in this work provide low accuracy in evaluating the microphysical properties of single hydrometeors.

The difference between results obtained for the two output telegrams of the Thies LPM is quite large in terms of drop diameters, while it is more limited for the fall velocity. This suggests that the instrument applies some form of correction on the drop size, that is handled differently depending on its operational settings. On the other hand, differences in the drop velocity are compatible with the error introduced by the binning operation. No similar comparison was possible for the Biral VPF-750 because only one of the available telegrams contains data about the microphysical properties of precipitation. This fact, nevertheless, implies that calibration of NCGs should be conducted using the same software configuration that will be used in the field, especially since correction algorithms inside the gauge firmware are usually undisclosed by the manufacturers.

Results obtained in terms of the drop size from the two telegrams of the Thies LPM are here compared against results from the work of de Moraes Frasson et al. (2011). Figure 4.30 shows the comparison in terms of the average percentage error.

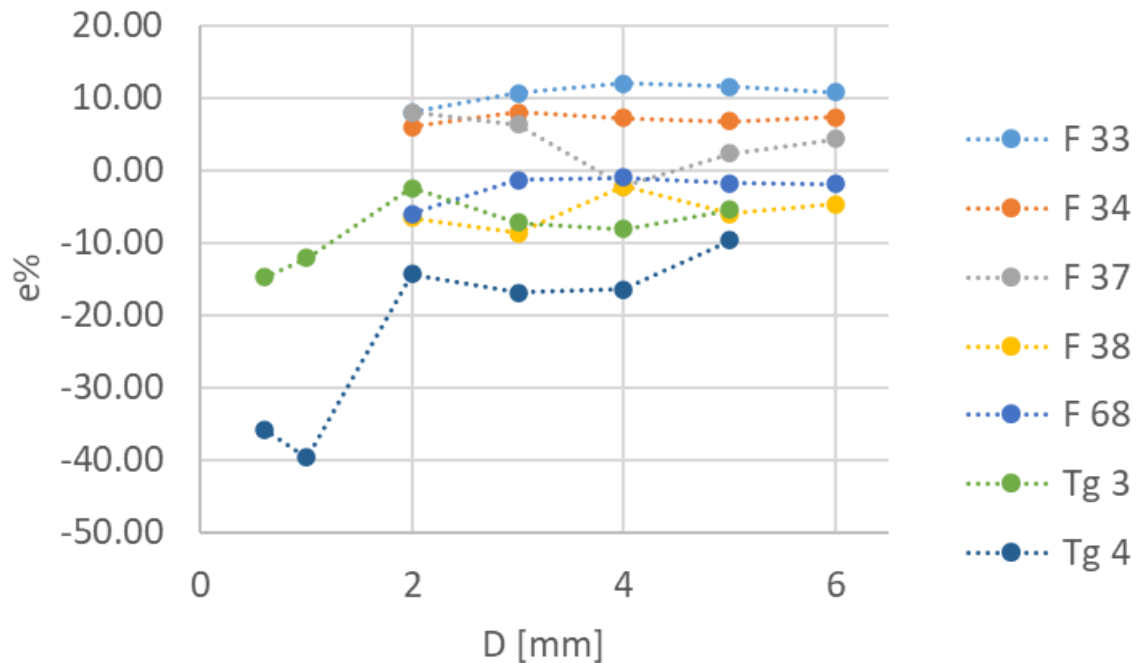


Figure 4.30: Comparison of the mean relative percentage error on the drop diameter between literature results (F 33, F 34, F 37, F 38 and F 68 as per the authors' notation) and the results obtained from the CRG test (Tg 3 and Tg 4) on the Thies LPM.

The instruments used in the work of de Moraes Frasson et al. (2011) present large instrument to instrument variability, with some reporting an overestimation up to 10% for all drop sizes, while others presenting an underestimation between -5% and -10%. Results from the output telegram 3 are in reasonable agreement with results from F 38 and F 68 (as per the authors' notation) while they are far from the other results. On the other hand, the output telegram 4 is always far from literature results. These differences may be due to the use of metal spheres instead of water drops as the reference target in the work of de Moraes Frasson et al. (2011).

In the case of the Biral VPF-750, the behaviour highlighted by laboratory testing was also observed in the field in the work of Wauben et al. (2016), where several optical disdrometer and present weather sensors were compared by the Royal Netherlands Meteorological Institute (KNMI). In that work, during six months of field testing, the Biral VPF-750 reported 331.93 mm of cumulated precipitation (both liquid and solid) while the KNMI reference gauge reported 443.54 mm. This results in an underestimation of about 25%, that is in very good agreement with the findings of the laboratory tests.

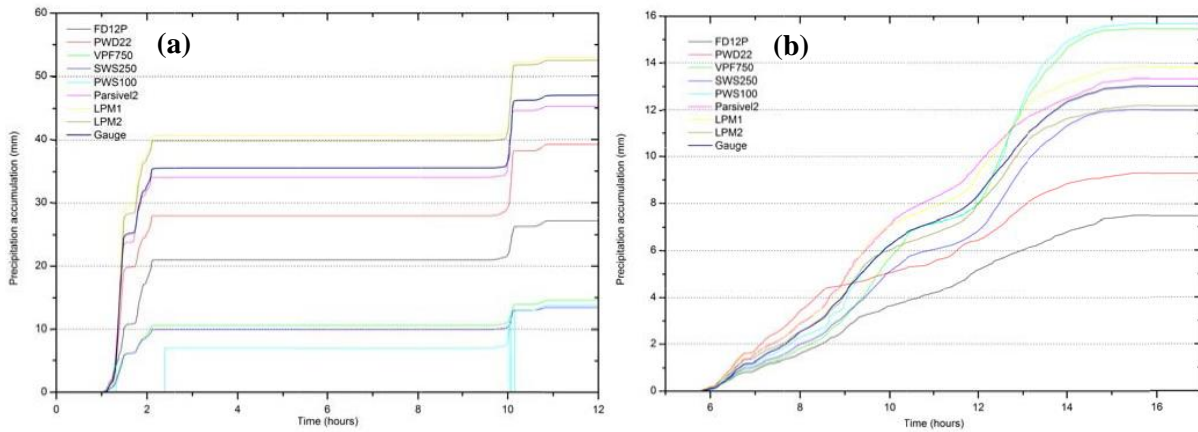


Figure 4.31: Cumulated precipitation for two real-world events from the work of Wauben *et al.* (2016). Panel (a) is from June 23rd, 2016, between 00:00 and 12:00 UT while panel (b) is from March 4th, 2016, between 00:00 and 16:00 UT. The reference gauge is plotted with a blue line while VPF-750 measurements are shown with a green line.

Figure 4.31 (a) shows a typical event presented in the work of Wauben *et al.* (2016), where the Biral VPF-750 reports significant lower precipitation than both the reference and most of the other instruments tested. However, the event presented in Figure 4.31 (b) (March 4th, 2016, between 00:00 and 16:00 UT) shows that the VPF-750 reports considerably higher RI and cumulated precipitation than the reference and all other gauges (except the Campbell Scientific PWS-100). This may suggest that some other external factors, not reported in that work, may strongly influence the instrument performance in the field.

The results showed here for both the Thies LPM and the Biral VPF-750 prove that instrumental errors for the tested NCGs are significant and strongly affect the measurement accuracy. The need for calibrating such instruments using a traceable method before installation in the field is therefore demonstrated.

5 BLUFF-BODY AERODYNAMICS AND TRANSFER FUNCTIONS FOR NCGs

Further to instrumental errors, several other factors may affect precipitation measurements. For traditional CGs for example, errors can be due to splashing at the collector, meaning hydrometeors that due to the impact break in smaller droplets that could fall outside or inside the collector, producing under- or over-catch, respectively. Wetting is also often considered, producing a net volume loss due to a certain amount of water that remain attached to the funnel surface. Evaporation could also have a role, in hot climates, reducing the amount of water collected, especially for weighing type gauges (WMO, 2021). While NCGs may not be subject to some or all the previously mentioned errors, due to their different design and measurement principles, they may be affected by different sources of bias. As an example, it was shown for the 2DVD, used as ground reference in several works, that an anomaly due to static drops partially obstructing the optical path is always present during all precipitation events investigated, see Larsen & Schönhuber (2018) and Larsen & Blouin (2020). However, an environmental factor that is universally recognized as responsible of considerable measurement biases for both CGs and NCGs is wind.

5.1 THE EXPOSURE PROBLEM

First documented by Jevons (1861), the exposure problem indicates a wind-induced bias, that is a form of environmental bias, common to all precipitation gauges installed in the field and exposed to the wind. The exposure effect is due to the complex interaction that arises between the wind itself, the instrument body, and the incoming hydrometeors. The gauge, immersed in a wind field behaves like a bluff body obstacle, that produces strong velocity gradients and turbulence. When incoming hydrometeors, approaching the instrument sensing area, interact with the disturbed velocity field, both their trajectories and fall speed can be modified.

In traditional CGs, this bias usually results in an undercatch bias, meaning that, on average, the number of hydrometeors that are swiped away by wind exceed the number of hydrometeors that are diverted inside the instrument collecting funnel. Traditionally, correction curves are derived using data from experimental sites, where precipitation gauges are installed in operational conditions to be compared against a reference one. In the field, the ratio between the precipitation measured by a gauge in operational conditions (h_{meas} , usually in [mm]) for a given wind speed (U_{ref}) and the reference one (h_{ref} [mm]) is called the Collection Efficiency (CE, Equation 5.1).

$$CE = \frac{h_{meas}(U_{ref})}{h_{ref}}$$

5.1

Following the work of Jevons, numerous attempts were made to reduce and mitigate the exposure effect, mainly using wind shields (Nipher, 1878). Another aspect that was also thoroughly researched is the quantification of the exposure effect, by computing correction curves. Several approaches can be addressed:

field intercomparisons (see e.g. Pollock et al., 2018; Wolff et al., 2015), wind tunnel tests (see e.g. Green & Helliwell, 1972; Robinson & Rodda, 1969) and numerical simulation (see e.g. Nespor & Sevruk, 1999; Colli et al., 2015; Colli et al., 2018). From those approaches, it was demonstrated that the wind-induced bias in precipitation measurements is a non negligible source of error and in some cases is the primary one. Sevruk (1982) reported that the typical magnitude of the wind related losses for the precipitation amount is 2-10 % in case of liquid precipitation and 10-50 % in case of solid precipitation. Pollock et al. (2018) reported an observed undercatch of about 10 to 23 % for liquid precipitation at a lowland and upland site, respectively. Further studies focusing on solid precipitation (Rasmussen et al., 2012; Colli et al., 2015) showed collection losses up to 70-80 %. Nevertheless, the implementation of correction curves in operational conditions is still rare.

The overall body of knowledge and correction curves developed in the past years were mainly focused on traditional CGs. In the case of NCGs, the amount of available information regarding the quantification of the wind-induced bias is still scarce. An example of the observed wind-induced effects for a specific NCG is shown in the work of Friedrich et al. (Friedrich et al., 2013), where particle size velocity laser disdrometers (PAR-SIVEL, manufactured by OTT Hydromet) in a typical stationary installation were compared with others having an automatic variable orientation and tilting capacity, according to the wind direction. Under high-speed wind and heavy rain conditions, the authors reported artifacts in the measured drop size distribution from the stationary disdrometers that were not observed when the instrument sampling area was rotated into the wind.

Another instrument that showed discrepancies due to the wind effects in field comparisons is the Thies Laser Precipitation Monitor (LPM). The work of Upton and Brawn (2008), showed that, even at limited wind speed, two such instruments installed with two different orientations (rotated by 90°) may report differences of up to 20% in the total number of detected hydrometeors suggesting that the wind direction, further than the wind speeds, also affects their operational performance.

Wind-induced biases were also reported for the 2DVD, in the work of Greenberg (2001), that noted a tendency to underestimate precipitation, with part of the sensing area of the instrument that did not receive precipitation in some specific wind conditions. Further studies on the improved version of the 2DVD conducted by Testik & Pei (2017) showed that the effect of wind on precipitation is still present and that it affects not only the measurement of precipitation amount and intensity but also the DSD.

It is possible to assume that, in the case of NCGs, the wind induced bias is, potentially, even more significant than for CGs, because it can produce both underestimation and overestimation of the precipitation amount, depending on several environmental conditions, affecting not only the precipitation rate but also other parameters that are provided by the gauge, like the DSD.

To quantify the wind induced bias for NCGs, four influence parameters should be considered. Obviously, the first is the gauge shape, including the size and position of its sensing area. Since NCGs have complex, non-radially symmetric shapes, that are dictated by the measuring principle employed, this directly determines the resulting aerodynamic response and the pattern of the diverted hydrometeors. Also, even by neglecting the aerodynamic effect close to the instrument body, its shape can affect incoming hydrometeors (inducing partial or total blockage), meaning that a geometric effect may be present, like in the case of some peculiar CGs (Cauteruccio et al., 2021c). The second factor is of course the wind speed, that is also an

important influence parameter because it determines the slope of hydrometeors trajectories, both far and close to the instrument and the amount of updraft/downdraft and turbulence that is produced near the gauge. The third parameter, that is not considered in the case of CGs due to their symmetrical shape, is the wind direction. Finally, the fourth influence parameter is the DSD of precipitation events, since hydrometeors of different size respond differently to the wind (the larger ones are less susceptible to the wind effect while the smaller ones are easily influenced), the proportion of large and small size hydrometeors do affect the measurement of the precipitation rate in windy conditions.

5.2 HARDWARE SOLUTION: THE WIND SHIELD

The simplest and most straightforward way to mitigate the exposure effect is to shield the instrument against incoming wind. Prime example of this is the adoption of the pit gauges as the WMO field reference. By positioning the instrument at ground level, in an enclosed pit, wind cannot reach the instrument body, effectively excluding any exposure effect. Another example of such idea is the use of vegetation around the instrument that, once is clipped at the same level of the instrument collecting funnel, produces an effect very similar to the pit. This solution is known as the bush gauge (Yang, 2014), usually preferred for solid precipitation measurements.

Further example of wind shields commonly used for precipitation measurements are the WMO DFIR, the WMO DFAR and the single-Alter shield, nevertheless several other wind shields may be employed. The first is an “octagonal vertical double-fence inscribed into circles of 12 m and 4 m in diameter, with the outer fence 3.5 m high and the inner fence 3.0 m high surrounding a Tretyakov precipitation gauge mounted at a height of 3.0 m. In the outer fence there is a gap of 2.0 m and in the inner fence of 1.5 m between the ground and the bottom of the fences”, as described in (Ryu, 2012). This type of shield was extensively used in the WMO intercomparisons (Sevruk et al., 2009), but the measure is manually obtained by an operator.

Meanwhile the DFAR, that stands for Double Fence Automatic Reference, uses the same external fences as the DFIR, but inside an automatic gauge (usually of the weighing type) coupled with a single Alter shield is installed. The DFAR was introduced due to the necessity of high temporal resolution reference measurements in the SPICE project (Ryu et al., 2012, Lanza & Vuerich, 2018, Nitu et al., 2018).

Finally, the Alter shield, originally proposed by J. Cecil Alter (Alter, 1937) and eventually modified by the Norwegian Meteorological Institute (Smith et al., 2012), is composed of 32 stainless steel blades (or slats) hinged at a support ring. The upper edge of the blades is positioned slightly above the gauge orifice level. The single-Alter shield is considerably smaller than the DFIR, and the blades are free to adapt their inclination according to the wind to inhibit snow capping through their motion. All those shielding solutions are commonly used in combination with traditional CGs, however the same idea can be applied to the NCGs, in literature some examples of shielded NCGs are available, yet the use of shielded NCGs is not as common as for traditional CGs. This is probably due to them being marketed, at least initially, as less influenced by wind than traditional CGs, and while in some case it may be true (see e.g. Grossklauss et al., 1998) not all of them have the same performance in windy conditions.

The most extensive use of shielded NCGs is from the sites that participated in the WMO SPICE project, where e.g., a Thies LPM was installed inside a small, purposefully built shield, made of thin metal sheet

fins attached to a metal frame (at the Marshall and Weissfluhjoch experimental sites), as shown in Figure 5.1.



Figure 5.1: *Thies LPM installed inside a wind shield at the Marshall site from Nitu et al. (2019). The wind shield is composed of thin metallic blades fixed to a rigid structure.*

At the Formigal-Sarros WMO-SPICE test site in Spain another Thies LPM was initially installed inside the DFAR reference to provide present weather information (Buisàn et al., 2018) and was then joined by an OTT Parsivel², also inside the DFAR shield (Begueria et al., 2018), as shown in Figure 5.2



Figure 5.2: *Thies LPM and OTT Parsivel² inside a DFAR shield at the Formigal-Sarros experimental site from Begueria et al. (2018). The DFAR shield is composed by two octagonal fences of 12 m and 4 m in diameter.*

Further examples of shielded NCGs come from the work of Notaros et al. (2016) that, at Easton Valley View Airport, south of Greeley (Colorado), built the MASCRAD field site, where a Multi-Angle Snowflakes Camera (MASC) (Garret et al., 2012), a 2DVD, a Pluvio2 (weighing type CG) and a Vaisala WXT-520 were positioned inside a 2/3 scaled (8-m outer diameter) DFIR wind shield. The same site was further expanded by Bringi et al. (2018) and Thurai et al. (2019) with the same setup being reproduced at the Huntsville test site (Alabama), where both a third generation 2DVD and a meteorological particle spectrometer (MPS) (Baumgardner et al., 2002) were installed within a 2/3-scale DFIR shield.

A similar setup is also found at the NASA Wallops precipitation research facility in the Delmarva Peninsula, where a MPS, a 2DVD and a Pluvio weighing gauge are placed inside a full scale DFIR shield (Thurai et al., 2020). Another example is found in the work of Capozzi et al. (2021), where a Thies LPM was installed in the Montevergine observatory using a metallic shield, similar to the ones used during the WMO-SPICE project. Although effective, this approach is usually viable only in test sites, for research applications, while it is less practical for operational meteorological stations, especially in urban areas where the available space is often limited.

5.3 NUMERICAL SIMULATION AND TRANSFER FUNCTIONS

To quantify the wind induced bias caused by the airflow deformation near the gauge, field campaigns, Wind Tunnel (WT) testing and numerical simulation can be employed. Experimental approaches are, in general, expensive in terms of both time and resources and, in the case of field experiments, are strictly limited to the experienced precipitation and wind climatology at the test site. As an alternative, numerical simulation allows to investigate various configurations in terms of influence parameters, see, e.g., (Colli et al., 2018, Cauteruccio et al., 2021c), within limited cost and time effort.

The numerical simulation approach is based on Computational Fluid Dynamic (CFD) models that reproduce the airflow velocity pattern induced by the instrument and is generally coupled with Lagrangian Particle Tracking (LPT) models to simulate hydrometeor trajectories. This approach was adopted by Nešpor and Sevruck (1999) on gauges with cylindrical shape, characterized by various design and thickness of the collector. Finite volume CFD simulations were run, solving the three-dimensional Reynolds-Averaged Navier–Stokes (RANS) equations by means of the k - ε turbulence closure model (where k is the turbulent kinetic energy and ε is the turbulent dissipation rate per unit mass). The limited computational resources available at that time forced the adoption of a coarse computational mesh. Thériault et al. (2012) performed RANS k - ε simulations on a shielded weighing gauge with chimney shape. In the work of Colli et al. (2015, 2016a, 2016b), after increasing the detail of the computational mesh, both RANS simulations with a k - ω shear stress transport (SST) closure model (Menter, 1994) (with ω being the turbulent specific dissipation rate) and Large Eddy Simulations (LES) were performed on the same gauge geometry.

To the author's knowledge, the only previous attempt to numerically quantify the wind-induced bias of NCGs was presented by Nešpor et al. (2000). In that work, the basic method and the computational capabilities were the same as Nešpor and Sevruck (1999). Quite a coarse computational mesh was implemented and no validation of the CFD results against WT measurements was provided. A two-dimensional video disdrometer (2DVD) was studied, but its simulated outer shape is now obsolete and

differs significantly from the current version of the instrument. Finally, the 2DVD is a very special case of NCG, mainly used in field test sites for research purposes, while other NCGs are generally used at operational measurement sites. The geometry of the 2DVD is also rather simplified with respect to typical NCGs and the work of Nešpor et al. (2000) cannot be extrapolated to provide information about the complex outer shape of other optical disdrometers.

In the present thesis work, CFD simulations were performed to investigate the airflow pattern near the complex outer geometry of different NCGs, using the open source OpenFOAM software package. Due to the non-radially symmetrical shape of such instruments, simulations were run by varying both the incoming wind speed and direction. The supporting pole of the instrument was also included in the computational domain, since for some cases it may have an influence on the airflow velocity magnitude and direction at the sensing area. Alongside the CFD model a LPT model was used to compute hydrometeor trajectories, simulating the effect of wind on incoming precipitation.

5.3.1 Computational Fluid-dynamics (URANS and LES)

In fluid mechanics, the momentum transport inside a fluid continuum is described by the Cauchy equation and can be written as:

$$\frac{d(\rho \mathbf{U})}{dt} = \rho \mathbf{f} + \nabla \cdot \mathbf{T} \quad 5.2$$

Where \mathbf{U} is the fluid velocity, ρ is the fluid density, \mathbf{f} is the resultant of the volume forces applied to it and \mathbf{T} is the stress tensor, furthermore $\frac{d}{dt}$ is the material derivative. By developing the material derivative in Equation 5.2 the Cauchy equation can be rewritten as:

$$\frac{\partial(\rho \mathbf{U})}{\partial t} + \mathbf{U} \cdot \nabla(\rho \mathbf{U}) = \rho \mathbf{f} + \nabla \cdot \mathbf{T} \quad 5.3$$

For an incompressible, viscous and Newtonian fluid, the density is constant, furthermore the stress tensor \mathbf{T} is equal to the sum of the pressure forces (P) and the shear stresses ($\boldsymbol{\tau}$), therefore making Equation 5.3 become:

$$\rho \frac{\partial \mathbf{U}}{\partial t} + \rho \mathbf{U} \cdot \nabla \mathbf{U} = \rho \mathbf{f} + \nabla \cdot (P\mathbf{I} + \boldsymbol{\tau}) \quad 5.4$$

Under these hypotheses, the shear stress tensor is equal to:

$$\tau_{ij} = 2\mu D_{ij} = 2\mu \frac{1}{2} \left(\frac{\partial u_i}{\partial u_j} + \frac{\partial u_j}{\partial u_i} \right)$$

5.5

Where μ is the dynamic viscosity of the fluid. Substituting Equation 5.5 in Equation 5.4 provides the Navier Stoke (NS) equation for and incompressible viscous fluid.

$$\rho \frac{\partial \mathbf{U}}{\partial t} + \rho \mathbf{U} \cdot \nabla \mathbf{U} = -\nabla P + \mu \nabla^2 \mathbf{U} + f$$

5.6

An analytical solution of such equation is however possible only in simplified cases. This is due to the onset of instability, that arises under common flow conditions. This instability due to the nature of the equations themselves, is random in nature and is called turbulence. Turbulence in the flow arises when the ratio between the inertial forces, that favours the onset of instability, and the viscous forces, that dampens it, becomes much larger than one. This ratio is usually expressed by the Reynolds number (Re), that is a dimensionless number shown in equation (5.7).

$$Re = \frac{UL}{\nu}$$

5.7

Where ν is the kinematic viscosity and L is the characteristic length of the flow, that depends on the specific problem investigated. For low Re numbers, viscous forces prevail over inertial ones and no instability is present in the domain, this regime is called laminar flow. This condition is typical of very slow moving and/or very viscous fluids, possibly interacting with small scale features. Increasing the Reynolds number, viscous forces are unable to prevent the onset of instability in the whole domain, where turbulence start to appear. From laminar, the flow first enters the transition stage and then becomes turbulent. Turbulent flow is characterized by very large values of the Reynolds number, meaning that the dampening effect of the viscous forces is almost negligible, and instability is present over the whole domain. Turbulence is extremely common in both natural and artificial flows and is manifested in the eddies that are often visible in them.

Even if an analytical solution for the NS equation is often not available, the problem can still be solved numerically. For this reason, CFD is the ideal tool to obtain the high-resolution velocity field around the complex geometry of NCGs when immersed in a wind field. Turbulence, however, still remains the primary challenge in CFD, since its analytical solution is not available and cannot be neglected for large Re number flows. Over the years several numerical approaches and approximate models were developed to close the turbulence problem and obtain a numerical solution. Differences in these approaches are primarily in the assumptions made on turbulence, that directly impact the computational cost necessary to run the simulation. In this thesis work, two such approaches are used. The first one provides information about the

flow after a steady state condition is reached and in the hypothesis of stationary turbulence characteristics, solving the average part of the flow variables while modelling the turbulence induced fluctuations. The second approach provides information on both the steady state and the transient conditions, solving all flow components above a certain threshold, defined by a spatial filtering operation usually bounded to the mesh size, and modelling only the smallest turbulent fluctuations. The choice of considering two different approaches was dictated by the significant difference in computational requirements between the two models. Solving the wind velocity field around the complex, non-radially symmetric, shape of NCGs can be achieved, in a reasonable time, by a stand-alone workstation, using the first, time-independent, approach, while the second, time-dependent, approach requires computational performances that are typical of very large cluster PCs.

5.3.1.1 Time-independent simulation

The time-independent approach is based on the numerical solution of the Unsteady Reynold Averaged Navier-Stokes (URANS) equations (Reynolds 1895), derived from the NS equations (Equation 5.6), and the continuity equation (Equation 5.8).

$$\nabla \cdot \mathbf{U} = 0 \quad 5.8$$

To obtain the URANS equation, the flow can be imagined as composed by the sum of two components, an average part, that represent the overall flow behaviour and a fluctuating part, that represent the turbulent fluctuations and has an average equal to zero. Using this decomposition approach, both pressure and velocity can be expressed as shown in Equations 5.9 and 5.10.

$$\mathbf{U} = \bar{\mathbf{u}} + \mathbf{u}' \quad 5.9$$

$$P = \bar{p} + p' \quad 5.10$$

Where $\bar{\mathbf{u}}$ is the average part of velocity, while \mathbf{u}' is the fluctuating part. The same notation applies for pressure. Considering an incompressible fluid, after neglecting the forcing term, Equations 5.9 and 5.10 can be inserted in Equations 5.6 and 5.8.

$$\rho \frac{\partial(\bar{\mathbf{u}} + \mathbf{u}')}{\partial t} + \rho(\bar{\mathbf{u}} + \mathbf{u}') \cdot \nabla(\bar{\mathbf{u}} + \mathbf{u}') = -\nabla(\bar{p} + p') + \mu \nabla^2(\bar{\mathbf{u}} + \mathbf{u}') \quad 5.11$$

$$\nabla \cdot (\bar{\mathbf{u}} + \mathbf{u}') = 0 \quad 5.12$$

Remembering that $\nabla \cdot (\mathbf{U}\mathbf{U}) = \mathbf{U} \cdot \nabla \mathbf{U} + \mathbf{U} \nabla \cdot \mathbf{U}$ and the result of the continuity equation (Equation 5.8) for an incompressible fluid, Equation 5.11 becomes:

$$\rho \frac{\partial \bar{\mathbf{u}}}{\partial t} + \rho \frac{\partial \mathbf{u}'}{\partial t} + \rho \nabla(\bar{\mathbf{u}}\bar{\mathbf{u}}) + \rho \nabla(\bar{\mathbf{u}}\mathbf{u}') + \rho \nabla(\mathbf{u}'\bar{\mathbf{u}}) + \rho \nabla(\mathbf{u}'\mathbf{u}') = -\nabla \bar{p} - \nabla p' + \mu \nabla^2 \bar{\mathbf{u}} + \mu \nabla^2 \mathbf{u}' \quad 5.13$$

Both Equation 5.12 and 5.13 can be averaged. Recalling that the average of an average value is equal to itself and the average of the fluctuations is equal to zero, the two equations therefore becomes:

$$\rho \frac{\partial \bar{\mathbf{u}}}{\partial t} + \rho \nabla(\bar{\mathbf{u}}\bar{\mathbf{u}}) = -\nabla \bar{p} + \mu \nabla^2 \bar{\mathbf{u}} - \rho \nabla(\overline{\mathbf{u}'\mathbf{u}'}') \quad 5.14$$

$$\nabla \cdot \bar{\mathbf{u}} = 0$$

5.15

where $\overline{\mathbf{u}'\mathbf{u}'}$ is the average of the product of the fluctuating part of the solution and is not null. The term $-\rho \nabla(\overline{\mathbf{u}'\mathbf{u}'})$ is the Reynolds stress tensor $\boldsymbol{\tau}^R$, which introduces six additional unknowns that cannot be directly solved but must be modelled. Using the Boussinesq hypothesis, the Reynold stress tensor can be expressed as in Equation 5.16.

$$\boldsymbol{\tau}^R = -\rho \nabla(\overline{\mathbf{u}'\mathbf{u}'}) = 2\mu_T[\nabla \bar{\mathbf{u}} + (\nabla \bar{\mathbf{u}})^T] - \frac{2}{3}\rho k \mathbf{I} \quad 5.16$$

where μ_T is the turbulent viscosity and k is the flow turbulent kinetic energy. The use of Equation 5.16 in Equation 5.14 provides:

$$\frac{\partial \bar{\mathbf{u}}}{\partial t} + \nabla \cdot (\bar{\mathbf{u}}\bar{\mathbf{u}}) = -\frac{1}{\rho} \nabla \bar{p} + (\nu + \nu_T) \nabla^2 \bar{\mathbf{u}} \quad 5.17$$

The only unknown in Equation 5.17 is ν_T , that is the eddy viscosity (μ_T/ρ), and is computed by means of a turbulence model, allowing to numerically solve the URANS equations (Alfonsi, 2009). The modelling approach chosen in this work is the k - ω shear stress transport (SST) turbulence model, where k is the turbulent kinetic energy and ω the specific turbulent dissipation rate, developed by Menter (1994) and slightly revised in (Menter et al, 2003). This is a two-equations model, meaning that the solution of two additional equations for k and ω , respectively, is required.

The adopted turbulence model combines the best trait of both the baseline k - ω model, developed by Wilcox (1988), and the k - ε model from Jones & Launder (1972), exploiting the excellent performances of the k - ω model near the wall and the stability of the k - ε model in the free stream. The zonal formulation that combines the two models is based on blending functions, which ensure a smooth and automatic transition between the k - ω and k - ε modelled zones. The main additional complexity in the model formulation compared to standard models lies in the necessity to compute the distance from the wall, which is required in the blending functions. The SST model was originally used for aeronautics applications, but has since made its way into most industrial, commercial and many research codes, becoming a de facto industry standard. The two additional equations that are used to compute the evolution of the turbulence kinetic energy (Equation 5.18) and the turbulence specific dissipation rate (Equation 5.19) are shown below.

$$\rho \frac{dk}{dt} = \boldsymbol{\tau}^R : \nabla \bar{\mathbf{u}} - \beta^* \rho \omega k + \nabla \cdot [(\mu + \sigma_k \mu_T) \nabla k] \quad 5.18$$

$$\rho \frac{d\omega}{dt} = \frac{\gamma}{\nu_T} \boldsymbol{\tau}^R : \nabla \bar{\mathbf{u}} - \beta \rho \omega^2 + \nabla \cdot [(\mu + \sigma_\omega \mu_T) \nabla \omega] + 2\rho(1 - F_1) \frac{\sigma_\omega}{\omega} \nabla k : \nabla \omega \quad 5.19$$

where F_1 is the blending function between the k - ε and the k - ω behaviour, defined as:

$$F_1 = \tanh \left\{ \min \left[\max \left(\frac{\sqrt{k}}{\beta^* \omega y}, \frac{500\nu}{y^2 \omega} \right); \frac{4\rho\sigma_{\omega 2} k}{CD_{k\omega} y^2} \right]^4 \right\} \quad 5.20$$

where y is the distance from the wall and $CD_{k\omega}$ is the cross-diffusion term:

$$CD_{k\omega} = \max \left(2\rho\sigma_{\omega 2} \frac{1}{\omega} \nabla k : \nabla \omega ; 10^{-10} \right) \quad 5.21$$

Once both k and ω are known, using the k - ω SST model the eddy viscosity is obtained as:

$$\nu_T = \frac{a_1 k}{\max(a_1 \omega; \mathbf{S} F_2)} \quad 5.22$$

where F_2 is the SST blending function shown in Equation 5.23 and \mathbf{S} is the strain rate $\frac{1}{2}[\nabla\mathbf{u} + (\nabla\mathbf{u})^T]$. Meanwhile, the coefficients of the model are obtained by blending the coefficients of both the k - ω and k - ε (shown in Table 5.1) by means of Equation 5.24.

$$F_2 = \tanh \left[\max \left(2 \frac{\sqrt{k}}{\beta^* \omega y}, \frac{500\nu}{y^2 \omega} \right)^2 \right]$$

5.23

$$\phi = F_1 \phi_1 + (1 - F_1) \phi_2$$

5.24

Table 5.1: Parameters for the k - ω SST turbulence model as proposed by Menter et al. (2003)

Parameter	σ_{ki}	a_i	$\sigma_{\omega i}$	β_i	β^*	κ	γ_i
$i = 1$ (from k - ω)	0.85	0.31	0.5	0.075	0.09	0.41	5/9
$i = 2$ (from k - ε)	1.0	-	0.856	0.0828			0.44

Numerical solution of the URANS equations previously presented, was obtained using the OpenFOAM (Open Field Operation And Manipulation) software, an open-source C++ modelling toolbox for fluid dynamics related problems (Cheng et al., 2014). The chosen solving algorithm is PIMPLE, a combination of the PISO (Pressure Implicit with Splitting of Operator) (Issa, 1986) and SIMPLE (Semi-Implicit Method for Pressure-Linked Equations) algorithms (Caretto et al. 1972, Patankar & Spalding, 1972). These algorithms are iterative solvers, commonly used for the NS equations, but PISO and PIMPLE are both used for transient cases whereas SIMPLE is used for steady-state cases. Coupling the PIMPLE algorithm with a pseudo-transient approach based on a local time stepping (LTS) numerical scheme (Jeanmasson et al., 2019) allowed to considerably reduce the computational burden. In this approach, the simulation is forced towards a steady state condition similarly to the RANS approach, but with no need to remove the time derivative in the NS equations, therefore improving stability especially for complex geometries. The condition used to evaluate the stability of the solution is given by the Courant-Friedrichs-Lewy inequality (Equation 5.25):

$$C = \Delta t \sum_{i=1}^n \frac{u_{xi}}{\Delta x_i} < C_{max}$$

5.25

where u_{xi} is the speed in the i -th cell, Δx_i is the length of the i -th cell in the direction of u_{xi} , Δt is the chosen time step and C_{max} is the maximum Courant number. For most explicit schemes a Courant number

strictly below one over the whole domain is needed, requiring an extremely small timesteps, whose consequence is a high computational cost, since the entire simulation is controlled by the single cell with the highest Courant number. Instead, by means of the LTS approach a different time step for each cell of the computational domain is used, according to the imposed value of the Courant number, therefore enhancing numerical convergence and removing the limitations imposed in the case of a fixed timestep. Suitable functions are then used to smooth the solution over the domain. Further numerical schemes needed to solve the Navier-Stokes equations are listed below:

- Time scheme: is used to discretize time derivatives. Due to the use of the LTS approach, a special numerical scheme is used, called “localEuler” in OpenFOAM. It is a first order pseudo transient scheme, designed for steady cases with a spatially varying, cell-based time scale set by specific Local Time Stepping (LTS) solvers.
- Gradient scheme: is used to discretize the gradient terms. The Gauss entry specifies the standard finite volume discretization of Gaussian integration which requires the interpolation of values from the cell centres to the face centres. The interpolation scheme is then given by the linear entry, meaning linear interpolation or central differencing. It is also possible to set limiters to achieve stability. The cellLimited option bounds the cell gradient to ensure that the face values obtained by extrapolating the cell value to the cell faces using the gradient are bounded by the minimum and maximum of the neighbouring cells. Computations were performed using a standard Gauss scheme with linear interpolation and cell limiter.
- Divergence schemes: are used to evaluate the divergence term and then calculate the flux of the properties through the cell faces using the Gauss integration, these schemes are also usually limited to improve the stability, the limiter can be calculated in all three directions or only in the direction of the resultant vector. These are the most critical schemes because they affect the advection terms. In this work the Upwind scheme, which is first order and bounded, was used for all variables except the turbulence term and the flow velocity where the Linear and LinearUpwind schemes were used, respectively. Both are second order unbounded schemes and were chosen to improve accuracy. A blending function was applied to improve stability in regions with high values of the Courant number.
- Surface normal gradient schemes: these are required to solve the Laplacian term using Gaussian integration. The solution can be stabilized by introducing a limiter, with a correction factor set between 0 (great stability/low accuracy) and 1 (low stability/great accuracy). Here a value of 0.5 is used, applying a moderate correction for non-orthogonality.
- Laplacian scheme: it is used to discretize the Laplacian term. The Gauss scheme is the only choice of discretization and requires a selection of both an interpolation scheme for the diffusion coefficient and a surface normal gradient scheme. In this work linear interpolation and a bounding coefficient of 0.5 are used.
- Interpolation scheme: it is used to transform cell-centre quantities to face centres. The operation is used in many of the finite volume calculations, e.g., for the calculation of gradient, divergence, and Laplacian terms. Here the meshwave method was chosen, considering that usually the

increase in precision of more sophisticated schemes is negligible if confronted with the increase in computational requirement.

The numerical schemes used are listed in Table 5.2.

Table 5.2: Numerical schemes used in the time-independent approach.

Term	OpenFOAM scheme	
Time	localEuler	
Gradient	cellLimited Gauss linear 1	
Divergence	For $\bar{\mathbf{u}}$	Gauss linearUpwind grad(U)
	For k and ω	Gauss upwind
	For $\nu_{eff}(\nabla \bar{\mathbf{u}})^T$	Gauss linear
Laplacian	Gauss linear limited 0.5	
Interpolation	Linear	
Surface normal gradient	Limited 0.5	

Simulations were conducted by setting air as an incompressible fluid, with a density of 1.0 kg/m^3 and a kinematic viscosity of $1.5 \times 10^{-5} \text{ m}^2/\text{s}$. The free stream turbulence intensity was set equal to 1%. From preliminary simulations the dimensionless wall distance (y^+) was evaluated. Depending on the wind velocity, its average value indicates whether the cells closest to the instrument surface are positioned in the buffer or the log-law layer. Appropriate wall functions (independent on y^+) were used for k , ω , and the turbulent viscosity (ν_t) as near-wall boundary conditions at all solid surfaces (Liu, 2016).

5.3.1.2 The time-dependent approach

The time-dependent approach is based on the LES model. This is conceptually similar to the URANS model but while the latter is based on time averaging of the turbulent variables, the LES approach uses spatial filtering. Like before, it is possible to decompose both velocity and pressure as shown in Equations 5.26 and 5.27:

$$\mathbf{U} = \tilde{\mathbf{u}} + \mathbf{u}' \quad 5.26$$

$$P = \tilde{p} + p' \quad 5.27$$

Here, $\tilde{\mathbf{u}}$ is the spatially filtered velocity, while \mathbf{u}' is the sub-grid scale velocity, meaning that \mathbf{u}' is the fluctuating part that is characterized by a length scale smaller than the filter size, and is filtered out; the

same holds true for pressure. Filtering of the solution is performed, by means of a convolution integral, in the form:

$$\tilde{\mathbf{u}} = \iiint G(\mathbf{r}, \mathbf{x}) \mathbf{U}(\mathbf{x} - \mathbf{r}, t) d\mathbf{r} \quad 5.28$$

where $G(\mathbf{r}, \mathbf{x})$ is the filter function.

Like in the URANS approach, Equations 5.26 and 5.27 can be used in the NS equations (Equation 5.6) and in the continuity equation (Equation 5.8), assuming the fluid as incompressible and after neglecting the forcing term. The Filtered Navier -Stokes (FNS) equation is therefore obtained as:

$$\frac{\partial \tilde{\mathbf{u}}}{\partial t} + \nabla \cdot (\tilde{\mathbf{u}} \tilde{\mathbf{u}}) = -\frac{1}{\rho} \nabla \tilde{p} + \nu \nabla^2 \tilde{\mathbf{u}} + \nabla \cdot \boldsymbol{\tau}_{SGS} \quad 5.29$$

$$\nabla \cdot \tilde{\mathbf{u}} = 0 \quad 5.30$$

It is worth noting that, contrary to averaging, in the case of filtering $\tilde{\tilde{\mathbf{u}}} \neq \tilde{\mathbf{u}}$ and $\tilde{\mathbf{u}}' \neq 0$. In Equation 5.29, the term $\boldsymbol{\tau}_{SGS}$ is the sub-grid scale stress tensor and represents, in the equation, the effect of the small-scale components. The tensor $\boldsymbol{\tau}_{SGS}$ is formed by three components as show below:

$$\boldsymbol{\tau}_{SGS} = \underbrace{(\tilde{\tilde{\mathbf{u}}\mathbf{u}} - \tilde{\mathbf{u}}\tilde{\mathbf{u}})}_L + \underbrace{(\tilde{\mathbf{u}}\mathbf{u}' - \mathbf{u}'\tilde{\mathbf{u}})}_C + \underbrace{\mathbf{u}'\mathbf{u}'}_R = \mathbf{L} + \mathbf{C} + \mathbf{R} \quad 5.31$$

where \mathbf{L} is the Leonard stresses tensor, \mathbf{C} is the cross-term stress tensor and \mathbf{R} is the sub-grid scale Reynolds stress tensor, that is conceptually equivalent to the Reynolds stress tensor in the URANS approach. Of these three components, only the Leonard stresses tensor can be directly computed, while the other two terms contain sub-grid quantities that must be modelled. Several approaches exist in literature to model the sub-grid scale stress tensor, from algebraic to one- and two-equations models. In this work, the Wall-Adaptive Local Eddy (WALE) algebraic model was chosen (Nicoud & Ducros, 1999). Using the Boussinesq hypothesis, the sub-grid scale stress tensor becomes:

$$\boldsymbol{\tau}_{SGS} = -2\nu_{SGS}\tilde{\mathbf{S}} \quad 5.32$$

where $\tilde{\mathbf{S}}$ is the filtered strain-rate tensor and ν_{SGS} is the sub-grid scale eddy viscosity. Like in the time-independent approach, the modelling of turbulence is reduced to the evaluation of ν_{SGS} . Being an algebraic model, the sub-grid scale, eddy viscosity term can be directly calculated from:

$$\nu_{SGS} = (C_w \Delta)^2 \frac{(S_{ij}^d S_{ij}^d)^{3/2}}{(\tilde{S}_{ij} \tilde{S}_{ij})^{5/2} + (S_{ij}^d S_{ij}^d)^{5/4}} \quad 5.33$$

where the Einstein index notation on repeated indices is used, Δ is the filter width and S_{ij}^d is the filtered velocity gradient tensor, defined as:

$$S_{ij}^d = \frac{1}{2} \left(\frac{\partial \tilde{u}_i}{\partial x_k} \frac{\partial \tilde{u}_k}{\partial x_j} + \frac{\partial \tilde{u}_j}{\partial x_k} \frac{\partial \tilde{u}_k}{\partial x_i} \right) - \frac{1}{3} \delta_{ij} \frac{\partial \tilde{u}_k}{\partial x_l} \frac{\partial \tilde{u}_l}{\partial x_k} \quad 5.34$$

The symbol δ_{ij} denotes the Kronecker delta and C_w is the model coefficient, varying between 0.3 and 0.6. In this work, C_w was assumed equal to 0.325 as suggested by the OpenFOAM User Manual for external aerodynamics. To solve the equations the same PIMPLE scheme used for the steady state approach was used, able to compute the fully transient phenomenon without resorting to the LTS scheme. To ensure stability of the solution, a constrain on the Courant number was introduced, by limiting its value below 0.8. The numerical schemes used for the time-dependent approach are listed in Table 5.3.

Table 5.3: Numerical schemes used in the time-dependent approach.

Term	OpenFOAM scheme	
Time	CrankNicolson 0.9	
Gradient	For \tilde{p}	Gauss linear
	For $\tilde{\mathbf{u}}$	cellMDLimited Gauss linear 1
Divergence	For $\tilde{\mathbf{u}}$	Gauss linearUpwind grad(U)
	For $\nu_{eff}(\nabla \tilde{\mathbf{u}})^T$	Gauss linear
Laplacian	Gauss linear limited 1	
Interpolation	Linear	
Surface normal gradient	Limited 1	

The physical properties of air used in this case are the same as in the time-independent approach. To speedup convergence to a steady state condition of the LES simulations, the velocity and pressure fields previously obtained from the URANS simulations were mapped on the higher resolution mesh and the solution was advanced for 3000 steps using the time-independent approach. Results from this step were then used as initial conditions for the time-dependent simulations.

5.3.1.3 Meshing requirements

Due to the complexity of the geometry of typical NCGs, accurate evaluation of the mesh resolution requirements was necessary. Preliminary simulations conducted for a limited run time were used to calculate the ratio between the integral length scale and the grid length scale, named R_L . This parameter represents, for each cell, the ratio between the turbulence length scale and the cell size. It is a common CFD practice to refine the mesh in the zones of interest using R_L as a reference. For URANS simulations, it is advisable to keep $R_L \geq 5$, so that the larger eddies, summing-up to 80% of the turbulence kinetic energy, are discretized by at least 5 cells (Pope, 2000). In the case of LES simulations, a higher percentage of turbulent kinetic energy should be directly solved, meaning that R_L should be above 10 to 12 to resolve those eddies that are responsible for more than 90% of the turbulent kinetic energy. Mesh refinement was evaluated, both for the time-independent and time-dependent approach, by running simulations with the $k-\omega$ shear stress transport (SST) turbulence model. Therefore, the integral length scale (L_0) is calculated from Equation 5.35 (Menter, 1994), while R_L is calculated from Equation 5.36.

$$L_0 = \frac{k^{1/2}}{C_\mu \cdot \omega} \quad 5.35$$

$$R_L = \frac{L_0}{\sqrt[3]{V}} \quad 5.36$$

where the coefficient C_μ is equal to 0.09 and V is the volume of the cell. For the time-independent approach, the computational mesh was progressively refined until the criterion $R_L \geq 5$ was satisfied in most of the domain. Only in the proximity of the straight and sharp edges the R_L criterion could not be always met. Coarser meshes were also tested, using a slightly simplified version of the geometry that allowed reducing the cell count to about 1M elements, while still preserving the instrument features. These meshes, however, failed to meet the R_L criterion and showed poor agreement with the real-world measurements. It is concluded that, for the geometries used in this work, no meaningful reduction of the cell count can be achieved without sacrificing the simulation accuracy. The same approach was also adopted for the meshes used in the time-independent approach, by refining the mesh until a value of $R_L > 10$ was achieved.

Also, values of typical mesh size and quality parameters, including the non-orthogonality, skewness, and aspect ratio, were evaluated for all meshes. These are used to identify highly distorted cells that could affect the solution and their value should be as low as possible. During meshing it was ensured

that these parameters fell inside the range that is considered acceptable for external aerodynamic simulations. A more in-depth explanation can be found in Aqilah et al. (2018) and Baker (2005).

5.3.2 Lagrangian Particle Tracking

The second step in evaluating the wind-induced bias for NCGs consists in modelling incoming hydrometeor trajectories and computing their deviations due to the wind. The behaviour of a particle immersed in a fluid can be generally characterized using the Stokes number (St), that is a dimensionless number defined as the ratio between the particle response time and the fluid time scale.

$$St = \frac{\tau_p}{\tau_f}$$

5.37

Where τ_p is the particle response time, that represent the time required for the particle to modify its trajectory after a change in the flow conditions around it and τ_f is the fluid time scale, that instead represent the period of the eddies that characterize the flow. Particles having a large St number are mostly insensitive to the change in the flow conditions and their trajectories remains unchanged. Particles having small St number, instead, tend to closely follow the flow and see their trajectories change accordingly, behaving like a passive scalar.

The response time for a generic particle, not necessarily in the Stokes regime, can be obtained as:

$$\tau_p = \frac{4 d_p^2 \rho_p}{3 \mu_f C_D Re_p}$$

5.38

Where ρ_p is the particle density, μ_f is the fluid dynamic viscosity, d_p is the particle diameter, C_D is the drag coefficient and Re_p is the particle Reynolds number. For hydrometeors in flight, it is possible to compute their response time once a drag coefficient relationship is defined. In the case of raindrops, the response time ranges between 5 to 10 hundredths of a second for very small drops, up to 1 to 1.5 seconds for larger and heavier drops. Multiplying the response time for the hydrometeor terminal velocity is also possible to estimate the hydrometeors travel distance before their trajectories can be affected by a change in the flow conditions. A small, 0.25 mm diameter drops, is affected in as little as 8 cm of travel while for a larger 8 mm diameter one, almost 20 m of travel are required.

From these considerations it is therefore expected to observe considerable deviations in the smaller hydrometeors trajectories when approaching a precipitation gauge, while larger drops trajectories should continue almost undisturbed. However smaller diameter hydrometeors are the most abundant in precipitation events and account for a substantial portion of the total precipitation volume. Quantitative evaluation of trajectories deflection is therefore required for computing the instrument CE. The modelling

of hydrometeor trajectories is performed, in this work, by means of a Lagrangian Particle Tracking (LPT) model; a common numerical approach used to track moving particles in fluids.

Computations are made using the particle tracking capabilities of the OpenFOAM software, able to simulate the trajectory of multiple independent particles released in a velocity field, returning both the particle positions along time and the possible impact location at the chosen boundary.

Lagrangian models are generally divided in four main categories that are listed here according to their increasing complexity: uncoupled, one-, two- and four-way coupled models. The difference is in the amount of interaction that is considered between the fluid and the particles and between the particles themselves. Uncoupled models are used to evaluate particle trajectories using already computed velocity fields, that do not change during the simulation. One-way coupled models on the other hand, consider the evolution in time of the flow, and the CFD solution is advanced at the same time of the trajectory computation, however the effect of the presence of particles on the flow is neglected. Two-way models are obtained considering also the effect of particles on the flow evolution while in four-way models also the particle-to-particle interaction is computed. In this work, both an uncoupled and a one-way coupled model are used, the first combined with both the time-independent and time-dependent CFD approach while the one-way coupled was used only within the time-independent approach.

Since the volume fraction of hydrometeors in the air during a precipitation event is generally low even for high precipitation rates (Uijlenhoet et al., 2006), particle-to-particle interactions are very limited, at least close to the ground where precipitation gauges are positioned. Due to the typical time scale of a hydrometeor crossing the computational domain, varying between about 0.1 and 1 seconds, the assumption of a steady state condition for the wind field is also in reasonable accordance with typical field conditions. Therefore, in this work, an uncoupled Lagrangian Particle Tracking model is initially used to simulate natural precipitation. Being uncoupled means that the flow field is not influenced by the presence of the particles, and trajectories are computed only after the end of the CFD simulation using a static velocity field (the steady state solution), also neglecting particle to particle interactions. Under these hypotheses, the equation of the particle motion is shown in Equation 5.39, which is identical to Equation 2.11 but is repeated here for the sake of clarity.

$$V_p \rho_p \mathbf{a}_p = -C_D A_p \rho_a 0.5(\mathbf{v}_p - \mathbf{v}_a) |\mathbf{v}_p - \mathbf{v}_a| + V_p(\rho_p - \rho_a)\mathbf{g} \quad 5.39$$

where V_p is the volume of the particle, ρ_p and ρ_a are respectively the density of the particle and of the air, A_p is the cross-sectional area of the particle, \mathbf{a}_p and \mathbf{v}_p are the particle acceleration and velocity, \mathbf{v}_a is the air velocity, C_D is the particle drag coefficient and \mathbf{g} is the gravity acceleration. Using this model, the particle is subjected only to three forces: gravity, buoyancy, and aerodynamic forces. From Equation 5.39, the components of the particle acceleration are therefore:

$$a_{px} = -\frac{1}{2} C_D A_p \frac{\rho_a}{\rho_p V_p} (u_p - u_a) |\mathbf{v}_p - \mathbf{v}_a|$$
5.40

$$a_{py} = -\frac{1}{2} C_D A_p \frac{\rho_a}{\rho_p V_p} (v_p - v_a) |\mathbf{v}_p - \mathbf{v}_a|$$
5.41

$$a_{pz} = -\frac{1}{2} C_D A_p \frac{\rho_a}{\rho_p V_p} (w_p - w_a) |\mathbf{v}_p - \mathbf{v}_a| + \frac{(\rho_p - \rho_a)}{\rho_p} g$$
5.42

where u , v and w represent the stream wise, crosswise, and vertical components of the velocity vector. Since trajectories are numerically computed, the particle acceleration components are obtained at the start of each time-step (Δt). Once the acceleration is known, it is used to update the particle velocity as shown below:

$$u_p^{(i+1)} = u_p^{(i)} + a_{px}^{(i)} \cdot \Delta t$$
5.43

$$v_p^{(i+1)} = v_p^{(i)} + a_{py}^{(i)} \cdot \Delta t$$
5.44

$$w_p^{(i+1)} = w_p^{(i)} + a_{pz}^{(i)} \cdot \Delta t$$
5.45

While the particle position at the beginning of the new time-step is obtained as:

$$x^{(i+1)} = x^{(i)} + \left(u_p^{(i)} + \frac{1}{2} a_{px}^{(i)} \cdot \Delta t \right)$$
5.46

$$y^{(i+1)} = y^{(i)} + \left(v_p^{(i)} + \frac{1}{2} a_{py}^{(i)} \cdot \Delta t \right)$$
5.47

$$z^{(i+1)} = z^{(i)} + \left(w_p^{(i)} + \frac{1}{2} a_{pz}^{(i)} \cdot \Delta t \right)$$
5.48

where $x^{(i)}, y^{(i)}, z^{(i)}$ and $x^{(i+1)}, y^{(i+1)}, z^{(i+1)}$ are the spatial coordinates of the particle at the previous and current time step, respectively. Once the new position of the hydrometeor is known, acceleration is updated considering the new flow characteristics and the process is repeated until necessary.

In LPT models, particles may be injected in the computational domain from a boundary or directly inside its volume, and their trajectories are computed until they reach their destination or exit the domain. In this work, particles are inserted directly in the domain starting from a regular grid and are tracked until they impact on the instrument body, the instrument sensing area (that in this case is physically modelled in the domain) or exit from one of the other boundaries. Simulations are stopped only once all released particles travelled significantly below the instrument sensing area.

5.3.3 Drag coefficient

The drag coefficient C_D is a dimensionless quantity used to represent the resistance of an object in motion inside a fluid, such as air or water. The estimation of the drag coefficient is not easy since it may be the sum of several components, like skin friction, form drag or lift-induced drag. It is also directly connected to the shape and orientation of the object, and it varies depending on the fluid velocity, density, and viscosity.

In the literature, for hydrometeors falling through the atmosphere, various experiments were carried out to identify a relationship between the drag coefficient and the particle dimension and/or its terminal velocity. This is necessary since the drag coefficient is the crucial parameter that controls the particle behaviour while falling to the ground, because it directly affects the hydrometeor terminal velocity and its response after a change in wind speed.

The OpenFOAM library contains several drag models, none of which is formulated for raindrops or snow crystals. Therefore, a new model for liquid hydrometeors was added to the source code. The drag coefficient equations were implemented for various ranges of particle Reynolds number as established a priori among those proposed in the literature by Folland (1988) and formulated starting from data published by Beard (1976) and Khvorostyanov and Curry (2005). This model, shown in Equation 5.49, was already adopted, and validated in the work of Cauteruccio et al. (2020) and is here slightly improved by modifying the Reynolds number intervals to adjust the continuity of the drag function over the entire range.

$$C_D = \begin{cases} 2547 & \text{if } Re_p < 0.01 \\ 1.06 \cdot \left(\frac{24}{Re_p} + 2.4 \cdot Re_p^{-0.045} \right) & \text{if } 0.01 \leq Re_p < 2 \\ 1.06 \cdot \left(\frac{24}{Re_p} + 2.64 \cdot Re_p^{-0.19} \right) & \text{if } 2 \leq Re_p \leq 21 \\ 1.06 \cdot \left(\frac{24}{Re_p} + 4.536 \cdot Re_p^{-0.368} \right) & \text{if } 21 < Re_p \leq 320 \\ 0.442 + \frac{72.745}{21.383 + Re_p} & \text{if } Re_p > 320 \end{cases}$$

Analogously, for solid precipitation the drag model formulated for snow crystals by Khvorostyanov and Curry (2005) was implemented in the OpenFOAM source code. The model is detailed in Equation 5.50.

$$CD = \begin{cases} 29.25 \cdot Re_p^{-0.8466} & \text{if } Re_p < 3 \\ 0.7089 + 24.86 \cdot Re_p^{-0.7638} & \text{if } 3 \leq Re_p \leq 720 \\ 0.5967 + 5.928 \cdot Re_p^{-0.4675} & \text{if } Re_p > 720 \end{cases}$$

5.50

The combination of CFD simulations with a suitable LPT model was extensively validated in the work of Cauteruccio (2020) using dedicated experiments after releasing water drops in the wind tunnel and detecting the airflow pattern and the drop trajectories by means of pressure probes, PIV (Cauteruccio et al., 2021a), and image processing from a high-speed camera (Cauteruccio et al., 2021d).

5.4 WIND-TUNNEL MEASUREMENTS

CFD is an incredible tool available to researchers, that allows to tackle fluid dynamics related problems without requiring complex and expensive experimental setup. However, numerical models are often subject to approximations, for example due to grid resolution, or may require simplifying assumptions, for example in the modelling of turbulence. Therefore, experimental validation is often required to ensure that the numerical model is correctly capturing the essential features of the phenomenon.

Various experimental results can be used for validating the numerical model, for example by measuring forces (like lift or drag), pressure or – most often – velocity. In the case of external aerodynamics, the most used experimental setup is the Wind Tunnel (WT). WT are usually closed tubular pipes in which a constant speed flow can be maintained by means of powerful fans, which can be precisely controlled. Inside these tunnels, models or even real objects can be immersed in the flow and then various methods are used to measure and visualize the velocity and pressure fields, evaluating the effects of different wind speeds and configurations. Inside a WT, velocity can be measured by following two main approaches, point measurements, often using pressure probes, and areal measurements, by means of e.g., Particle Image Velocimetry (PIV).

The earliest wind tunnels were invented towards the end of the 19th century, in the early days of aeronautic research, when a lot of efforts were devoted to developing successful heavier-than-air flying machines. With the rapid progress of the aeronautic industry, wind tunnels became the primary instrument for developing innovative technologies. Especially during WWII and the Cold War, enormous wind tunnels were built, capable of fitting even entire aircrafts and in some cases even capable of supersonic speed flow. In more recent years, wind tunnels were also heavily used by the automotive industries and for structural engineering applications. Today, with the rapidly increasing capabilities of modern High-Performance Computing (HPC), the role of wind tunnel experimentation is declining in favour of a CFD approach, but still scaled or real-size experimentation remains indispensable for validating the numerical models.

5.4.1 Probe measurements

The Pitot-static tube is one of the oldest methods used to measure flow velocity and it is still extensively used for aerodynamic measurements. When a body is inserted in the flow of any fluid, the pressure distribution over its surface varies from a maximum at the stagnation point to lowest pressures, possibly close to the static pressure, that is found near the regions where the inclination of the surface of the body is parallel to the free stream. This may not be always true if the flow over bluff bodies separate. A Pitot-static tube, by evaluating the pressure at the stagnation point and the static pressure, can generate accurate velocity measurements when the flow is uniform, and the probe is nearly aligned with the direction of the flow velocity.

Both requirements represent significant limitations for the measurement of the velocity at any point within a flow field. To overcome these limitations, multi-hole pressure probes were developed, which obtain the three-dimensional velocity vector using a careful positioning of the pressure ports over the surface of the immersed body. These probes may have different shapes that suits different needs and can measure a wide range of the flow speed. The number of holes at the tip of the probe, or further back, enables a probe to return the incidence angles with the desired accuracy. The larger the number of holes, the better the accuracy of a probe in detecting the direction of the flow at even large angles of incidence. Roughly Pitot-static probes are limited to incidence angles less than 10 degrees, five-hole probes are limited to 55 degrees and seven-hole probes to 75 degrees. For incidence angles larger than 75 degrees, twelve- or eighteen-hole probes are necessary (Telionis et al., 2009). In Figure 5.3, an example of two pressure probes with a different number of holes is shown.

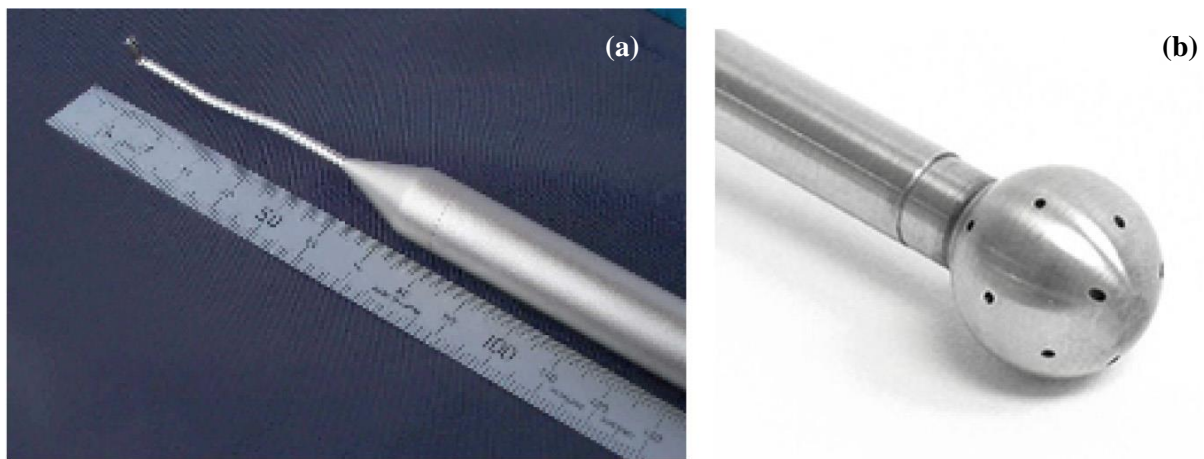


Figure 5.3: Images of multi hole pressure probes, a four-hole “cobra” pressure probe (a) and a twelve-hole “aeroprobe” (b). The first has a limited acceptance cone of 45° while the latter has an acceptance cone of 300° .

5.4.2 Particle image velocimetry

The Particle Image Velocimetry (PIV) is an optical method used to visualize the flow and measure its velocity and direction. A passive tracer, usually smoke, able to follow the streamlines, is injected in the incoming airflow until it is uniformly dispersed in the wind tunnel measurement chamber. A thin beam of light, usually a laser sheet, is then used to illuminate the flow section under investigation and to highlight

the dispersed particles. Using high-speed photography techniques, it is possible to capture two images of the particle positions at very close intervals, that are called pairs. The information is then extracted from the pairs after matching the particles in both images, by using a cross-correlation algorithm that computes the speed and direction (the velocity field) of the flow.

While the method of adding particles or objects to a fluid to observe its flow is likely to have been used from time to time through the ages no sustained application of the method is known. The first use of particles for evaluating flow in a more rigorous manner can be attributed to Ludwig Prandtl, in the early 20th century (Willert & Kompenhans, 2010). The modern particle image velocimetry finds its roots in Laser speckle velocimetry, a technique that several groups began experimenting in the late 1970s. In the early 1980s it was found that it was advantageous to decrease the particle concentration down to levels where individual particles could be observed. Using smaller particles density, researchers noticed that it was easier to study the flow analysing only one small portion of space at a time, using cross-correlation between particles to evaluate their speed and direction. The images of the particles in motion were at first recorded using analogic cameras and required immense amount of computing power, for the time, to be analysed. Also because of the speed limitation of analogic cameras multiple time steps were recorded on the same film, increasing the effort needed for applying cross-correlation techniques. Today, with the introduction of digital camera fast enough to capture multiple images in rapid succession, particle image velocimetry has become extremely popular and is being used in many applications. The typical PIV apparatus consists of a camera, a strobe or laser with an optical arrangement to limit the physical region illuminated, a synchronizer to act as an external trigger, controlling both the camera and the laser, the particles, and the fluid under investigation.

A common problem to PIV measurements is the reflection caused by the surface of the object that can compromise the results, for this reason the models are usually covered with a thin layer of black opaque paint to reduce to a minimum reflection. A mask is also often applied to the result, with the intent of completely suppressing interference near the object walls. This limits the applicability of this approach in the case of NCGs, because their complex shapes would, in most cases, block the laser beam or the camera view close to their sensing area. Also, since PIV is not well suited to measure velocity close to the instrument body, most of the region near the sensing area of these instrument would be discarded from the investigated area.

5.4.3 Experimental campaign in the DICCA wind tunnel

An experimental campaign was conducted in the WT facility available at the Department of Civil, Chemical and Environmental Engineering (DICCA) of the University of Genova for two of the NCGs investigated in this work. The wind tunnel – located in the DICCA laboratory – is a closed-circuit system made of metal carpentry, with a footprint of $8 \times 21\text{m}^2$ and a cross section of the test chamber of $1.35 \times 1.70\text{ m}$. Images of the WT measurement chamber are shown in Figure 5.4.



Figure 5.4: Photos of the measuring section of the DICCA wind tunnel. The cross-section is 1.35×1.70 m and is 8.8 m long. Inside of it a motorized arm can be used to position pressure probes for flow measurement.

The measurement portion of the tunnel has a length of 8.8 m and is divided into two parts, the first section is located at the entrance of the room, 1.5 m downstream of the convergent and is used for measurements in homogeneous flow, being characterized by very low values of the index of turbulence. In this section various types of grids or masks can be inserted to increase the turbulence of the downstream flow. The second section is used mainly for aerodynamic and aeroelastic tests of sectional models of elements and structural portions such as bridge decks, tower blocks or components of industrial buildings. This section is in the terminal part of the test chamber and is equipped with a rotary table used for positioning the models immersed in the flow.

After the measuring sections the tunnel changes from a rectangular cross-section to a circular section, where the fan is located. The fan, the motor, and the flow straightener (stator) are placed on a steel base with dampening pads and the base is anchored to a rigid foundation made of reinforced concrete, isolated from the rest of the pavement. The fan, with a maximum speed of 900 rev/min, is controlled by a frequency converter that allows to continuously adjust the speed in the test chamber with accuracy of $\pm 0.1 \text{ m s}^{-1}$. The reference speed of the flow inside the tunnel is detected by means of a Pitot static tube positioned near the roof of the test chamber, upstream of the section engaged by the model, in an undisturbed region of the flow. The kinetic pressure is obtained as the difference between the total pressure and the static pressure and is measured by a differential pressure gauge. The value of the air density used to convert the kinetic pressure measurement into the corresponding velocity value is assessed based on the air temperature measured in the test chamber.

6 SYNTHESIS OF TRANSFER FUNCTIONS FOR CGs

Regarding traditional CGs, literature extensively reports of the wind-induced bias observed when comparing precipitation measurements from multiple locations having wind climatology differences (Pollock et al., 2018) and between shielded and unshielded instrument configurations (see e.g., Duchon and Essenberg, 2001; Colli et al., 2016a,b). The impact of the resulting bias on derived variables was also recognised and documented e.g., by Rodda and Smith (1986) who noted that the deposited acidity values of precipitation can be larger by up to 20% and more than those reported based on the UK standard gauge measurements in case of wind. Duchon and Essenberg (2001) reported a mean undercatch bias of 4% after comparing pit and aboveground low-elevation rain gauges with and without wind shields. Muchan and Dixon (2019) found a magnitude of the undercatch bias equal to 12.7% in a field test study, while Utsumi et al. (2008) reported an increase of daily precipitation of about 10% after accounting for the wind-induced undercatch in a nation-wide rainfall climatology study in Japan.

The wind induced bias on CGs is even more relevant if solid precipitation is considered. Yang et al. (1999) presented experimental results for the Hellmann non-recording gauge obtained at four different stations in Finland, Russia, Germany, and Croatia, with percentage undercatch biases of about 10% for liquid-, 25% for mixed- and 50% for solid precipitation. Rasmussen et al. (2012) and Colli et al. (2015) show collection losses for solid precipitation up to 70-80% from a field site in Colorado, US. The extensive, multiple site campaign of the Solid Precipitation Intercomparison Experiment (SPICE) – held by the WMO – reported of a large impact of wind on the measured solid precipitation with an estimated undercatch approaching 80% in the wind speed range between 4 and 6 m/s (Nitu et al., 2018). Masuda et al. (2019) applied different adjustment methods to the mean monthly precipitation yielding an increase in the winter (December–February) precipitation amount in Japan by 12.7%, while the bias in the annual hydrological balance was reduced from 33% to 26% over the mountainous terrain.

To mitigate the impact of wind induced bias on precipitation measurements, adjustments to account for the wind-induced bias have been proposed in the literature, mostly based on in-field and/or wind tunnel experiments (see e.g., Wolff et al., 2015; Mueller and Kidder, 1972) and numerical simulation (see e.g., Nešpor and Sevruk, 1999; Theriault et al., 2012). To adjust the measured precipitation and match the amount that would be measured by a reference installation under the same wind conditions, various transfer functions were also developed (see e.g., Kochendorfer et al., 2018). The transfer functions proposed within the WMO SPICE and more recent follow-up developments are described in Kochendorfer et al. (2022) and the references therein. Chubb et al. (2015) applied different transfer functions to a series of precipitation measurements in Australia with improvements between 3 and 52% over the unadjusted precipitation. Smith et al. (2022) applied transfer functions limited to undercatch values of 50 to 60% to accumulated precipitation measurements at the hourly scale in a Canadian nationwide study.

However, a comprehensive assessment of the performance of the most common and commercially available instruments for both liquid and solid precipitation is still lacking due to the difficulty of testing the instruments in the field under a variety of instrument shape, precipitation intensity and wind speed combinations. These are indeed hardly observed within (even long-term) in-field experimental campaigns

due to the specific local climatology of any single test site. Numerical simulation of the wind-induced measurement bias based on Computational Fluid Dynamics (CFD) and particle tracking is a viable solution to overcome such difficulties (see e.g., Folland, 1988; Nešpor and Sevruck, 1999; Theriault et al., 2012; Colli et al., 2016a,b), although comprehensive studies involve a significant computational burden. A detailed comparison of numerical results for instruments with various outer shapes was proposed by Colli et al. (2018) but the study was limited to the analysis of their aerodynamic performance, with no quantitative information about the associated measurement bias.

To provide a baseline reference of the performance of commercially available CGs commonly deployed by NMHSs, here a comparison between six different precipitation measurement instruments is presented. CFD numerical simulations are used both to investigate the aerodynamic interaction between the gauge body and the wind, while a LPT model is used to evaluate the impact on the trajectories of incoming hydrometeors. This study focuses on the following six rain gauge models, chosen among the most widely diffused, and featuring the typical geometrical shape of their outer body. As an example of cylindrical gauges the CAE PG10 and the Lambrecht rain[e]H3 were chosen, the first having a large diameter collector while the latter is quite compact. Representing the gauges with a chimney shape both the Geonor T-200B and the OTT Pluvio2 were tested, due to them presenting a quite different geometry of the collector rim. Finally, more aerodynamic gauges were also considered, the EML SBS500 with an inverted conical shape and the AES Nipher that is a shielded gauge.

6.1 MESHING AND FLUID DYNAMIC SETUP

Simulations are run using the time-independent approach, for which a numerical model of each of the instruments considered, including their supporting pole, was realised in the Standard Triangulation Language (STL) format. The computational mesh was produced within OpenFOAM, for a 5 m long, 3 m wide, and 2.5 m high simulation domain. All instruments are radially symmetric. The longitudinal axis (X) of the computational mesh is set parallel to the wind direction, the vertical axis (Z) is directed upward, while the Y axis is normal to the (X, Z) plane. The origin of the reference system is along the instrument symmetry axis and positioned at the quote of the collecting area of each gauge. The internal mesh has a maximum cell size of 0.125 m and is progressively refined up to 2.5 mm near the instrument walls to correctly reproduce the surface curvature and geometric details of the gauge body. Six wind speed values (U_{ref}) equal to 2, 5, 10, 15, and 20 m/s were tested for each instrument.

For the gauge geometries investigated, the final meshes contains between three and six million cells, depending on the size of the instrument, and the values of typical mesh size and quality parameters, including the non-orthogonality, skewness, and aspect ratio, are listed in Table 6.1. These are used to identify highly distorted cells that could affect the solution and their value should be as low as possible. In Table 6.1, the parameters for all meshes are shown to fall inside the range that is considered acceptable for external aerodynamic simulations.

A sample (X, Z) section of the mesh at $Y = 0$ is presented, for two of the five gauge considered, in Figure 6.1.

Table 6.1: Mesh size and quality parameters for the six gauges investigated.

Gauge	Collector area [cm ²]	n° Cells	Avg. Non-orthogonality	Max Non-orthogonality	Max Skewness	Max Aspect ratio
CAE PG10	1000	5263038	64.85	6.46	4.61	21.37
Lambrecht rain[e]H3	200	5869672	64.45	6.20	1.97	22.73
Geonor T-200B	200	5607023	64.53	6.64	3.99	18.04
AES Nipher	200	2858560	64.38	6.31	3.38	18.42
OTT Pluvio ²	500	3438901	64.63	6.37	3.45	20.48
EML SBS500	150	5835018	63.70	6.99	3.19	20.80

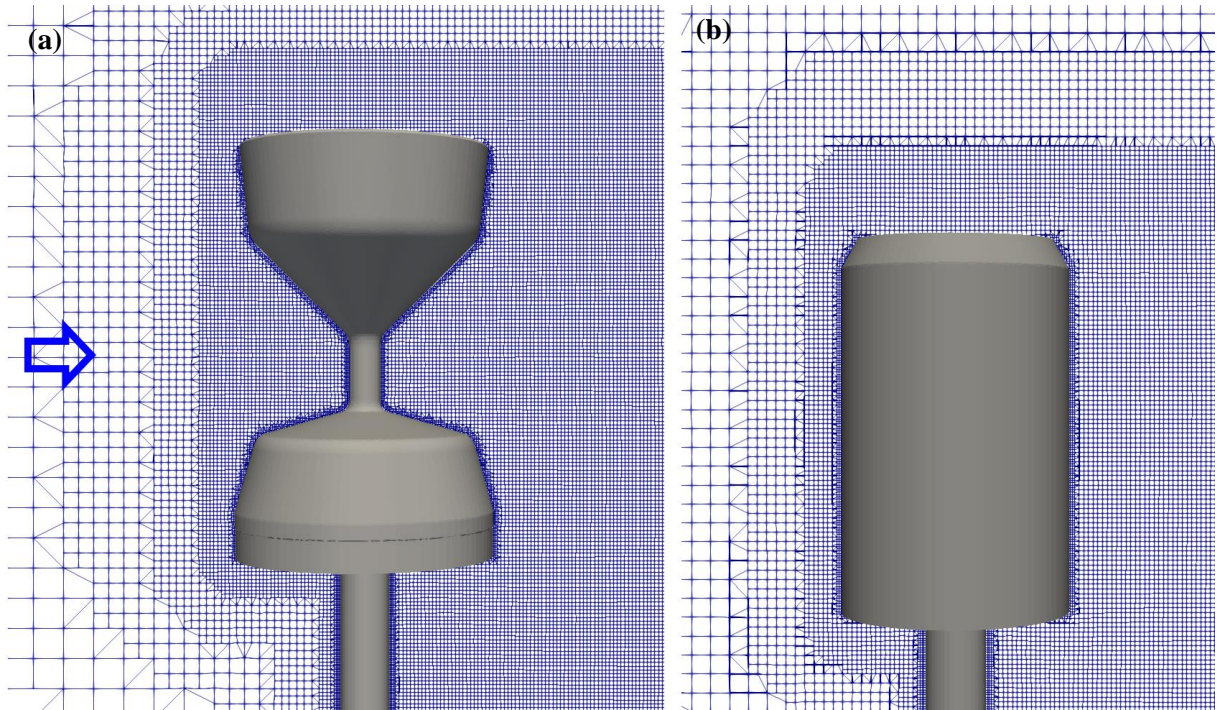


Figure 6.1: The computational mesh along the longitudinal cross-section of the domain around the EML SBS500 at $Y = 0$ (a) and around the Lambrecht rain[e]H3 (b). The arrow indicates the direction of the incoming undisturbed wind flow.

6.2 CFD SIMULATION RESULTS

CFD simulation results are shown in terms of maps of the normalized magnitude and vertical component of the flow velocity (indicated with $U_{\text{mag}}/U_{\text{ref}}$ and U_z/U_{ref} , respectively) and maps of the normalized turbulent kinetic energy (k/U_{ref}^2).

As a sample of the large numerical dataset obtained from CFD simulations for the different gauges, wind velocity maps in the (X, Z) section of the flow field at $Y=0$, for $U_{\text{ref}} = 10$ m/s are presented for each gauge

in Figures 6.2 to 6.7, for the CAE PG10, Geonor T-200B, Lambrecht rain[e]H3, AES Nipher, OTT Pluvio² and EML SBS500 gauge, respectively. In the left-hand panels, the red zones indicate a larger flow velocity than the undisturbed wind speed, therefore $U_{\text{mag}}/U_{\text{ref}} > 1$, while in the blue zones the flow velocity is lower than the undisturbed wind, and $U_{\text{mag}}/U_{\text{ref}} < 1$. In the right-hand panels, the red zones indicate upward flow velocity components, with $U_z/U_{\text{ref}} > 0$, while downward components occur in the blue zones, where $U_z/U_{\text{ref}} < 0$.

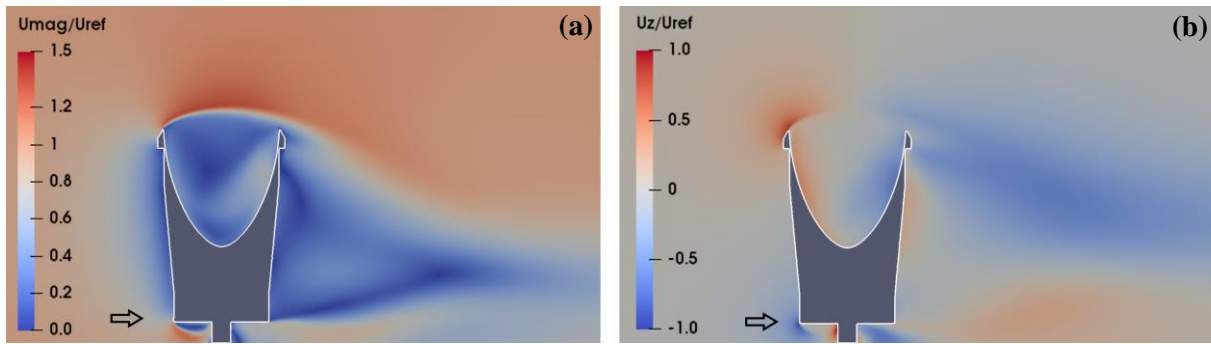


Figure 6.2: CFD simulation for the CAE PG10 gauge at $U_{\text{ref}} = 10$ m/s; maps of the normalized magnitude $U_{\text{mag}}/U_{\text{ref}}$ (a) and vertical component U_z/U_{ref} (b) of the flow velocity, along the (X, Z) section of the flow field at $Y = 0$. The small arrow indicates the undisturbed flow direction.

In Figure 6.2, a strong separation layer is evident over the instrument collecting area, with strong recirculation inside the instrument collector, due to the low position of the separation layer, that “closes” at the downwind edge. Strong updraft is also evident in the first half of the instrument collecting area while in the downwind half downdraft is prevalent. Strong turbulence is generated below the separation layer and inside of the gauge body, further than in its wake (see Figure 6.8a).

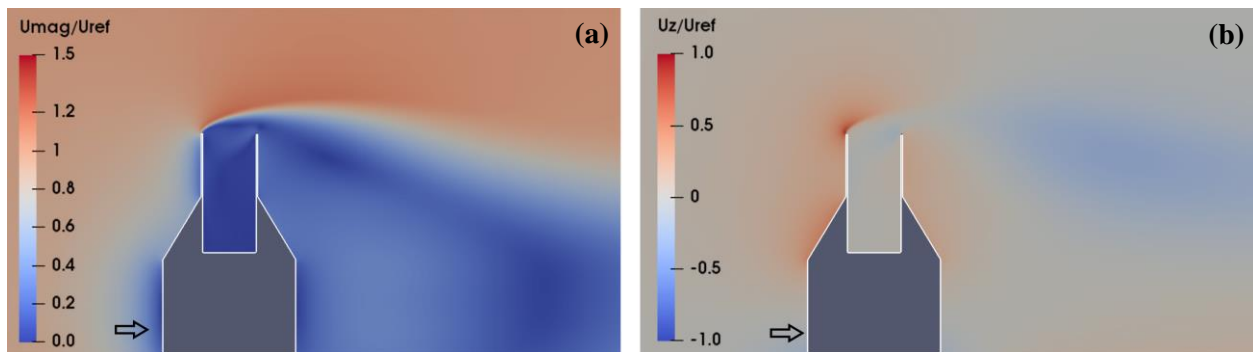


Figure 6.3: CFD simulation for the Geonor T-200B gauge at $U_{\text{ref}} = 10$ m/s; maps of the normalized magnitude $U_{\text{mag}}/U_{\text{ref}}$ (a) and vertical component U_z/U_{ref} (b) of the flow velocity, along the (X, Z) section of the flow field at $Y = 0$. The small arrow indicates the undisturbed flow direction.

Figure 6.3 shows that in the case of the Geonor T-200B, the separation layer is angled upward and away from the instrument body. No significant recirculation occurs inside of the instrument collector, also due to the position of the separation layer. Strong updraft is evident upstream of the instrument and propagates

above the whole instrument collecting area. No appreciable downdraft is instead observed. Strong turbulence develops over the whole collecting area, being however quite low in the wake (see Figure 6.8b).

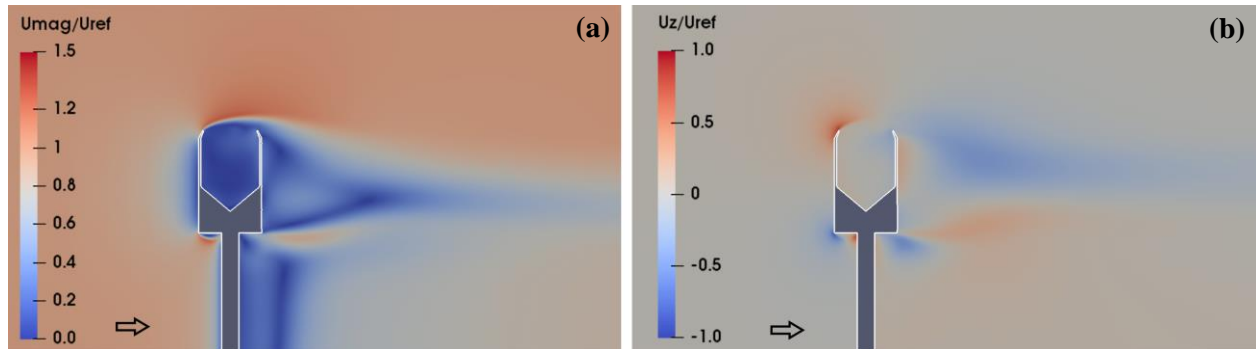


Figure 6.4: CFD simulation for the Lambrecht rain[e]H3 gauge at $U_{ref} = 10$ m/s; maps of the normalized magnitude U_{mag}/U_{ref} (a) and vertical component U_z/U_{ref} (b) of the flow velocity, along the (X, Z) section of the flow field at $Y = 0$. The small arrow indicates the undisturbed flow direction.

In Figure 6.4, the separation layer remains close to the instrument, similarly to the case of the CAE, but, due to the collector shape, no significant recirculation occurs inside of the gauge body. Strong updraft is present upstream of the gauges and propagates over its collecting area for about two thirds of its length, then switching to downdraft. Relevant turbulence develops over the instrument collecting area and in its wake (see Figure 6.8c).

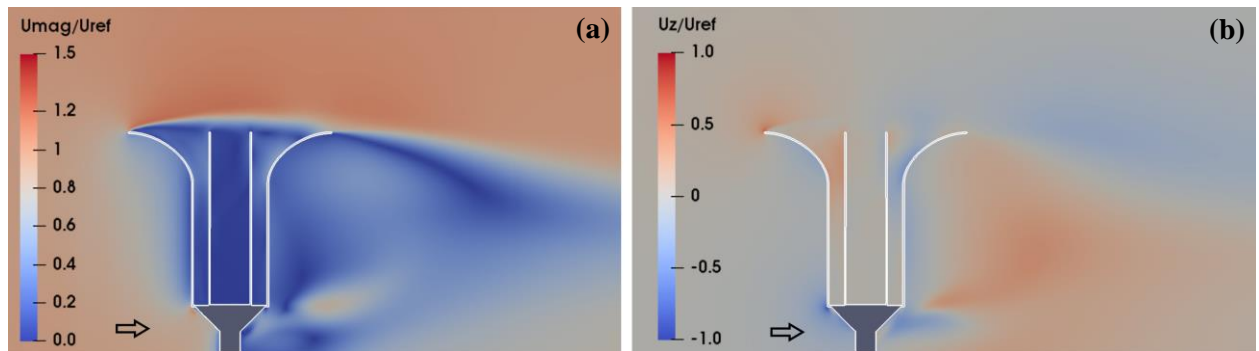


Figure 6.5: CFD simulation for the AES Nipher shield at $U_{ref} = 10$ m/s; maps of the normalized magnitude U_{mag}/U_{ref} (a) and vertical component U_z/U_{ref} (b) of the flow velocity, along the (X, Z) section of the flow field at $Y = 0$. The small arrow indicates the undisturbed flow direction.

Figure 6.5 shows the aerodynamic behaviour of the AES Nipher, which is equipped with an integrated wind shield. The separation layer tends to reattach towards the end of the shield and presents a lower overall flow velocity. No recirculation is visible inside of the collecting area (the innermost part). Weak updraft is present upstream of the gauge and decays along its collecting area where, after the midpoint, it is replaced by weak downdraft. Strong updraft is instead evident in the wake of the gauge. Despite lower flow velocity, turbulence is quite high and distributed over the whole instrument, especially in its wake (see Figure 6.8d).

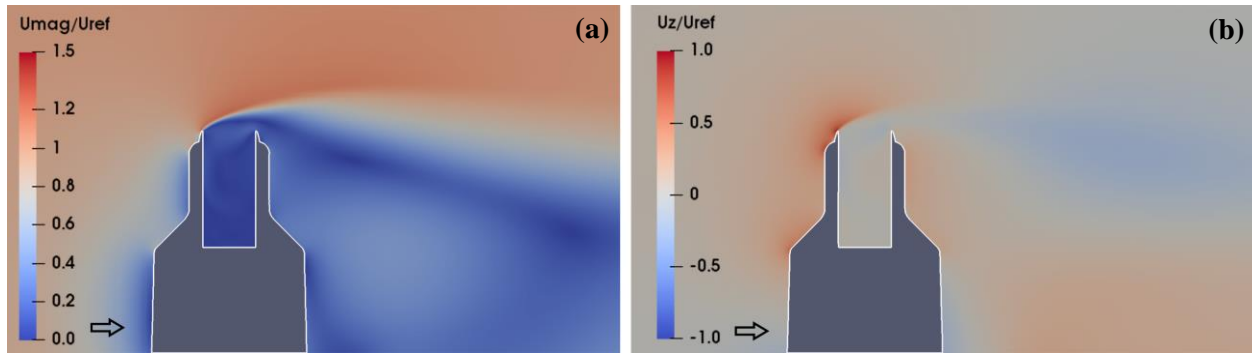


Figure 6.6: CFD simulation for the OTT Pluvio² gauge at $U_{ref} = 10$ m/s; maps of the normalized magnitude U_{mag}/U_{ref} (a) and vertical component U_z/U_{ref} (b) of the flow velocity, along the (X, Z) section of the flow field at $Y = 0$. The small arrow indicates the undisturbed flow direction.

Figure 6.6 shows that the OTT Pluvio² behaves very similar to the Geonor T-200B, with a separation layer that is angled upward and away from the instrument body. No significant recirculation occurs inside of the instrument collector while very strong updraft is evident upstream and propagates over the whole instrument collecting area. A very limited amount of downdraft occurs below the separation layer. Turbulence is slightly lower than for the Geonor T-200B, but its distribution over the whole collecting area is identical (see Figure 6.8e).

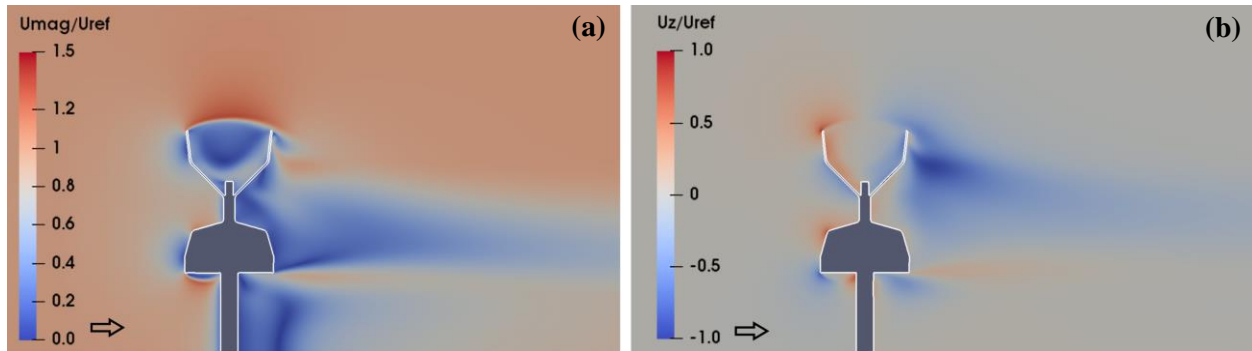


Figure 6.7: CFD simulation for the EML SBS500 gauge at $U_{ref} = 10$ m/s; maps of the normalized magnitude U_{mag}/U_{ref} (a) and vertical component U_z/U_{ref} (b) of the flow velocity, along the (X, Z) section of the flow field at $Y = 0$. The small arrow indicates the undisturbed flow direction.

In Figure 6.7 another aerodynamic gauge is shown, in this case due to the shape of its body. The separation layer is very close to the instrument and closes over the collector. Due to this fact, recirculation occurs inside the collector area. Updraft is still present upstream of the gauge, but with lower intensity (even still higher than for the AES Nipher gauge). After the mid-point of the collector, updraft is replaced by downdraft, which becomes progressively stronger while proceeding downstream and reaches its maximum in the wake of the gauge. Low turbulence develops over the instrument collecting area, below the separation layer, but the gauge presents high turbulence intensity in its wake (see Figure 6.8f).

The turbulence intensity maps, shown in Figure 6.8 for the gauges here investigated, confirm that their shape strongly influences the development of turbulence over their collecting area.

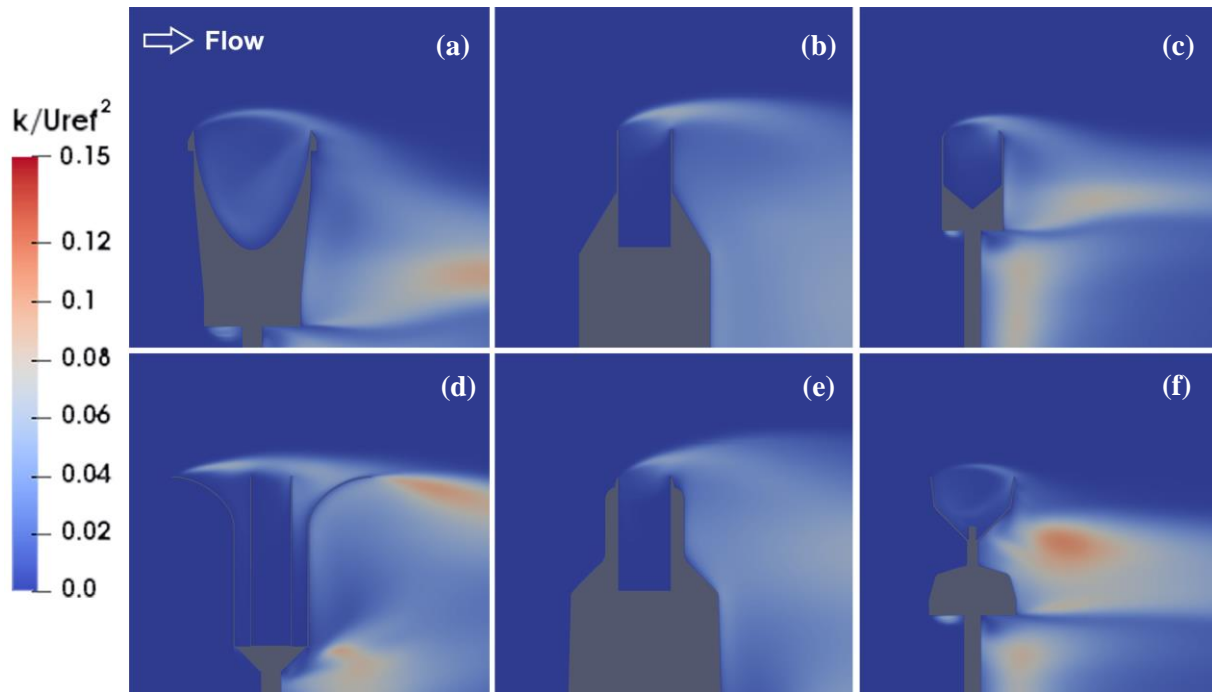


Figure 6.8: Maps of the normalized turbulent kinetic energy (k/U_{ref}^2) from CFD simulations at $U_{ref} = 10$ m/s along the (X, Z) section of the flow field at $Y = 0$ for The CAE PG10 (a), Geonor T-200B (b), Lambrecht rain[e]H3 (c), AES Nipher (d), OTT Pluvio² (e) and EML SBS500 (f).

Furthermore – to better compare instruments – a synthetic representation of their aerodynamic behaviour is presented in Figure 6.9. Where the longitudinal profile of the position of the maximum value of the normalized flow velocity magnitude (U_{mag}/U_{ref}) above the instrument collector is reported. Results are colour coded according to its numerical value. The entire profile for the shielded gauge (AES Nipher) is far above the collector (always more than half a diameter) with very low values of the maximum velocity (that remains always less than 15% above the U_{ref}), implying a limited impact on the hydrometeor trajectories. The two chimney shaped instruments (Geonor T-200B and OTT Pluvio²) also show relatively low maximum velocity patterns (about 20% higher than U_{ref}), but their profiles start at very low elevation and increase with the longitudinal coordinate while increasing the velocity as well, reaching a higher elevation at the downwind edge of the collector than all other instruments, yielding a strong deflection of the hydrometeor trajectories.

The inverted conical instrument (EML SBS500) initially shows a similar pattern, but with a slightly larger velocity, about 30% higher than U_{ref} , in the central part of the profile and a lower elevation at the downstream edge, with an expected positive impact on the hydrometeor trajectories. The two cylindrical instruments are quite different from each other, with the CAE PG10 showing the strongest velocity pattern (up to about 33% higher than U_{ref}), which spans for most part of the profile above the instrument collector, yielding a sustained effect on the falling hydrometeors. The maximum velocity profile for the Lambrecht rain[e]H3 mimics the one of the EML SBS500 above the first half of the collector, but with much lower

velocity values (approximately 25% higher than U_{ref}), then rises to reach the same value of the CAE PG10 at the downstream edge.

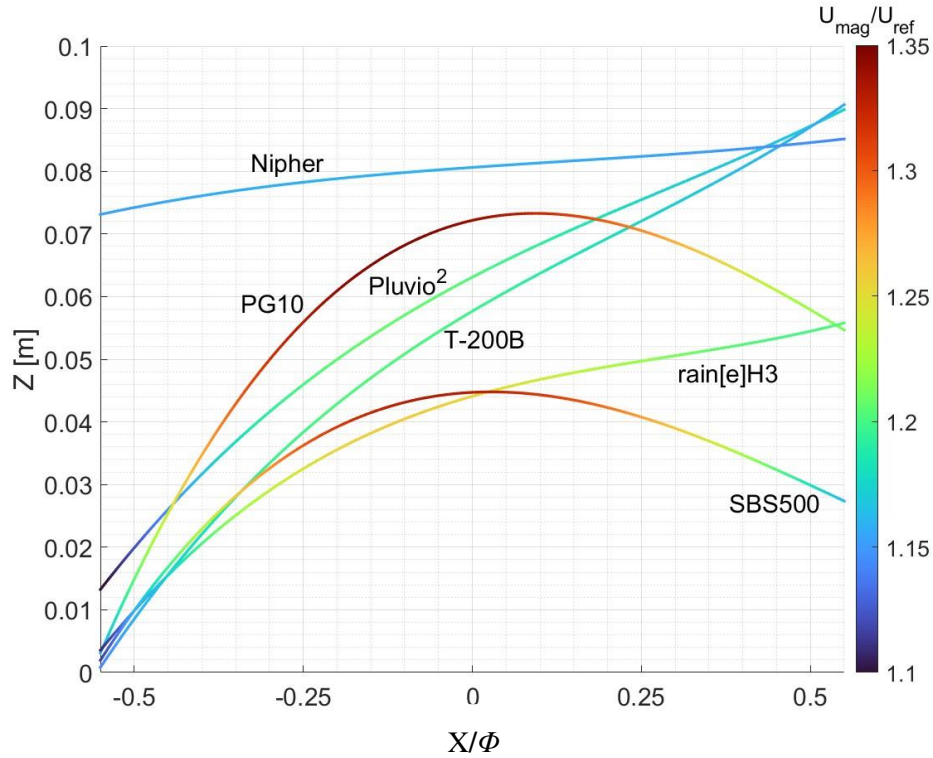


Figure 6.9: Longitudinal profiles of the position of the maximum non-dimensional airflow velocity U_{mag}/U_{ref} over the collector of the investigated instruments, colour coded according to the associated numerical value and obtained from numerical simulation performed at $U_{ref} = 5 \text{ m s}^{-1}$.

In Figure 6.10, the vertical profiles of the normalized vertical velocity (U_z/U_{ref}) at the upstream edge ($X/\Phi = -0.5$) and at the centre ($X/\Phi = 0$) of the collector are reported, where Φ is the collector diameter. The AES Nipher gauge has a very limited updraft at the collector's edge, which even reverse into a slight downdraft component at the centre of the collector, appearing optimal in terms of catching performance. The two chimney shaped gauges (Geonor T-200B and OTT Pluvio²), indicated with solid black and grey lines, show very strong updraft components at both longitudinal sections, with significant values even at the centre of the collector. This results into a continued, sustained uplift effect on the falling hydrometeors enhancing the diversion from their undisturbed trajectory. The EML-SBS500 shows the least updraft at the edge of the collector after the AES Nipher and a nearly null updraft at the centre of the collector, foreshadowing a very limited impact on the hydrometeor trajectories. The two cylindrical instruments (CAE PG10 and Lambrecht rain[e]H3) show opposite behaviour, with the CAE PG10 having the strongest updraft among all instruments at the collector's edge, while the updraft at the centre of the collector is larger for the Lambrecht rain[e]H3, yielding an inconclusive assessment of the impact on the hydrometeor trajectories. Differences in the aerodynamic behaviour of the two cylindrical gauge is mainly ascribable to the protruding rim mounted on the CAE PG10. The role of the rim is confirmed by the difference in the

aerodynamic behaviour of the two chimney shaped gauges, since their geometries differ to each other mainly for the presence of a shaped rim in the OTT Pluvio².

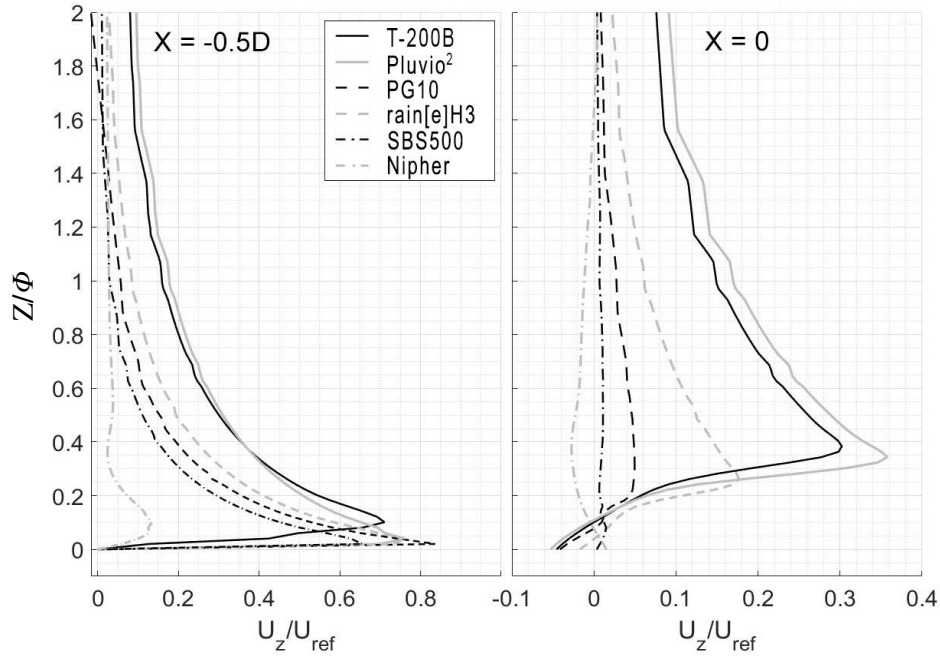


Figure 6.10: Vertical profiles of the non-dimensional vertical velocity U_z/U_{ref} over the upstream edge of the collector (left-hand panel) and in its centre (right-hand panel) of the six investigated instruments, obtained from numerical simulation performed at $U_{ref} = 5 \text{ m s}^{-1}$.

6.3 PARTICLE TRAJECTORIES

Since in the approach used in this work particle to particle interaction is neglected, hydrometeors are inserted in the domain along a regular grid, with variable dimension and spacing. Grids used are based on the gauge orifice diameter (Φ), grid spacing is about 1.5% of Φ , rounded to the closest 0.5 mm, while the grid is 2Φ wide and 4.5Φ long to ensure that all possible trajectories that could potentially cross the instrument sensing area are considered. Both the position of the centre of the rectangle and its height is computed by solving, for a single hydrometeor, the equation of motion, to compute the fall distance and horizontal travel in an undisturbed velocity field. The grid is then positioned in space so that it is at least 0.05 m away from the domain boundaries and, under a uniform velocity field, the trajectory starting from its centre would reach the plane $Z = 0$ at 1.25Φ before the centre of the instrument collecting area. The grid has more particles upstream of the gauge since those are the ones most likely to fall inside the gauge collecting funnel.

Liquid precipitation was modelled by considering 11 equivalent diameters, 0.25 mm, 0.5 mm, 0.75 mm and from 1 to 8 mm at 1 mm increments. The hydrometeors density ρ was set equal to 1000 kg/m^3 .

The numerical model of the instrument was separated at the collecting funnel by creating an internal and an external surface in the mesh. For each particle impacting these two surfaces, the relative information is saved separately for future post-processing, including the individual trajectories. Simulations are stopped

after all particles impacted on a surface or exited the domain or fell below significantly below the $Z = 0$ plane.

Trajectories of incoming hydrometeors of two different diameters are presented in Figures 6.11 to 6.16.

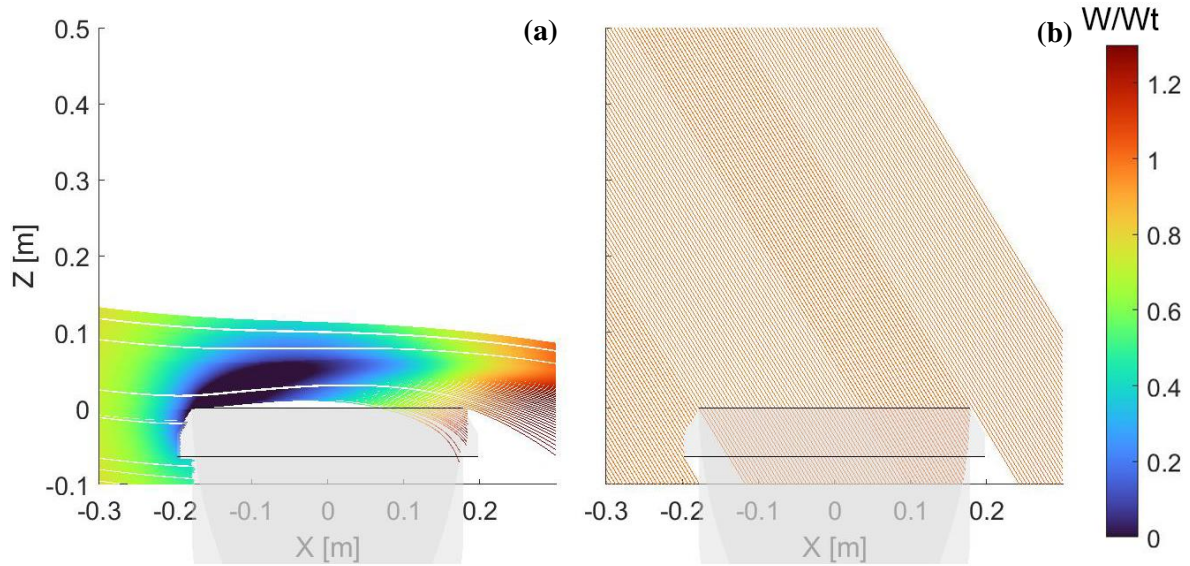


Figure 6.11: Drop trajectories along the $y=0$ plane, for the CAE PG10 gauge, at $U_{ref} = 5$ m/s and for two drop diameters, 0.25 mm (a) and 3 mm (b). Colour coding is used to show the fall velocity.

Figure 6.11 shows that for the CAE PG10 gauge, the updraft upstream of the instrument collector strongly affect small-size drops (Figure 6.11a), which reduce their fall velocity to zero or even negative values over the instrument collecting area. These fall velocity changes make deviate the incoming trajectories out of the instrument funnel, while large hydrometeors (Figure 6.11b) are mostly unaffected.

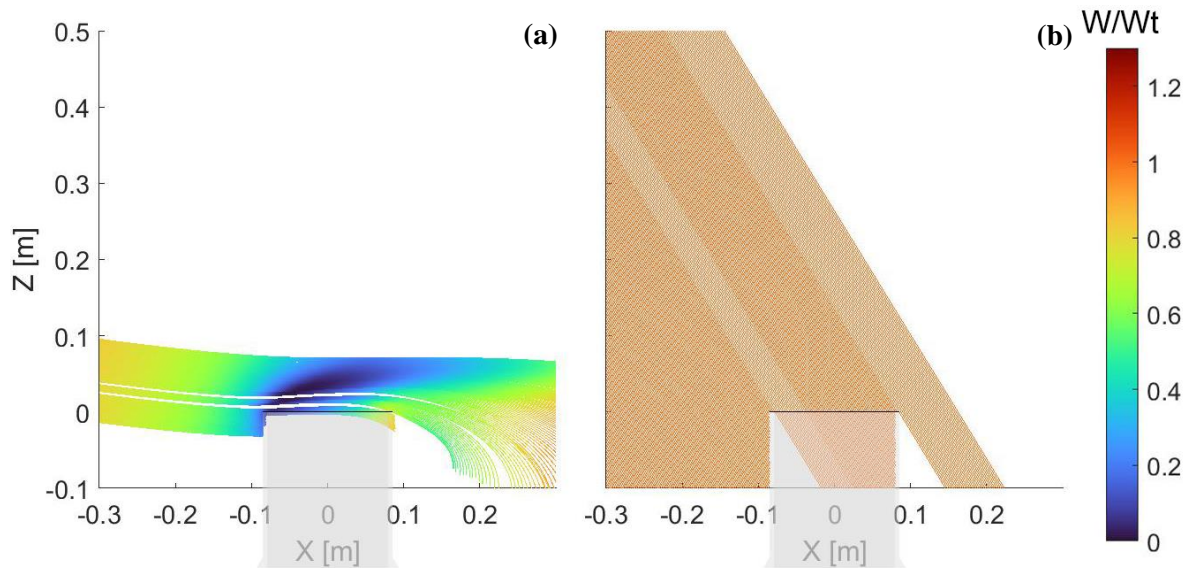


Figure 6.12: Drop trajectories along the $y=0$ plane, for the Geonor T-200B gauge, at $U_{ref} = 5$ m/s and for two drop diameters, 0.25 mm (a) and 3 mm (b). Colour coding is used to show fall velocity.

Figure 6.12 shows that in the case of the Geonor T-200B gauge, the zone affected by the updraft is smaller, but still affects small-size drops (Figure 6.12a). Furthermore, the combination of small diameter and strong updraft diverts even more trajectories to fall outside of the collecting area. Large hydrometeors (Figure 6.12b) are again mostly unaffected.

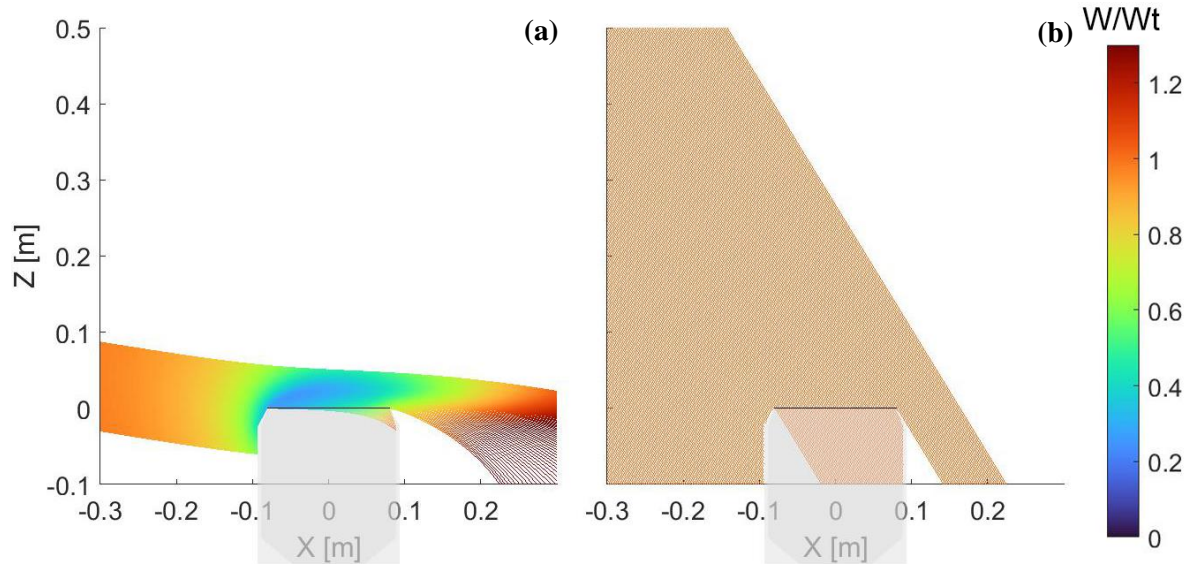


Figure 6.13: Drop trajectories along the $y=0$ plane, for the Lambrecht rain[e]H3 gauge, at $U_{ref} = 5$ m/s and for two drop diameters, 0.25 mm (a) and 3 mm (b). Colour coding is used to show fall velocity.

Results for the Lambrecht rain[e]H3 gauge are presented in Figure 6.13, where much lower updraft is observed, with small size drop trajectories being not strongly deviated (Figure 6.13a) but still significantly affected. Trajectories of larger drops (Figure 6.13b) are again mostly unchanged.

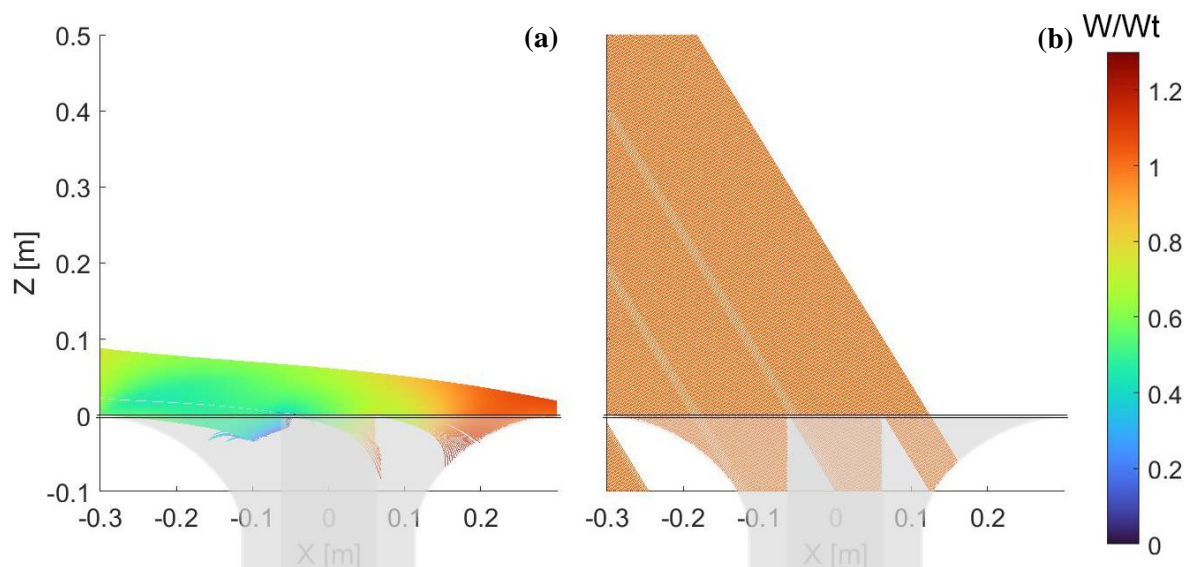


Figure 6.14: Drop trajectories along the $y=0$ plane, for the AES Nipher gauge, at $U_{ref} = 5$ m/s and for two drop diameters, 0.25 mm (a) and 3 mm (b). Colour coding is used to show fall velocity.

The Nipher gauge results are shown in Figure 6.14, where the aerodynamic performance of such gauge is evident. The fall velocity of small-size drops (Figure 6.14a) is significantly less affected, and the number of trajectories diverted outside of the collector is still significant but largely reduced. Trajectories of larger drops (Figure 6.14b) are again nearly unaffected.

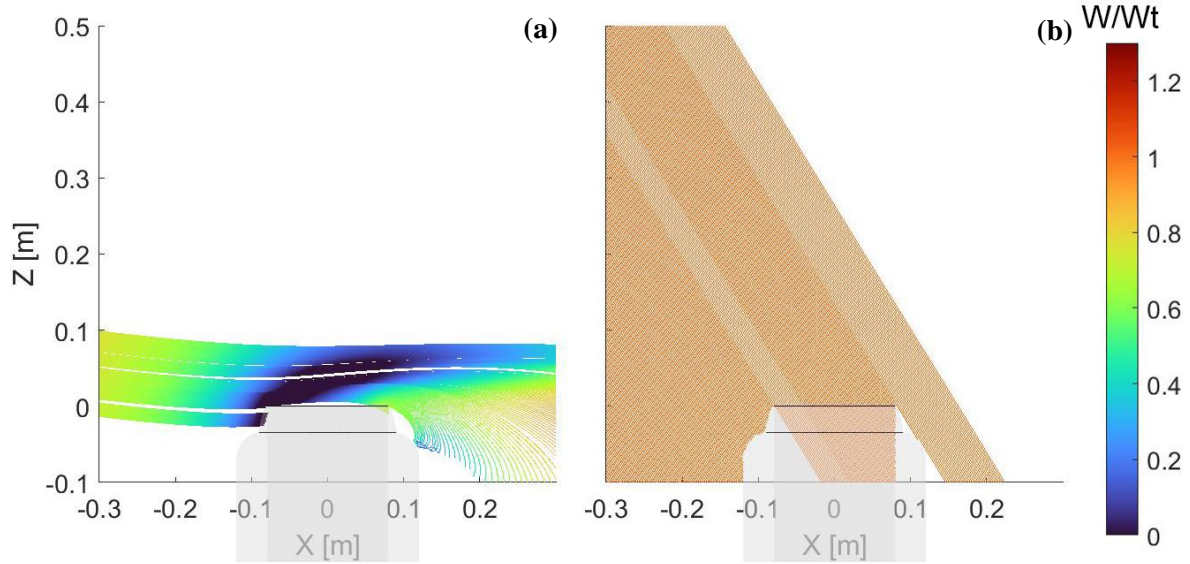


Figure 6.15: Drop trajectories along the $y=0$ plane, for the OTT Pluvio² gauge, at $U_{ref} = 5$ m/s and for two drop diameters, 0.25 mm (a) and 3 mm (b). Colour coding is used to show fall velocity.

Particle tracking results for the OTT Pluvio², shown in Figure 6.15, are very similar to those presented above for the Geonor T-200B (see Figure 6.12), due to the similar geometric features, but with higher updraft and consequently a larger number of diverted trajectories for the small-size drops (Figure 6.15a).

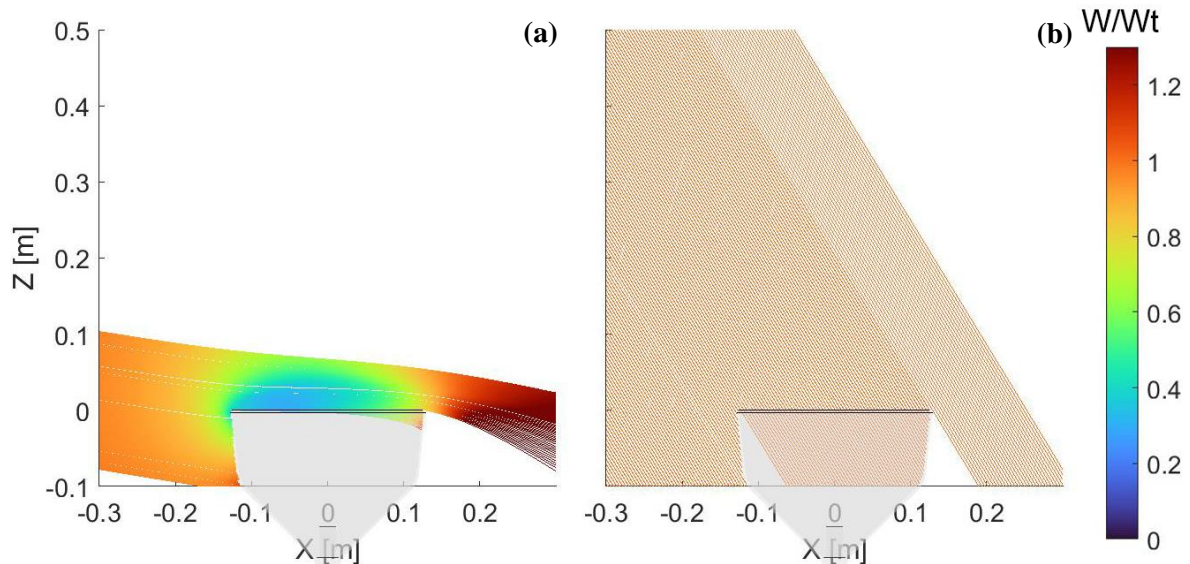


Figure 6.16: Drop trajectories along the $y=0$ plane, for the EML SBS500 gauge, at $U_{ref} = 5$ m/s and for two drop diameters, 0.25 mm (a) and 3 mm (b). Colour coding is used to show fall velocity.

Figure 6.16 shows particle tracking results for the EML SBS500 gauge, an aerodynamic gauge with a typical hourglass geometry. The fall velocity of small-size drops (Figure 6.16a) are less affected, like in the case of the Nipher gauge. The number of small size drops falling outside of the funnel is however still significant, while larger drops are again unaffected.

As example of the considered gauges performance, the deflection of the trajectories of a sample particle (a single raindrop with diameter 0.25 mm) is shown in Figure 6.17a for an undisturbed wind velocity $U_{\text{ref}} = 5 \text{ m s}^{-1}$. Comparison of the fate of a single drop starting from a fixed normalized position ($X/\Phi = -2$, $Y/\Phi = 0$, $Z/\Phi = 0.25$) upstream of the collector within the disturbed airflow field produced by each investigated instrument is provided. The evolving slope of the trajectory $S = dZ/dX$, normalized with the slope at the starting position S^* , is also reported in Figure 6.17b to better highlight the deviation from the undisturbed trajectory, which is expected to have $S/S^* = 1$.

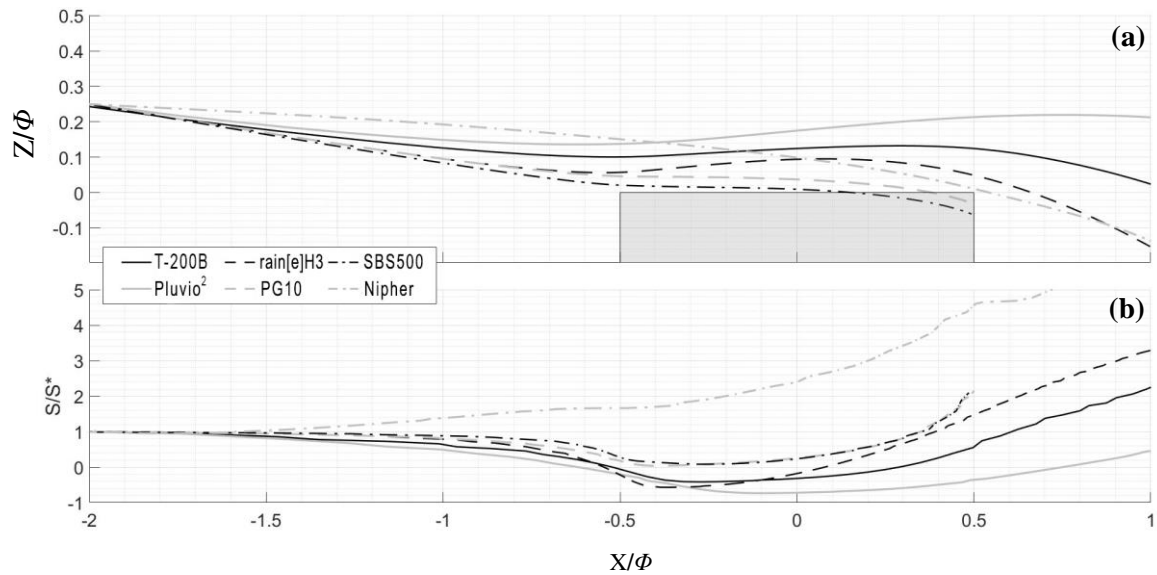


Figure 6.17: Trajectories of a water drop starting from the normalized fixed position ($X/D = -2$, $Y/D = 0$, $Z/D = 0.25$) within the airflow field induced by the investigated gauges (a) and local slope along each trajectory (b), normalized with the slope at the starting position.

In Figure 6.17a, the most deviated trajectories are those aiming at the collector of the two chimney shaped instruments (Geonor T-200B and OTT Pluvio²), with the OTT Pluvio² underperforming all other instruments, while the less deviated is the one aiming at the shielded instrument (AES Nipher). Note that, since it is normalized with the collector's diameter, the initial slope of the trajectories starting in the same normalized position is not the same for all instruments. The drop aiming at the EML SBS500 instrument is deviated very late along its trajectory, close to the collector and only slightly. The two cylindrical instruments show a different behaviour, with the Lambrecht rain[e]H3 experiencing a limited and late deviation, while the CAE PG10 is significantly deviated similarly to the chimney shaped instruments. Note, however, that the latter instrument has the largest collector's diameter, therefore the normalization adopted in the graph visualizes a reduced deviation than the chimney shaped instruments, while the actual deviation is substantially larger.

For this reason, Figure 6.17b is also provided, where the normalized slope of each trajectory is reported. Values lower than unity indicate an upward deviation of the drop trajectory, meaning that significant updraft is reducing the fall velocity of the drop, while accelerated flow is increasing the longitudinal velocity. When the normalized slope reaches its minimum value and starts to increase, the drop trajectory is aiming downward by recovering the contribution of the gravity acceleration, which is less evidently counteracted by the airflow velocity components. All instruments show this effect, which starts early for the AES Nipher, with normalized slope always larger than unity (because of the large size shield), while it is mostly evident above the downstream half of the collector for all other instruments. Note that the downward slope of the trajectory is recovered very late for the two chimney shaped instruments (Geonor T-200B and OTT Pluvio²) and mainly beyond the edge of the collector, too late to significantly contribute to drop collection. The trajectory aiming at the CAE PG10 has a similar behaviour, with both an earlier upward deviation and an earlier downward deviation. The normalized slope curves for the EML SBS500 and the Lambrecht rain[e]H3 are very close to each other (about superimposed in the graph), reflecting very close performance.

6.4 OVERALL CATCH RATIO

For each instrument geometry, given the size of the incoming hydrometeor, numerical simulation allows computing the Catch Ratio (CR) as a function of the wind speed. The CR is defined as the ratio between the number of hydrometeors that are collected by the instrument under the effect of wind and the number of hydrometeors that would have been collected if the instrument was transparent to the wind. The CR is independent on the local climatic characteristics and is therefore representative of the aerodynamic behaviour of the specific instrument geometry alone, with respect to individual hydrometeors.

In Figures 6.18, numerical CR values (symbols) are reported for drops of sample diameters. As expected, the investigated instruments show a similar behaviour, where the CR values decrease with increasing the wind speed and decreasing the equivolumetric particle diameter (D) (from circles to diamonds in the graphs). The rate of decrease depends on the instrument geometry but is also a function of the particle size, with the CR values of small size particles decreasing more abruptly than those of large size particles. This is due to the larger influence of wind on the small-size light particles, which have a lower Stokes number and therefore tend to more closely follow the flow streamlines, having their fall velocity affected by the aerodynamic behaviour of the instrument.

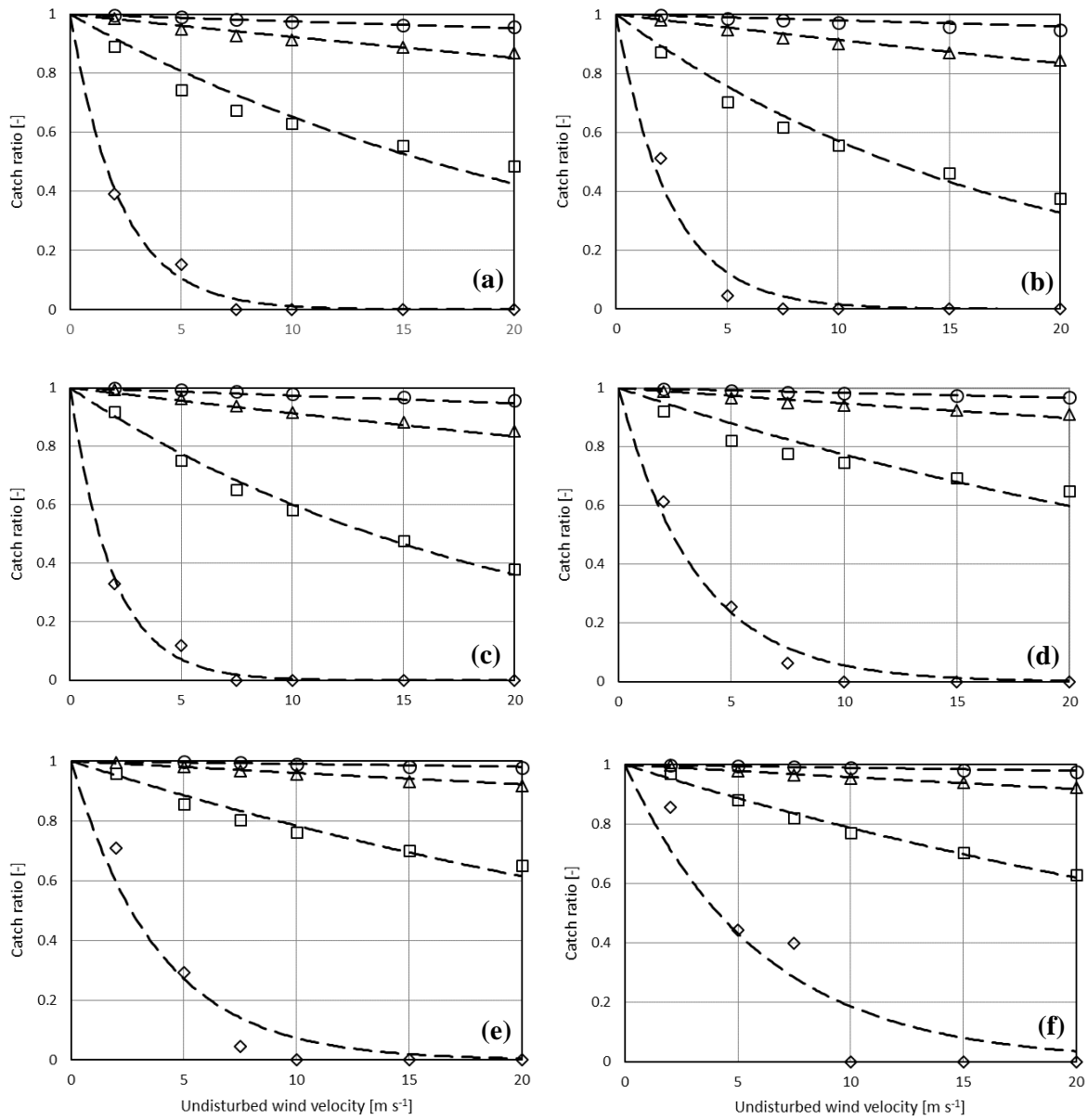


Figure 6.18: Catch ratio for sample selected drop diameters as a function of wind speed for the Geonor T-200B (a), OTT Pluvio² (b), CAE PG10 (c), Lambrecht rain[e]H3 (d), EML SBS500 (e) and AES Nipher (f) instruments. Symbols indicate numerical simulation results for $D = 0.25$ (diamonds), $D = 0.5$ (squares), $D = 1$ (triangles), and $D = 2$ mm (circles), while dashed lines represent the best-fit exponential functions per each sample diameter.

For each gauge geometry, the numerical CR values were fitted with an exponential function (dashed lines in Figures 6.18) as:

$$CR(D, U) = \exp[-\lambda(D) \cdot U]$$

where λ expressed in $(\text{m s}^{-1})^{-1}$ is the best-fit parameter, the values of which are reported in Table 6.2, together with the mean correlation (Pearson) coefficient per each tested geometry.

Table 6.2: Exponential best-fit parameter, λ , of the CR of liquid precipitation, different gauge geometries and various equivolumetric particle diameters. The average Pearson coefficient over all particle diameters is reported in the last column.

Gauge	Drop diameter [mm]							R^2_{avg}
	0.25	0.5	0.75	1	2	4	8	
CAE PG10	0.5266	0.0514	0.0163	0.0082	0.0021	0.0006	0.0002	0.970
Geonor T-200B	0.4474	0.0428	0.0149	0.008	0.0024	0.0008	0.0002	0.915
Lambrecht rain[e]H3	0.2885	0.0259	0.0097	0.0053	0.0017	0.0007	0.0003	0.951
AES Nipher	0.168	0.024	0.0081	0.0042	0.0012	0.0005	0.0002	0.914
OTT Pluvio ²	0.4174	0.056	0.018	0.0093	0.0027	0.0009	0.0003	0.969
EML SBS500	0.2603	0.0242	0.0085	0.0044	0.0011	0.0003	-0.0001	0.959

The variation of the exponential parameter λ with the equivolumetric drop diameter can be expressed by fitting an inverse second-order polynomial, as follows:

$$\lambda = \frac{(c + kD)}{(1 + mD + nD^2)}$$

6.2

where c, k, m and n are best-fit parameters. The adopted fitting function (solid line) is compared with a power law (dashed line) in the log-log plot of Figure 6.19. The best-fit parameters for the variation of the exponent λ with the drop size, together with the associated complement of the Pearson coefficient R^2 , are reported in Table 6.3.

Table 6.3: Best-fit parameters for the variation of λ with the particle size for the investigated instruments.

Gauge	c	k	m	n	$1-R^2$
CAE PG10	0.0345	0.0504	-7.6296	15.9486	5.43E-06
Geonor T-200B	0.0329	0.049	-7.888	17.1673	7.84E-07
Lambrecht rain[e]H3	0.0469	0.0547	-10.0965	27.7452	1.04E-06
AES Nipher	0.0522	0.0118	-8.2305	22.1696	6.07E-06
OTT Pluvio ²	0.0916	0.0158	-7.7242	18.5584	3.51E-06
EML SBS500	0.0474	0.0118	-8.8349	22.4347	7.13E-06

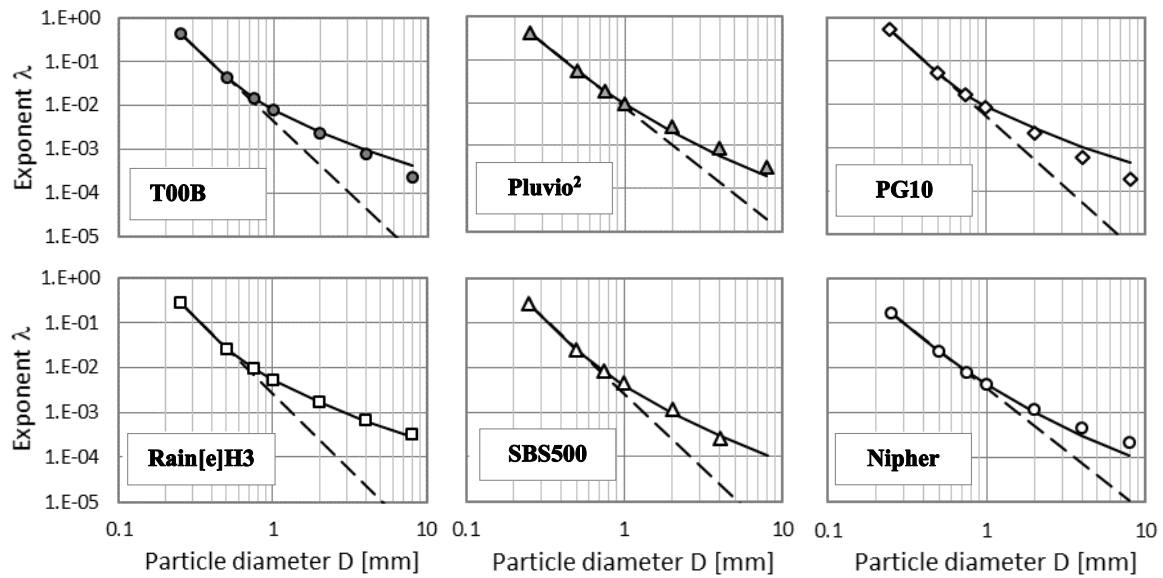


Figure 6.19: Decay with the drop size of the exponential parameter λ of the catch ratio dependency on the wind speed for the investigated gauges. In each graph, symbols indicate numerical simulation results, the solid line is described by Equation 6.2, while the dashed line is the best-fit power law.

In Figure 6.20, a comparison of the exponential parameter λ for liquid precipitation as a function of the drop diameter is provided for different instruments. As expected, the general tendency of λ for all gauges is to decrease with increasing the drop diameter. The obtained functional dependence shows that one instrument (the OTT Pluvio²) has a strong decay of the CR with the wind velocity in the small size drop range and does recover a more uniform behaviour when the drop size increases, while another one (the Lambrecht rain[e]H3) has the opposite trend. However, the instruments visually cluster broadly in two groups, one with a generally stronger decay (larger values of λ) and a second one with a generally weaker decay (lower values of the parameter λ) at all drop size bins.

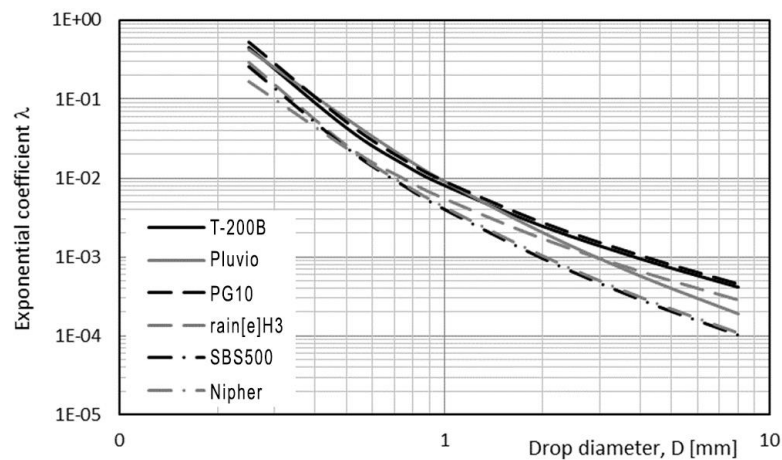


Figure 6.20: Comparison of the exponential parameter λ as a function of the drop size, for the six investigated gauges.

Per each particle size, the dependence of the CR on the wind velocity is a characteristic of the instrument geometry alone and makes no assumptions about the local wind and rainfall climatology at a specific measurement site. In this respect, the comparison of the CR functions is the most general representation of the result of the present work. To better highlight the consequences of choosing any given instrument geometry on the overall measurement bias (e.g., over the yearly precipitation amount), a specific drop size distribution and a local wind climatology must be assumed.

To avoid selecting any specific measurement site, in this work, a uniform wind climatology is chosen, i.e., with any wind velocity being observed with the same frequency at a virtual demonstrative site. As a representative variable for the behaviour of a generic instrument, the Overall Catch Ratio (OCR) is introduced and calculated as the average CR obtained under a uniform wind climatology, as:

$$OCR(D) = \frac{1}{U_{max}} \int_{U=0}^{U_{max}} CR(D, U) dU \quad 6.3$$

where D is the equivolumetric particle diameter and U the undisturbed wind velocity.

The OCR is obtained by taking the integral of the monodisperse catch ratio over a range of wind speed values that is reasonably expected in natural conditions. This formulation assumes that the distribution of wind speed is uniform i.e., every wind speed value is equally likely to occur. The assumption, although scarcely realistic at any specific measurement site, is proposed here to highlight the overall performance of each instrument, with some emphasis on the high wind speed range where the impact of the wind-induced bias is large. This is useful to compare the instrument aerodynamic behaviour under the most demanding conditions. Using the derived exponential expression for the dependency of the CR on the wind velocity, the OCR becomes:

$$OCR(D) = \frac{1}{U_{max}} \int_{U=0}^{U_{max}} e^{-\lambda(D)U} dU = \frac{1}{U_{max}} \frac{1}{\lambda(D)} (1 - e^{-\lambda(D)U_{max}}) \quad 6.4$$

An example of the resulting OCR as a function of the particle size for both liquid and solid precipitation is shown and compared for all the investigated instruments in Figure 6.21. A uniform wind climatology is assumed with a maximum wind speed equal to 10 m s^{-1} . To help interpreting the impact of the instrument performance on precipitation measurements, the liquid water content (LWC) of precipitation events having different intensity between 1.5 and 30 mm h^{-1} is also reported in the graphs.

The LWC [kg m^{-3}] is defined as the integral of the water mass fraction associated with the number of hydrometeors contained within the i -th size bin of diameter width ΔD [mm], and is calculated as:

$$LWC(D) = \rho(D)V(D)N(D)\Delta D \quad 6.5$$

where $\rho(D)$ is the density [kg m^{-3}], $V(D)$ the volume [m^3], and $N(D)$ the numerosity [$\text{m}^{-3} \text{mm}^{-1}$] of the particles having an equivolumetric diameter equal to D . The number of hydrometeors per each size bin is given by the PSD equation, here formulated according to the exponential form proposed by Marshall and Palmer (1948), see Equation 2.4, using the coefficients proposed by Cauteruccio and Lanza (2020) (see Equations 4.2 and 4.3).

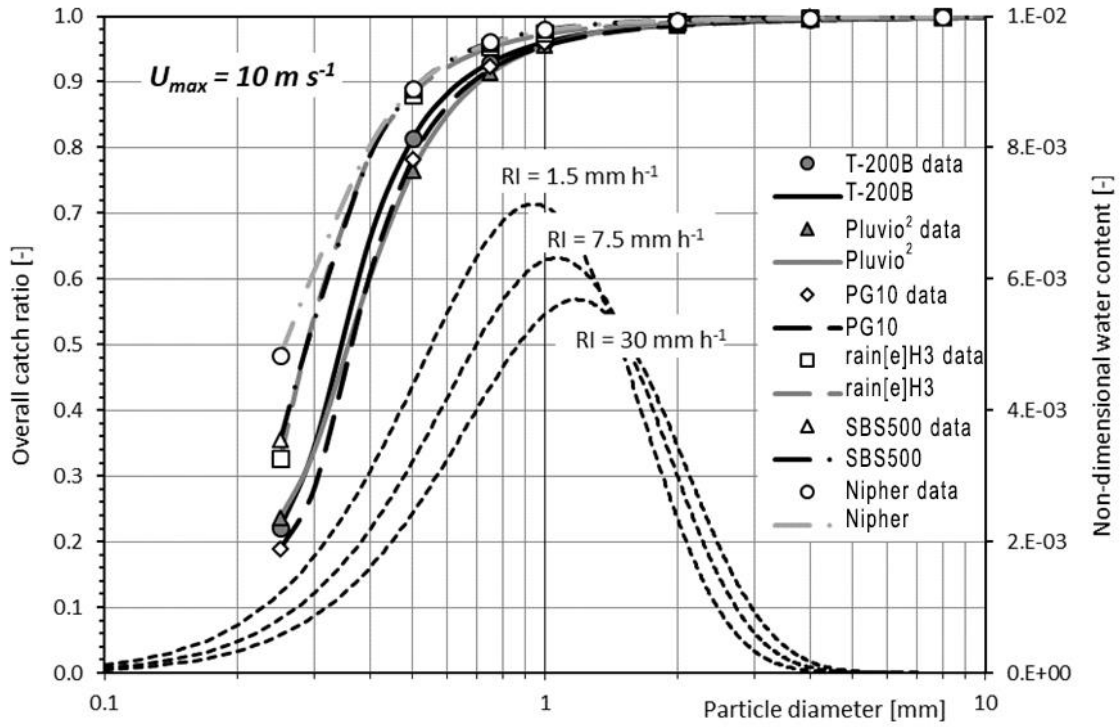


Figure 6.21: OCR of the investigated instruments as a function of the particle size, calculated under the hypothesis of uniform wind climatology with a maximum wind speed of 10 m s^{-1} . The non-dimensional water content is also shown with dotted lines for sample precipitation intensity events, based on the PSD formulation proposed by Cauteruccio and Lanza (2020) according to disdrometer measurements from Caracciolo et al. (2008).

Based on the above microphysical characterization of the hydrometeors, the LWC assumes the following simple forms:

$$LWC = \frac{\pi}{6} \cdot 10^{-6} \cdot N_0(RI) \cdot D^3 \cdot \exp(-\lambda_0(RI)D) \cdot \Delta D$$

6.6

as a function of the rainfall intensity (RI). Meanwhile, the non-dimensional water content (NWC) is obtained as the ratio between the LWC and its integral (WC) over the whole range of diameters, and is defined as:

$$NWC = \frac{LWC_L(D)}{WC_L} = \frac{\frac{\pi}{6} \cdot 10^{-6} \cdot N_0(RI) \cdot D^3 \cdot \exp(-\lambda_0(RI)D) \cdot \Delta D}{\frac{\pi N_0}{\lambda_0^4 10^6}} = \lambda_0^4 \frac{D^3}{6} \exp(-\lambda_0(RI)D) \cdot \Delta D$$

6.7

Where the integral of the LWC can be written as:

$$WC = \frac{\pi N_0}{6 \cdot 10^6} \left[\frac{1}{\lambda_0} \exp(-\lambda_0 D) \left(-D^3 + 3 \left(-\frac{D^2}{\lambda_0} - \frac{2D}{\lambda_0^2} - \frac{2}{\lambda_0^3} \right) \right) \right]_0^\infty = \frac{\pi N_0}{\lambda_0^4 10^6}$$

6.8

In Figure 6.21, all instruments show a reduced OCR (below 80%) at the lower range of equivolumetric drop diameters ($D < 0.4$ mm), while all of them have very high OCR (above 95%) for $D > 1$ mm. The Percentage Mass Fraction (PMF) of raindrops having $D < 0.4$ mm is however limited, corresponding to about 5% of the total water volume at low precipitation intensity (see Figure 6.22). Instead, raindrops with $D > 1$ mm account for the most part of the rainfall volume, between 60 and 75% at precipitation intensities from 1.5 to 30 mm h⁻¹. Therefore, the range where all instruments experience limited OCRs due to the wind is the less relevant portion of the PSD at any precipitation intensity level.

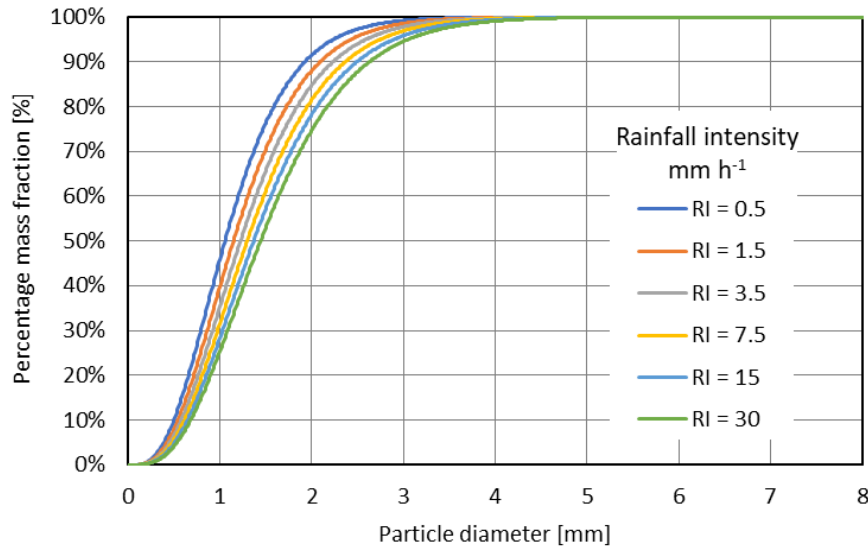


Figure 6.22: Percentage Mass Fraction of hydrometeors with the particle size, $PMF(D)$, for liquid precipitation at different precipitation intensity. Calculation is performed using the PSD formulation obtained by Cauteruccio and Lanza (2020) based on disdrometer data measured by Caracciolo et al. (2008).

Clustering of different instrument is evident in Figure 6.21, with the CAE PG10, Geonor T-200B and OTT Pluvio² gauges presenting similar values of the OCR, but significantly lower than those of the other instruments. This difference is evident at drop size bins up to 1 mm, while beyond that value all instruments

present an OCR close to unity. The AES Nipher gauge is the best performing one in terms of OCR, especially for the smallest drops, due to its aerodynamic shape; however, the improvement over the EML SBS500 and Lambrecht gauges is limited. This is because the AES Nipher gauge was designed primarily for solid precipitation measurements.

6.5 TRANSFER FUNCTION FOR A SAMPLE PRECIPITATION CLIMATOLOGY

The collected water content (CWC), per each diameter bin, measured by the gauge when exposed to the wind is obtained as the LWC weighted with the OCR as follows:

$$CWC(D) = V(D) \cdot \rho(D) \cdot N(D) \cdot OCR(D) \cdot \Delta D$$

6.9

The CWC is compared with the actual one (the LWC) in Figure 6.23 for a sample gauge (the CAE PG10), as a function of the particle diameter and for selected values of the precipitation intensity. Continuous and dashed lines represent the collected and actual water content, respectively. Underestimation of the LWC is limited to drop diameters lower than about 2 mm.

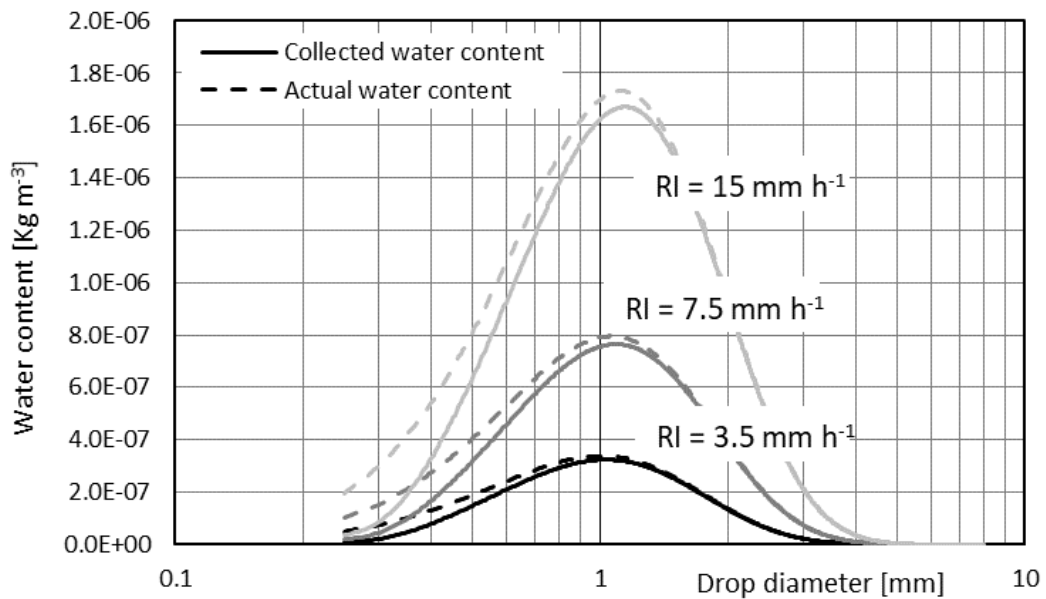


Figure 6.23: Comparison between the collected and actual water content with the particle size for a sample instrument (the CAE PG10) in case of liquid precipitation of various intensity.

The integral collection efficiency was introduced by Nespor and Sevruck (1999) and used by Hoover et al. (2022) to extend the definition of the CE from mono- to multi-disperse precipitation. To compare the expected performance in the field for the six investigated CGs, the Overall Collection Efficiency (OCE) is here defined as:

$$OCE(RI) = \frac{1}{OCE_{max}(RI)} \int_{D=D_{min}}^{D_{max}} CWD(D) dD = \frac{1}{OCE_{max}(RI)} \int_{D=D_{min}}^{D_{max}} V(D) \cdot \rho(D) \cdot N(D) \cdot OCR(D) dD \quad 6.10$$

where the maximum of the overall collection efficiency is obtained for an OCR equal to unity for each particle size, wind speed and precipitation intensity. Considering the Marshall Palmer formulation of the PSD and the definition of OCR, the OCE can be written as:

$$OCE(RI) = \frac{1}{OCE_{max}(RI)} \int_{D=D_{min}}^{D_{max}} \pi \frac{D^3}{6 \cdot 10^6} \cdot N_0(RI) \exp[-\lambda_0(RI)D] \cdot \frac{1}{U_{max}} \frac{1}{\lambda} (1 - e^{-\lambda U_{max}}) dD \quad 6.11$$

By substituting the dependency of λ on D (Equation 6.2) in Equation 6.11, the OCE becomes:

$$OCE(RI) = \frac{1}{OCE_{max}(RI)} \frac{\pi}{6 \cdot 10^6} N_0(RI) \frac{1}{U_{max}} \int_{D=D_{min}}^{D_{max}} D^3 \cdot \exp[-\lambda_0(RI)D] \cdot \frac{1 + mD + nD^2}{c + kD} \left(1 - e^{-\frac{(c+kD)}{(1+mD+nD^2)} U_{max}} \right) dD \quad 6.12$$

Where $OCE_{max}(RI)$ is computed for $OCR(D) = 1$, becoming:

$$OCE_{max}(RI) = \frac{\pi}{6 \cdot 10^6} N_0(RI) \int_{D=D_{min}}^{D_{max}} D^3 \cdot \exp[-\lambda_0(RI)D] dD \quad 6.13$$

Therefore, after substituting this Equation 6.13 in Equation 6.11, the OCE can be written as:

$$OCE(RI) = \frac{\int_{D=D_{min}}^{D_{max}} D^3 \cdot \exp[-\lambda_0(RI)D] \cdot \frac{1 + mD + nD^2}{c + kD} \left(1 - e^{-\frac{(c+kD)}{(1+mD+nD^2)} U_{max}} \right) dD}{U_{max} \int_{D=D_{min}}^{D_{max}} D^3 \cdot \exp[-\lambda_0(RI)D] dD} \quad 6.14$$

The OCE values computed by using Equation 6.14 therefore provide the expected performance of the gauge in the case of uniform wind climatology, as a function of the RI.

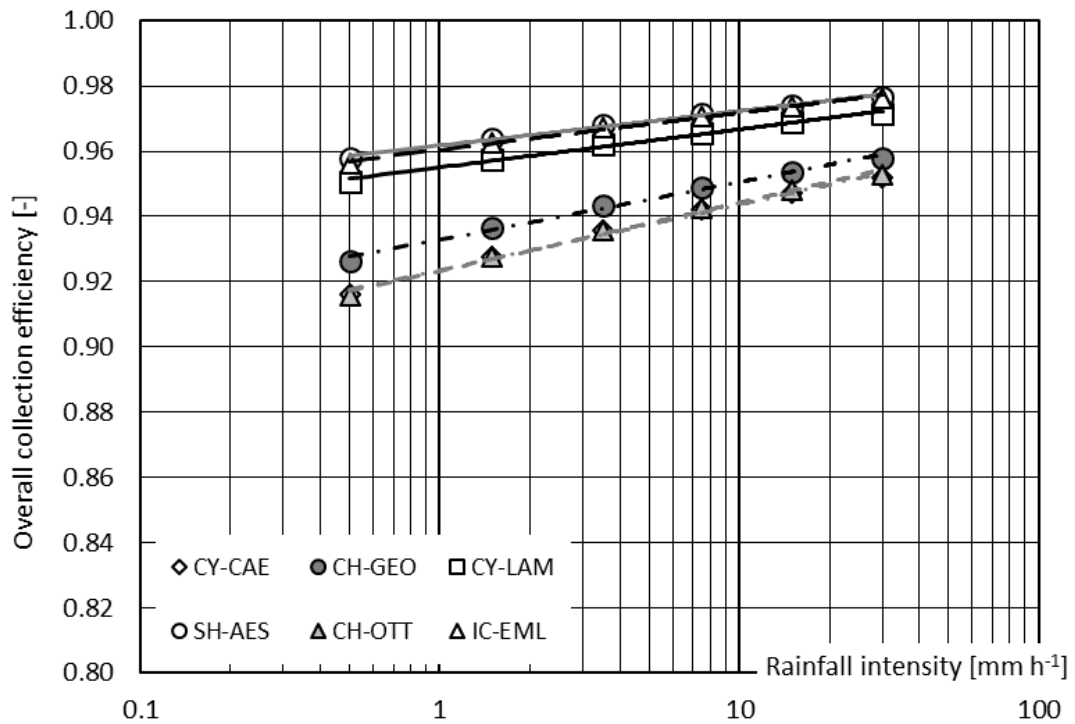


Figure 6.24: Calculated OCE values (symbols) as a function of RI for the investigated instruments, under the hypothesis of uniform wind climatology with a maximum wind speed of 10 m s^{-1} , based on the PSD formulation proposed by Cauteruccio and Lanza (2020) from disdrometer data measured on the Italian territory by Caracciolo *et al.* (2008).

Figure 6.24 shows the OCE of the different CGs considered in this work in the case of liquid precipitation. Like in the case of the OCR, the CAE PG10, Geonor T-200B, and OTT Pluvio² instruments show lower performance than the other gauges in the measurement of liquid precipitation, with the Geonor T-200B performing slightly better. Meanwhile the AES Nipher instrument is the best performing one, for the whole range of RI considered, closely followed by the other aerodynamic gauge, the EML SBS500. The Lambrecht rain[e]H3 instrument is slightly less performant than the two aerodynamic gauges, but significantly better than the first group.

Overall, instruments cluster in two distinct groups with chimney shaped (Geonor T-200B and OTT Pluvio²) and one cylindrical gauge (CAE PG10) underperforming at all precipitation intensity events, while the rest of the gauges perform significantly better.

OCE values as a function of RI can be fitted using a power law as:

$$OCE(RI) = q \cdot RI^r$$

6.15

where q and r are the best-fit parameters, whose values are shown, for each investigated gauge, in Table 6.4.

Table 6.4: Power law best-fit parameters for the dependency of OCE on the liquid and solid precipitation intensity for the investigated instruments.

Gauge	q	r	R ²
CAE PG10	0.909	0.009	0.998
Geonor T-200B	0.904	0.010	0.998
Lambrecht rain[e]H3	0.891	0.010	0.998
AES Nipher	0.853	0.014	0.999
OTT Pluvio ²	0.849	0.015	0.999
EML SBS500	0.781	0.021	0.999

For instruments having the same outer geometry, a relevant role is ascribable to the shaping of the collector's rim. Indeed, the less performant chimney shaped instrument is the OTT Parsivel², having an abrupt change of its axial symmetric profile close to the top section with a resulting stronger updraft than the Geonor T-200B above the collector. Also, despite the about cylindrical geometry, the presence of a protruding rim strongly affects the performance of the CAE PG10 with reference to the Lambrecht rain[e]H3, lowering them to the level of the two chimney shaped instruments. The best performing instruments, the EML SBS500, Lambrecht rain[e]H3 and AES Nipher, have no abrupt geometrical variations close to their collector, thus limiting their bluff-body aerodynamic impact above the collector.

The results of this work can be exploited by operational users to select the most suitable outer geometry for instruments to be installed at sites with frequent wind. This would help managers of hydro-meteorological monitoring networks to minimize the impact of the wind-induced bias on the measurement accuracy and therefore improve the overall quality of the collected precipitation datasets.

For instruments that are already installed in sites with frequent windy conditions, this work also provides the basic information needed to apply adjustments to the measured data. Indeed, provided a relationship between the parameters of the PSD and precipitation intensity is available, the CR values reported above for six commonly employed precipitation measuring instruments allow calculating the CE for the given site and therefore the adjusted precipitation measurements (both in real time or a posteriori).

This work would finally help manufacturers of precipitation measuring instruments in that it provides hints about the most performing design solutions for aerodynamically efficient instruments. It also supports them in the possible upgrade of instruments with the existing design by introducing on-board adjustments of the measured precipitation that only require contemporary measurement of the wind velocity (often included in typical meteorological stations).

7 CFD RESULTS AND VALIDATION FOR SAMPLE NCGs

In this chapter the aerodynamic performance of three sample NCGs when immersed in a wind field are presented. The selected instruments are characterized by very different outer shapes and measurement technology, commercially available and widely used in field measurements. The first investigated instrument is the Thies LPM, already described in section 4.4.1., while the other two instruments are the OTT Parsivel² and the Vaisala WXT-520, described below.

7.1 OTT PARSIVEL²

The Parsivel², manufactured by OTT HydroMet (see OTT, 2017), is – like the Thies LPM – an optical NCG that uses optical transmission principles to detect hydrometeors in flight. As shown in Figure 7.1, the instrument body presents two symmetry axes, one parallel to the laser beam and the other perpendicular to it. The receiving and emitting heads are contained in two identical housings opposing to each other.

The instrument uses a visible light (650 nm) laser diode, coupled with suitable optics, to produce an infrared light sheet 180 mm long and 30 mm wide with a thickness of 1 mm. The functioning principle is analogous to the one of the Thies LPM (paragraph 4.4.1), the hydrometeors size is computed by measuring the beam power reduction due to the resulting obstruction, while the duration of the beam power reduction is used to compute the fall velocity. The same shortcomings are also valid, meaning that the instrument cannot differentiate between multiple hydrometeors simultaneously crossing the laser beam, and either interpret them as a single particle of a larger diameter or discard them. Furthermore, hydrometeors crossing the beam near its edges, blocking the laser beam only partially, may be detected as smaller particles leading to some underestimation of the water volume.



Figure 7.1: The OTT Parsivel² (OTT, 2017) mounted on a supporting pole, with the two symmetric heads (containing the laser emitter and receiver) and the cylindrical box holding the two supporting arms for the sensor heads and containing the circuitry.

Contrary to the Thies LPM, installation instructions from the manufacturer (OTT, 2017) do not specify the need of orientating the instrument with the main symmetry axis aligned with the North direction, stating however that glaring and intense sunlight may still have a small impact on measurements. Nevertheless, the possibility to suitably align the instrument according to the prevalent wind direction at the installation site may be beneficial in reducing the wind induced bias.

7.2 VAISALA WXT-520

The WXT-520, manufactured by Vaisala Inc. (see Vaisala, 2012), is a compact weather station that includes an impact type NCG used to evaluate precipitation characteristics. The instrument, having an almost cylindrical body, is shown in Figure 7.2. A circular, metallic cover, used to measure precipitation, is positioned at the top of the instrument, surrounded by three small arms supporting the wind speed sensors (using and ultrasonic principle). A series of slits is positioned below these sensors, to shield the temperature and pressure probes.



Figure 7.2: The Vaisala WXT-520 (Vaisala, 2012) weather station. Visible are the three “arms” used to house the ultrasonic wind sensors. The instrument sensing area is the metallic surface that is present at the top of the gauge.

The Vaisala WXT-520 derives precipitation characteristics by measuring the kinetic energy of hydrometeors impacting on the metallic cover, which is a function of their mass and fall velocity. From the analysis of the amplitude and duration of the signal produced by the impact, the drop diameter and fall velocity are obtained based on an empirical relationship between the two variables. The relationship is valid

under the assumption that drops fall at their terminal velocity following perfectly vertical trajectories. Once the microphysical characteristics of precipitation are measured, integral variables, like precipitation intensity, are computed since the area of the sensor cover and the time window of the measurement are known. The instrument is also able to distinguish between rain drops and graupels, by analysing the characteristics of the waveform of the signal produced by the impacting hydrometeors.

A limitation of this method is that, after the impact of large hydrometeors, some delay is needed before the instrument is again able to detect further impacts of small particles. This is due to the time required for the signal produced by large drops to decay to a level where it does not overshadow the signal of small drops. This time interval is usually referred to as the dead-time and may result in some underestimation of precipitation.

Due to its almost radially symmetric shape and measuring principle, instructions from the manufacturer (Vaisala, 2012) do not require any specific orientation of the instrument for installation in the field. This therefore allows the instrument to be oriented according to the prevalent wind direction at the installation site.

7.3 MESHING AND FLUID DYNAMIC SETUP

To evaluate the wind induced response of the selected instruments using CFD simulation, a numerical model of their outer geometry, including the supporting pole, was realised in the STL format. The computational mesh was produced within OpenFOAM, with overall dimensions of the simulation domain equal to a box 4 m long, 2.4 m wide, and 2 m high, which remains unchanged for all instruments.

Here results are presented for the three simulation approaches. First an uncoupled LPT model (see chapter 5.3.2) is used in combination with the CFD results of the time-independent approach (see chapter 5.3.1.1). This is the least computationally expensive approach and was applied to all gauges for all combinations of wind speed, wind direction and hydrometeor size.

For a selected number of wind speeds and wind directions the same uncoupled model was also used in conjunction with the CFD results of the time-dependent approach (see chapter 5.3.1.2). In this case, the LPT model remains computationally inexpensive, however the evaluation of the CFD results using the time-dependent approach becomes a considerable burden.

Lastly, for a few combinations of wind speed, wind directions and hydrometeor size, a one-way coupled LPT model is used in conjunction with the time-dependent CFD model. This is by far the most computationally expensive approach; however, it allows for the effects of small scale turbulent fluctuations to be taken into account.

7.3.1 Thies LPM time independent approach

In the case of the Thies LPM, the longitudinal axis (X) is set along the main symmetry axis of the instrument, the vertical axis (Z) is directed upward, while the Y axis is normal to the (X, Z) plane. The origin of the reference system is in the centre of the sensing area (the IR light sheet). The internal mesh has a maximum cell size of 0.04 m and is progressively refined (up to 1 mm near the instrument walls) to

reproduce the finer geometrical details and to correctly model the turbulence generated by the gauge-flow interaction.

The direction of the incoming wind was initially set parallel to the X axis, while nine different meshes were realized to simulate various wind directions, from $\alpha = 0^\circ$ to $\alpha = 180^\circ$ with increments of 22.5° , where α is the angle between the wind direction and the main symmetry axis of the instrument. In the configuration at $\alpha = 0^\circ$, the wind impacts first on the receiving sensor while, in the configuration at $\alpha = 180^\circ$, it first impacts on the supporting pole and the circuitry box. For each wind direction, five wind speed values (U_{ref}) equal to 2, 5, 10, 15, and 20 m s^{-1} were tested for a total of 45 simulated wind direction/velocity configurations.

The computational mesh was progressively refined until the criterion $R_L \geq 5$ was satisfied in most of the domain (see section 5.3.1.3). As shown in the maps of Figure 7.3, along the (X, Z) and (X, Y) sections of the domain at $Y = 0$ and $Z = 0$, respectively, only in the proximity of the straight and sharp edges the R_L criterion could not be met.

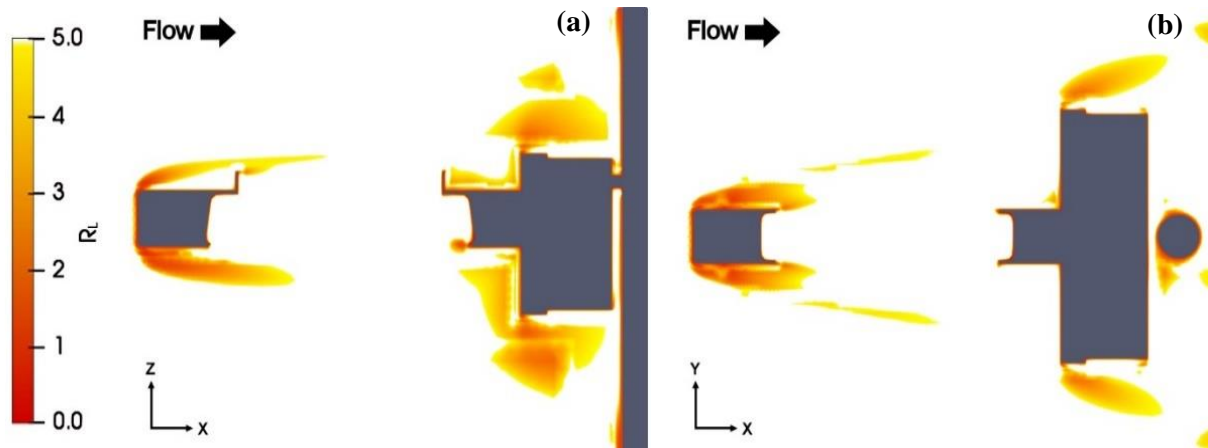


Figure 7.3: Maps of the R_L ratio at $U_{ref} = 10 \text{ m s}^{-1}$ for $\alpha = 0^\circ$, along the (X, Z) section at $Y = 0$ (a) and (X, Y) section at $Z = 0$ (b). Values are obtained for the mesh used in the case of the time-independent approach.

For the nine wind directions investigated, the final mesh contains between four and five million cells and the values of typical mesh size and quality parameters, including the non-orthogonality, skewness, and aspect ratio, are listed in Table 7.1. These are used to identify highly distorted cells that could affect the solution and their value should be as low as possible. In Table 7.1, the parameters for all meshes are shown to be acceptable for external aerodynamic simulations.

A sample (X, Z) section of the mesh at $Y = 0$ is presented in Figure 7.4 for the configuration at $\alpha = 0^\circ$, with details of the region close to the surface of the instrument emitting head. Coarser meshes were also tested, using a slightly simplified version of the geometry that allowed to reduce the cell count to about 1M elements, while still preserving the instrument features. These meshes, however, failed to meet the R_L criterion and showed poor agreement with the WT measurements. It can be concluded that, for the geometries used in this work, no meaningful reduction of the cell count can be achieved without sacrificing the simulation accuracy.

Table 7.1: Mesh size and quality parameters for the nine configurations investigated.

Wind Direction	n° Cells	Avg. Non-orthogonality	Max Non-orthogonality	Max Skewness	Max Aspect ratio
0.0 °	4'022'992	6.44	54.87	3.45	13.35
22.5°	4'070'482	6.88	54.98	3.93	11.05
45.0°	4'144'606	6.81	55.46	3.96	13.28
67.5°	4'372'642	6.69	54.98	4.00	11.62
90.0°	4'626'698	6.19	54.98	3.45	13.35
112.5°	4'807'780	6.52	55.47	3.95	11.05
135.0°	4'943'269	6.45	55.47	3.95	13.28
157.5°	5'062'277	6.40	54.98	3.99	11.15
180.0°	5'081'405	5.99	54.88	3.45	13.35

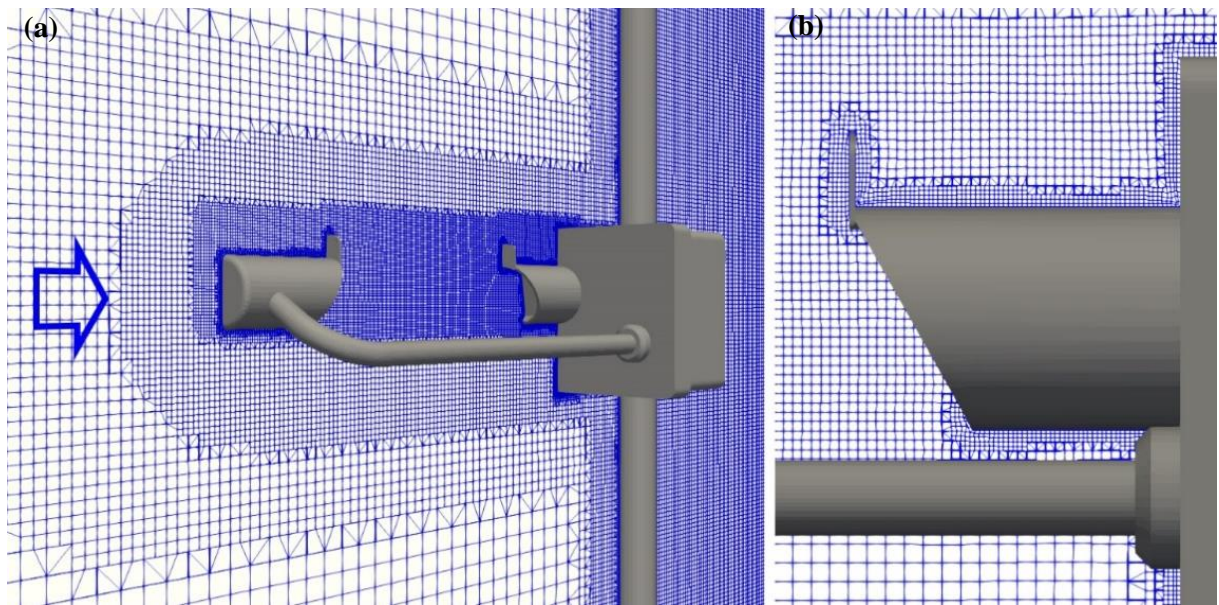


Figure 7.4: The computational mesh along the longitudinal cross-section of the domain around the Thies LPM at $Y = 0$ for the configuration at $\alpha = 0^\circ$ (a). The arrow indicates the direction of the incoming undisturbed wind flow. Close-up details of the mesh near the instrument emitting head (b).

7.3.2 Thies LPM time dependent approach

For the time dependent simulations of the Thies LPM, the same geometrical configuration was maintained. Due to the higher meshing requirements of the time dependent model, the internal mesh – though still having a maximum cell size of 0.04 m – is progressively refined up to 0.5 mm near the instrument walls.

Two directions for the incoming wind were simulated, $\alpha = 0^\circ$ and $\alpha = 90^\circ$, maintaining the same definition of the angle α as for the time independent simulations. For each wind direction, two wind speed values (U_{ref}) equal to 5 and 10 m s^{-1} were tested.

The computational mesh, like in the previous case, was progressively refined until the criterion $R_L \geq 10$ was satisfied in most of the domain. As shown in the maps of Figure 7.5, along the (X, Z) and (X, Y) sections of the domain at $Y = 0$ and $Z = 0$, respectively, only in the proximity of the straight and sharp edges of the instrument body the R_L criterion could not be met.

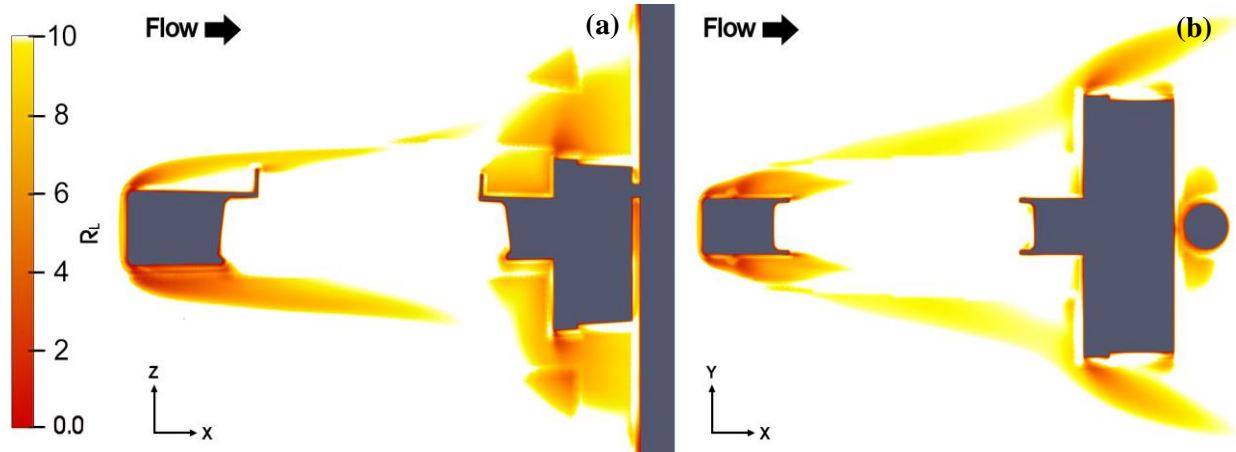


Figure 7.5: Maps of the R_L ratio at $U_{ref} = 10 \text{ m s}^{-1}$ for $\alpha = 0^\circ$, along the (X, Z) section at $Y = 0$ (a) and (X, Y) section at $Z = 0$ (b). Values are obtained for the mesh used in the case of the time-dependent approach.

For the two wind directions investigated, the final meshes contain about 19 and 25 million cells, respectively. The mesh size and quality parameters are listed in Table 7.2. Even considering the higher meshing requirements, these parameters, for both meshes, can be considered acceptable.

A sample (X, Z) section of the mesh at $Y = 0$ is presented in Figure 7.6 for the configuration at $\alpha = 0^\circ$, with details of the region close to the surface of the instrument emitting head.

Table 7.2: Mesh size and quality parameters for the two configurations investigated.

Wind Direction	n° Cells	Avg. Non-orthogonality	Max Non-orthogonality	Max Skewness	Max Aspect ratio
0.0 °	19'729'994	4.70	49.95	3.32	15.58
90°	25'436'709	4.21	49.93	3.31	14.60

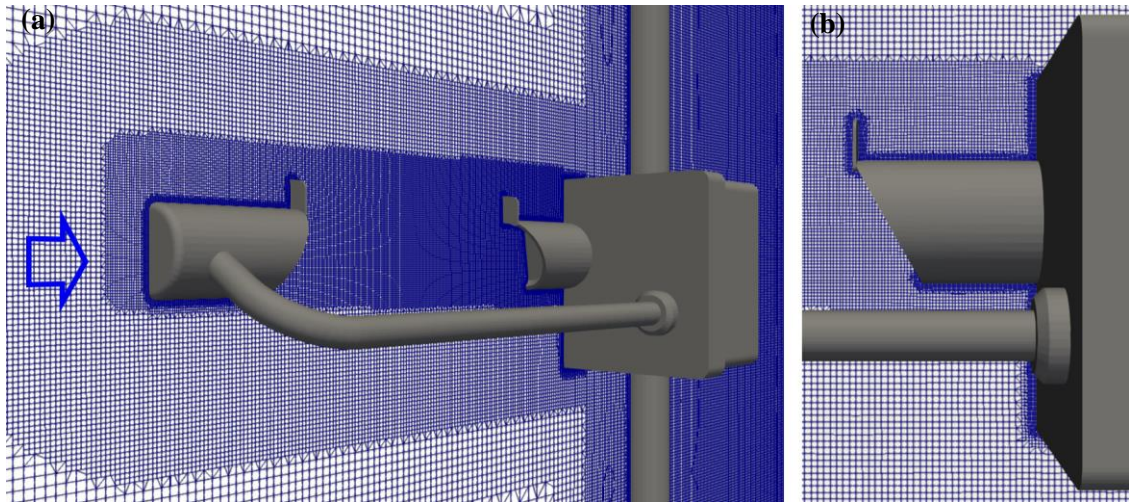


Figure 7.6: The computational mesh along the longitudinal cross-section of the domain around the Thies LPM at $Y = 0$ for the configuration at $\alpha = 0^\circ$ (a). The arrow indicates the direction of the incoming, undisturbed wind flow. Close-up details of the mesh near the instrument emitting head (b).

7.3.3 OTT Parsivel2

For the mesh of the OTT Parsivel², the longitudinal axis (X) is set parallel to the laser beam of the instrument, the vertical axis (Z) is directed upward, while the Y axis is normal to the (X, Z) plane. The origin of the reference system is in the centre of the sensing area (the light sheet). The internal mesh has a maximum cell size of 0.05 m and is progressively refined (up to 0.75 mm near the instrument walls) to reproduce the finer geometrical details and to correctly model the turbulence generated by the gauge-flow interaction.

The direction of the incoming wind was initially set parallel to the X axis and, since the instrument presents two symmetry axis, five different meshes were realized to simulate various wind directions, from $\alpha = 0^\circ$ to $\alpha = 90^\circ$ with increments of 22.5° , where α is the angle between the directions of wind and the laser beam of the instrument. In the configuration at $\alpha = 0^\circ$, the wind impacts first on one of the sensor heads, while in the configuration at $\alpha = 90^\circ$, it impacts the instrument from the side. For each wind direction, seven wind speed values (U_{ref}) equal to 1, 2.5, 5, 7.5, 10, 15, and 20 m s^{-1} were tested for a total of 35 simulated wind direction/velocity configurations.

The computational mesh was progressively refined until the criterion $R_L \geq 5$ was satisfied in most of the domain, as shown in the maps of Figure 7.7, along the (X, Z) and (X, Y) sections of the domain at $Y = 0$ and $Z = 0$, respectively. Due to the higher refinement level of the mesh, in this case a value of $R_L \geq 5$ is obtained everywhere in the domain, except close to the stagnation point of the instrument and in the wake of the supporting arms.

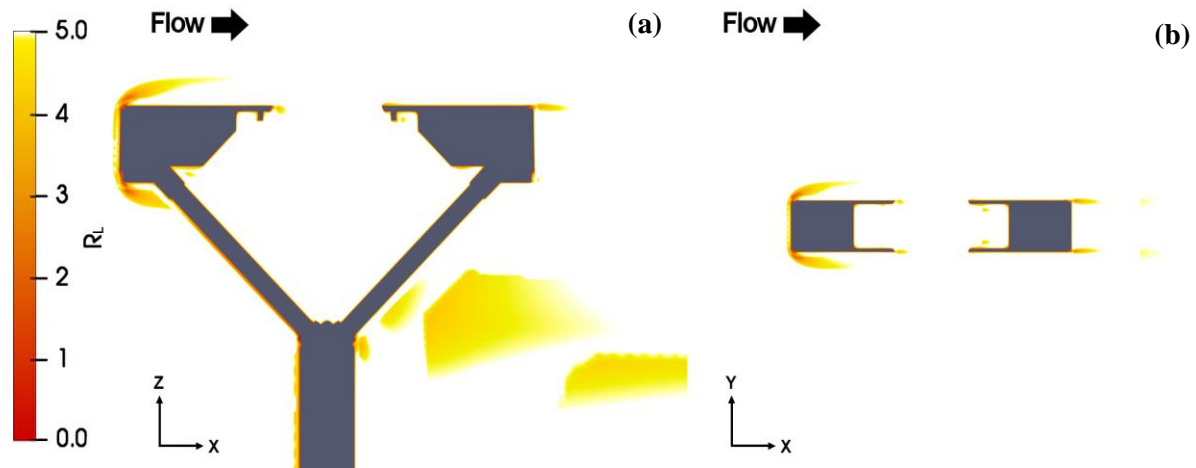


Figure 7.7: Maps of the R_L ratio at $U_{ref} = 10 \text{ m s}^{-1}$ and $\alpha = 0^\circ$, along the (X, Z) section at $Y = 0$ (a) and (X, Y) section at $Z = 0$ (b).

For the five wind directions investigated, the final mesh contains between six and eight million cells. The values of typical mesh size and quality parameters, including the non-orthogonality, skewness, and aspect ratio, are listed in Table 7.3, and appears as acceptable for external aerodynamic simulations.

A sample (X, Z) section of the mesh at $Y = 0$ is presented in Figure 7.8 for the configuration at $\alpha = 0^\circ$, with details of the region close to the surface of the instrument. Due to the experience gained from the Thies LPM simulations, in this case no coarser mesh was tested since it was established that no meaningful reduction of the cell count can be achieved without sacrificing the simulation accuracy.

Table 7.3: Mesh size and quality parameters for the five configurations investigated.

Wind Direction	n° Cells	Avg. Non-orthogonality	Max Non-orthogonality	Max Skewness	Max Aspect ratio
0.0 °	6'437'616	5.34	64.60	3.64	22.00
22.5°	7'134'222	5.39	64.95	3.99	30.99
45.0°	7'733'644	5.27	64.99	3.14	20.23
67.5°	8'157'556	5.13	64.80	4.00	30.96
90.0°	7'687'848	4.98	64.60	3.64	22.00

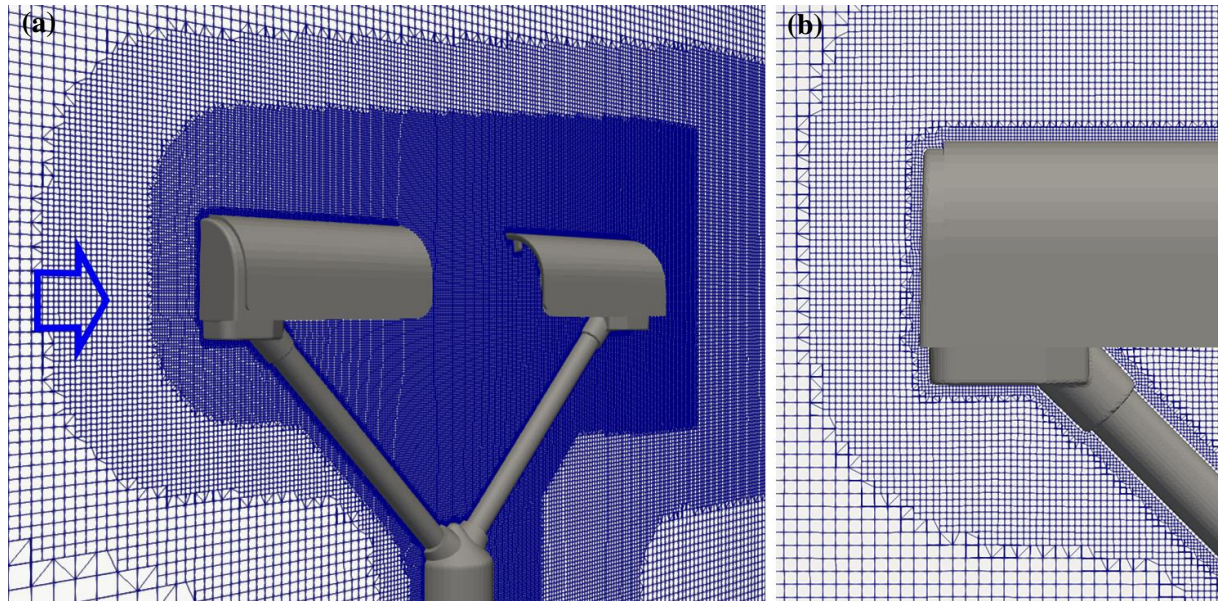


Figure 7.8: The computational mesh along the longitudinal cross-section of the domain around the OTT Parsivel² at $Y = 0$ for the configuration at $\alpha = 0^\circ$ (a). The arrow indicates the direction of the incoming, undisturbed wind flow. Close-up details of the mesh near the instrument emitting head (b).

7.3.4 Vaisala WXT-520

Considering the Vaisala WXT-520, the longitudinal axis (X) is directed from the centre of the instrument towards one of the three arms, the vertical axis (Z) is directed upward, while the Y axis is normal to the (X, Z) plane and parallel to the plane containing the two remaining arms. The origin of the reference system is in the centre of the metal cover at its topmost point. The internal mesh has a maximum cell size of 0.04 m and is progressively refined up to 1 mm near the instrument walls, to reproduce the finer geometrical details and to correctly model the turbulence generated by the gauge-flow interaction.

The direction of the incoming wind was initially set parallel to the X axis, while three different meshes were realized to simulate various wind directions, $\alpha = 0^\circ$, $\alpha = 30^\circ$ and $\alpha = 60^\circ$, where α is the angle between the wind direction and the initial orientation of the instrument. In the configuration at $\alpha = 0^\circ$, the wind impacts first the two arms, parallel to the Y axis and then the one along the X axis, in the configuration at $\alpha = 60^\circ$, the situation is reversed.

For each wind direction, seven wind speed values (U_{ref}) equal to 1, 2.5, 5, 7.5, 10, 15, and 20 m s^{-1} were tested for a total of 21 simulated wind direction/velocity configurations.

The computational mesh was progressively refined until the criterion $R_L \geq 5$ was satisfied in most of the domain, as shown in the maps of Figure 7.9, along the (X, Z) and (X, Y) sections of the domain at $Y = 0$ and $Z = 0$, respectively. In this case, due to the limited dimension of the gauge and the moderately coarser mesh, slightly lower values of R_L are obtained inside the separation layer that is formed over the instrument sensing area due to its bluff-body shape.

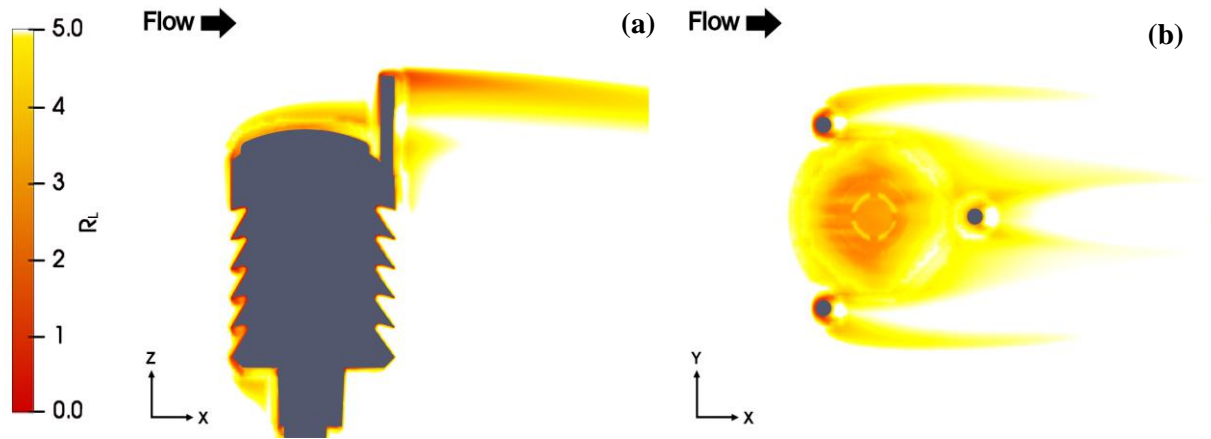


Figure 7.9: Maps of the R_L ratio at $U_{ref} = 10 \text{ m s}^{-1}$ for $\alpha = 0^\circ$, along the (X, Z) section at $Y = 0$ (a) and (X, Y) section at $Z = 0$ (b).

For the three wind directions investigated, the final mesh contains slightly less than three million cells and the values of typical mesh size and quality parameters, including the non-orthogonality, skewness, and aspect ratio, are listed in Table 7.4. As in the previous cases, the parameters for all meshes are acceptable for external aerodynamic simulations.

A sample (X, Z) section of the mesh at $Y = 0$ is presented in Figure 7.10 for the configuration at $\alpha = 0^\circ$, with details of the region close to the sensing area of the instrument and of one of the wind measuring arms.

Table 7.4: Mesh size and quality parameters for the three configurations investigated.

Wind Direction	n° Cells	Avg. Non-orthogonality	Max Non-orthogonality	Max Skewness	Max Aspect ratio
0°	2'866'639	64.84	6.09	3.17	17.94
30°	2'866'598	64.67	6.09	3.05	17.94
60°	2'866'491	64.98	6.10	3.18	17.83

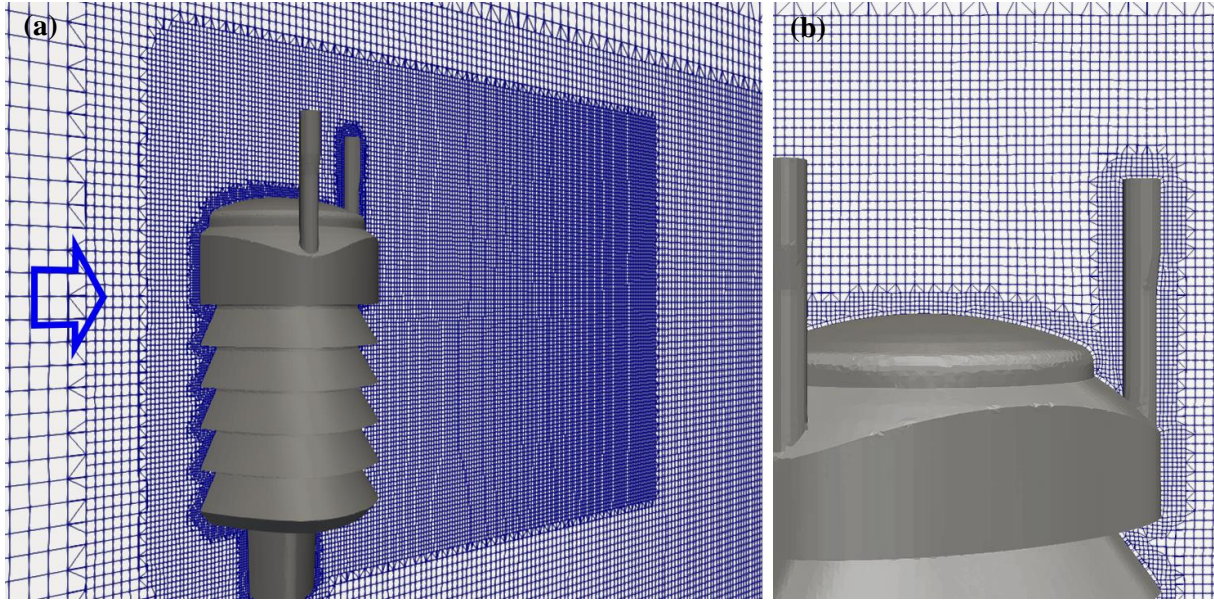


Figure 7.10: The computational mesh along the longitudinal cross-section of the domain around the Vaisala WXT-520 at $Y = 0$ for the configuration at $\alpha = 0^\circ$ (a). The arrow indicates the direction of the incoming undisturbed wind flow. Close-up details of the mesh near the instrument sensing area (b).

7.4 CFD SIMULATION RESULTS

Results of the CFD simulation are shown in terms of maps of the normalized magnitude and vertical component of the flow velocity (indicated with $U_{\text{mag}}/U_{\text{ref}}$ and U_z/U_{ref} , respectively) and maps of the normalized turbulent kinetic energy (k/U_{ref}^2). A 3-D visualisation of the turbulent structures, using the Q-criterion (Hunt et al., 1988), is also included. CFD statistics for selected performance parameters are also computed for a control volume representative of the sensing area of each gauge, allowing for direct comparison of the instrumental induced disturbance close to its sensing area for the different wind directions considered.

7.4.1 Thies LPM time independent approach

As a sample of the large numerical dataset obtained from CFD simulations, wind velocity maps in the (X, Z) section of the flow field at $Y=0$, for $U_{\text{ref}} = 10 \text{ m s}^{-1}$ and $\alpha = 0^\circ, 90^\circ$, and 180° are shown in Figures 7.11, 7.12, 7.13, respectively. In the left-hand panels, the red zones indicate a larger flow velocity than the undisturbed wind speed, therefore $U_{\text{mag}}/U_{\text{ref}} > 1$, while in the blue zones the flow velocity is lower than the undisturbed wind, and $U_{\text{mag}}/U_{\text{ref}} < 1$. In the right-hand panels, the red zones indicate upward flow velocity components, with $U_z/U_{\text{ref}} > 0$, while downward components occur in the blue zones, where $U_z/U_{\text{ref}} < 0$.

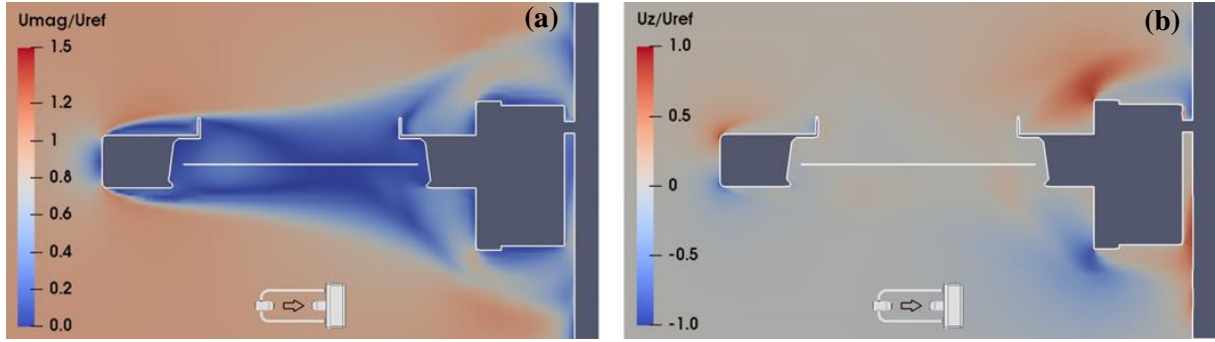


Figure 7.11: CFD simulation at $U_{ref} = 10 \text{ m s}^{-1}$ and $\alpha = 0^\circ$; maps of the normalized magnitude U_{mag}/U_{ref} (a) and vertical component U_z/U_{ref} (b) of the flow velocity, along the (X, Z) section of the flow field at $Y = 0$. The white horizontal line indicates the position of the sensing area of the instrument, while the small arrow indicates the undisturbed flow direction.

In Figure 7.11, at $\alpha = 0^\circ$, the receiver head is the first bluff-body obstacle to the flow, which generates accelerated zones (7.11a) and vertical velocity components (7.11b) above and below the sensing area of the instrument (white horizontal line), and a recirculation zone just downstream of the obstacle, with reduced velocity and high turbulence (as shown Figure 7.14a).

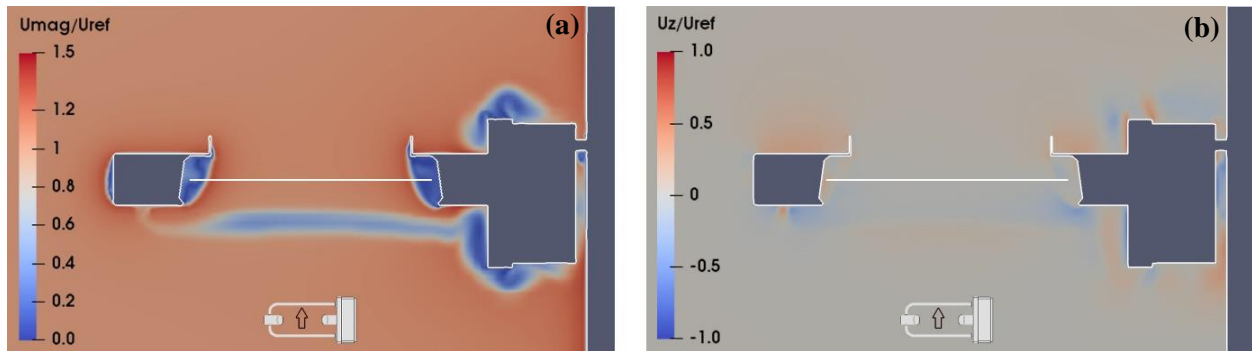


Figure 7.12: CFD simulation at $U_{ref} = 10 \text{ m s}^{-1}$ and $\alpha = 90^\circ$; maps of the normalized magnitude U_{mag}/U_{ref} (a) and vertical component U_z/U_{ref} (b) of the flow velocity, along the (X, Z) section of the flow field at $Y = 0$. The white horizontal line indicates the position of the sensing area of the instrument, while the small arrow indicates the undisturbed flow direction.

In Figure 7.12, at $\alpha = 90^\circ$, the flow near the sensing area is mostly undisturbed. The shedding of vortices generated by the supporting arms produces only a limited influence on the velocity magnitude and remains below the sensing area, while recirculation zones are concentrated near the receiving head, the instrument box, and the emitting head. Vertical velocity components are present only close to the instrument body, except for a limited amount of downdraft and updraft, generated by the vortex shedding, below the sensing area. Turbulence close to the laser beam is minimal (see Figure 7.14b).

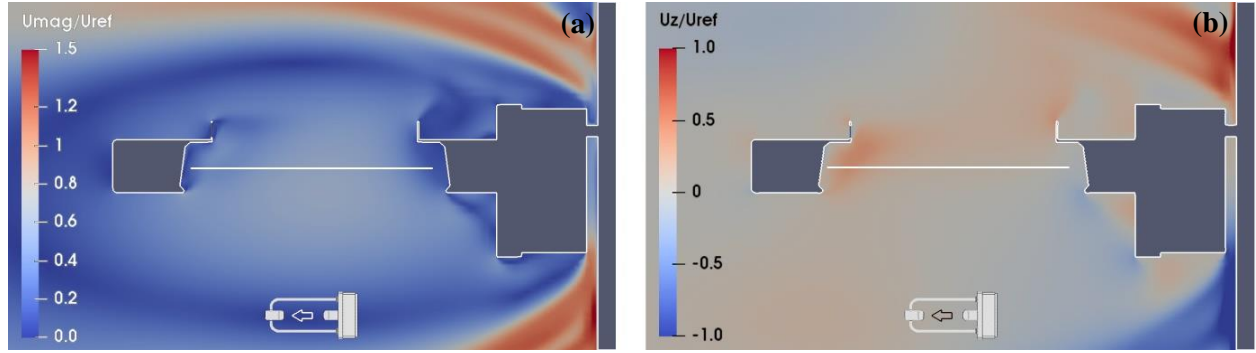


Figure 7.13: CFD simulation at $U_{ref} = 10 \text{ m s}^{-1}$ and $\alpha = 180^\circ$; maps of the normalized magnitude U_{mag}/U_{ref} (a) and vertical component U_z/U_{ref} (b) of the flow velocity, along the (X, Z) section of the flow field at $Y = 0$. The white horizontal line indicates the position of the sensing area of the instrument, while the small arrow indicates the undisturbed flow direction.

In Figure 7.13, at $\alpha = 180^\circ$, the circuitry box acts as a large bluff-body obstacle for the flow and, together with the supporting pole, generates a large recirculation zone completely enclosing the instrument body. Above the sensing area, two zones of first accelerated and then decelerated flow are present, with a considerable updraft and generation of turbulence due to the recirculation effect (see Figure 7.14c).

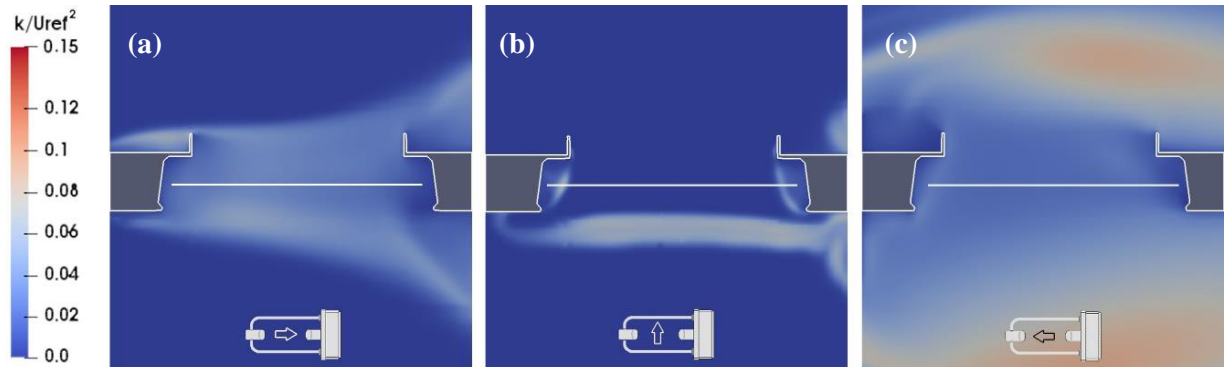


Figure 7.14: Maps of the normalized turbulent kinetic energy (k/U_{ref}^2) from CFD simulations at $U_{ref} = 10 \text{ m s}^{-1}$ along the (X, Z) section of the flow field at $Y = 0$ and for $\alpha = 0^\circ$, 90° , and 180° in the left-, central, and right-hand panels, respectively. The white horizontal line indicates the position of the sensing area of the instrument, while the small arrow indicates the undisturbed flow direction.

The presence of turbulence and vortex structures near the instrument body is visualized in Figure 7.15 by means of the Q-criterion (Hunt et al., 1988). At $\alpha = 0^\circ$ (Figure 7.15a), the wake generated by the instrument receiving head is highlighted, affecting the sensing area of the instrument and the flow region above it. At $\alpha = 90^\circ$ (Figure 7.15b), neither the turbulence structures produced by the two heads and the circuitry box, nor the turbulent wake produced by the supporting arm affect the sensing area of the instrument. At $\alpha = 180^\circ$ (Figure 7.15c), the circuitry box produces large vortex structures that completely envelop the instrument sensing area.

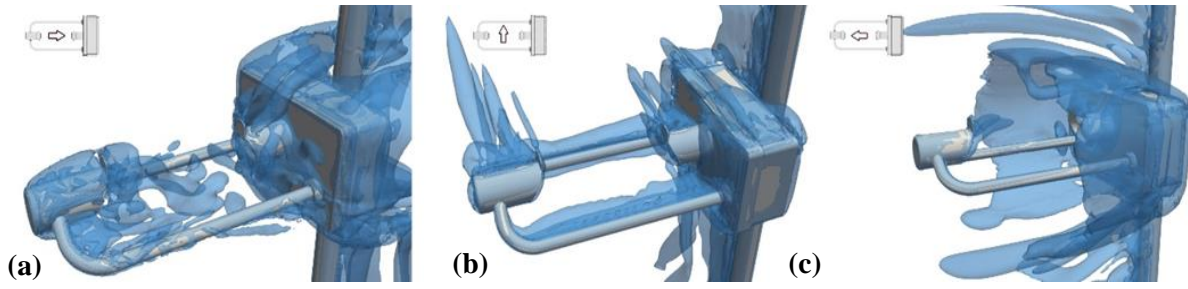


Figure 7.15: Visualization of the turbulent structures around the instrument using the Q -criterion at $U_{ref} = 10 \text{ m s}^{-1}$ and $\alpha = 0^\circ, 90^\circ$, and 180° in the left-, central-, and right-hand panels, respectively.

Comparable results were obtained at further wind velocity and directions. Recirculation and vertical velocity components near the sensing area non-linearly decrease from the 0° configuration to the 90° configuration, where a minimum is reached, and then increase again approaching the 180° configuration, where the maximum amount of flow disturbance is obtained.

To compare the effects of the wind between different instrument configurations, a control volume is defined (just above the sensing area) as a box with a length of 0.228 m, a height of 0.1 m, and a width of 0.05 m. The lower face of the control volume coincides with the laser beam. This volume represents the portion of the wind field having a strong potential to influence hydrometeors when approaching the instrument sensing area and provides an overall indication of the wind field deformation due to the presence of the instrument body.

The average of the results obtained for the five wind speed values simulated is reported for each wind direction in terms of normalised velocity components and turbulent kinetic energy. Additionally, the percentage of the control volume where updraft or downdraft is observed is shown, defined as the ratio between the volume of the cells where vertical velocity is positive (updraft) or negative (downdraft) and the total size of the control volume.

Maximum and average values of the vertical velocity components are reported in Table 7.5. It is confirmed that the lower impact is associated with the two configurations at 0° and 90° (and nearby angles). Maximum values are in general higher when the wind impacts at an angle with respect to the instrument axis. The 22.5° , 45° , 135° , and 157.5° configurations produce the highest values, because the flow is not blocked like in the 0° or 180° configurations, differently from angles close to 90° where the instrument presents the most favourable cross-section obstacle to the flow.

In terms of average values and extension (percentage within the control volume), updraft is predominant (see the second-last column). The only two exceptions are the 135° and 157.5° configurations, where the circuitry box, with its large, slanted, bluff-body obstruction to the flow, produces predominant downdraft components in the control volume (see last column).

Table 7.6 shows the horizontal velocity components. As expected, the longitudinal velocity is predominantly influenced by the flow blockage due to the instrument body. Maximum and average longitudinal velocities gradually increase from the 0° configuration to the 90° configuration, then decrease towards the configuration at 180° . A sudden jump is evident between 157.5° and 180° due to the impact of the circuitry box that produces strong recirculation, which is also responsible of the change of sign of the

average velocity. The minimum longitudinal velocity shows quite limited variations, with comparable backward components between the various configurations, except at $\alpha = 180^\circ$.

Table 7.5: Updraft and downdraft components within the control volume, obtained from CFD simulations as an average over the five wind speed values investigated.

Wind Direction	Max Updraft U_z/U_{ref}	Max Downdraft U_z/U_{ref}	Avg. Updraft U_z/U_{ref}	Avg. Downdraft U_z/U_{ref}	% Volume Updraft	% Volume Downdraft
0°	0.240	0.097	0.052	0.020	74.5	25.5
22.5°	0.629	0.386	0.095	0.052	79.3	20.7
45°	0.679	0.254	0.077	0.035	86.5	13.5
67.5°	0.410	0.150	0.057	0.022	91.3	8.7
90°	0.281	0.257	0.030	0.025	82.9	17.1
112.5°	0.553	0.158	0.041	0.030	92.9	7.1
135°	0.709	0.257	0.068	0.070	30.6	69.4
157.5°	0.649	0.410	0.068	0.159	3.2	96.8
180°	0.430	0.258	0.098	0.048	93.9	6.1

Table 7.6: Normalised longitudinal and transversal components within the control volume, obtained from CFD simulations as an average over the five wind speed values investigated.

Wind Direction	Max U_x/U_{ref}	Avg. U_x/U_{ref}	Min U_x/U_{ref}	Max U_y/U_{ref}	Avg. U_y/U_{ref}	Min U_y/U_{ref}
0°	0.995	0.328	-0.287	0.130	-0.001	-0.125
22.5°	1.036	0.629	-0.200	0.592	0.068	-0.472
45°	1.122	0.810	-0.299	0.643	0.097	-0.529
67.5°	1.163	0.956	-0.265	0.551	0.080	-0.647
90°	1.272	1.041	-0.287	0.656	0.025	-0.647
112.5°	1.236	0.936	-0.127	0.118	-0.048	-0.409
135°	1.203	0.663	-0.250	0.247	-0.099	-0.731
157.5°	1.092	0.366	-0.179	0.342	-0.097	-0.888
180°	0.172	-0.337	-0.551	0.255	0.001	-0.253

Transversal velocity components have a clearly different behaviour. For the 0° and 180° configurations, the average velocity is close to zero to indicate, as expected, that the flow is symmetrical, and the maximum

and minimum values are limited. The other configurations present higher values of maximum, minimum, and average transversal velocity. At $\alpha = 90^\circ$, where the gauge surfaces are mostly parallel or perpendicular to the flow, high maximum and minimum but low average values are obtained, because transversal velocity components are only present near the instrument receiving and transmitting heads.

Table 7.7 shows the standard deviation of the normalised velocity components and turbulent kinetic energy. The standard deviation of the longitudinal component suggests that the flow is more uniform for angles near 90° and that the strong recirculation observed at $\alpha = 180^\circ$ is relatively uniform close to the instrument sensing area. The standard deviation for both the transversal and vertical velocity components shows that the least uniform fields occur for shallow angles between the wind direction and the main symmetry axis of the instrument.

The maximum turbulent kinetic energy has a limited variability, while the average values change significantly depending on the wind direction. This means that the maximum energy of the generated eddies does not change much with the wind direction, but the number and distribution of those eddies (and therefore the overall turbulence) is strongly affected by the instrument blockage. The standard deviation of the turbulent kinetic energy shows the highest values at $\alpha = 22.5^\circ$ and 135° .

Table 7.7: Standard deviation of the normalised velocity components and statistics of the turbulent kinetic energy within the control volume, obtained from CFD simulations as an average over the five wind speed values investigated.

Wind Direction	Std. Dev. U_x/U_{ref}	Std. Dev. U_y/U_{ref}	Std. Dev. U_z/U_{ref}	Max k/U_{ref}^2	Avg. k/U_{ref}^2	Std. Dev. k/U_{ref}^2
0°	0.337	0.030	0.049	0.057	0.026	0.013
22.5°	0.345	0.115	0.110	0.084	0.012	0.020
45°	0.333	0.125	0.084	0.096	0.006	0.015
67.5°	0.257	0.111	0.058	0.086	0.003	0.009
90°	0.200	0.087	0.043	0.057	0.002	0.005
112.5°	0.292	0.064	0.047	0.067	0.007	0.014
135°	0.433	0.130	0.101	0.077	0.016	0.019
157.5°	0.346	0.199	0.111	0.057	0.030	0.015
180°	0.131	0.061	0.078	0.086	0.028	0.011

Depending on the wind direction, near and above the sensing area the normalised average updraft is between 3% and 10% (with peak velocities up to 70% of the freestream value), while the normalised downdraft is between 2% and 16% (with peaks up to 40% of the freestream value). The horizontal velocity component also increases significantly, up to 27%, and even reverses its direction (with values up to 55% of the freestream velocity) due to the induced recirculation. Strong transversal velocity components are also present, with normalised peak values up to 88% and average values up to 10%. These strong velocity

gradients near the instrument body are non-negligible and potentially affect the approaching hydrometeors. These are indeed slowed down by strong updraft components or diverted away from the sensing area by strong transversal velocity components. Turbulence also changes considerably depending on the wind direction, with configurations that on average reach up to 15 times the kinetic energy of the less impacting ones.

The most favourable configuration is at $\alpha = 90^\circ$, presenting the lowest value of turbulence and among the lowest values of both updraft and downdraft components. It is therefore expected that this configuration would introduce the least amount of bias in measurements taken under the influence of wind. Angles close to 90° also present favourable results while the configurations at 0° and especially 180° are the worst performing ones, with the latter producing the strongest impact on the nearby airflow conditions. The occurrence of such configurations should be minimised in field installations, and extreme care should be taken in analysing measurements taken in such conditions, since the associated wind-induced bias is expected to be significant.

7.4.2 Thies LPM time dependent approach

Consistently with the results of the time independent approach, wind velocity maps in the (X, Z) section of the flow field at $Y=0$, for $U_{ref} = 10 \text{ m s}^{-1}$ and $\alpha = 0^\circ$ and 90° are shown in Figures 7.16, 7.17, 7.18 and 7.19, for both the average and the instantaneous flow fields of the time dependent simulation (LES). The same colour coding is also maintained to present the results.

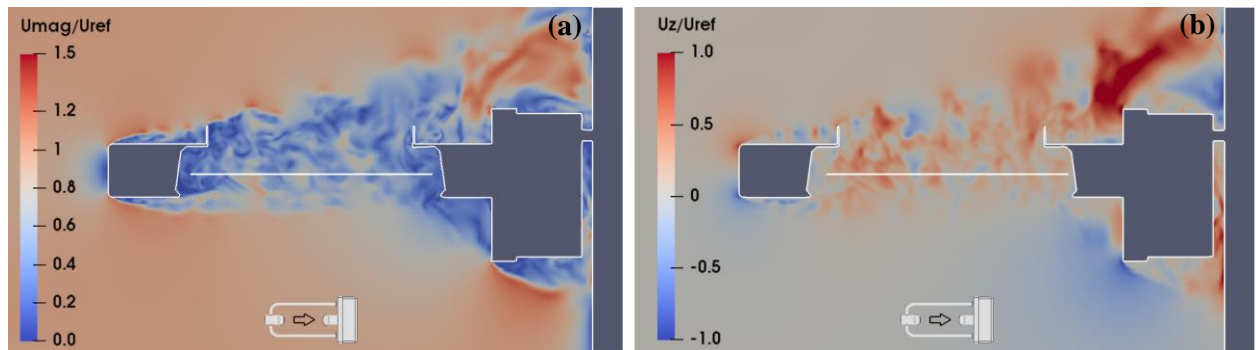


Figure 7.16: Instantaneous velocity field from the LES at $U_{ref} = 10 \text{ m s}^{-1}$ and $\alpha = 0^\circ$; maps of the normalized magnitude U_{mag}/U_{ref} (a) and vertical component U_z/U_{ref} (b) of the flow velocity, along the (X, Z) section of the flow field at $Y = 0$. The white horizontal line indicates the position of the sensing area of the instrument, while the small arrow indicates the undisturbed flow direction.

Figure 7.16 shows strong recirculation and turbulence close to the instrument sensing area, due to the wind impacting the instrument head. In terms of vertical velocity components, a slight prevalence of updraft components is shown. The average field, presented in Figure 7.17, is in good accordance with the time independent simulations results, but shows lower velocity gradients and a moderate influence of the updraft, like for the instantaneous flow field.

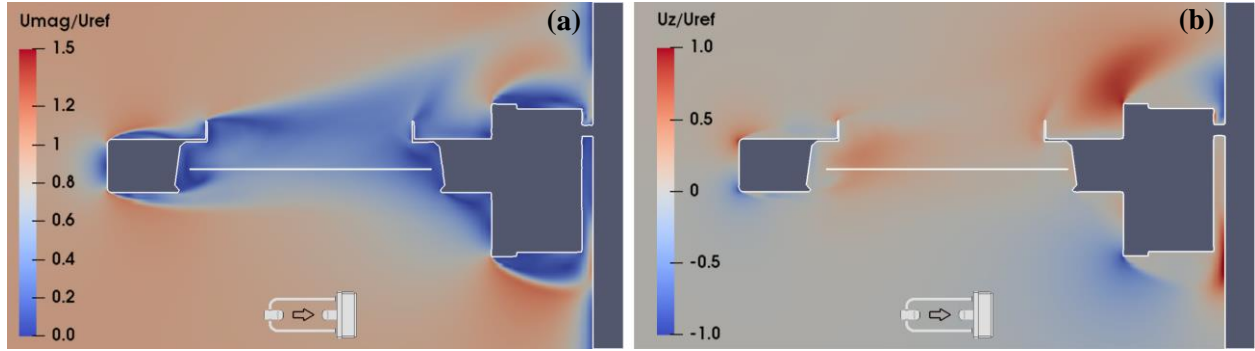


Figure 7.17: Averaged velocity field from the LES at $U_{ref} = 10 \text{ m s}^{-1}$ and $\alpha = 0^\circ$; maps of the normalized magnitude U_{mag}/U_{ref} (a) and vertical component U_z/U_{ref} (b) of the flow velocity, along the (X, Z) section of the flow field at $Y = 0$. The white horizontal line indicates the position of the sensing area of the instrument, while the small arrow indicates the undisturbed flow direction.

Figure 7.18 (instantaneous velocity field) and Figure 7.19 (average velocity field) show that the flow near the sensing area is mostly undisturbed. Especially in Figure 7.18, the shedding of vortices generated by the supporting arms is clearly visible, having a limited influence on the velocity magnitude and remaining confined below the sensing area. Recirculation zones are concentrated near the receiving head, the instrument box, and the emitting head while turbulence close to the laser beam is minimal. Results are in good agreement with the time independent simulation, showing slightly lower velocity gradients, which may be due to turbulence induced diffusion that produces a smoothing effect.

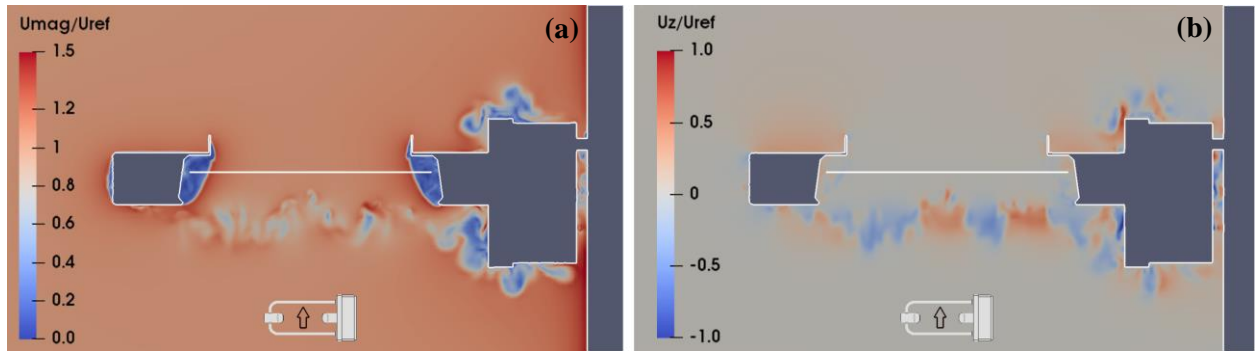


Figure 7.18: Instantaneous velocity field from the LES at $U_{ref} = 10 \text{ m s}^{-1}$ and $\alpha = 90^\circ$; maps of the normalized magnitude U_{mag}/U_{ref} (a) and vertical component U_z/U_{ref} (b) of the flow velocity, along the (X, Z) section of the flow field at $Y = 0$. The white horizontal line indicates the position of the sensing area of the instrument, while the small arrow indicates the undisturbed flow direction.

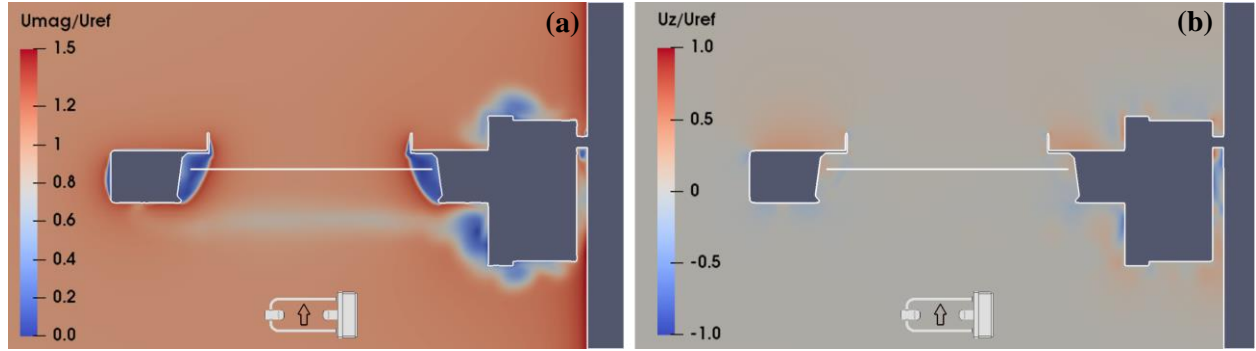


Figure 7.19: Averaged velocity field from the LES at $U_{ref} = 10 \text{ m s}^{-1}$ and $\alpha = 90^\circ$; maps of the normalized magnitude U_{mag}/U_{ref} (a) and vertical component U_z/U_{ref} (b) of the flow velocity, along the (X, Z) section of the flow field at $Y = 0$. The white horizontal line indicates the position of the sensing area of the instrument, while the small arrow indicates the undisturbed flow direction.

In Figure 7.20, turbulence and vortex structures are highlighted near the instrument body by means of the Q -criterion. At $\alpha = 0^\circ$ (Figure 7.20a), the wake generated by the instrument receiving head strongly affects the sensing area of the instrument and the flow region above it. At $\alpha = 90^\circ$ (Figure 7.20b), neither the turbulence structures produced by the two heads and the circuitry box, nor the turbulent wake produced by the supporting arm significantly affect the sensing area of the instrument.

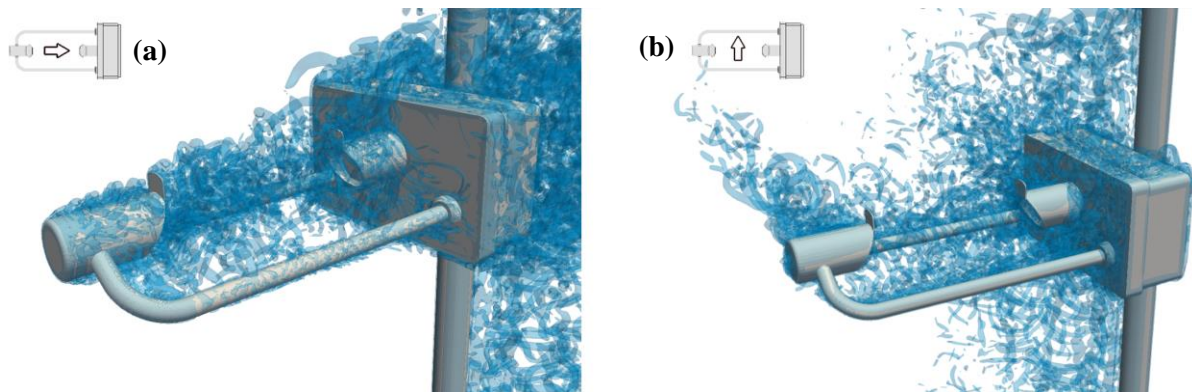


Figure 7.20: Visualization of the turbulent structures around the instrument using the Q -criterion at $U_{ref} = 10 \text{ m s}^{-1}$ for $\alpha = 0^\circ$ (a) and $\alpha = 90^\circ$ (b).

Conclusions similar to those presented for the time independent simulation can be reached: recirculation and vertical velocity components near the sensing area are stronger for the 0° configuration, while the 90° configuration presents the least amount of flow disturbance.

The effects of wind in the different instrument configurations are again computed using the same control volume as defined before (0.228 m long, 0.1 m tall and 0.05 m wide). Maximum and average values of the vertical velocity components are reported in Table 7.8. Results show larger maximum values of the updraft and downdraft (for both the 0° and the 90° configurations) if compared with the time independent simulation. Averages are higher for the 0° configuration while they are very close for the 90° configuration.

In terms of extension (percentage of the control volume), updraft is predominant (see the second-last column), especially for the 0° configuration where downdraft almost completely disappears.

Table 7.8: Updraft and downdraft components within the control volume, obtained from the LES as an average over the four combinations of wind speed and direction investigated.

Wind Direction	U_{ref}	Max Updraft U_z/U_{ref}	Max Downdraft U_z/U_{ref}	Avg. Updraft U_z/U_{ref}	Avg. Downdraft U_z/U_{ref}	% Volume Updraft	% Volume Downdraft
0°	5	0.400	0.426	0.113	0.067	96.93	3.07
0°	10	0.441	0.447	0.125	0.073	96.47	3.53
90°	5	0.338	0.524	0.021	0.039	82.53	17.47
90°	10	0.331	0.516	0.020	0.048	72.84	27.16

In Table 7.9, the horizontal velocity components are reported. Longitudinal and transversal velocities are in good agreement with the time independent simulation, in terms of both the extreme and average values.

As before, the longitudinal velocity is predominantly influenced by the flow blockage due to the instrument body. Maximum and average longitudinal velocities are lower for $a = 0^\circ$ than for the $a = 90^\circ$ configuration. The minimum longitudinal velocity reflects the presence of strong recirculation zones, quite widespread for the $a = 0^\circ$ configuration while more contained close to the instrument body for $a = 90^\circ$.

Table 7.9: Normalised longitudinal and transversal velocity components within the control volume, obtained from the LES as an average over the four combinations of wind speed and direction investigated.

Wind Direction	U_{ref}	Max U_x/U_{ref}	Avg. U_x/U_{ref}	Min U_x/U_{ref}	Max U_y/U_{ref}	Avg. U_y/U_{ref}	Min U_y/U_{ref}
0°	5	0.957	0.322	-0.341	0.331	0.000	-0.336
0°	10	0.950	0.332	-0.333	0.364	-0.002	-0.363
90°	5	1.351	1.042	-0.252	0.764	0.021	-0.773
90°	10	1.354	1.049	-0.176	0.750	0.016	-0.769

Transversal velocity components also show a clear difference between the two configurations, with larger extremes for the configuration at $a = 90^\circ$. The average velocity is always close to zero, indicating, as expected, that the flow is symmetrical for $a = 0^\circ$, while at $a = 90^\circ$, where the gauge surfaces are mostly parallel or perpendicular to the flow, large maximum and minimum but low average values are obtained, because transversal velocity components are only present near the receiving and transmitting heads of the instrument.

7.4.3 OTT Parsivel² time independent approach

For the OTT Parsivel², results are presented, consistently with the previous cases, as wind velocity maps in the (X, Z) section of the flow field at $Y=0$, for $U_{ref} = 10 \text{ m s}^{-1}$ and $\alpha = 0^\circ$, 45° , and 90° in Figures 7.21, 7.22, 7.23, respectively (using the same colour coding).

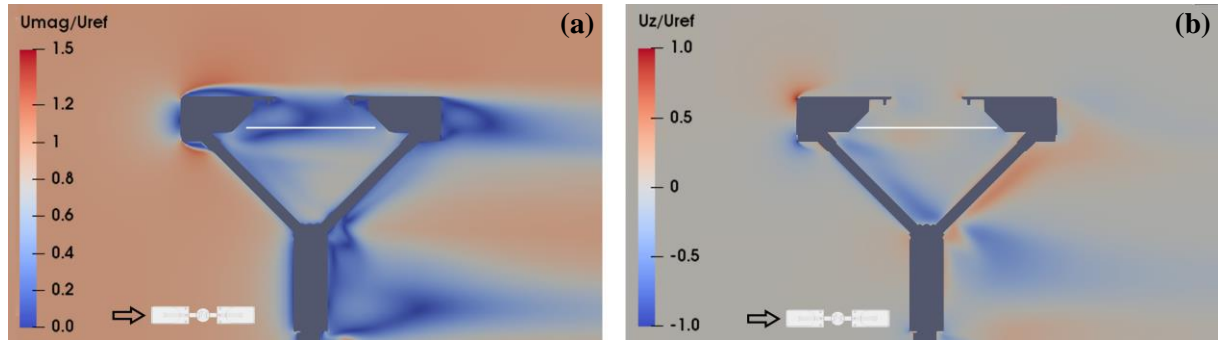


Figure 7.21: CFD simulation at $U_{ref} = 10 \text{ m s}^{-1}$ and $\alpha = 0^\circ$; maps of the normalized magnitude U_{mag}/U_{ref} (a) and vertical component U_z/U_{ref} (b) of the flow velocity, along the (X, Z) section of the flow field at $Y = 0$. The white horizontal line indicates the position of the sensing area of the instrument, while the small arrow indicates the undisturbed flow direction.

In Figure 7.21, at $\alpha = 0^\circ$, the flow first impacts one of the two heads, which shields the sensing area of the instrument. Accelerated zones (Figure 7.21a) are generated above the instrument body and a separation layer is formed, that however tends to remain confined close to the surface. Strong recirculation is observed near the laser beam and above it. Vertical velocity components (Figure 7.21b) are for the most part concentrated near the stagnation point, where the flow first impact the instrument body. Nevertheless, due to recirculation, both updraft and downdraft components are visible near and above the sensing area (white horizontal line). The supporting arms also contribute to the formation of a recirculation zone below them. Intense turbulence is observed both above and especially below the sensing area (see Figure 7.24a).

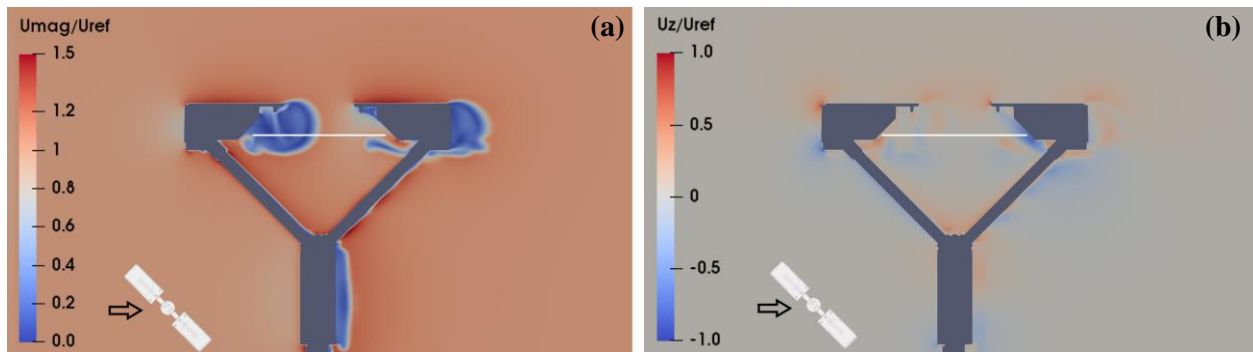


Figure 7.22: CFD simulation at $U_{ref} = 10 \text{ m s}^{-1}$ and $\alpha = 45^\circ$; maps of the normalized magnitude U_{mag}/U_{ref} (a) and vertical component U_z/U_{ref} (b) of the flow velocity, along a vertical section of the flow field at $Y = 0$. The white horizontal line indicates the position of the sensing area of the instrument, while the small arrow indicates the undisturbed flow direction.

In Figure 7.22, at $\alpha = 45^\circ$, the flow near the sensing area presents a non-symmetrical behaviour, with recirculation and turbulence that are limited to only one of the instrument heads. The shedding of vortices generated by the supporting arms is not visible in these images since it is in the wake and does not produce disturbance to the flow near the sensing area. Vertical velocity components are present both in terms of downdraft and updraft above and below the sensing area. Turbulence close to the laser beam is very high in the wake of one of the heads while it is minimal in the rest of the domain (see Figure 7.24b).

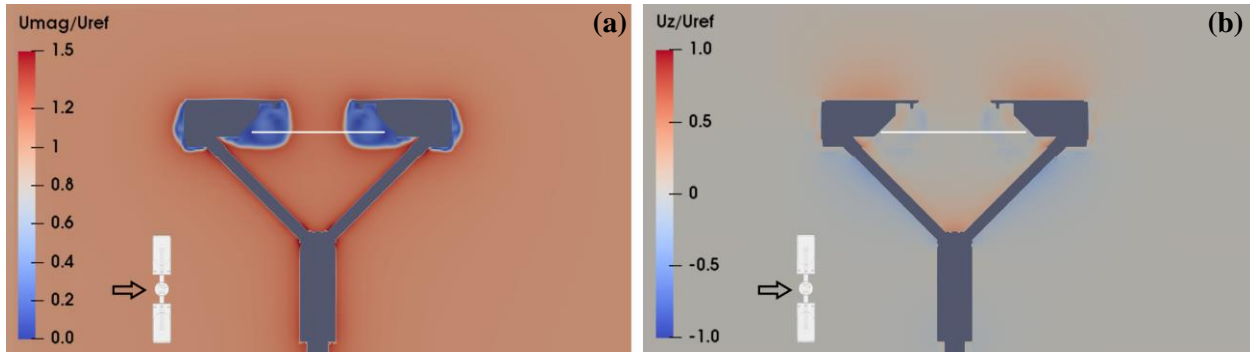


Figure 7.23: CFD simulation at $U_{ref} = 10 \text{ m s}^{-1}$ and $\alpha = 90^\circ$; maps of the normalized magnitude U_{mag}/U_{ref} (a) and vertical component U_z/U_{ref} (b) of the flow velocity, along the (Y, Z) section of the flow field at $X = 0$. The white horizontal line indicates the position of the sensing area of the instrument, while the small arrow indicates the undisturbed flow direction.

In Figure 7.23, at $\alpha = 90^\circ$, the flow pattern is symmetrical, and disturbance is confined close to the instrument heads. A slight increase in flow velocity is visible close to the instrument sensing area. Furthermore, vertical velocity components are present, in the form of downdraft close to the instrument head and updraft in between. Strong updraft is also visible over the two heads due to their shape. Turbulence is minimal and is confined near the instrument body (see Figure 7.24c).

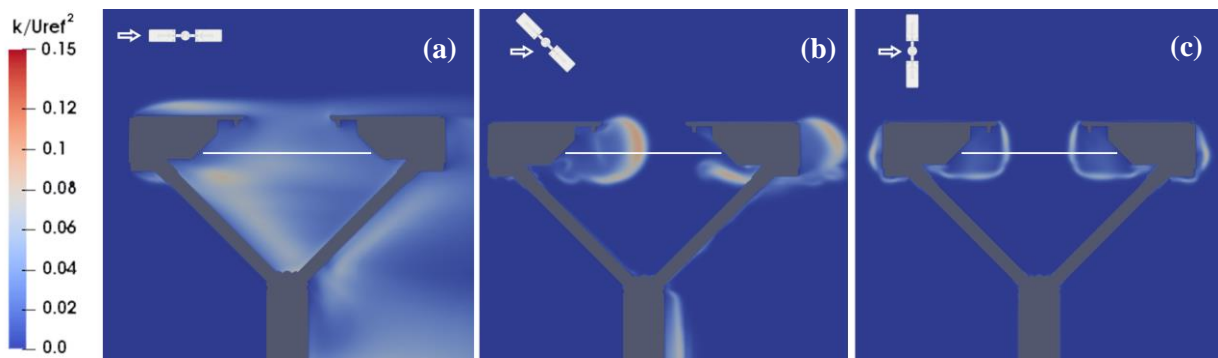


Figure 7.24: Maps of the normalized turbulent kinetic energy (k/U_{ref}^2) from CFD simulations at $U_{ref} = 10 \text{ m s}^{-1}$ along vertical sections of the flow field at the origin and for $\alpha = 0^\circ$, 45° , and 90° in the left-, central, and right-hand panels, respectively. The white horizontal line indicates the position of the sensing area of the instrument, while the small arrow indicates the undisturbed flow direction.

The presence of turbulence and vortex structures near the instrument body is visualized in Figure 7.25 by means of the Q -criterion. At $\alpha = 0^\circ$ (Figure 7.25a), the wake generated by the instrument body strongly affects the sensing area and the flow region above it. At $\alpha = 45^\circ$ (Figure 7.25b), turbulent structures are still present near the sensing area, even if most of the turbulence is shown to develop in the wake. At $\alpha = 90^\circ$ (Figure 7.25c), the turbulence structures produced by the two heads and the turbulent wake produced by the supporting arm are advected by the flow away from the sensing area, minimizing their impact.

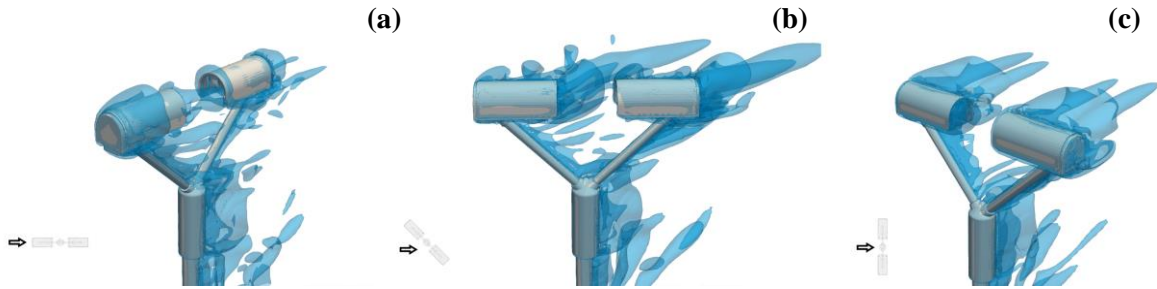


Figure 7.25: Visualization of the turbulent structures around the instrument using the Q -criterion at $U_{ref} = 10 \text{ m s}^{-1}$ and $\alpha = 0^\circ$ (a), 45° (b), and 90° (c).

Similar results were obtained at further wind velocity and directions. Recirculation and vertical velocity components near the sensing area non-linearly decrease moving from the $\alpha = 0^\circ$ configuration to the $\alpha = 90^\circ$ configuration, where a minimum is reached.

To compare the effects of the wind between different instrument configurations, a control volume is defined (just above the sensing area) as a box with a length of 0.18 m, a height of 0.1 m, and a width of 0.05 m. The lower face of the control volume coincides with the laser beam. This volume represents the portion of the wind field having a strong potential to influence hydrometeors when approaching the instrument sensing area and provides an overall indication of the wind field deformation due to the presence of the instrument body.

The average of the results obtained for the seven wind speed values simulated is reported for each wind direction in terms of normalised velocity components and turbulent kinetic energy. Additionally, the percentage of the control volume where updraft or downdraft is observed is shown, defined as the ratio between the volume of the cells where vertical velocity is positive (updraft) or negative (downdraft) and the total size of the control volume.

The maximum and average values of the vertical velocity components are reported in Table 7.10. It is confirmed that the lower impact is associated with the configuration at $\alpha = 90^\circ$. Maximum values are instead higher when the wind impacts at a shallow angle with respect to the instrument axis ($\alpha = 22.5^\circ$). This is due to the separation layer that – for a shallow angle – directly intersects the instrument sensing area. The same is observed in terms of average values, with a maximum for $\alpha = 22.5^\circ$ and non-linearly decreasing with increasing the angle α . In terms of the percentage volume of updraft and downdraft it is evident that, starting from $\alpha = 0^\circ$, downdraft is prevalent, while with increasing the angle α the downdraft quickly decreases, and the updraft is prevalent for the other configurations.

Table 7.10: Updraft and downdraft components within the control volume, obtained from CFD simulations as an average over the five wind speed values investigated.

Wind Direction	Max Updraft U_z/U_{ref}	Max Downdraft U_z/U_{ref}	Avg. Updraft U_z/U_{ref}	Avg. Downdraft U_z/U_{ref}	% Volume Updraft	% Volume Downdraft
0°	0.392	0.172	0.055	-0.058	21.1	78.9
22.5°	0.539	0.165	0.117	-0.060	79.3	20.7
45°	0.403	0.145	0.095	-0.044	86.9	13.1
67.5°	0.158	0.020	0.065	-0.008	99.8	0.2
90°	0.097	0.022	0.032	-0.002	90.2	9.8

Table 7.11 shows the horizontal velocity components. As expected, the longitudinal velocity is predominantly influenced by the flow blockage due to the instrument body. Maximum and average longitudinal velocities gradually increase from the $\alpha = 0^\circ$ configuration to the $\alpha = 90^\circ$ configuration. It is also evident that for $\alpha = 67^\circ$ and $\alpha = 90^\circ$ no reversal flow is present since the minimum values are still positive (and close to the undisturbed velocity). The maximum recirculation instead occurs for the $\alpha = 0^\circ$ configuration.

Table 7.11: Normalised longitudinal and transversal components within the control volume, obtained from CFD simulations as an average over the five wind speed values investigated.

Wind Direction	Max U_x/U_{ref}	Avg. U_x/U_{ref}	Min U_x/U_{ref}	Max U_y/U_{ref}	Avg. U_y/U_{ref}	Min U_y/U_{ref}
0°	0.909	0.245	-0.356	0.171	-0.002	-0.158
22.5°	1.111	0.330	-0.269	0.700	0.030	-0.379
45°	1.134	0.813	-0.161	0.579	0.038	-0.409
67.5°	1.197	1.091	0.974	0.239	0.020	-0.250
90°	1.196	1.109	0.968	0.090	0.001	-0.089

Average values of the transversal velocity remain low in all cases, while intermediate angles present strong maximum and minimum values, also due to the separation layer that is generated, at least partially, inside the control volume. Furthermore, the low values of transversal velocity components visible for the $\alpha = 0^\circ$ and $\alpha = 90^\circ$ configurations, indicate, as expected, that the flow is symmetrical in those two cases.

Table 7.12 shows the standard deviation of the normalised velocity components and turbulent kinetic energy. The standard deviation of the longitudinal component suggests that the flow is more uniform for

angles near 90° , while higher values of standard deviation are observed for angles close to 0° . The standard deviation for both the transversal and vertical velocity components shows a similar pattern, suggesting that the least amount of disturbance of the flow field is for the configuration at $\alpha = 90^\circ$.

The maximum turbulent kinetic energy is higher for the $\alpha = 45^\circ$ configuration and then decreases to negligible levels for $\alpha = 90^\circ$. Furthermore, average values and standard deviations show the same behaviour as the maximum values. This means that the strongest eddies are obtained for $\alpha = 22.5^\circ$ and $\alpha = 45^\circ$, while they are not as strong for the configuration at $\alpha = 0^\circ$. Meanwhile, the other two angles ($\alpha = 67.5^\circ$ and $\alpha = 90^\circ$) do not show any significant eddy production.

Table 7.12: Standard deviation of the normalised velocity components and statistics of the turbulent kinetic energy within the control volume, obtained from CFD simulations as an average over the five wind speed values investigated.

Wind Direction	Std. Dev. U_x/U_{ref}	Std. Dev. U_y/U_{ref}	Std. Dev. U_z/U_{ref}	Max k/U_{ref}^2	Avg. k/U_{ref}^2	Std. Dev. k/U_{ref}^2
0°	0.307	0.039	0.070	0.045	0.027	0.007
22.5°	0.430	0.128	0.101	0.092	0.037	0.023
45°	0.363	0.145	0.077	0.095	0.025	0.032
67.5°	0.049	0.093	0.034	0.009	0.000	0.001
90°	0.066	0.032	0.030	0.000	0.000	0.000

Near and above the sensing area of the instrument, depending on the wind direction, the normalised average updraft is between 3% and 12% (with peak velocities of up to 54% of the freestream value), while the normalised downdraft is between 0% and 7% (with peaks up to 17% of the freestream value). The horizontal velocity component can increase up to 20% or sharply decrease to 25%, and, in some cases, can reverse its direction (with values up to 35% of the freestream velocity) due to the induced recirculation. Strong transversal velocity components are also present, with normalised peak values up to 58% while average values remain low with a maximum of 4%. The strong velocity gradients near the instrument body are non-negligible and potentially affect the approaching hydrometeors. These may change their trajectory due to strong updraft components or diverted away from the sensing area by strong transversal velocity components. Turbulence also changes considerably depending on the wind direction, with some configurations showing strong turbulence and others where it is negligible.

The most favourable configuration is at $\alpha = 90^\circ$, presenting the lowest value of turbulence and among the lowest values of both updraft and downdraft components. It is therefore expected that this configuration would introduce the least amount of bias in measurements taken under the influence of wind. Angles close to $\alpha = 90^\circ$ also present favourable results while the configurations at $\alpha = 22.5^\circ$ and $\alpha = 45^\circ$ are the worst performing ones, with the first producing the strongest impact on the nearby airflow conditions. The occurrence of such configurations should be minimised in field installations, and extreme care should be

taken in analysing measurements taken in such conditions, since the associated wind-induced bias is expected to be significant.

7.4.4 Vaisala WXT-520 time-independent approach

Sample results obtained from CFD simulations of the Vaisala WXT-520 are presented as wind velocity maps in the (X, Z) section of the flow field at $Y=0$, for $U_{ref} = 10 \text{ m s}^{-1}$ and three wind directions in Figures 7.26 ($\alpha = 0^\circ$), 7.27 ($\alpha = 30^\circ$) and 7.28 ($\alpha = 60^\circ$). The same colour coding as in the previous cases is used.

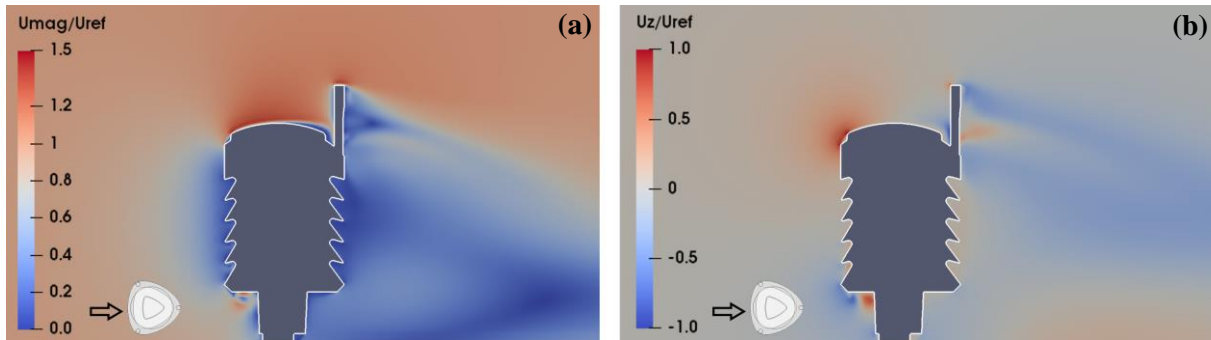


Figure 7.26: CFD simulation at $U_{ref} = 10 \text{ m s}^{-1}$ and $\alpha = 0^\circ$; maps of the normalized magnitude U_{mag}/U_{ref} (a) and vertical component U_z/U_{ref} (b) of the flow velocity, along the (X, Z) section of the flow field at $Y = 0$. The small arrow indicates the undisturbed flow direction.

In Figure 7.26, at $\alpha = 0^\circ$, the flow develops a strong separation layer over the instrument metal cover, which remains quite attached to the surface due to its curvature. An intense acceleration zone appears above the instrument sensing area (Figure 7.26a). The downstream wind measuring arm is impacted by wind after the metallic cover and therefore its wake develops downstream of the instrument, with no produced turbulence impacting the sensing area. Strong updraft occurs upstream of the instrument (Figure 7.26b), just before the metal cover, while downdraft is prevalent in the wake of the gauge. Also, turbulence is mostly developed in the wake of the instrument and close to the wind measuring arm, while it is very limited for the most part of the instrument sensing area (see Figure 7.29a).

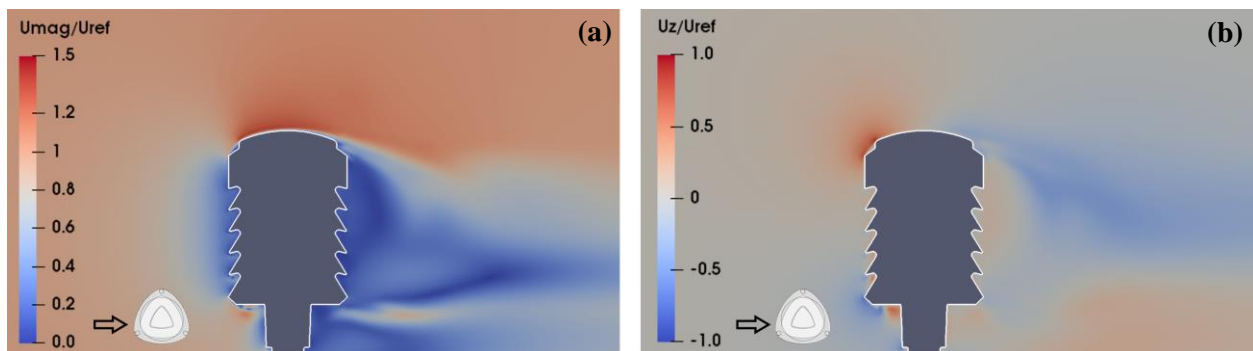


Figure 7.27: CFD simulation at $U_{ref} = 10 \text{ m s}^{-1}$ and $\alpha = 30^\circ$; maps of the normalized magnitude U_{mag}/U_{ref} (a) and vertical component U_z/U_{ref} (b) of the flow velocity, along the (X, Z) section of the flow field at $Y = 0$. The small arrow indicates the undisturbed flow direction.

In Figure 7.27, at $\alpha = 30^\circ$, the same behaviour is shown, with the flow forming a strong separation layer over the instrument metal cover. In this configuration, vortex shedding produced by the wind measuring arms is far from the $Y = 0$ plane and its effects are not visible. Strong recirculation is still present in the wake of the gauge. In terms of vertical velocity, strong updraft is still evident upstream of the instrument sensing area, which propagates downstream up to the half point of the metal cover, beyond which downdraft mostly occurs. In the wake, higher updraft components develop, but downdraft remains prevalent. Strong turbulence occurs in the wake, while over the instrument sensing area turbulence is even less intense than in the previous case (see Figure 7.29b).

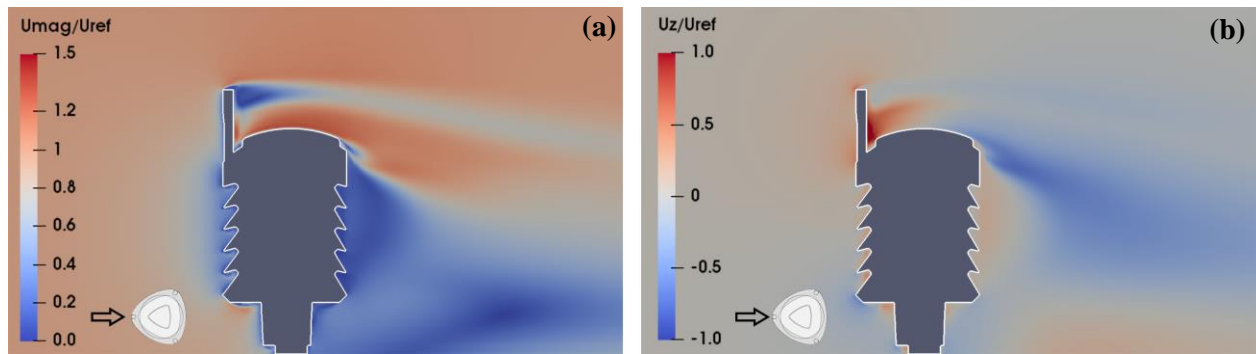


Figure 7.28: CFD simulation at $U_{ref} = 10 \text{ m s}^{-1}$ and $\alpha = 60^\circ$; maps of the normalized magnitude U_{mag}/U_{ref} (a) and vertical component U_z/U_{ref} (b) of the flow velocity, along the (X, Z) section of the flow field at $Y = 0$. The small arrow indicates the undisturbed flow direction.

In Figure 7.28, at $\alpha = 60^\circ$, one of the wind-measuring arms is upstream of the instrument sensing area and its wake propagates above it. The separation layer is still evident and, in this case, even more attached to the instrument surface. Above the sensing area, two accelerated and then decelerated flow zones are present. Strong updraft still occurs upstream of the metal cover, but the presence of the wind-measuring arm favours the downdraft flow, which is more widespread above the instrument. Stronger downdraft is also evident in the wake of the instrument while moderate turbulence, due to the recirculation effect generated by the wind-measuring arm, develops above the instrument sensing area (see Figure 7.29c).

The presence of turbulence and vortex structures near the instrument body is visualized in Figure 7.30 by means of the Q-criterion. At $\alpha = 0^\circ$ (Figure 7.30a), the wake generated by the three wind-measuring arms is advected away from the instrument sensing area. The incoming flow that impacts the instrument is, for the most part, able to smoothly surround it and turbulence due to its bluff-body shape is confined within the instrument wake. An almost identical behaviour occurs at $\alpha = 30^\circ$ (Figure 7.30b), where the wake of the wind-measuring arms still does not affect the flow directly above the instrument metal cover. Meanwhile, at $\alpha = 60^\circ$ (Figure 7.30c), one of the wind-measuring arms is directly blocking the flow and the generated turbulence that divides the flow over the instrument in two portions is clearly evident.

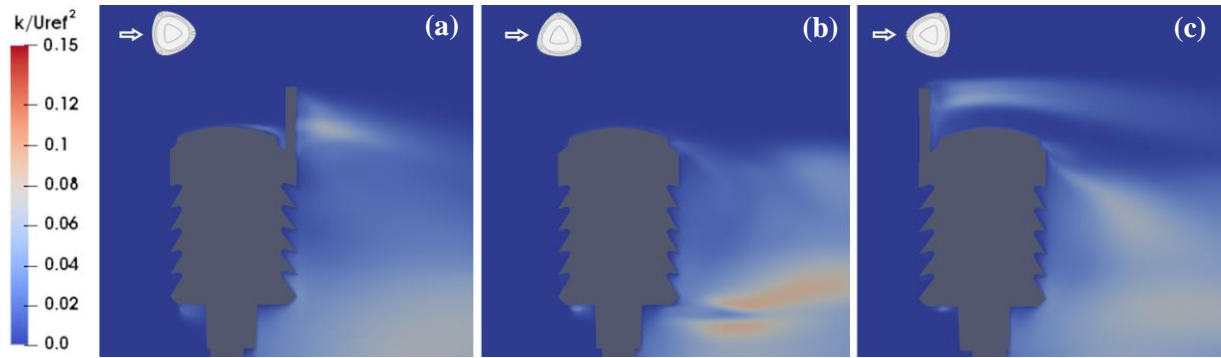


Figure 7.29: Maps of the normalized turbulent kinetic energy (k/U_{ref}^2) from CFD simulations at $U_{ref} = 10 \text{ m s}^{-1}$ along the (X, Z) section of the flow field at $Y = 0$ and for $\alpha = 0^\circ$ (a), 30° (b), and 90° (c). The small arrow indicates the undisturbed flow direction.

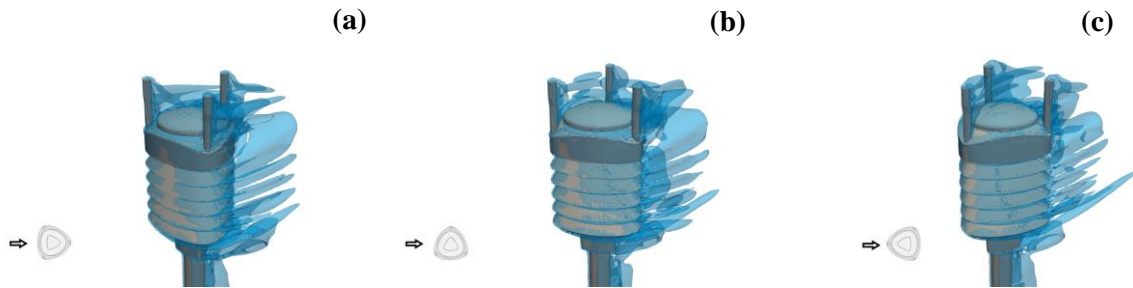


Figure 7.30: Visualization of the turbulent structures around the instrument using the Q -criterion at $U_{ref} = 10 \text{ m s}^{-1}$ and for $\alpha = 0^\circ$ (a), 30° (b), and 90° (c).

Among the three configurations investigated, the one at $\alpha = 60^\circ$ produces most of the disturbance over the instrument sensing area, while the other two configurations behave similarly and produce almost identical flow conditions above the instrument metal cover.

To compare the effects of wind between the different configurations, a control volume is defined (just above the sensing area) as a cylinder with a diameter of 0.09 m and a height of 0.1 m. The lower face of the control volume coincides with the topmost point of the instrument sensing area. This volume represents the portion of the wind field having a strong potential to influence hydrometeors when approaching the instrument sensing area and the flow characteristics inside this volume provide an overall indication of the wind field deformation due to the presence of the instrument body.

The average of the results obtained for the seven wind speed values simulated is reported in terms of normalised velocity components and turbulent kinetic energy, for each wind direction. Additionally, the percentage of the control volume where updraft or downdraft is observed is defined as the ratio between the volume of the cells where vertical velocity is positive (updraft) or negative (downdraft) and the total size of the control volume.

Maximum and average values of the vertical velocity components are reported in Table 7.13. It is confirmed that the highest impact is associated with the configuration at 60° . However, except for the maximum values, the average of both the updraft and downdraft is similar for all three configurations. In

particular, the average updraft is almost identical between the three configurations while downdraft is only slightly lower (in modulus) for the cases at $\alpha = 30^\circ$ and $\alpha = 60^\circ$, and sensibly lower at $\alpha = 0^\circ$. In terms of extension (percentage within the control volume), updraft is largely predominant (see the second-last column) for all the investigated configurations.

Table 7.13: Updraft and downdraft components within the control volume, obtained from CFD simulations as an average over the seven wind speed values investigated.

Wind Direction	Max Updraft U_z/U_{ref}	Max Downdraft U_z/U_{ref}	Avg. Updraft U_z/U_{ref}	Avg. Downdraft U_z/U_{ref}	% Volume Updraft	% Volume Downdraft
0°	0.521	-0.321	0.106	-0.069	96.659	3.341
30°	0.491	-0.411	0.109	-0.094	91.446	8.554
60°	0.784	-0.379	0.100	-0.093	87.546	12.454

Table 7.14 reports the horizontal velocity components. The maximum and average longitudinal velocity are close in the three configurations, while the minimum values increase with increasing α , due to the recirculation produced by the wind-measuring arms. Transversal components also show a similar behaviour, and both their maximum and minimum values increase with increasing the angle α . In terms of average transversal velocity, the two symmetrical configurations with respect to the flow ($\alpha = 0^\circ$ and $\alpha = 60^\circ$) show, as expected, nearly null average values, while at $\alpha = 30^\circ$ a limited net flow towards the positive Y is observed.

Table 7.14: Normalised longitudinal and transversal components within the control volume, obtained from CFD simulations as an average over the seven wind speed values investigated.

Wind Direction	Max U_x/U_{ref}	Avg. U_x/U_{ref}	Min U_x/U_{ref}	Max U_y/U_{ref}	Avg. U_y/U_{ref}	Min U_y/U_{ref}
0°	1.339	1.104	-0.022	0.216	-0.001	-0.217
30°	1.329	1.084	-0.093	0.275	0.039	-0.219
60°	1.312	1.087	-0.129	0.385	-0.001	-0.387

Table 7.15 shows the standard deviation of the normalised velocity components and turbulent kinetic energy. The standard deviation of the longitudinal velocity shows similar values in the three configurations, which indicates that blockage produced by the wind measuring arms is limited. The transversal velocity shows increasing standard deviation with increasing the angle α , and this is easily explained by the lack of symmetry of the instrument at $\alpha = 30^\circ$ and by the flow separation produced by one of the arms at $\alpha = 60^\circ$. Finally, the vertical velocity shows very similar values of the standard deviation. Both the maximum and

average turbulent kinetic energy have a limited variability with the wind direction, while the standard deviation remains low for all configurations. This means that the maximum energy of the generated eddies is in general low, and does not change much with the wind direction, even considering the presence of one of the wind-measuring arms in the flow path.

Table 7.15: Standard deviation of the normalised velocity components and statistics of the turbulent kinetic energy within the control volume, obtained from CFD simulations as an average over the seven wind speed values investigated.

Wind Direction	Std. Dev. U_x/U_{ref}	Std. Dev. U_y/U_{ref}	Std. Dev. U_z/U_{ref}	Max k/U_{ref}^2	Avg. k/U_{ref}^2	Std. Dev. k/U_{ref}^2
0°	0.178	0.038	0.117	0.061	0.004	0.005
30°	0.173	0.067	0.122	0.074	0.005	0.007
60°	0.185	0.082	0.126	0.059	0.005	0.007

For all wind directions, near and above the sensing area the normalised average updraft is between 11% and 12% (with peak velocities up to almost 80% of the freestream value), while the normalised downdraft is between 7% and 9% (with peaks up to 40% of the freestream value). The horizontal velocity component also increases significantly, up to 34%, and even reverses its direction (with values up to 13% of the freestream velocity) due to the recirculation induced by the wind measuring arm. Transversal velocity components are limited, with normalised peak values up to 38% and average values close to zero. The velocity gradients near the instrument body, mostly due to the flow acceleration and updraft, are non-negligible and potentially affect the approaching hydrometeors. These may be swiped away by the strong flow acceleration and their fall velocity may change significantly due to the strong updraft. The generated turbulence is for the most part absent from the instrument sensing area and is in general relatively weak.

The instrument behaves similarly under all the tested wind directions. However, while the configurations at $\alpha = 0^\circ$ and $\alpha = 30^\circ$ are expected to introduce a limited amount of bias in measurements taken under the influence of wind, for $\alpha = 60^\circ$, the presence of one of the wind-measuring arms upstream of the instrument sensing area is expected to produce a higher bias due to its shielding effect and increased turbulence. The occurrence of such configurations should be minimised in field installations; however, below results show that the wind direction is not the only factor influencing the wind-induced bias of the Vaisala WXT-520.

7.5 WIND TUNNEL TESTING AND VALIDATION

Validation of the CFD results was performed by means of an experimental campaign conducted in the WT facility available at the Department of Civil, Chemical and Environmental Engineering (DICCA) of the University of Genova. Measurements were taken using a multi-hole pressure probe, called “Cobra”, attached to a traversing arm with three degrees of freedom. By measuring the local pressure, the Cobra probe provides the three velocity components of the flow, in a range between 2 and 100 m s⁻¹ (TFI, 2011).

7.5.1 Validation of the time independent model for the Thies LPM

A full-scale Thies LPM instrument was installed on its supporting pole in the WT, fixed to a rotating baseplate. A laser beam was used to check the alignment between the longitudinal axis of the instrument and the head of the Cobra probe, fixed to the traversing system (see Figure 7.31). This operation was repeated by rotating the instrument around the supporting pole, for each of the nine wind directions investigated, to ensure that the WT flow did impact the instrument at the exact angle chosen for the numerical simulation.

For each rotation, the airflow velocity was set equal to 5 and 10 m s⁻¹, while for $\alpha = 0^\circ$, 45° , and 90° a reduced number of probe positions were sampled also at $U_{ref} = 3, 7.5$, and 15 m s⁻¹, to investigate the scalability (Reynolds dependency) of the flow field.

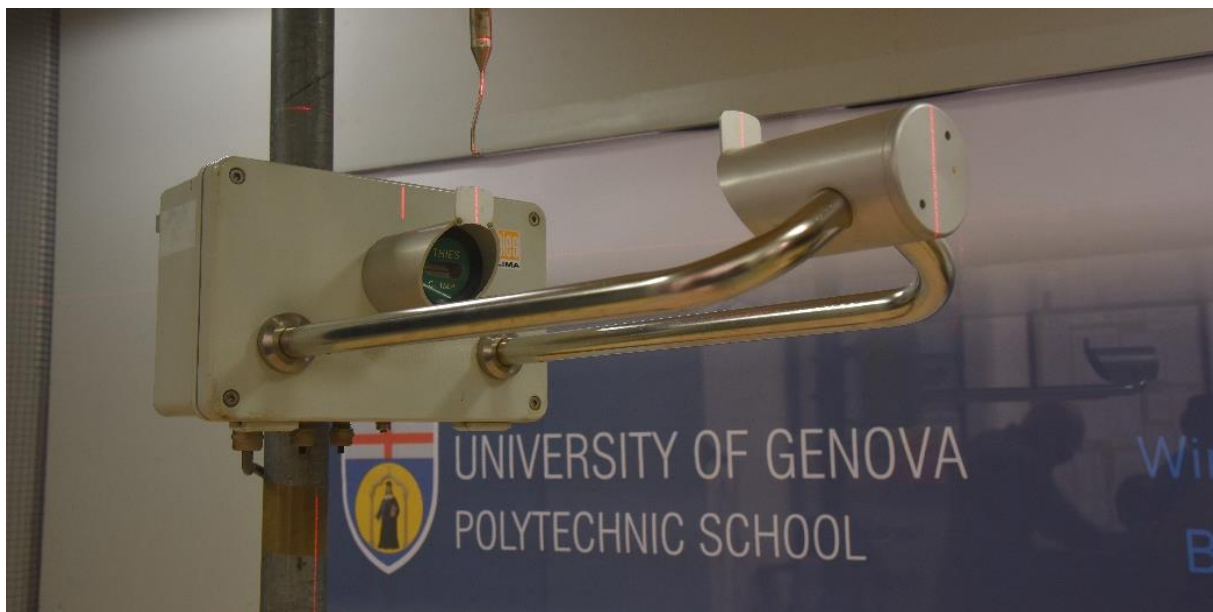


Figure 7.31: The Thies LPM during the installation procedure in the DICCA WT for the configuration at $\alpha = 0^\circ$. The instrument and the Cobra probe are aligned by employing the visualised laser beam.

For the nine wind directions investigated, the flow velocity was measured at the positions indicated with black circles in Figure 7.32, where the normalized sections (X/L, Z/L) and (X/L, Y/L) are depicted, and $L = 0.228$ m is the length of the sensing area of the instrument. For each position, measurements were taken at a frequency of 1000 Hz for intervals of 30 s. In total, 915 flow velocity measurements were obtained for nine rotations and two undisturbed airflow velocities.

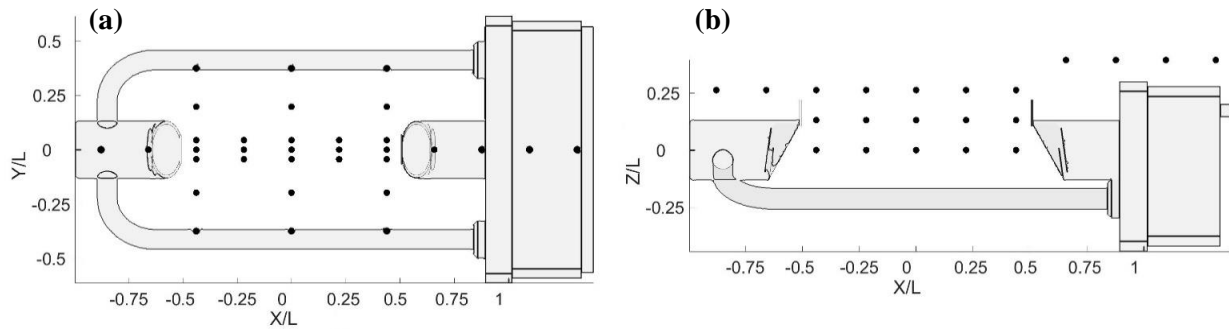


Figure 7.32: Normalized positions (black dots) of the Cobra probe measurements performed during the WT tests. Top view (a) and side view (b).

Raw data from the Cobra pressure probes used in the WT allowed performing some quality checks on the flow velocity measurements. First, the probe returns a null value in case of relevant airflow components reaching the probe from directions that are outside of a 45° acceptance cone, since the positioning of the pressure holes on the probe head does not allow detection of the flow velocity in such conditions. This typical occurs in case of recirculating flow and strong turbulence conditions. Second, the probe has a lower sensitivity of about 2 m s^{-1} , below which the measurement is deemed unreliable.

For each position sampled in the WT experiment, an assessment of the measurement quality was therefore performed by counting the number of null values obtained during the 30s acquisition time frame. The measurement was discarded in case null values exceeded 20% of the total sample. Measurements were also discarded when falling below the minimum velocity of 2 m s^{-1} or presenting a turbulent intensity larger than 30%, as indicated by the probe manufacturer specifications.

Table 7.16: Quality parameters of the WT measurements for a wind speed of 5 m s^{-1} .

$U_{\text{ref}} = 5 \text{ m s}^{-1}$				
Wind Direction	% Accepted	% Low Quality	%Low Speed	Mean Turb. Int.
0°	36.92	49.23	60.00	0.376
22.5°	67.39	15.22	30.44	0.157
45°	95.75	4.26	4.26	0.048
67.5°	100	0	0	0.015
90°	100	0	0	0.017
112.5°	100	0	0	0.013
135°	82.50	10.00	17.50	0.094
157.5°	46.34	34.15	48.78	0.261
180°	0	82.35	94.12	0.646

The measured turbulence intensity and percentage of discarded measurements are shown in Table 7.16 and Table 7.17. As expected, the most critical configuration is at $\alpha = 180^\circ$, where the combined effect of the circuitry box and the supporting pole produces strong recirculation zones and high turbulence intensity, with almost all measurements being rejected. On the other hand, the configurations at 67.5° , 90° , and 112.5° , since orienting the obstacle to the incoming flow along a favourable cross section, are the least disturbed, with all measurements satisfying the quality, velocity, and turbulence intensity criteria.

Table 7.17: Quality parameters of the WT measurements for a wind speed of 10 m s^{-1} .

$U_{\text{ref}} = 10 \text{ m s}^{-1}$				
Wind Direction	% Accepted	% Low Quality	% Low Speed	Mean Turb. Int.
0°	43.08	44.62	46.62	0.353
22.5°	86.96	13.04	8.70	0.118
45°	95.75	4.26	2.13	0.037
67.5°	100	0	0	0.010
90°	100	0	0	0.015
112.5°	100	0	0	0.010
135°	87.50	12.50	10.00	0.095
157.5°	60.53	28.95	26.32	0.241
180°	20.00	60.00	80.00	0.422

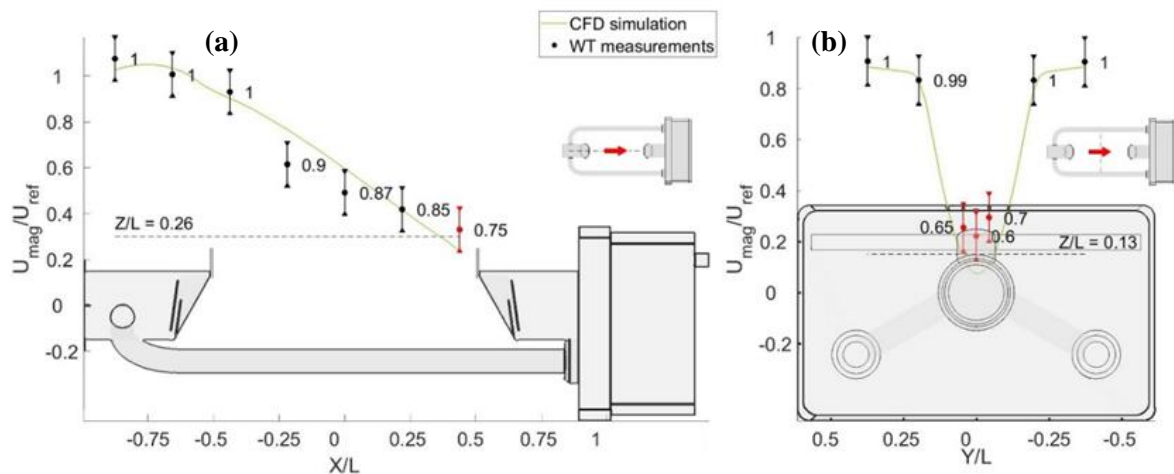


Figure 7.33: Comparison of the simulated profiles of the magnitude of flow velocity against WT measurements for the configuration at $\alpha = 0^\circ$ and $U_{\text{ref}} = 5 \text{ m s}^{-1}$. Side view (a) and front view (b).

Validation of the CFD simulation results was performed by comparing the average simulated velocity with the measurements obtained in the WT experiment. In Figures 7.33, 7.34 and 7.35, simulated profiles and measured data are reported. Error bars represent the measurement tolerance specified by the probe manufacturer, while for each probe position a quality index is shown both numerically and by colour coding. This index is defined as the ratio between the number of samples correctly acquired and the total number of samples. Therefore, unity indicates valid measurements where no null values are present, while zero indicates that all values are null. The simulation is visually shown to be in good agreement with the WT measurements for the three angles reported.

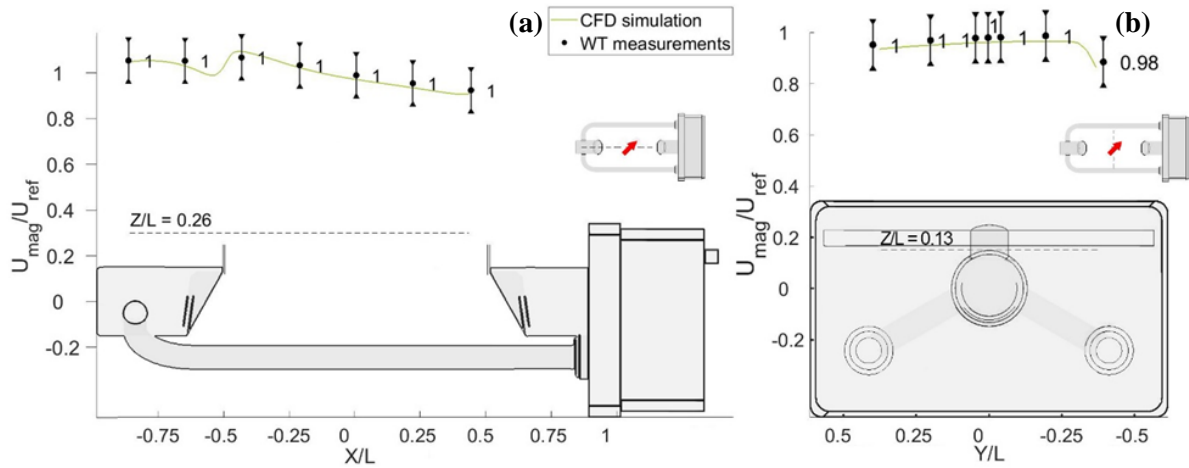


Figure 7.34: Comparison of the simulated profiles of the magnitude of flow velocity against WT measurements for the configuration at $\alpha = 45^\circ$ and $U_{ref} = 5 \text{ m s}^{-1}$. Side view (a) and front view (b).

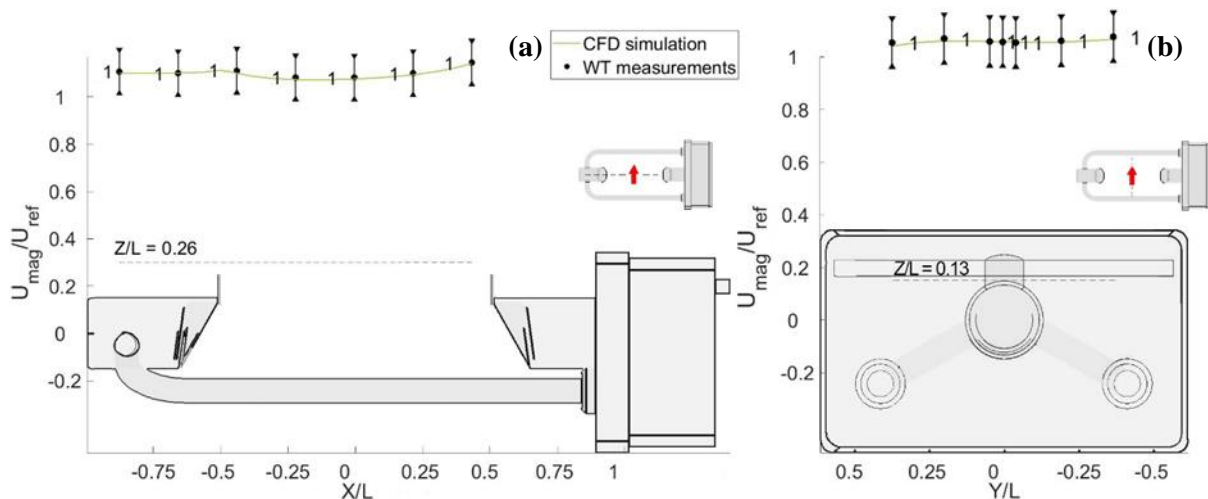


Figure 7.35: Comparison of the simulated profiles of the magnitude of flow velocity against WT measurements for the configuration at $\alpha = 90^\circ$ and $U_{ref} = 5 \text{ m s}^{-1}$. Side view (a) and front view (b).

Quantitative validation of the CFD results is achieved by calculating the mean error between the simulated and measured flow velocity at each single probe position. Due to the large number of

measurements, a statistical approach was used, whose results are presented in Table 7.18 and Table 7.19, where the mean error and the associated standard deviation are calculated per each combination of the wind velocity and direction. For this analysis, only the 661 measurements satisfying suitable quality (>0.8), velocity ($>2 \text{ m s}^{-1}$), and turbulence intensity (<0.3) criteria are considered. The percentage of samples that fall within 2σ and 3σ was calculated, with σ being the instrument accuracy (0.5 m s^{-1}). Under the hypothesis of a Gaussian distribution of measurement errors, 95.45% of the points are expected to be within 2σ , while 99.73% should be within 3σ .

Table 7.18: Statistics of the WT measurements results for a wind velocity of 5 m s^{-1} .

$U_{\text{ref}} = 5 \text{ m s}^{-1}$					
Wind Direction	Mean Error [m s^{-1}]	Std. Dev. [m s^{-1}]	% Out of Tolerance	% Data within 2σ	% Data within 3σ
0°	0.376	0.554	25.00	83.33	95.83
22.5°	0.345	0.538	12.00	92.00	92.00
45°	0.117	0.267	2.22	97.78	97.78
67.5°	0.103	0.192	4.08	100.00	100.00
90°	0.084	0.156	1.56	98.44	100.00
112.5°	0.102	0.245	2.22	97.78	97.78
135°	0.228	0.448	15.63	90.63	96.88
157.5°	0.322	0.446	10.53	94.74	100.00
180°	1.806	1.185	33.33	58.33	75.00

Table 7.19: Statistics of the WT measurements results for a wind velocity of 10 m s^{-1} .

$U_{\text{ref}} = 10 \text{ m s}^{-1}$					
Wind Direction	Mean Error [m s^{-1}]	Std. Dev. [m s^{-1}]	% Out of Tolerance	% Data within 2σ	% Data within 3σ
0°	0.370	0.590	33.33	75.00	91.67
22.5°	0.410	0.351	15.79	92.11	97.37
45°	0.098	0.147	0.00	100.00	100.00
67.5°	0.157	0.280	4.44	97.78	100.00
90°	0.139	0.218	4.69	98.44	100.00
112.5°	0.121	0.151	0.00	100.00	100.00
135°	0.236	0.256	6.67	96.67	100.00

157.5°	0.540	0.758	27.78	83.33	88.89
180°	3.722	0.879	100	0.00	0.00

Most rotations satisfy this criterion, although with a few outliers. These could be explained by the fact that some points still present a high turbulence intensity that is barely below the imposed limit and that the presence of the probe itself locally modifies the velocity field, especially near the surface of the instrument. Additionally, because of the limited number of usable data for some angles, one single outlier could have a strong influence on the test result.

The influence of a limited number of outliers is reduced when considering the whole dataset. Only 44 out of the 661 measurements considered valid, 6.65% of the total, present a difference with respect to the simulation results larger than the instrument tolerance of 0.5 m s^{-1} , and these are mostly due to points that barely meet the criteria of measurement quality, minimum flow velocity and maximum turbulence intensity.

7.5.2 Reynolds number dependency

A scalability analysis was conducted to assess the validity of the solution at airflow velocities in between the simulated ones. Three further velocities ($3, 7.5$ and 15 m s^{-1}) were investigated to this end in the WT for three different wind directions ($0^\circ, 45^\circ$ and 90°) and a few simulated wind velocity profiles, at $Z/L = 0.26$ above the instrument measuring area, are illustrated in Figure 7.36. For $\alpha = 45^\circ$ and $\alpha = 90^\circ$, both the simulated profiles and measured data show almost no Reynolds number dependency, while for the 0° configuration some differences occur in both the measured data and simulated profiles in the areas with a higher turbulence intensity.

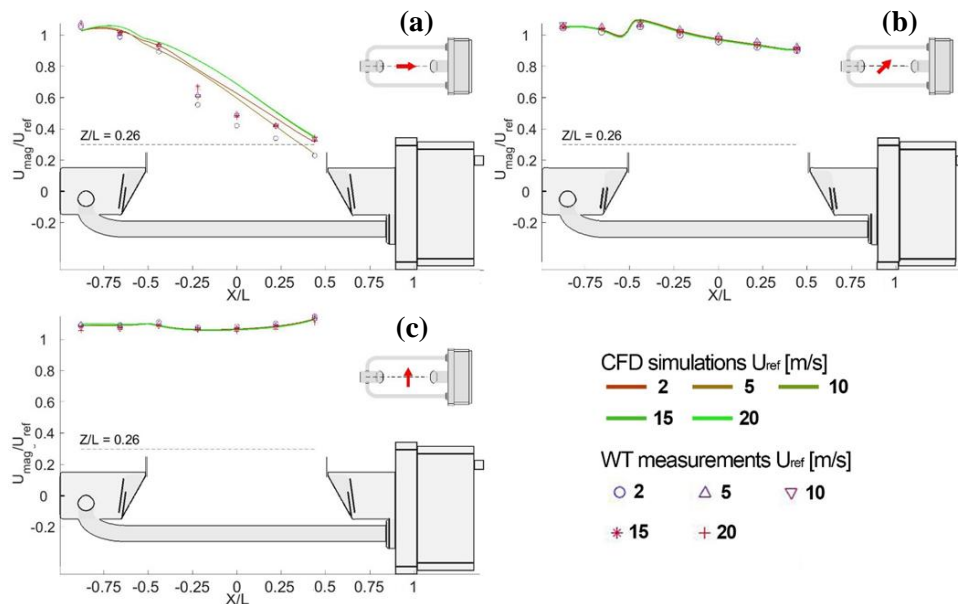


Figure 7.36: Reynolds number dependency of four simulated profiles (at $U_{ref} = 2, 5, 10, 15$, and 20 m s^{-1}) of the normalised magnitude of the airflow velocity at $Z/L = 0.26$ (dashed line) above the measuring area and WT measurements along the same profile at $3, 5, 7.5$, and 15 m s^{-1} for $\alpha = 0^\circ$ (a), 45° (b) and 90° (c).

7.5.3 WT comparison against the time dependent model for the Thies LPM

Comparing the LES results against the dedicated WT measurements indicates that recirculation zones are well resolved, as shown in Figure 7.37 where two profiles, one parallel and one transversal to the flow, are presented for $\alpha = 0^\circ$.

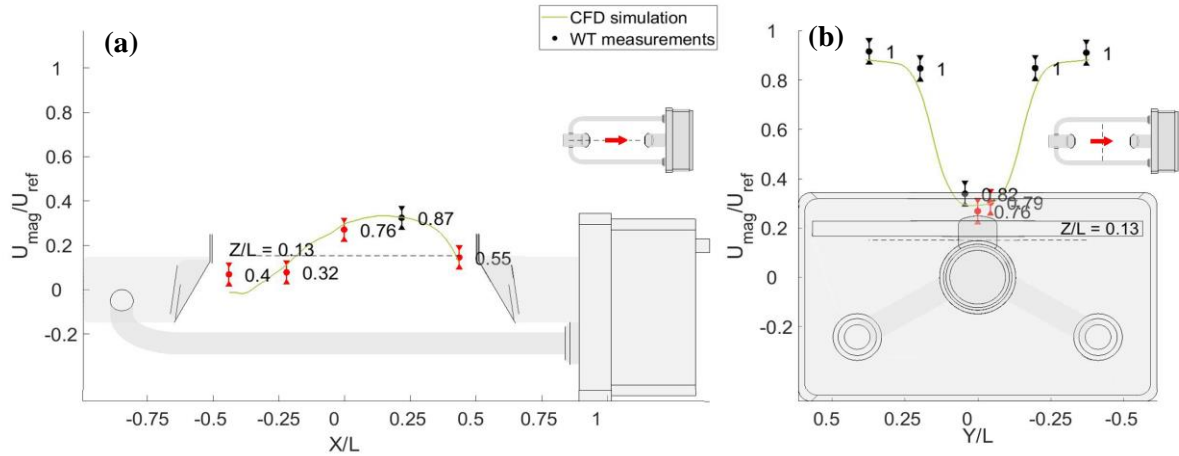


Figure 7.37: Comparison of the LES simulated profiles of the magnitude of flow velocity against WT measurements for the configuration at $\alpha = 0^\circ$ and $U_{\text{ref}} = 10 \text{ m s}^{-1}$. Side view (a) and front view (b).

However, Figure 7.38 shows that the separation layer above the instrument is not well resolved as in the case of the time independent simulation (Figure 7.33), meaning that an even finer grid and a wall resolving approach may be necessary to capture the local turbulence generated by the extremely thin metal shields attached to the emitting and receiving heads. Their effect is better captured by the ensemble average operated on turbulence by the time independent (URANS) approach.

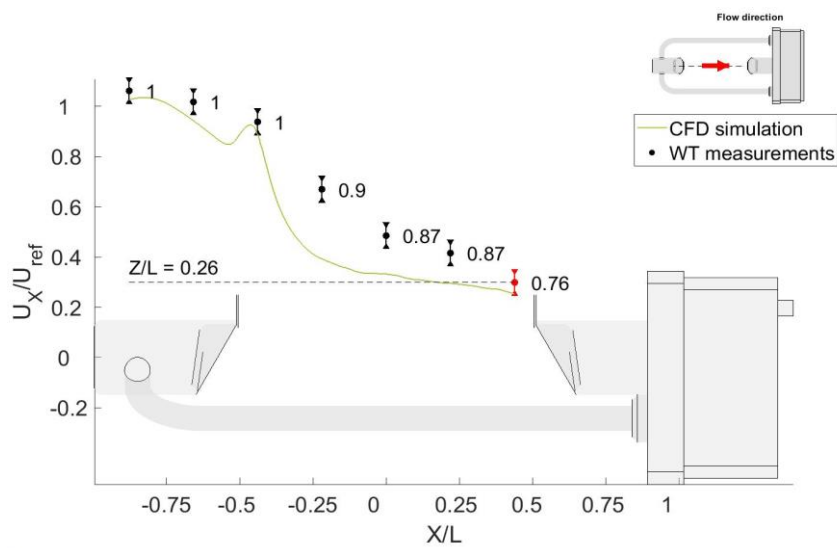


Figure 7.38: Comparison of the LES simulated profiles of the magnitude of flow velocity against WT measurements for the configuration at $\alpha = 0^\circ$ and $U_{\text{ref}} = 10 \text{ m s}^{-1}$.

On the contrary, considering the configuration at $\alpha = 90^\circ$ shown in figure 7.39, the LES model results are in almost perfect accordance with both the WT measurements and the time independent approach, meaning that, as expected, when recirculation is limited and the blockage produced by the instrument body is low, no tangible improvement is provided by the much more computationally expensive time dependent (LES) approach.

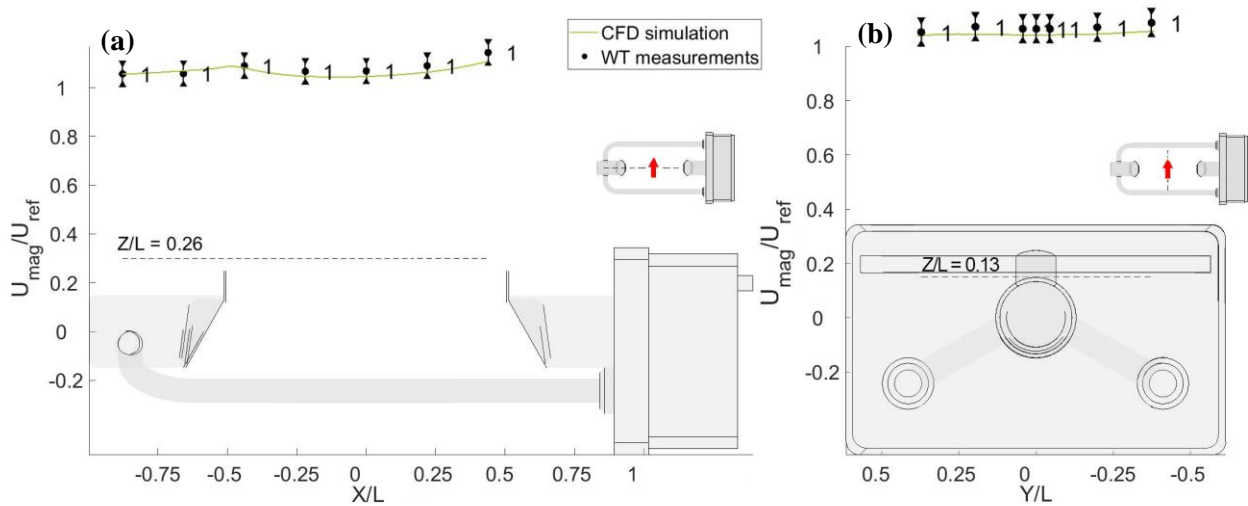


Figure 7.39: Comparison of the LES simulated profiles of the magnitude of flow velocity against WT measurements for the configuration at $\alpha = 90^\circ$ and $U_{ref} = 10 \text{ m s}^{-1}$. Side view (a) and front view (b).

7.5.4 Validation of the time independent model for the Vaisala WXT-520

The Vaisala WXT-520 instrument was installed in the WT with its supporting pole fixed on a rotating baseplate. Alignment with the traversing arm of the WT was tested using a laser beam and the operation was repeated for each of the three rotations investigated, to ensure that the WT flow did impact the instrument at the exact angle chosen for the numerical simulation.

In Figure 7.40, an example of the positioning of the “Cobra” pressure probe during measurements is shown. Since the Vaisala WXT-520 has a small size, the probe is relatively large with respect to the instrument size, meaning that it may have a non-negligible influence on the flow when positioned very close to the instrument body.

For each rotation, the airflow velocity was set equal to 5 and 10 m s^{-1} and measurements were taken for $\alpha = 0^\circ$, 30° , and 60° . For the three wind directions investigated, the flow velocity was measured at the positions indicated with black circles in Figure 7.41, where the normalized sections (X/L , Z/L) and (X/L , Y/L) are depicted, and $L = 0.091 \text{ m}$ is the diameter of the sensing area of the instrument. For each position, measurements were taken at a frequency of 1000 Hz for a duration of 30 s. In total, 268 flow velocity measurements were obtained for three rotations and two undisturbed airflow velocities.



Figure 7.40: The WXT-520 during the installation procedure in the DICCA WT for the configuration at $\alpha = 0^\circ$. The instrument and the Cobra probe were aligned by employing a laser beam.

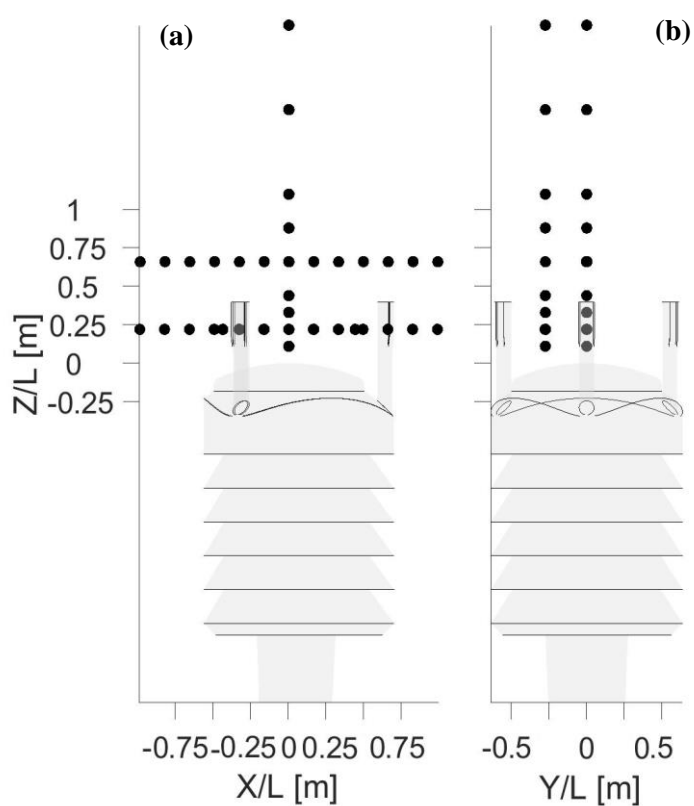


Figure 7.41: Normalized positions (black dots) of the Cobra probe measurements during the WT tests. Side view (a) and front view (b).

Quality checks were performed on the measured data, using the same criteria about the minimum flow velocity, measurement quality and maximum turbulence intensity described above for the case of the Thies LPM.

The measured turbulence intensity and percentage of discarded measurements are shown in Tables 7.20 and 7.21. Probes performed quite good in all configurations, however in the case of $\alpha = 60^\circ$, some measurements had to be discarded since the recirculation zone produced by the upstream wind measuring arm generates strong turbulence and too low flow velocities. This is also evident in the value of the mean turbulence intensity, being, in the case of $\alpha = 60^\circ$, about four times higher than the other two configurations.

Table 7.20: Quality parameters of the WT measurements at a wind speed of 5 m s^{-1} .

$U_{\text{ref}} = 5 \text{ m s}^{-1}$				
Wind Direction	% Accepted	% Low Quality	%Low Speed	Mean Turb. Int.
0°	100	0	0	0.015
30°	100	0	0	0.012
60°	97.78	2.22	2.22	0.046

Table 7.21: Quality parameters of the WT measurements at a wind speed of 10 m s^{-1} .

$U_{\text{ref}} = 10 \text{ m s}^{-1}$				
Wind Direction	% Accepted	% Low Quality	%Low Speed	Mean Turb. Int.
0°	100	0	0	0.011
30°	100	0	0	0.008
60°	97.78	2.22	2.22	0.037

Validation of the results was performed by comparing the average simulated velocity with the measurements obtained in the WT experiment. In Figures 7.42, 7.43 and 7.44, simulated profiles and measured data are compared. Error bars represent the measurement tolerance specified by the probe manufacturer, while for each WT probe a quality index is shown both numerically and by colour coding. The simulation is shown to be in very good agreement with the WT measurements for all angles. However, some discrepancies are visible in the profiles immediately downstream of the wind-measuring arms, where the flow behaviour is captured but with some differences, due to turbulence and recirculation.

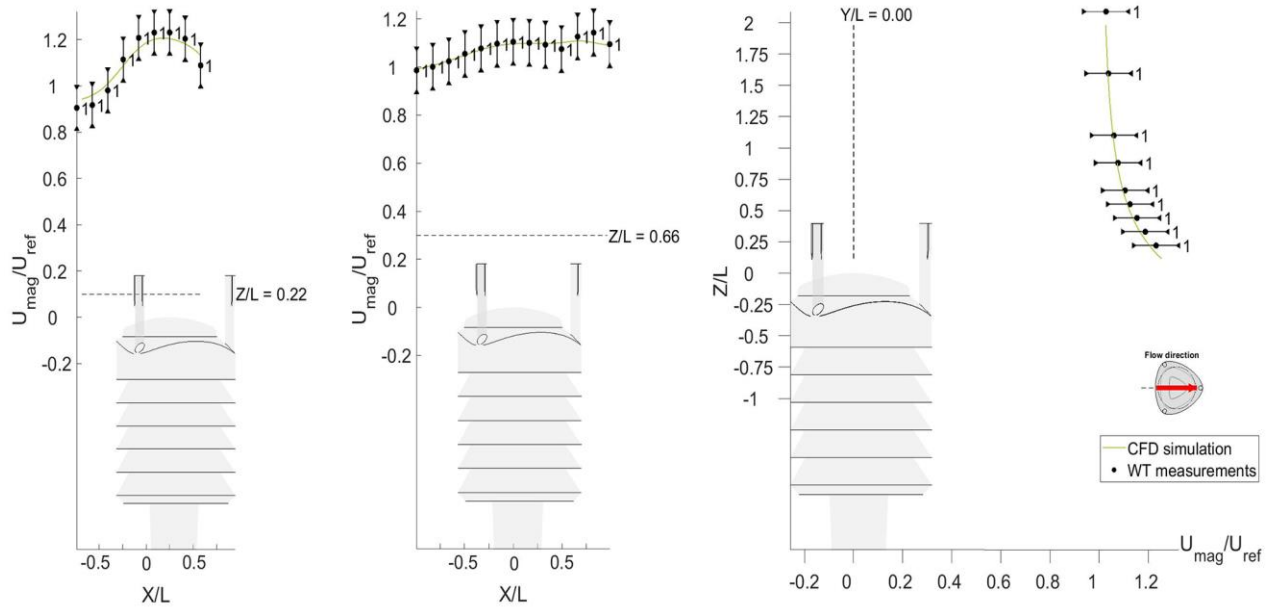


Figure 7.42: Comparison of the simulated profiles of the magnitude of flow velocity against WT measurements for the configuration at $\alpha = 0^\circ$ and $U_{\text{ref}} = 5 \text{ m s}^{-1}$.

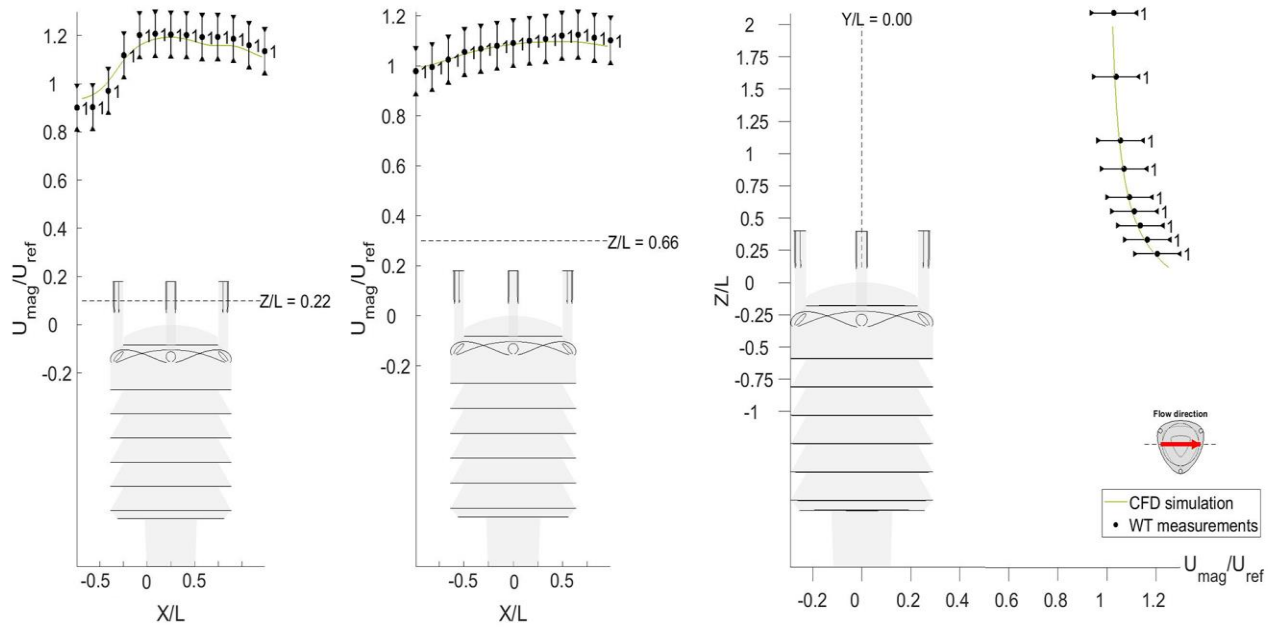


Figure 7.43: Comparison of the simulated profiles of the magnitude of flow velocity against WT measurements for the configuration at $\alpha = 30^\circ$ and $U_{\text{ref}} = 5 \text{ m s}^{-1}$.

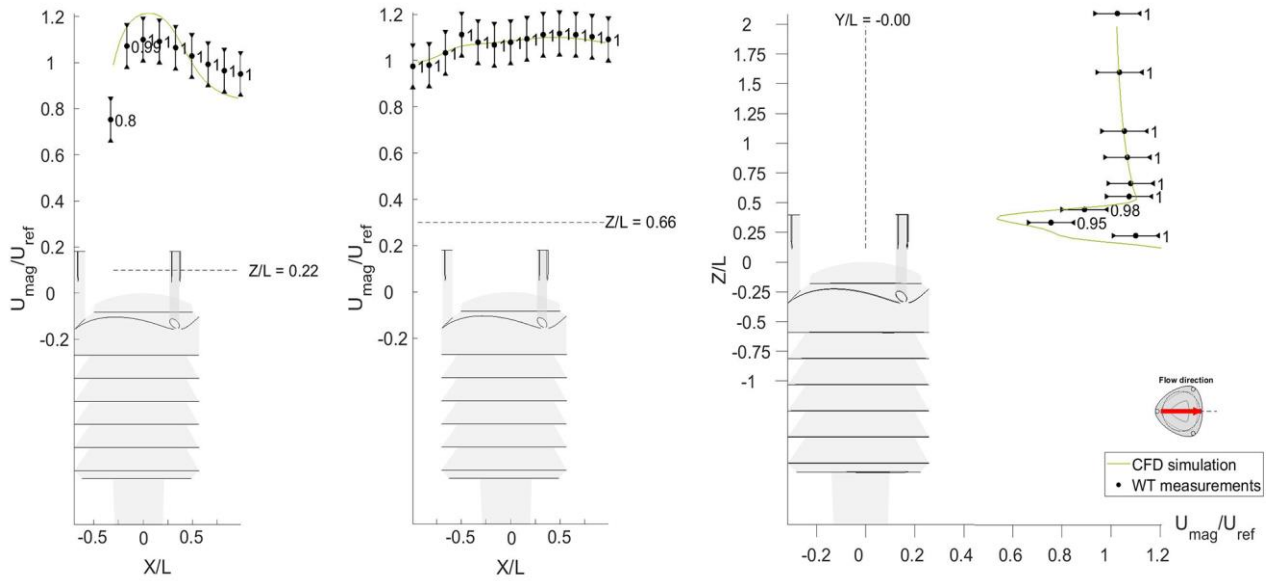


Figure 7.44: Comparison of the simulated profiles of the magnitude of flow velocity against WT measurements for the configuration at $\alpha = 60^\circ$ and $U_{ref} = 5 \text{ m s}^{-1}$.

Again, quantitative validation of the CFD results is achieved by calculating the mean error between the simulated and measured flow velocity at each single probe position. Due to the large number of measurements, a statistical approach is used, whose results are presented in Tables 7.22 and 7.23, where the mean error and the associated standard deviation are calculated per each combination of the wind velocity and direction. For this analysis, only the 266 measurements satisfying the quality (>0.8), velocity ($>2 \text{ m s}^{-1}$), and turbulence intensity (<0.3) criteria are considered. The percentage of samples that fall within 2σ and 3σ was calculated, with σ being the instrument accuracy (0.5 m s^{-1}). Under the hypothesis of a Gaussian distribution of measurement errors, 95.45% of the points are expected to be within 2σ , while 99.73% should be within 3σ .

Table 7.22: Statistics of the WT measurements results at a wind speed of 5 m s^{-1} .

$U_{ref} = 5 \text{ m s}^{-1}$					
Wind Direction	Mean Error [m s^{-1}]	Std. Dev. [m s^{-1}]	% Out of Tolerance	% Data within 2σ	% Data within 3σ
0°	0.080	0.103	0	100	100
30°	0.074	0.092	0	100	100
60°	0.242	0.516	15.91	95.45	95.45

The only rotation that does not completely satisfy this criterion is at $\alpha = 60^\circ$. This could be explained by the same reasons that required some measures to be discarded. In the wake of the wind-measuring arm,

high turbulence intensity and recirculation are present. Furthermore, the presence of the probe itself may locally modify the velocity field, especially near the surface of the instrument.

Table 7.23: Statistics of the WT measurements results at a wind speed of 10 m s^{-1} .

Uref = 10 m s^{-1}					
Wind Direction	Mean Error [m s^{-1}]	Std. Dev. [m s^{-1}]	% Out of Tolerance	% Data within 2σ	% Data within 3σ
0°	0.129	0.203	0	100	100
30°	0.112	0.167	0	100	100
60°	0.267	0.561	9.09	95.45	97.73

The influence of possible outliers is reduced when considering the whole dataset. Only 11 out of the 266 measurements considered valid (4.13% of the total) present a larger deviation, with respect to the simulation results, than the instrument tolerance of 0.5 m s^{-1} .

7.5.5 Discussion

The time independent numerical model was chosen for its relatively low computational cost. This is highly valuable, considering the large number of simulations required to represent the field conditions on NCGs in terms of wind speed and direction. Validation results show that the time independent model is in quite good accordance with WT measurements of the flow. For the more favourable configurations, the agreement between CFD and WT was shown to be almost perfect, and the model provides satisfactory results even in less favourable conditions of high turbulence and recirculating flow. This was shown to be true for both the Thies LPM, that has a highly non radially symmetric shape, and the Vaisala WXT-520, that instead has a more regular shape but with small and complex features. The model is therefore capable of correctly capturing the phenomenon.

Considering the time dependent model, tested only on the Thies LPM, the computational cost is considerably higher and only a limited number of simulations could be run. Comparison against both the WT measurements and the time independent model shows that the time dependent model better resolves turbulence in the recirculation zones and is in general in good agreement with the other two results. Differences however arise for the configuration at $\alpha = 0^\circ$ in some parts of the domain. For the configuration at $\alpha = 90^\circ$, the two approaches provide instead almost identical results. It can be therefore concluded that the time dependent approach does not provide a significant improvement over the time independent one, especially considering the much higher computational requirements. Results from the LES model will however be still relevant below to evaluate the influence of turbulence on the hydrometeors trajectories.

8 LPT RESULTS AND CATCH RATIOS

Hydrometeor trajectories and their deviation close to the instrument sensing area are computed using the LPT model and presented in this chapter for the geometry of different instruments. As discussed in chapter 5.3.2, from a back of the envelope analysis, significant deviations are expected for small size hydrometeors, while limited effects are expected for the larger ones. However, the goal of the numerical simulations is the quantitative assessment of the instrument performance under various typical environmental conditions that may be experienced in field installations. Several influencing factors can be identified, like the undisturbed slope of the incoming trajectories, the size and shape of the sensing area, the outer geometry of the instrument and the wind speed and direction. The LPT model allows identifying hydrometeor trajectories that would impact the gauge body, cross its sensing area or miss the instrument altogether under the effect of wind, and to compare them with the undisturbed conditions.

8.1 LPT MODEL SETUP

Since particle-to-particle interactions are neglected in the modelling approach used in this work, hydrometeors are inserted in the domain along a regular grid, with variable dimension and spacing. Two different grid types were tested for the Thies LPM while a single grid type was used for the other gauges.

Both the position of the centre of the grid and its height are computed by solving, for a single hydrometeor, the equation of motion, and computing the fall distance and horizontal travel within an undisturbed velocity field. The grid is then positioned in space at a minimum distance of 0.05 m from the domain boundaries and such that, if the velocity field was constant, the trajectory starting from its centre would perfectly cross the centre of the instrument sensing area. The length of the grid was extended, if necessary, in the case of small hydrometeors and high wind speeds, to ensure that all possible trajectories that potentially cross the instrument sensing area are considered.

For all simulations, liquid precipitation was modelled by considering 11 equivalent diameters, 0.25 mm, 0.5 mm, 0.75 mm and from 1 to 8 mm at 1 mm increments. The hydrometeor density ρ was set equal to 1000 kg/m³.

8.1.1 LPT simulation setup for the Thies LPM

Water drops were inserted in the domain at the start of the simulation from a rectangular, 2.5 mm spaced, grid that is 0.15 m wide and at least 0.45 m long, as shown, as an example, in Figure 8.1.

The grid orientation is maintained parallel to the laser beam axis and rotated according to the wind direction for the nine different meshes. This means that a different grid was defined for each combination of wind direction, wind speed, and hydrometeor size.

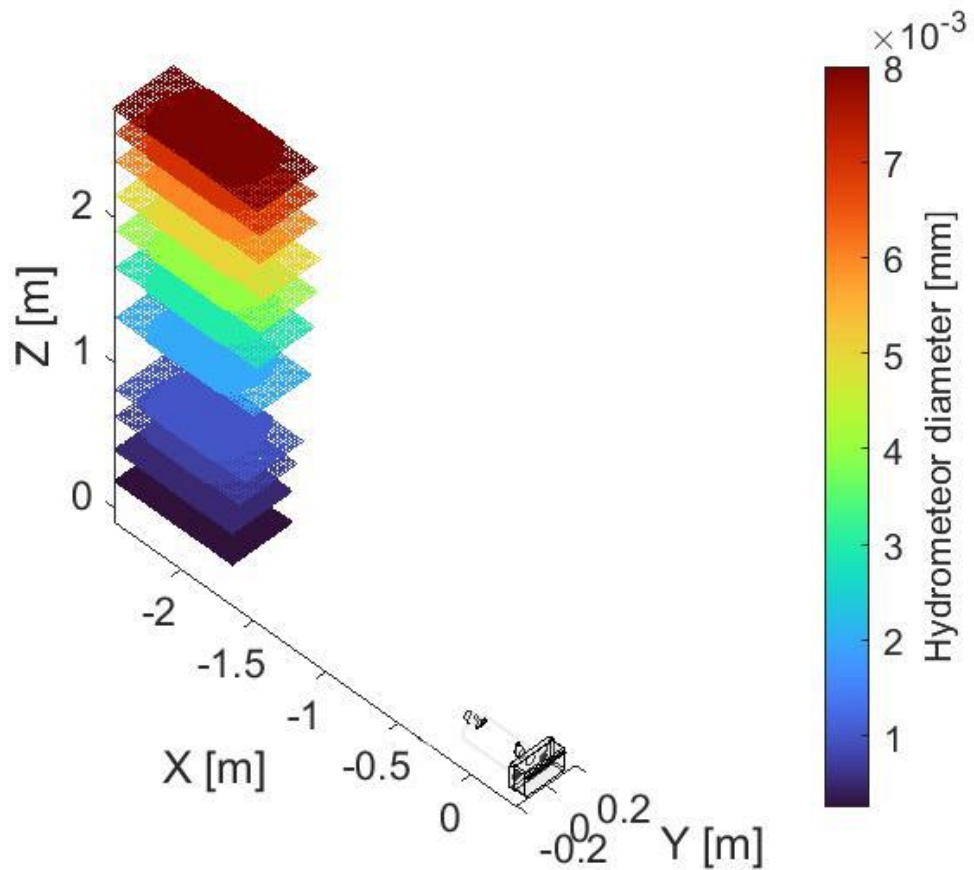


Figure 8.1: Visual representation of the adopted particle seeding grids (colour coded in the image) for $\alpha = 0^\circ$ and $U_{ref} = 10 \text{ m s}^{-1}$ above the Thies LPM (visible in the bottom right corner of the domain).

Coincident with the instrument sensing area is an internal surface, created within the mesh to represent the laser beam. For each particle impacting this virtual surface, or the surfaces of the instrument body and supporting pole, all related information are saved for post-processing, including the coordinates of individual trajectories. Simulations are stopped after all released particles either impact on a surface, exit the domain or further proceed below the instrument sensing area.

A second grid tested has the goal of improving the grid resolution without further increasing the computational burden. This was obtained by analysing the position of the particles that reached the sensing area of the instrument in the case of the previous grid. From the positions of detected particle, a variably spaced grid was produced, four times finer than the previous one where particles are expected to interact with the instrument sensing area and then progressively coarser far from the area of interest, therefore maintaining about the same number of tracked particles. This approach was also chosen to investigate a sudden jump in the number of hydrometeors that was noted for some specific combinations of wind speed, direction, and particle diameter, that could be due to the discrete nature of the grid. An example of the variably spaced grid is shown in Figure 8.2.

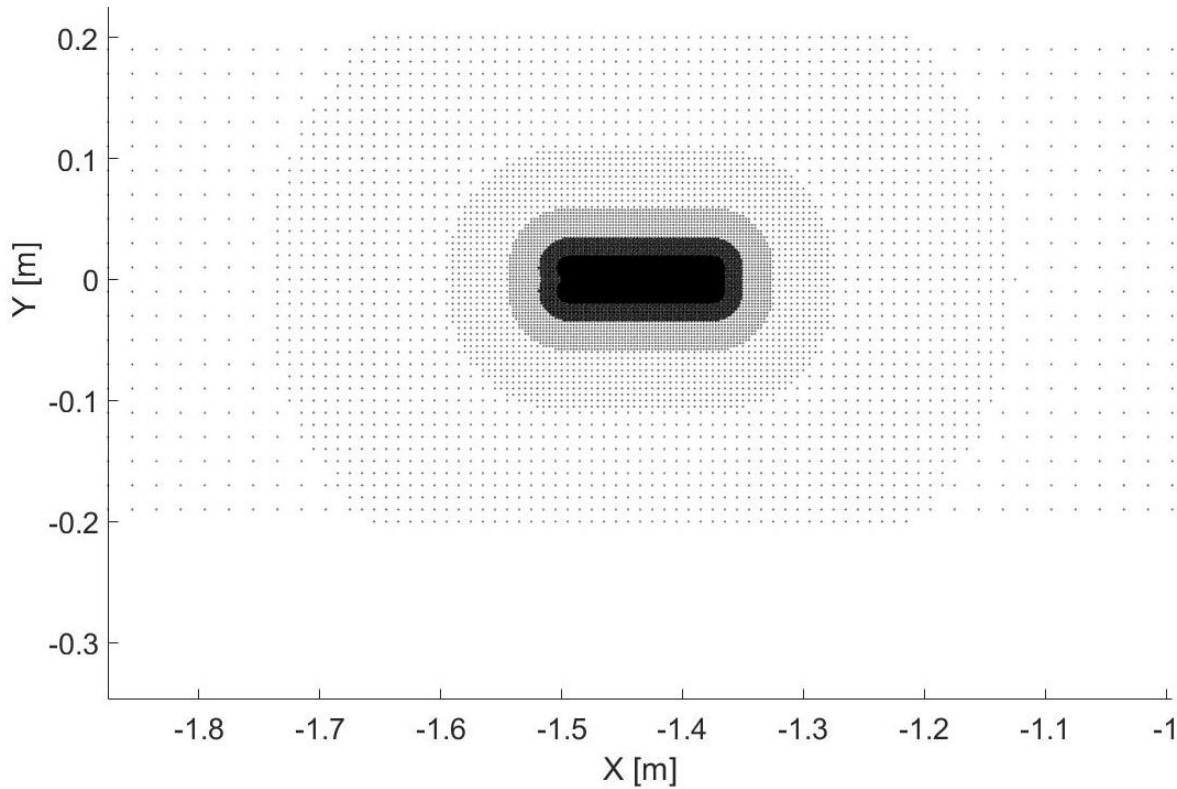


Figure 8.2: Sample image of the variable spacing grid used for the Thies LPM, with a resolution ranging between four times and one fourth of the resolution of the uniform grid.

These grids, however, did not produce a significant improvement in the results, meaning that the “jump” effect mentioned before is, for the most part, due to the complex geometry of the instrument interacting with the incoming trajectories, which either do or do not reach the instrument sensing area depending on their fall velocity and wind speed.

8.1.2 LPT simulation setup for the OTT Parsivel²

Particles were released in the domain using a regular, 2 mm spaced grid, 0.15 m wide and at least 0.45 m long. The grid orientation is maintained parallel to the laser beam axis and rotated according to the instrument configuration for 5 different meshes, constructing a different grid per each combination of wind direction, wind speed, and hydrometeors size. An example of different grids used is shown in figure 8.3.

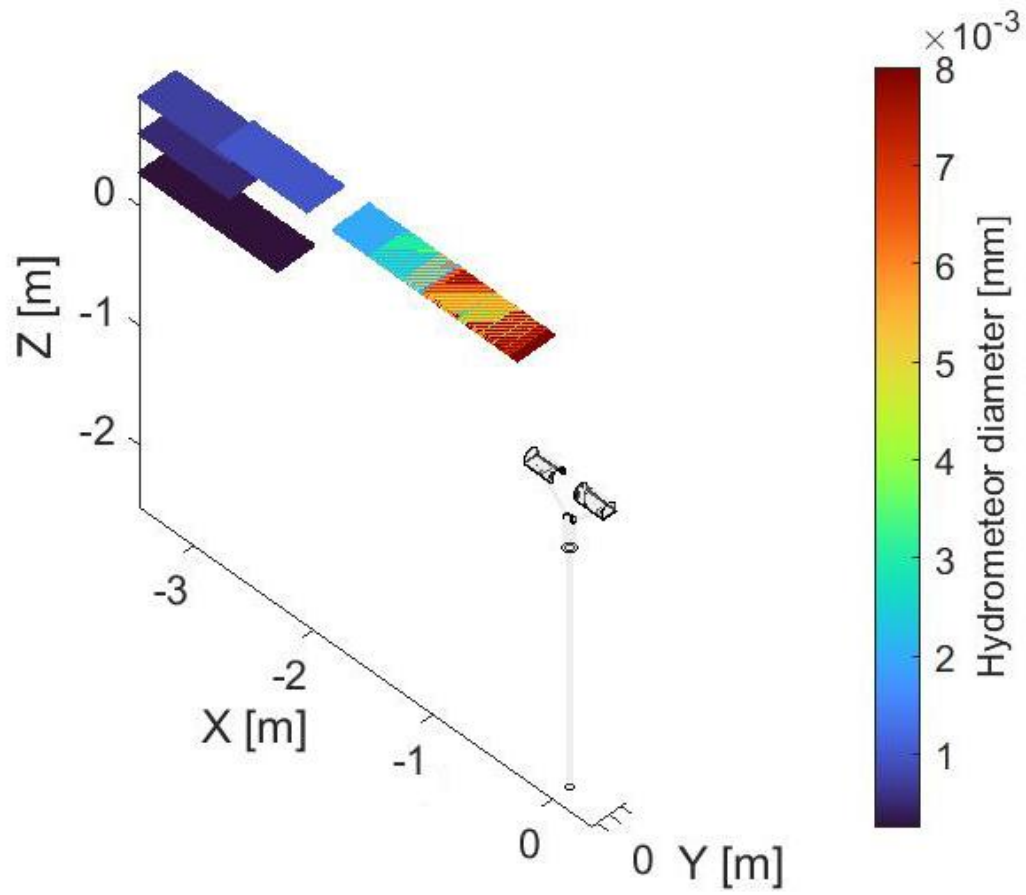


Figure 8.3: Visual representation of the adopted particle seeding grids (colour coded in the image) for $\alpha = 0^\circ$ and $U_{ref} = 10 \text{ m s}^{-1}$, above the OTT Parsivel² (also visible in the bottom right corner of the domain).

Since the OTT Parsivel² is a laser disdrometer, coincident with the instrument sensing area a virtual surface was created in the mesh to represent the laser beam. For each and every particle impacting this virtual surface, or the surfaces of the instrument body, all related information are saved for post-processing, including the coordinates of individual trajectories. Simulations are stopped after all released particles either impact on a surface, exit the domain or further proceed below the instrument sensing area.

8.1.3 LPT simulation setup for the Vaisala WXT-520

Particles were inserted in the domain using a regularly, 2 mm spaced grid, that is 0.15 m wide and at least 0.20 m long. Since the instrument sensing area is radially symmetric the main grid orientations are maintained parallel to the X and Y axis, and one single grid is suitable for multiple instrument configurations. An example of such grid is shown in Figure 8.4 for the configuration at $\alpha = 0^\circ$.

The instrument sensing area was modelled separately from the instrument body and a corresponding surface was created in the mesh. The model was set to separately identify every particle impacting the sensor surface or the instrument body. Individual trajectories were also saved for future post-processing. Simulations are stopped after all particles either impact on a surface or exit the domain or fall below the instrument sensing area.

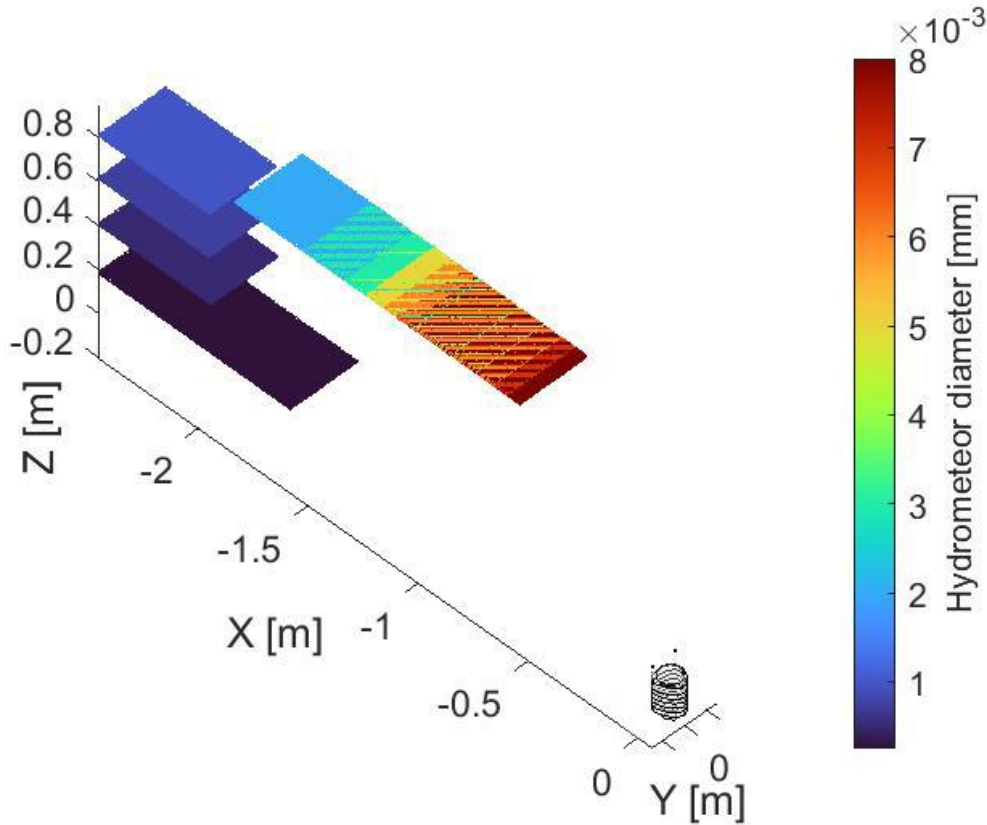


Figure 8.4: Visual representation of the adopted particle seeding grids (colour coded in the image) for $\alpha = 0^\circ$ and $U_{ref} = 10 \text{ m s}^{-1}$, the Vaisala WXT-520 is also visible in the bottom left corner of the domain.

8.2 VISUALIZATION OF PARTICLE TRAJECTORIES

Since numerous particles are released in each simulation, for visualization purposes this chapter only reports those particles starting along the XZ plane at $Y = 0$. Trajectories are also colour coded using the ratio between their actual fall velocity and their terminal velocity, as a mean to highlight the changes produced by the wind induced disturbance near the gauge.

8.2.1 Hydrometeor trajectories near the Thies LPM

Three LPT modelling approaches are used: time-independent uncoupled, time-dependent uncoupled and time-dependent one-way coupled. The first approach uses the CFD results of the time-independent approach (URANS) and computes the trajectories based on the static averaged velocity field. The second approach uses the results of the time-dependent CFD approach (LES), in terms of the average velocity field, being otherwise identical to the first approach. In the third and last approach, the LES solution is instead advanced alongside the trajectory computation. All three methods neglect both the influence of suspended particles on the flow and particle-to-particle interactions.

8.3.2.1 Time-independent uncoupled LPT simulation

Using the time-independent-uncoupled model, 495 combinations of wind speed, direction, and hydrometeor size were simulated. Sample trajectories for different particle diameters are shown in Figures 8.5, 8.6 and 8.7.

In Figure 8.5 (a), both the shielding effect due to the hydrometeors impacting the instrument body, and the aerodynamic effect of deviating particle trajectories by affecting e.g., their fall velocity, are evident. In general, light-weight hydrometeors show such a behaviour since they fall with a gentle slope and are more influenced by the local airflow pattern.

In Figure 8.5 (b) instead, drops with a larger diameter are considered, which fall with a steep slope and are less influenced by the local airflow pattern, meaning that both instrument shielding and aerodynamic effects have a reduced effect on trajectories. Fall velocities are therefore practically unaffected.

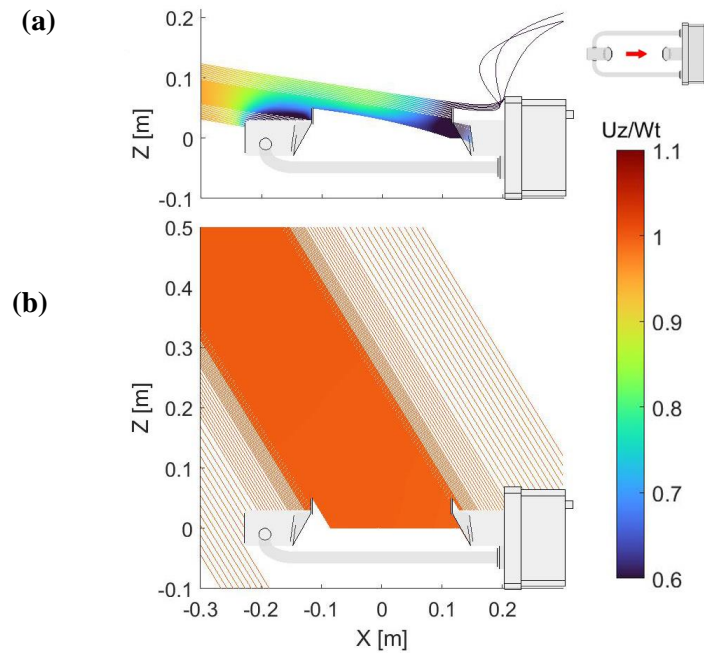


Figure 8.5: Simulated particle trajectories along the $Y=0$ plane, at $\alpha = 0^\circ$, $U_{ref} = 5 \text{ m s}^{-1}$ and two hydrometeor diameters, 0.25 mm (a) and 3 mm (b). Trajectories are colour coded according to the particle fall velocity.

When the wind direction is perpendicular to the instrument laser beam ($\alpha = 90^\circ$) (Figure 8.6), both shielding and aerodynamic effects are limited since the instrument offers the least amount of flow blockage in this configuration. A small number of hydrometeors cross the instrument laser beam outside of the expected sensing area, bypassing the sensor protective shield due to their very shallow angle of attack. This produces a limited amount of overcatch in the measurement for some wind speed and hydrometeor size combinations.

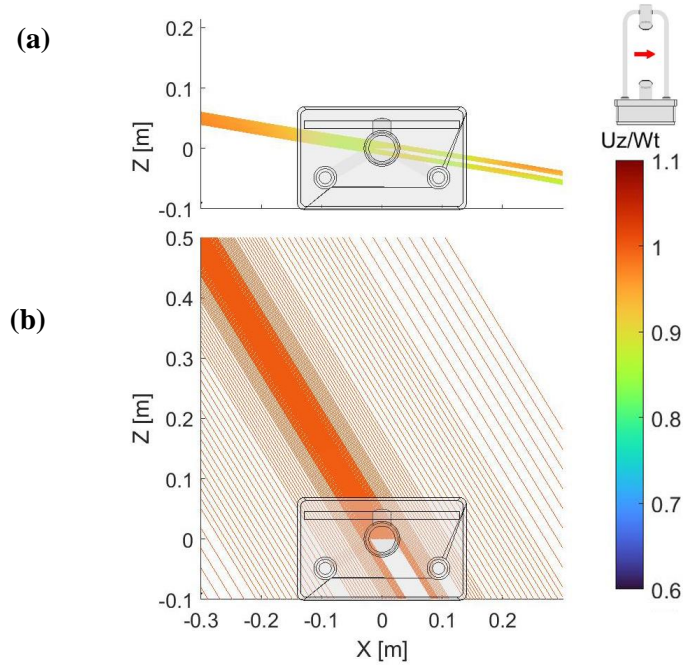


Figure 8.6: Trajectories along the $y=0$ plane, at $\alpha = 90^\circ$, $U_{ref} = 10 \text{ m s}^{-1}$ and two hydrometeor diameters, 0.25 mm (a) and 3 mm (b). Trajectories are colour coded according to the particle fall velocity.

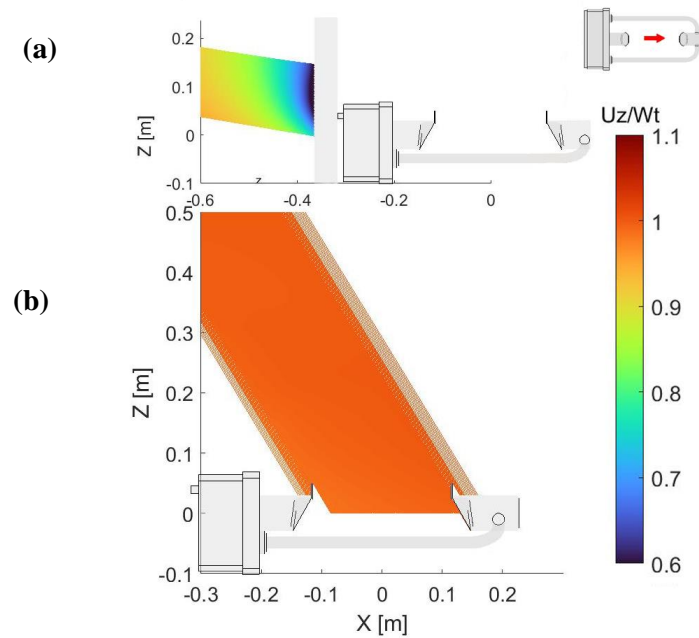


Figure 8.7: Particle trajectories along the $y=0$ plane, at $\alpha = 180^\circ$, $U_{ref} = 10 \text{ m s}^{-1}$ and two hydrometeor diameters, 0.25 mm (a) and 3 mm (b). Trajectories are colour coded according to the particle fall velocity.

When the worst performing configuration is considered ($\alpha = 180^\circ$), both the shielding and aerodynamic effects are so intense that the smallest and lightest hydrometeors are not even able to reach the instrument sensing area (8.7 a), while the larger ones are strongly affected and only partially reach the laser beam (8.7 b).

8.3.2.2 Time-dependent uncoupled simulation

For the time-dependent uncoupled approach, only four combinations of wind speed (5 and 10 m s⁻¹) and direction ($\alpha = 0^\circ$ and $\alpha = 90^\circ$) were simulated due to the much higher computational cost. The resulting trajectories are shown in Figures 8.8 and 8.9 for a wind speed of 10 m s⁻¹.

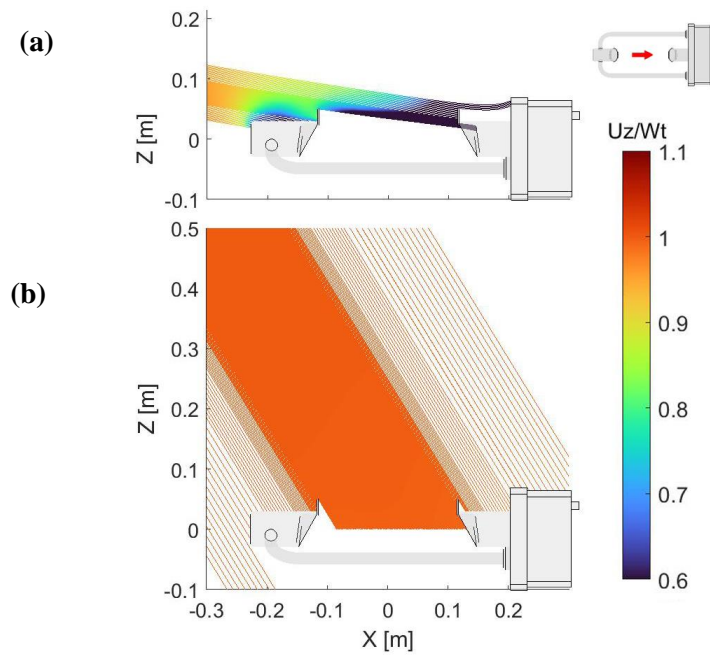


Figure 8.8: Particle trajectories along the $y=0$ plane, at $\alpha = 0^\circ$, $U_{ref} = 5 \text{ m s}^{-1}$ and two hydrometeor diameters, 0.25 mm (a) and 3 mm (b). Trajectories are colour coded according to the particle fall velocity.

Hydrometeor trajectories show a similar behaviour to the time-independent-uncoupled approach. Trajectories of hydrometeors with diameter $d = 0.25 \text{ mm}$, at $\alpha = 0^\circ$, present only a limited deviation in their terminal part, where the strong updraft noted in the CFD simulation prevents them reaching the instrument sensing area, while instead impacting on the instrument body. For larger hydrometeors, the deviation of their trajectories becomes quickly negligible. For the configuration at $\alpha = 90^\circ$, no significant differences in both the trajectories and fall velocities are appreciable.

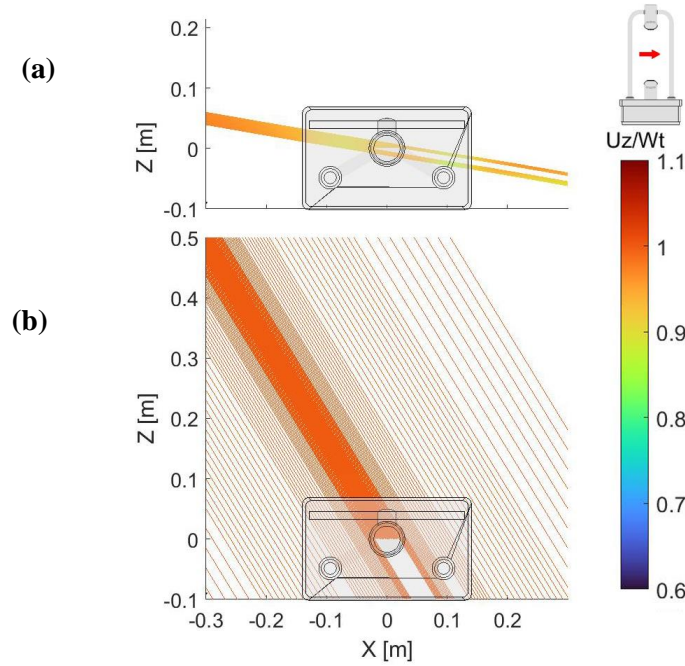


Figure 8.9: Particle trajectories along the $y=0$ plane, at $\alpha = 90^\circ$, $U_{ref} = 5 \text{ m s}^{-1}$ and two hydrometeor diameters, 0.25 mm (a) and 3 mm (b). Trajectories are colour coded according to the particle fall velocity.

8.3.2.3 Time-dependent one-way coupled simulation

The time-dependent-coupled model is the most computationally expensive of the three approaches considered, since the CFD solution evolves alongside the computation of particle trajectories. For this reason, only a limited number of diameters could be simulated.

Trajectories are shown, as in the previous cases, for two different diameters and one wind velocity in Figures 8.10 and 8.11. In this case, trajectories continue past the instrument sensing area since no virtual surface was added to avoid disturbances during the flow computation. From the plot of trajectories, it is evident that turbulence strongly affects the smaller hydrometeors, which on average, follow trajectories similar to the ones observed for the uncoupled models, but can locally be diverted considerably. Especially the transversal velocity components, due to recirculation and turbulence, can divert trajectories away from the instrument sensing area. However, hydrometeors with the higher diameters are less affected and their trajectories are much closer to both the time-independent-uncoupled and the time-dependent-uncoupled models. Fall velocities are similar to those obtained from the other approaches, although strong changes are observed in the wake of the instrument.

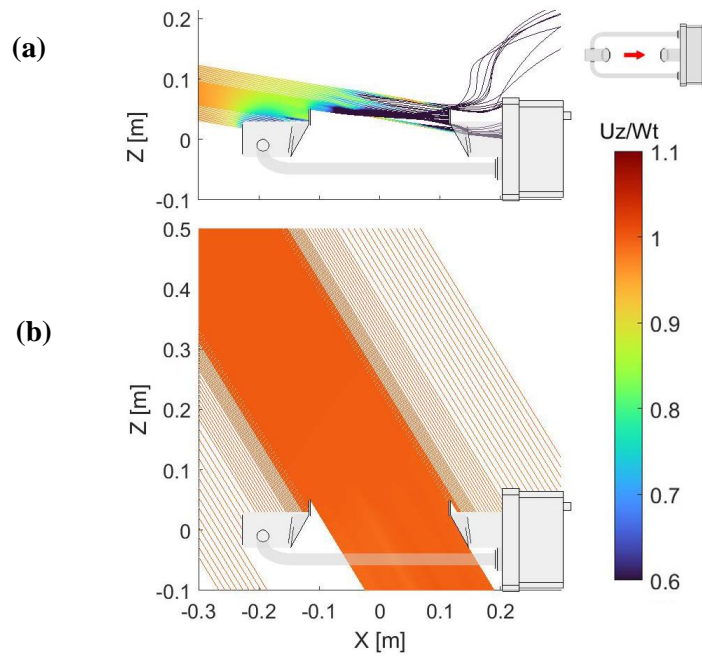


Figure 8.10: Particle trajectories along the $y=0$ plane, at $\alpha = 0^\circ$, $U_{ref} = 5 \text{ m s}^{-1}$ and two hydrometeor diameters, 0.25 mm (a) and 3 mm (b). Trajectories are colour coded according to the particle fall velocity.

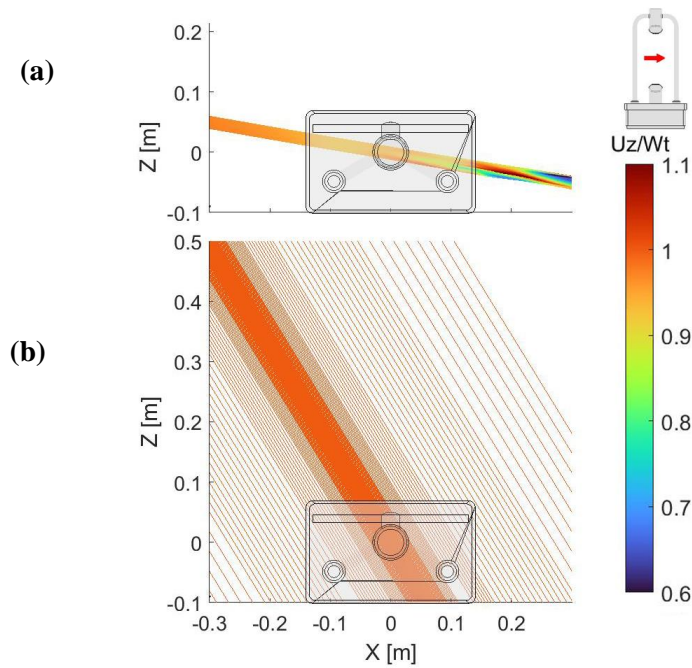


Figure 8.11: Particle trajectories along the $y=0$ plane, at $\alpha = 90^\circ$, $U_{ref} = 5 \text{ m s}^{-1}$ and two hydrometeor diameters, 0.25 mm (a) and 3 mm (b). Trajectories are colour coded according to the particle fall velocity.

8.2.2 Hydrometeor trajectories near the OTT Parsivel²

For the OTT Parsivel² only the time-independent uncoupled approach was used, since it was determined that it provides the best compromise between accuracy and computational burden, among the models tested

in this work. A total of 385 combinations of wind speed, direction and hydrometeor size were simulated. Sample trajectories for two different diameters are shown in Figures 8.12, 8.13 and 8.14.

In Figure 8.12 (a), both the shielding effect, due to hydrometeors impacting the instrument body, and the aerodynamic effect, modifying trajectories by affecting e.g., the fall velocity, are evident. In general, all light-weight hydrometeors show a similar behaviour since they fall with a shallow angle and are more influenced by wind.

In Figure 8.12 (b) instead, larger diameter drops are considered, which fall with a steeper angle and are less influenced by wind, meaning that both the instrument shielding and the aerodynamic behaviour have a reduced effect on trajectories. Fall velocities are, for the most part, unchanged.

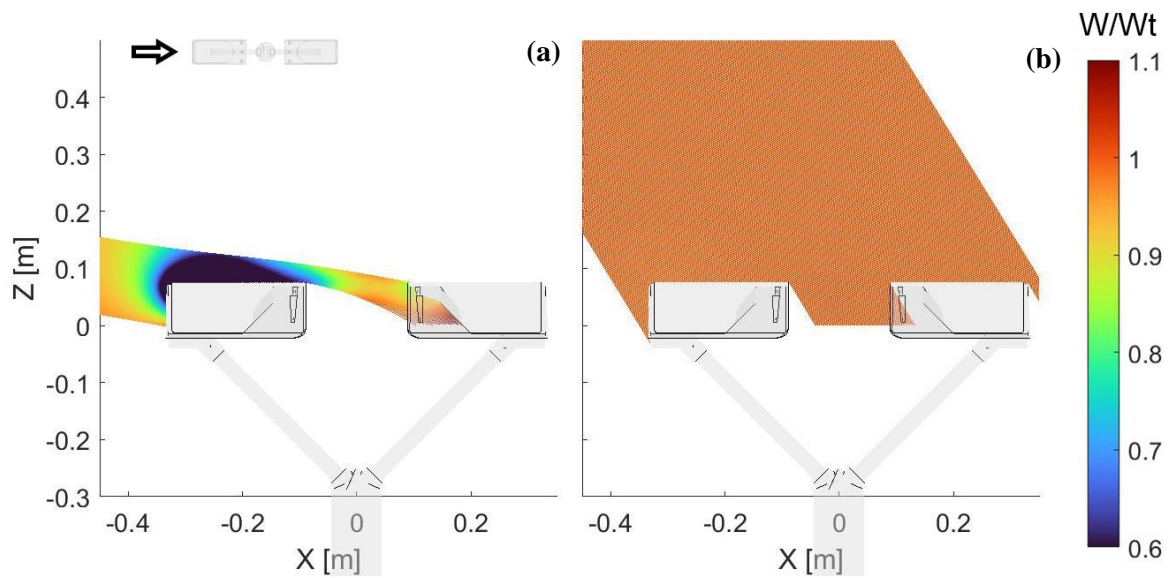


Figure 8.12: Particle trajectories along the $y=0$ plane, at $\alpha = 0^\circ$, $U_{ref} = 5 \text{ m s}^{-1}$ and two hydrometeor diameters, 0.25 mm (a) and 3 mm (b). Trajectories are colour coded according to the particle fall velocity.

When the wind direction is 45° with respect to the instrument laser beam (Figure 8.13), shielding is limited, since the obstruction caused by the instrument body is strongly reduced. However, aerodynamics effects are present for the lighter hydrometeors, since this configuration generates strong velocity gradients, as shown in the previous section. In this case, a small number of hydrometeors can cross the instrument laser beam outside of the expected sensing area, bypassing the sensor protective shields due to their very shallow angle of attack. This could produce not negligible amount of overcatch in the measurement for some wind speed and hydrometeor size combinations.

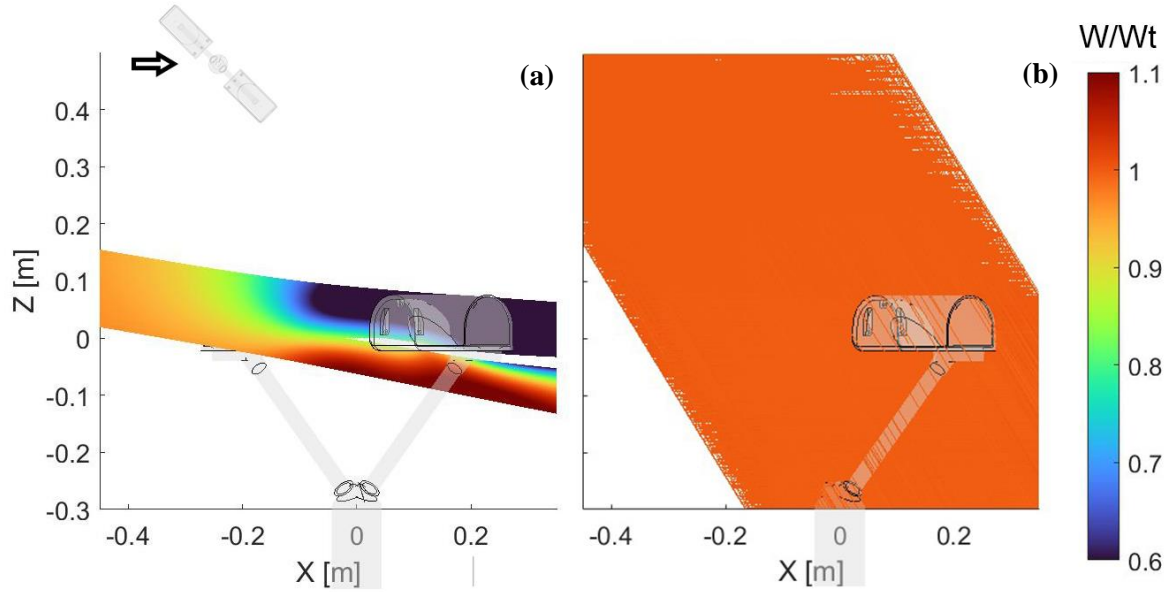


Figure 8.13: Particle trajectories along the $y=0$ plane, at $\alpha = 90^\circ$, $U_{ref} = 10 \text{ m s}^{-1}$ and two hydrometeor diameters, 0.25 mm (a) and 3 mm (b). Trajectories are colour coded according to the particle fall velocity.

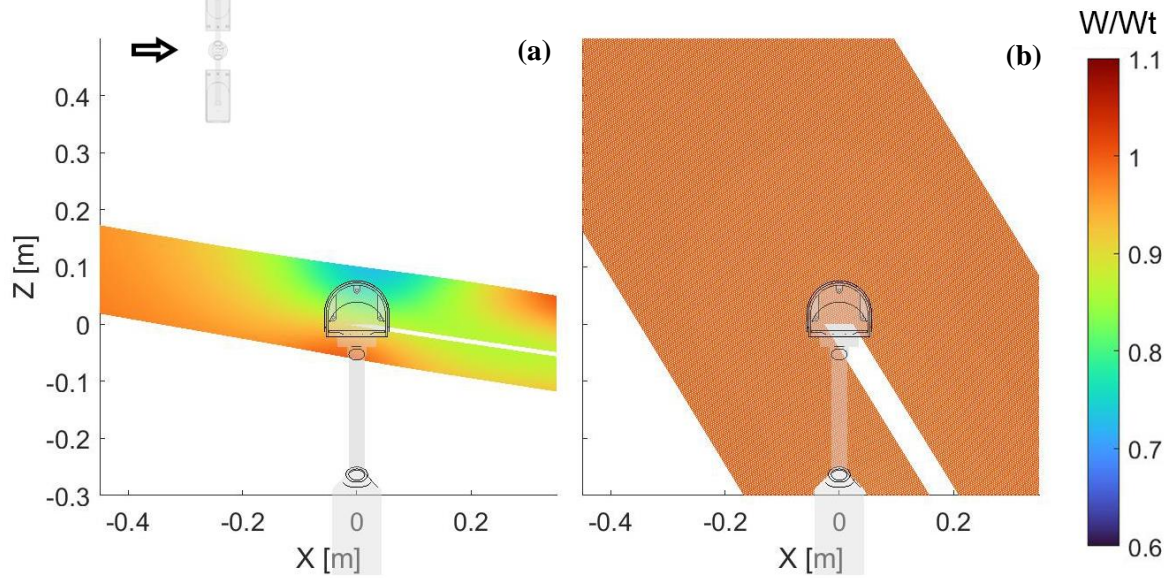


Figure 8.14: Particle trajectories along the $y=0$ plane, at $\alpha = 180^\circ$, $U_{ref} = 10 \text{ m s}^{-1}$ and two hydrometeor diameters, 0.25 mm (a) and 3 mm (b). Trajectories are colour coded according to the particle fall velocity.

Finally, the best performing configuration is considered ($\alpha = 90^\circ$). In this case, both the shielding and aerodynamic effects are minimal and even the smaller and lighter hydrometeors are only partially affected

by the aerodynamic effect (8.14 a), while the larger ones are undisturbed (8.14 b). The shielding due to the instrument body is also minimal in this configuration.

8.2.3 Hydrometeor trajectories near the Vaisala WXT-520

Consistently with the above results, only the time-independent-uncoupled approach was used for the Vaisala WXT-420. In total 231 combinations of wind speed, direction and hydrometeor size were simulated. Sample trajectories for two different diameters are shown in Figures 8.15, 8.16 and 8.17.

In Figure 8.15 (a), it is evident that the instrument body does not produce any significant shielding effect neither for small nor for large size hydrometeors. However, the aerodynamic effect is quite evident for the smallest hydrometeors, having their fall velocity considerably reduced near the instrument sensing area due to the strong updraft.

Instead, larger hydrometeors, shown in Figure 8.15 (b), are for the most part undisturbed, and reach the instrument sensing area without significant changes in their fall velocity. The steeper angle of their trajectories makes them even less susceptible to shielding from the instrument body.

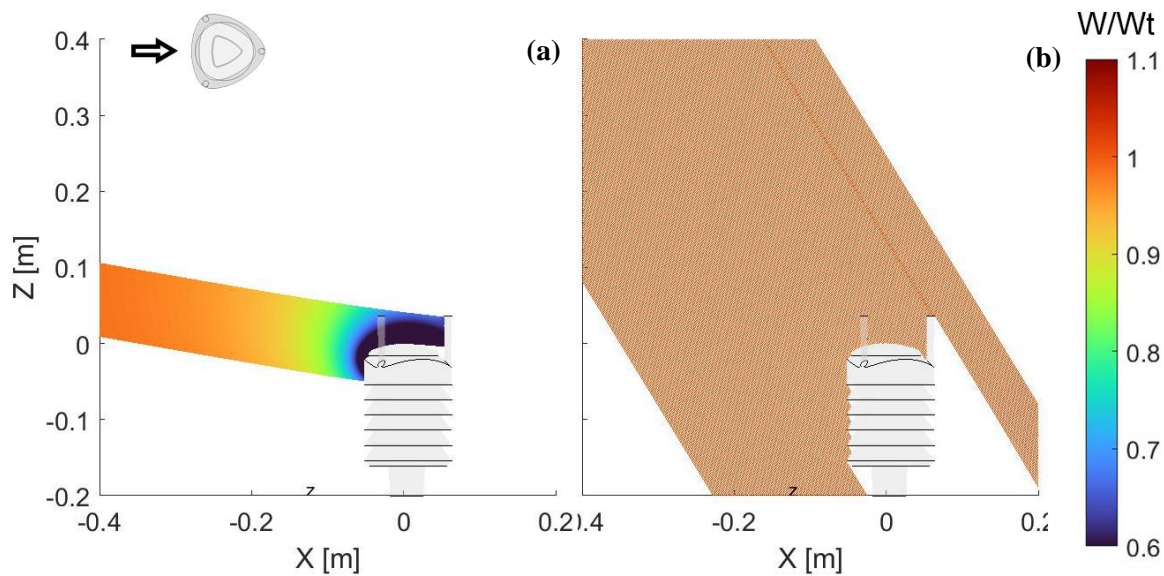


Figure 8.15: Trajectories along the $y=0$ plane, for the configuration at $\alpha = 0^\circ$, $U_{ref} = 5$ m/s and two hydrometeor diameters, 0.25 mm (a) and 3 mm (b). Trajectories are colour coded according to the particle fall velocity.

For the configuration at $\alpha = 30^\circ$ (Figure 8.16), no shielding due to the instrument body is evident. The aerodynamic effect is also quite visible for some hydrometeors that are diverted away from the instrument sensing area and continue their trajectory past the gauge. Small size, light-weight hydrometers are strongly affected by the aerodynamic behaviour of the instrument, while the larger ones are mostly unaffected.

This behaviour is mostly identical to the one observed in the previous case, meaning that similar performance of the instrument is expected in both cases.

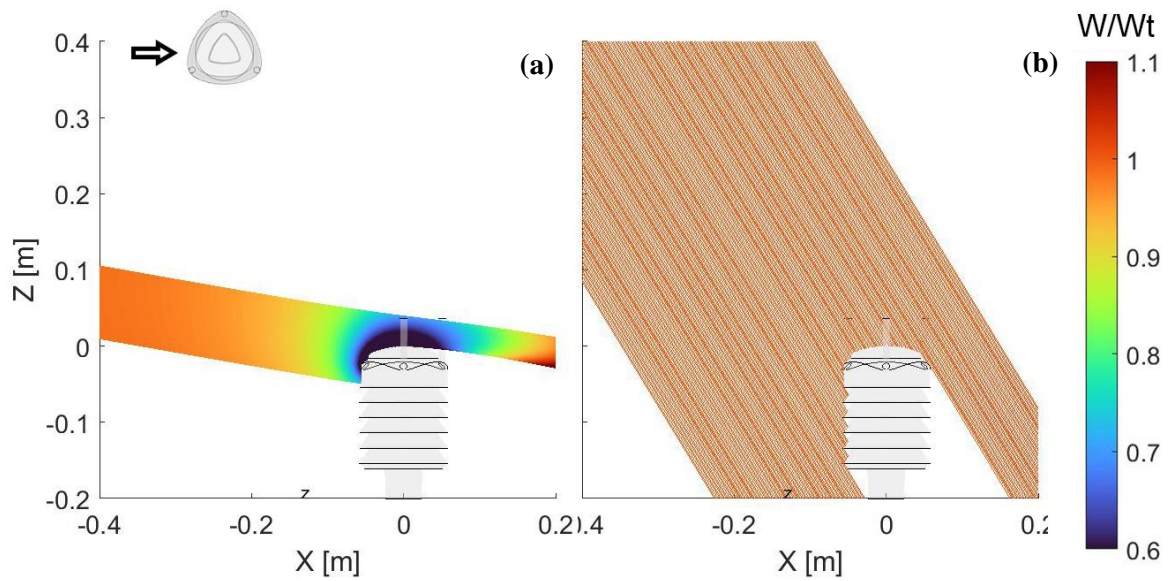


Figure 8.16: Trajectories along the $y=0$ plane, for the configuration at $\alpha = 30^\circ$, $U_{ref} = 10$ m/s and two hydrometeor diameters, 0.25 mm (a) and 3 mm (b). Trajectories are colour coded according to the particle fall velocity.

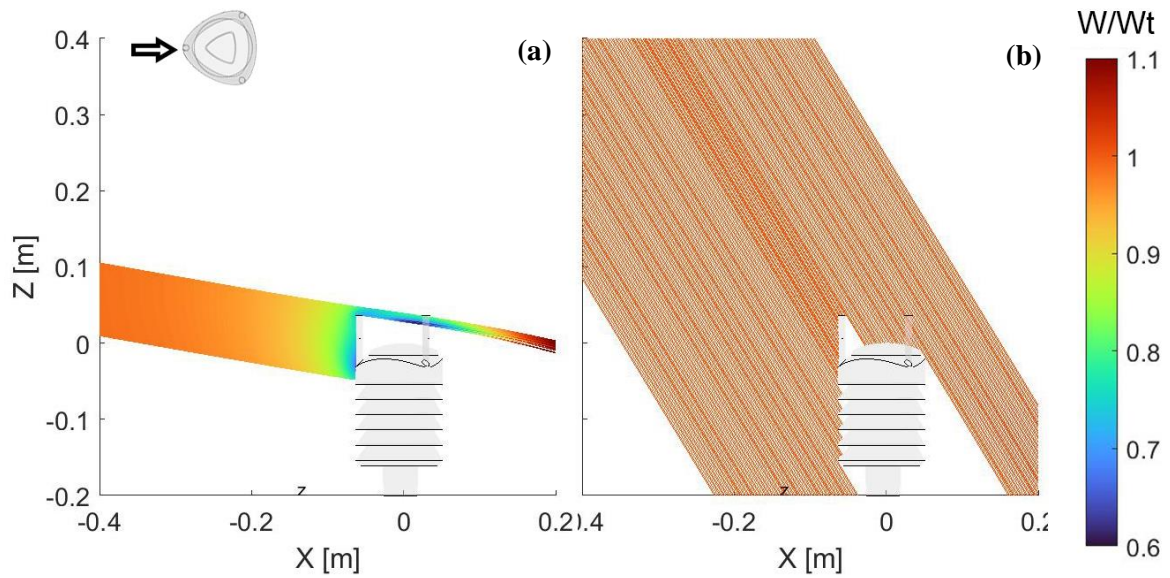


Figure 8.17: Trajectories along the $y=0$ plane, for the configuration at $\alpha = 60^\circ$, $U_{ref} = 10$ m/s and two hydrometeor diameters, 0.25 mm (a) and 3 mm (b). Trajectories are colour coded according to the particle fall velocity.

Finally, the last configuration ($\alpha = 60^\circ$) is shown in Figure 8.17. In this case, a certain amount of shielding occurs due to the presence of the wind-measuring arm upstream of the sensing area. This shielding effect remains even for large hydrometeors. The aerodynamic effect is evident for the smallest hydrometeors, that

see their fall velocity change significantly, while the larger ones are mostly unaffected. Shielding is visible in Figure 8.17; however, it is limited to a small portion of the sensing area since the size of the wind-measuring arm is much smaller than the width of the instrument sensing area.

8.3 CATCH RATIOS

The Catch Ratio (CR) is the primary information derived from the results of the LPT model. This is defined as the ratio between the number of hydrometeors that cross the instrument sensing area under the exposure effect and the number of hydrometeors that would have crossed the same area if the instrument was transparent to the wind and did not constitute an obstacle to incoming particles. CRs provides the expected performance of the gauge for each specific combination of wind speed, wind direction and hydrometeor size. Furthermore, they are independent from the site climatology and can be used to correct measurements taken in the field once the local environmental conditions are known. Due to the large number of CR values obtained for each gauge, only a selected sample is presented in this chapter. Appropriate fitting functions are however provided, suitable for the correction of field measurements and for further post-processing.

8.3.1 Catch ratios for the Thies LPM

Results from the three modelling approaches considered in this work are used to compute the CRs, for the simulated combinations of wind and hydrometeor characteristics. The time-independent uncoupled approach is used here as a reference for comparison against the other more computationally expensive approaches. This provides an insight on the improvements that may be gained by using more complex models for the assessment of the wind induced bias.

8.4.1.1 *Catch ratios from the time-independent uncoupled LPT model*

A sample of the CRs obtained from the time-independent uncoupled model applied to the Thies LPM is shown in Figure 8.18. Results are presented by varying the wind speed (on the x axis) and hydrometeor size (using colour coded bars) at $\alpha = 0^\circ$. At low wind speed the CR approaches unity, meaning that the combined impact of shielding and wind on hydrometeors trajectories is very limited. However, the CR values rapidly decrease with increasing the wind speed, especially for small-size light-weight particles, which do not even reach the instrument sensing area at the highest wind speed (dark blue shaded bars disappear).

To achieve a non-dimensional representation of the results, since the CR values are a function of both the hydrometeors size and wind velocity, results are presented here in terms of the particle Reynolds number (Re_p), that is computed as shown in Equations 8.1.

$$Re_p = \frac{\sqrt{U_{ref}^2 + W_t^2} \cdot D}{\nu}$$

where U_{ref} is the reference undisturbed wind speed, W_t is the hydrometeor terminal velocity, D is the hydrometeor diameter and ν is the kinematic viscosity of the fluid.

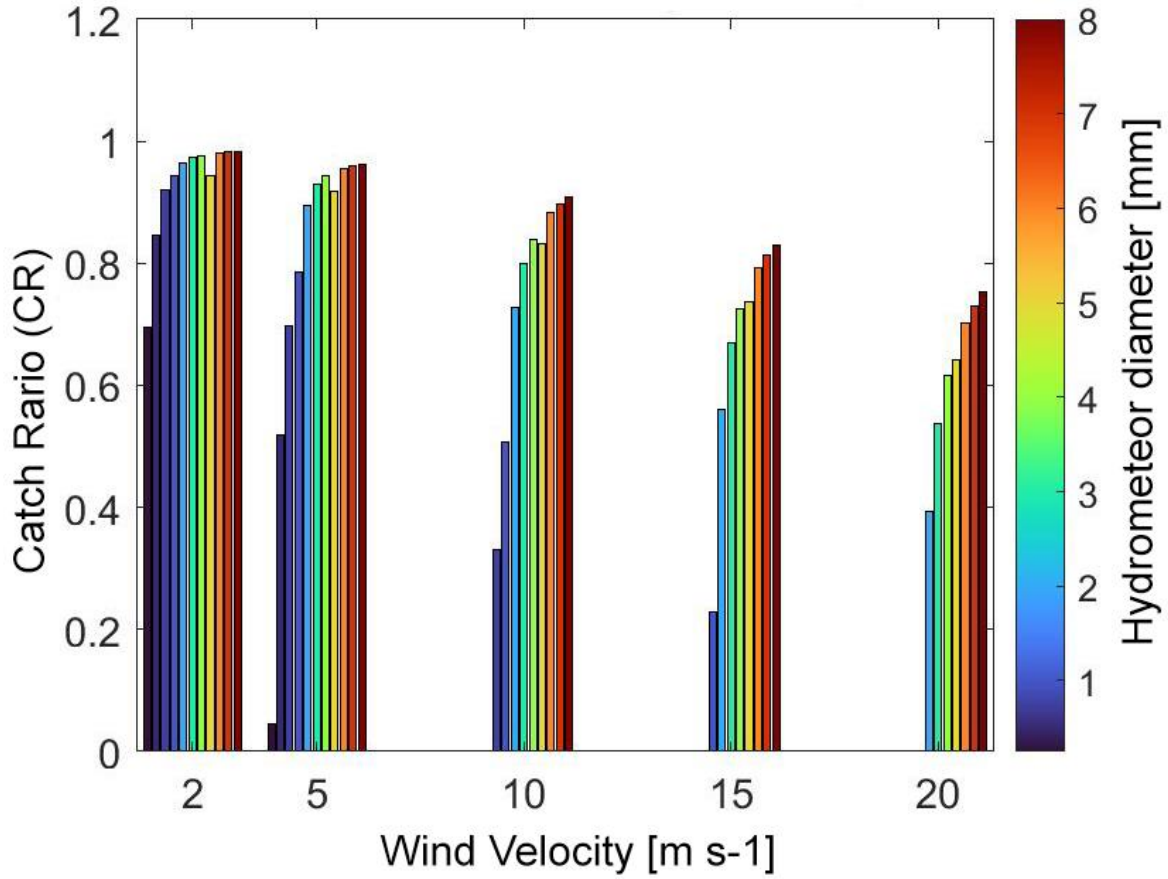


Figure 8.18: Catch ratio as a function of wind speed and hydrometeor size (colour coded) at $\alpha = 0^\circ$.

By using the particle Reynolds number as the independent variable, the computed CR values of the Thies LPM can be fitted by a second-order inverse polynomial function, as shown in Equation 8.2.

$$CR = \begin{cases} a(U_{ref}, \alpha) + \frac{b(U_{ref}, \alpha)}{Re_p} + \frac{c(U_{ref}, \alpha)}{Re_p^2} & \text{if } CR \geq 0 \\ 0 & \text{if } CR < 0 \end{cases}$$

8.2

where a , b , and c are three suitable parameters that are a function of the wind speed (U_{ref}) and direction (α) only. Results of this fitting operation are presented in Figure 8.19 for selected wind directions, together with the CR values obtained from the numerical simulation.

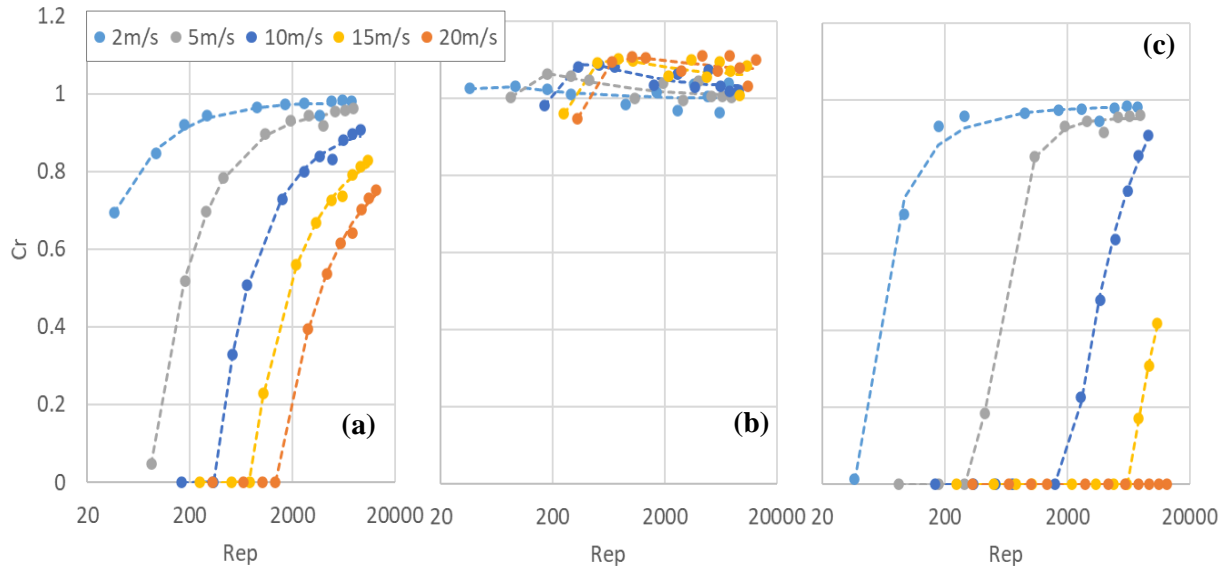


Figure 8.19: Catch ratios as a function of the particle Reynolds number for $\alpha = 0^\circ$ (a), $\alpha = 90^\circ$ (b) and $\alpha = 180^\circ$ (c). The CR values computed from numerical simulation results are indicated by dots while dashed lines represent the best-fit inverse polynomial functions.

For the configuration at $\alpha = 0^\circ$, the CRs decrease with increasing the wind speed and with decreasing the hydrometeor size. Even the lowest wind speed considered shows a considerable undercatch, which persists for particles up to 2 mm in diameter. At higher wind speeds, the CRs quickly decrease, and small size particles do not even reach the instrument sensing area (CR = 0). At the high wind speed of 10 m s^{-1} or above it, even the largest drops ($D = 8 \text{ mm}$) are affected by considerable undercatch. Note that for some combinations of particle size and wind speed (above 5 m s^{-1}), no one hydrometeor reaches the instrument sensing area. This tendency is also evident in other configurations ($\alpha = 22.5^\circ$) but to a lesser extent, with CRs that are always above 0.75.

For the configuration at $\alpha = 90^\circ$, CRs are closer to one and always above 0.9. A similar behaviour is shown at similar angles, where CRs are always above 0.85 ($\alpha = 45^\circ$ and $\alpha = 67.5^\circ$). Furthermore, a limited amount of overcatch is also present at higher wind speed. This phenomenon is due to the much-inclined trajectories of hydrometeors in such wind conditions, that are therefore able to overcome the shielding of the instrument and reach the laser beam in places that for vertically falling hydrometeors would be inaccessible. Some dispersion is also evident, due to the non-linear combination of the aerodynamic and the shielding effect, which is also a function of the sloped trajectories of incoming hydrometeors.

From $\alpha = 112.5^\circ$ to $\alpha = 157.5^\circ$, in general, the CR values decrease, especially for smaller hydrometeors and higher wind speed. Finally, for $\alpha = 180^\circ$ the worst performing conditions (in terms of CR) is obtained, with the smallest hydrometeors that do not reach the instrument sensing area even for the lowest wind speed considered. The CRs quickly decrease with increasing the wind speed, until at 20 m s^{-1} no one hydrometeor crosses the instrument laser beam.

Values of the three best-fit parameters of the inverse second-order polynomial functions for the CR are presented in Tables 8.1, 8.2 and 8.3 for all combinations of wind speed and direction considered.

Table 8.1: Values of the parameter $a(U_{\text{ref}}, \alpha)$.

a	$U_{\text{ref}} = 2 \text{ m s}^{-1}$	$U_{\text{ref}} = 5 \text{ m s}^{-1}$	$U_{\text{ref}} = 10 \text{ m s}^{-1}$	$U_{\text{ref}} = 15 \text{ m s}^{-1}$	$U_{\text{ref}} = 20 \text{ m s}^{-1}$
$\alpha = 0$	0.978	0.967	0.923	0.880	0.849
$\alpha = 22.5$	0.985	0.966	0.936	0.914	0.901
$\alpha = 45$	0.985	0.985	1.000	0.994	0.986
$\alpha = 67.5$	0.992	0.994	1.021	1.038	1.045
$\alpha = 90$	1.001	1.007	1.027	1.056	1.072
$\alpha = 112.5$	0.992	0.998	1.025	1.042	1.046
$\alpha = 135$	0.985	0.991	1.024	1.022	1.000
$\alpha = 157.5$	0.986	0.968	0.928	0.908	0.911
$\alpha = 180$	0.983	0.950	1.186	1.001	0.000

Table 8.2: Values of the parameter $b(U_{\text{ref}}, \alpha)$.

b	$U_{\text{ref}} = 2 \text{ m s}^{-1}$	$U_{\text{ref}} = 5 \text{ m s}^{-1}$	$U_{\text{ref}} = 10 \text{ m s}^{-1}$	$U_{\text{ref}} = 15 \text{ m s}^{-1}$	$U_{\text{ref}} = 20 \text{ m s}^{-1}$
$\alpha = 0$	-12.115	-79.572	-299.117	-716.663	-1434.513
$\alpha = 22.5$	-10.441	-30.881	-68.865	-99.301	-128.315
$\alpha = 45$	-3.127	-7.169	-23.311	-24.044	-12.406
$\alpha = 67.5$	1.671	13.938	20.891	22.634	28.641
$\alpha = 90$	3.987	19.497	47.524	60.640	69.399
$\alpha = 112.5$	2.715	10.870	14.389	14.869	21.130
$\alpha = 135$	0.104	-12.488	-134.307	-215.436	-274.166
$\alpha = 157.5$	-7.928	-26.282	8.653	57.951	151.993
$\alpha = 180$	-13.202	29.366	-2679.583	-6383.994	0.000

Table 8.3: Values of the parameter $c(U_{\text{ref}}, \alpha)$.

c	$U_{\text{ref}} = 2 \text{ m s}^{-1}$	$U_{\text{ref}} = 5 \text{ m s}^{-1}$	$U_{\text{ref}} = 10 \text{ m s}^{-1}$	$U_{\text{ref}} = 15 \text{ m s}^{-1}$	$U_{\text{ref}} = 20 \text{ m s}^{-1}$
$\alpha = 0$	62.757	132.720	-4768.011	36236.461	384125.964
$\alpha = 22.5$	185.971	1127.165	6656.178	16558.008	31059.792
$\alpha = 45$	13.358	-99.925	642.237	-1355.511	-8744.195
$\alpha = 67.5$	-89.596	-1590.934	-6601.725	-14845.244	-27936.357

$\alpha = 90$	-113.154	-1674.908	-9275.088	-21270.653	-37064.360
$\alpha = 112.5$	-190.780	-1913.006	-8551.494	-20790.352	-40791.453
$\alpha = 135$	-258.741	-2497.880	6965.837	18699.213	29387.632
$\alpha = 157.5$	238.735	-880.128	-111300.964	-618261.523	-3005808.649
$\alpha = 180$	-816.477	-148793.884	415171.710	582.429	0.000

Using these values, the catch ratio of the Thies LPM can be calculated for each hydrometeors size, under various environmental (wind speed) conditions.

8.4.1.2 Catch ratios from the time-dependent uncoupled LPT model

Results are again presented in non-dimensional terms, by plotting the CR as a function of the particle Reynolds number and are compared against the best fit curves already obtained from the time-independent-uncoupled approach.

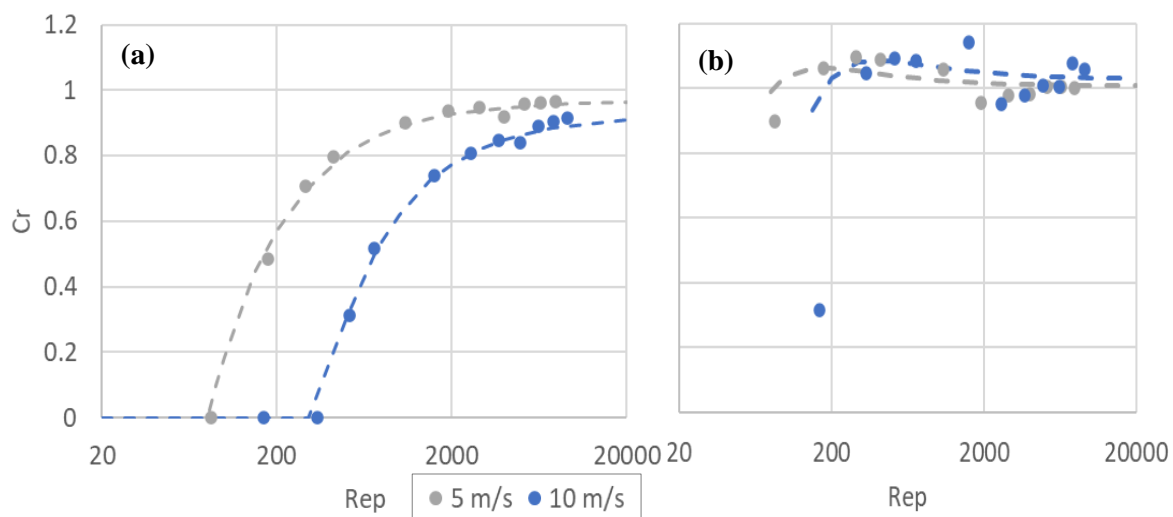


Figure 8.20: Catch ratios as a function of the particle Reynolds number at $\alpha = 0^\circ$ (a) and $\alpha = 90^\circ$ (b). The CR values computed from the time-dependent-uncoupled approach are indicated by dots while dashed lines represent the best-fit inverse polynomial functions obtained from the time-independent-uncoupled approach.

Figure 8.20 shows that, at $\alpha = 0^\circ$, the two approaches provide almost identical results, while in the case of $\alpha = 90^\circ$ results are in good agreement, even if data are more dispersed, except for the smallest hydrometeors (0.25 mm in diameter), which has considerably lower CR values if compared with the time-independent-uncoupled best-fit function.

These results suggest that the considerable computational burden of the time-dependent-coupled approach does not provide significant improvement over the much cheaper time-independent-uncoupled approach, as anticipated from the analysis of the airflow modelling approaches. They also suggest that the minor differences in the velocity field already noted at $\alpha = 0^\circ$ are negligible for computing particle trajectories, while the primary factor controlling the results is the instrument shape.

8.4.1.3 Catch ratios from the time-dependent one-way coupled LPT model

Due to the higher computational cost only a limited number of CR values are obtained from the time-dependent one-way coupled approach. Results are presented in Figure 8.21, compared, as above, against the best fit curves from the time-independent-uncoupled approach.

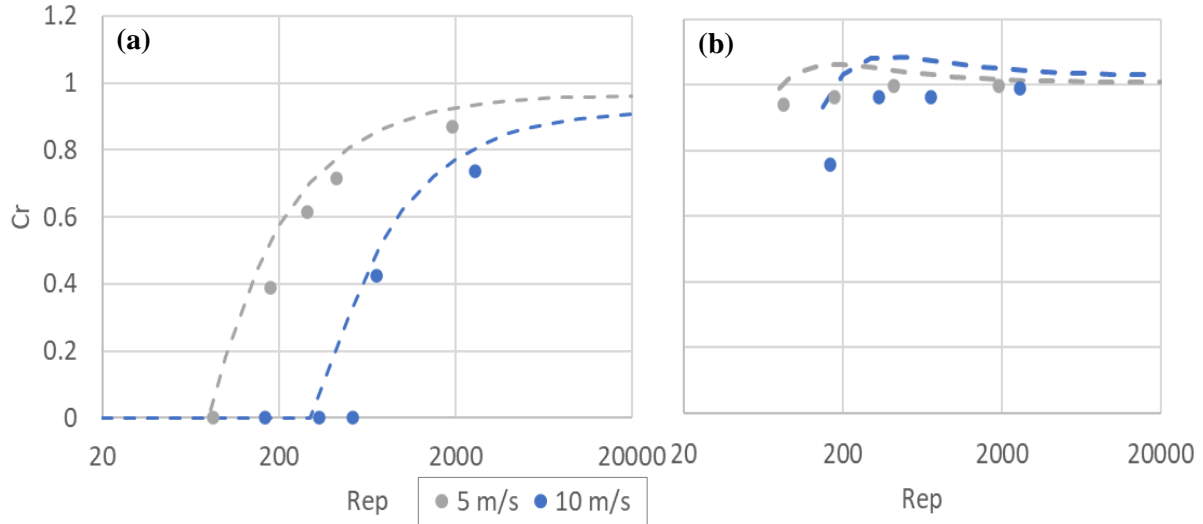


Figure 8.21: Catch ratios as a function of the particle Reynolds number at $\alpha = 0^\circ$ (a) and $\alpha = 90^\circ$ (b). CR values computed from the time-dependent-coupled approach are indicated by dots, while dashed lines represent the fitting inverse polynomial function obtained from the time-independent-uncoupled approach.

Figure 8.21 shows that CRs present the same overall behaviour as before, but with lower values. This may be explained by the enhanced trajectory deviations produced by turbulence, which may divert some hydrometeors away from the laser beam. However, since this effect depends on the instantaneous flow velocity in the recirculation zone, which is intrinsically turbulent, the opposite effect may also be observed at another instant. This could be highlighted by running the simulation multiple times, while changing the instant when particles are released in the domain. Nevertheless, the high computational burden of the time-dependent-coupled simulations limits the feasibility of such approach.

8.3.2 Catch ratios for the OTT Parsivel²

Only the time-independent uncoupled approach was considered for this instrument. This is acceptable since it was shown that for the two other approaches considered, one does not provide appreciable improvements while the other would require an amount of computational resources that makes it currently not suitable for widespread application.

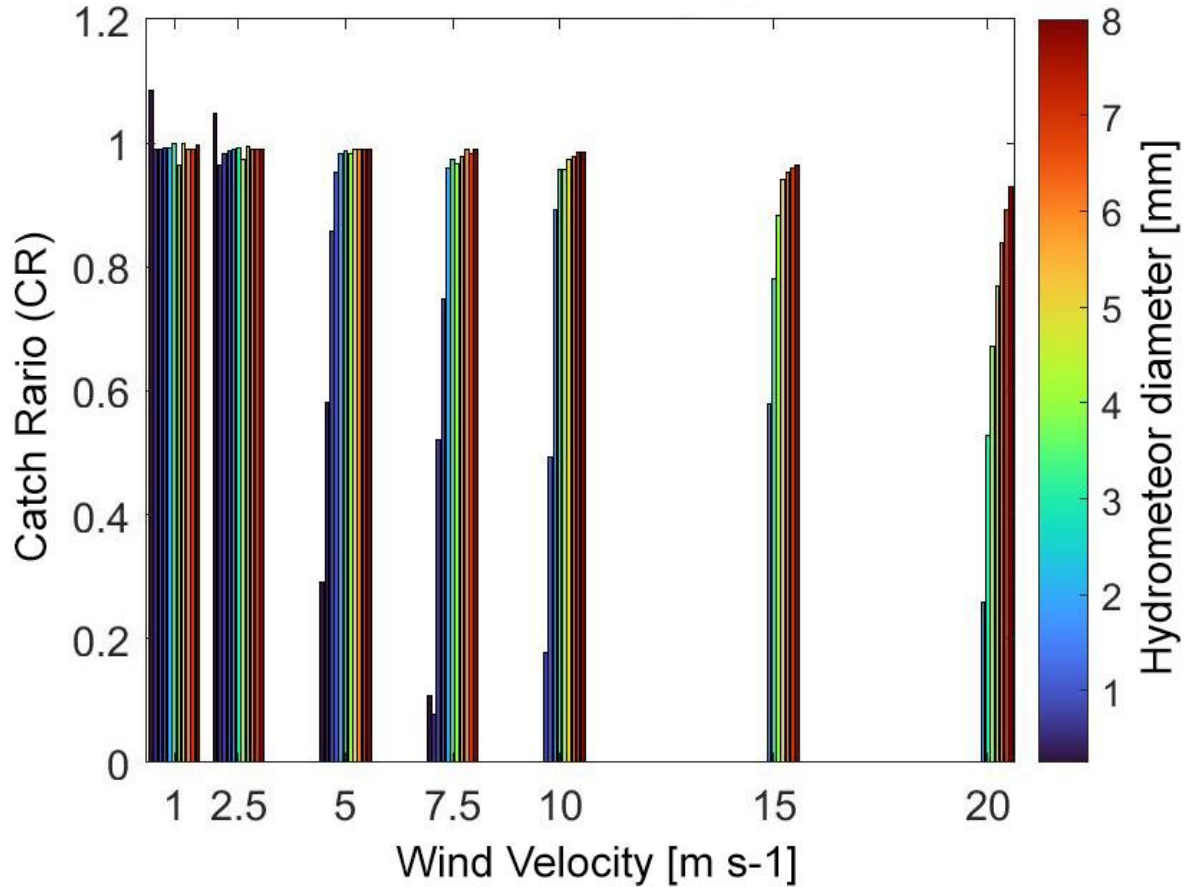


Figure 8.22: Catch ratios as a function of the wind speed and hydrometeor size at $\alpha = 0^\circ$.

Figure 8.22 shows an example of the obtained CRs when varying the wind speed (on the x-axis) and hydrometeor size (colour coded bars) at $\alpha = 0^\circ$. At low wind speed the CR approaches unity, meaning that the combined effect of shielding and wind is limited. However, a tendency to overcatch is evident for the smallest and lightest hydrometeors. Those are diverted towards the instrument sensing area by the downdraft that was previously highlighted, especially in combination with the less inclined trajectories that are observed at low wind speed. Furthermore, CR values decrease with increasing the wind speed, especially for small-size and light-weight particles, which do not even reach the instrument sensing area at high wind speed since they are swiped away by the separation layer close to the instrument body.

The CRs obtained from the simulations are presented here in non-dimensional terms as a function of the particle Reynolds number (Re_p), computed as in Equations 8.1. The CRs, function of Re_p , for the OTT Parsivel² are then fitted by using a polynomial function, as shown in Equation 8.3.

$$CR = \begin{cases} a(U_{ref}, \alpha) + b(U_{ref}, \alpha) \cdot Re_p^{-1} + c(U_{ref}, \alpha) \cdot Re_p^{\frac{1}{2}} & \text{if } CR \geq 0 \\ 0 & \text{if } CR < 0 \end{cases}$$

where the parameters a , b , and c are a function of the wind speed (U_{ref}) and direction (α) only. Results of the obtained best-fit are presented in Figure 8.23 for selected wind directions.

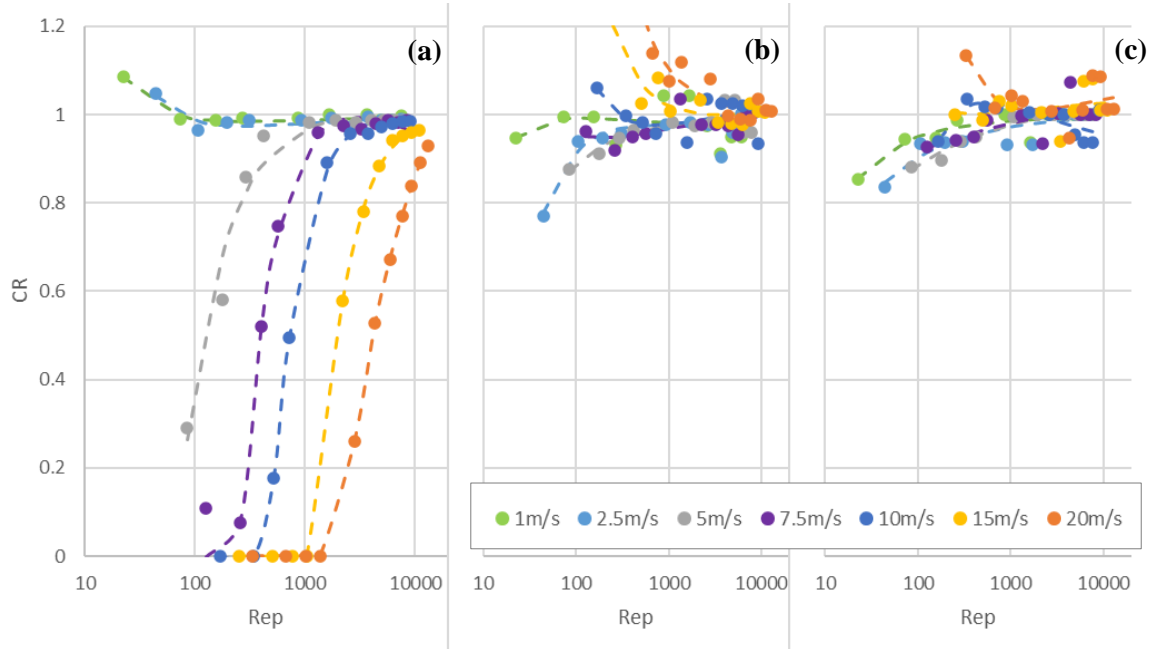


Figure 8.23: Catch ratios as function of the particle Reynolds number for $\alpha = 0^\circ$ (a), $\alpha = 45^\circ$ (b) and $\alpha = 90^\circ$ (c). Computed CR values are indicated by dots, while dashed lines represent the best-fit function.

For the configuration at $\alpha = 0^\circ$, the CRs show some limited overcatch of particles with the smallest diameter at a wind speed of 1 and 2.5 m s⁻¹, which quickly returns to unity for diameters above 0.5 mm. Considering higher wind speed, the CRs quickly decrease, and the small diameter drops do not even reach the instrument sensing area. At the very high wind speed of 20 m s⁻¹, even the largest drops ($D = 8$ mm) are affected, although only slightly. Note that for some particle size and wind speed combinations, above 10 m s⁻¹, no one hydrometeor reaches the instrument sensing area. This tendency is also evident at $\alpha = 22.5^\circ$ but to a lesser extent, with the CRs being always above 0.5.

For the configurations at $\alpha = 45^\circ$ and $\alpha = 90^\circ$, the CRs are closer to one and (with limited exceptions) are all above 0.9. A non negligible amount of overcatch is evident at high wind speed. This phenomenon is due to the much-inclined hydrometeor trajectories occurring in such wind conditions, able to overcome the shielding of the instrument and to reach the laser beam in places that would be inaccessible to the vertically falling hydrometeors. Considerable dispersion is also evident, due to the non-linear combination of the aerodynamic effect and the instrument body shielding, as a function of the inclined trajectories of the incoming hydrometeors. Comparable results are also obtained at $\alpha = 67.5^\circ$; however, in this particular configuration, no overcatch is observed even at high wind speed.

The numerical values of the three parameters of the CR best-fit functions are presented in Tables 8.4, 8.5 and 8.6 for all the environmental conditions considered in this study.

Table 8.4: Numerical values of the parameter $a(U_{ref}, \alpha)$.

a	$U_{ref} = 1$ m s^{-1}	$U_{ref} = 2.5$ m s^{-1}	$U_{ref} = 5$ m s^{-1}	$U_{ref} = 7.5$ m s^{-1}	$U_{ref} = 10$ m s^{-1}	$U_{ref} = 15$ m s^{-1}	$U_{ref} = 20$ m s^{-1}
$\alpha = 0$	0.998	0.983	0.967	0.974	0.999	0.998	0.983
$\alpha = 22.5$	1.003	0.949	0.960	0.970	1.001	1.003	0.949
$\alpha = 45$	0.983	0.946	1.002	1.011	1.027	0.983	0.946
$\alpha = 67.5$	0.835	0.990	1.013	0.982	1.030	0.835	0.990
$\alpha = 90$	0.799	1.088	1.043	0.965	0.906	0.799	1.088

Table 8.5: Numerical values of the parameter $b(U_{ref}, \alpha)$.

b	$U_{ref} = 1$ m s^{-1}	$U_{ref} = 2.5$ m s^{-1}	$U_{ref} = 5$ m s^{-1}	$U_{ref} = 7.5$ m s^{-1}	$U_{ref} = 10$ m s^{-1}	$U_{ref} = 15$ m s^{-1}	$U_{ref} = 20$ m s^{-1}
$\alpha = 0$	4.154	-0.833	-2.892	-4.209	-1.642	4.154	-0.833
$\alpha = 22.5$	8.064	-27.801	-14.567	-8.536	-0.758	8.064	-27.801
$\alpha = 45$	-78.764	-64.881	-5.208	-10.692	2.677	-78.764	-64.881
$\alpha = 67.5$	-473.584	-50.173	12.251	-27.927	6.658	-473.584	-50.173
$\alpha = 90$	-917.038	16.279	50.275	-43.677	-66.968	-917.038	16.279

Table 8.6: Numerical values of the parameter $c(U_{ref}, \alpha)$.

c	$U_{ref} = 1$ m s^{-1}	$U_{ref} = 2.5$ m s^{-1}	$U_{ref} = 5$ m s^{-1}	$U_{ref} = 7.5$ m s^{-1}	$U_{ref} = 10$ m s^{-1}	$U_{ref} = 15$ m s^{-1}	$U_{ref} = 20$ m s^{-1}
$\alpha = 0$	-0.469	0.254	0.518	0.384	-0.335	-0.469	0.254
$\alpha = 22.5$	-0.953	2.457	0.967	0.206	-0.916	-0.953	2.457
$\alpha = 45$	1.944	3.177	-0.629	-0.653	-1.692	1.944	3.177
$\alpha = 67.5$	17.371	-0.521	-1.793	0.640	-1.768	17.371	-0.521
$\alpha = 90$	26.074	-7.390	-3.667	1.554	5.668	26.074	-7.390

8.3.3 Catch ratios for the Vaisala WXT-520

Since the Vaisala WXT-520 is an impact disdrometer, which measures the kinetic energy of drops, computing of the sole number of hydrometers reaching the instrument sensing area is not sufficient to completely characterize its performance under varying wind conditions. In fact, both the particles fall velocity and changes in the angle and point of impact must be considered to provide a complete assessment

of the wind-induced bias. For this reason, the Kinetic Catch Ratio (KCR) is introduced, defined as the ratio between the kinetic energy flux that is transferred to the instrument sensing area under the effect of wind and the kinetic energy flux that would have been transferred to the same area if hydrometeors had fallen vertically at their terminal velocity. Evaluation of the energy transfer between hydrometeors and the instrument sensing area was obtained by decomposing the kinetic energy in a component normal to the surface of impact and one tangential to the surface. Only the component normal to the surface is considered to evaluate the kinetic energy flux for both the windy and reference conditions.

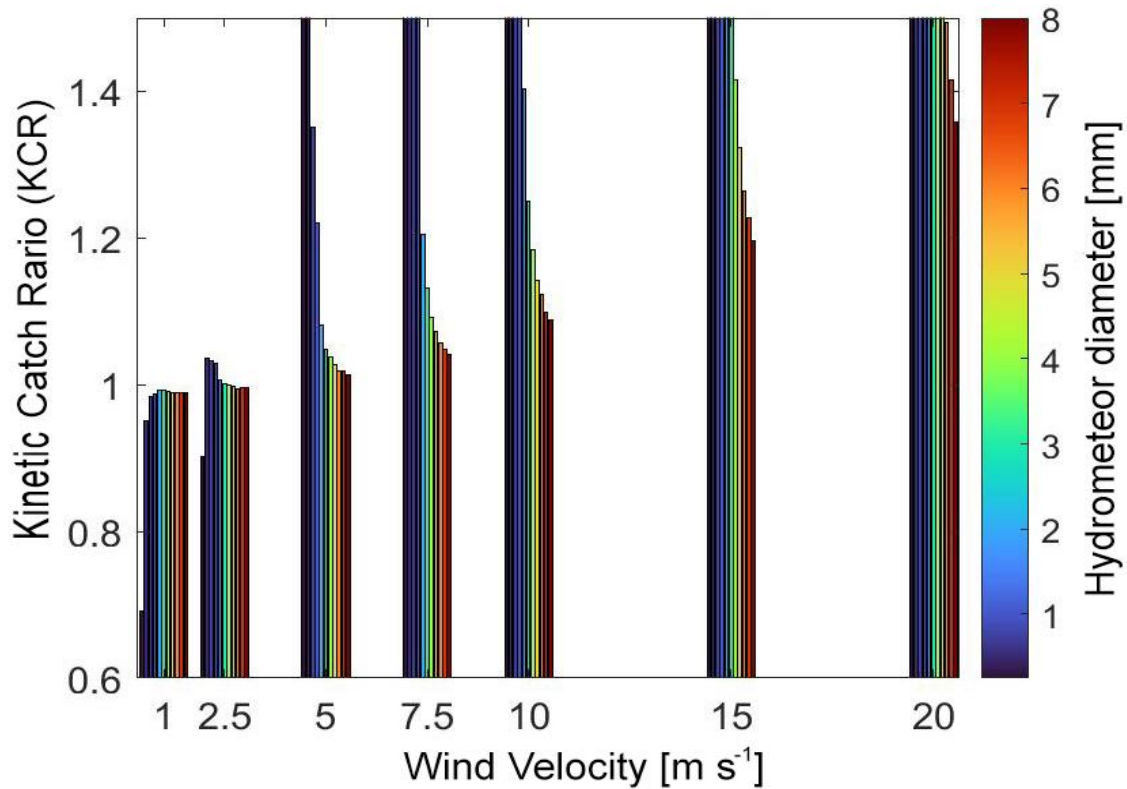


Figure 8.24: KCR for different wind speeds and hydrometeor sizes for $\alpha = 0^\circ$.

Figure 8.24 shows an example of the KCR obtained from numerical simulation as a function of the wind speed and hydrometeor size for the configuration at $\alpha = 0^\circ$. At low wind speed, KCR values below unity occur, especially for small hydrometeors that are more affected by the updraft and therefore have their kinetic energy reduced. However, for high wind speeds, the increase in kinetic energy due to the hydrometeors overall velocity being enhanced by wind greatly overcomes the reduction in fall velocity due to the updraft. This effect results in extremely high KCR for small size hydrometeors, even above 10 for the smallest hydrometeors and the highest wind speeds.

The large number of KCR values obtained from the simulation are presented in non-dimensional terms as a function of the particle Reynolds number (Re_p), computed as shown in Equation 8.1. When plotted against the particle Reynolds number, the CR of the Vaisala WXT-520 can be fitted by a four-parameter function, shown in Equation 8.4.

$$KCR = 1 + \frac{a(U_{ref}, \alpha)}{b(U_{ref}, \alpha) + c(U_{ref}, \alpha) \cdot Re_p + Re_p^{d(U_{ref}, \alpha)}}$$

8.4

Where a , b , c and d are best-fit parameters that are a function of the wind speed (U_{ref}) and direction (α) only. Results of this fitting operation are presented in Figure 8.25 for selected wind directions.

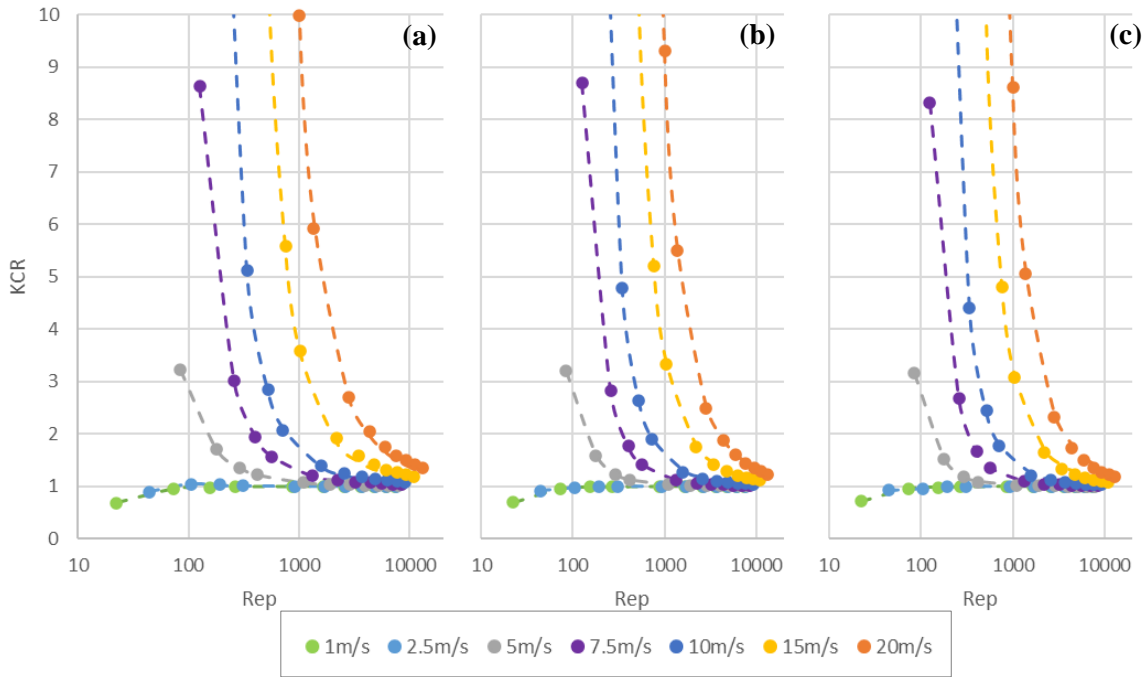


Figure 8.25: KCR as function of the particle Reynolds number at $\alpha = 0^\circ$ (a), $\alpha = 30^\circ$ (b) and $\alpha = 60^\circ$ (c). Computed KCR values are represented by dots (colour coded with the wind speed) while dashed lines are the best-fit functions.

All three configurations ($\alpha = 0^\circ$, $\alpha = 30^\circ$ and $\alpha = 60^\circ$) show similar behaviour, meaning that, contrary to previous gauges, the wind direction has a limited influence on the wind-induced bias for the Vaisala WXT-520. Wind velocity has instead a strong impact on the KCR. At the wind speed of 1 m/s and 2.5 m/s, the KCR values are close to unity for all diameters, except the smaller ones, that shows some undercatch. By increasing the wind speed, starting from 5 m/s, the KCR exponentially increases, especially for small size drops. This effect is due to the kinetic energy transferred by the wind to the hydrometeors that, for the smallest drops, may exceed ten times the kinetic energy of the same drop falling at terminal velocity. This increase in the drop kinetic energy can be observed also for larger hydrometeors, that shows a considerable amount of overcatch at high wind speed.

In Figure 8.25 (c), a slight reduction in the KCR values over the other two configurations is evident, due to the shielding operated by the wind-measuring arm, already discussed above. However, this effect is negligible if compared against the increase in the drops kinetic energy due to wind.

Values of the four parameters used to fit the KCR values for all the considered environmental conditions are presented in tables 8.7, 8.8, 8.9 and 8.10.

Table 8.7: Numerical values of the parameter $a(U_{ref}, \alpha)$.

a	$U_{ref} = 1 \text{ m s}^{-1}$	$U_{ref} = 2.5 \text{ m s}^{-1}$	$U_{ref} = 5 \text{ m s}^{-1}$	$U_{ref} = 7.5 \text{ m s}^{-1}$	$U_{ref} = 10 \text{ m s}^{-1}$	$U_{ref} = 15 \text{ m s}^{-1}$	$U_{ref} = 20 \text{ m s}^{-1}$
$\alpha = 0^\circ$	-0.35286	0.12820	0.15627	0.17348	0.23841	0.30192	0.50006
$\alpha = 30^\circ$	-0.02065	-0.00024	0.03053	0.08956	0.15784	0.30824	0.46073
$\alpha = 60^\circ$	-0.01130	-0.00137	0.01925	0.06224	0.13340	0.26814	0.41768

Table 8.8: Numerical values of the parameter $b(U_{ref}, \alpha)$.

b	$U_{ref} = 1 \text{ m s}^{-1}$	$U_{ref} = 2.5 \text{ m s}^{-1}$	$U_{ref} = 5 \text{ m s}^{-1}$	$U_{ref} = 7.5 \text{ m s}^{-1}$	$U_{ref} = 10 \text{ m s}^{-1}$	$U_{ref} = 15 \text{ m s}^{-1}$	$U_{ref} = 20 \text{ m s}^{-1}$
$\alpha = 0^\circ$	-1.70949	-4.36870	-0.51611	-0.38268	-0.31930	-0.27808	-0.21787
$\alpha = 30^\circ$	-0.28514	-0.47605	-0.47256	-0.36958	-0.31317	-0.28111	-0.21764
$\alpha = 60^\circ$	-0.16471	-0.59378	-0.47573	-0.36552	-0.31609	-0.28031	-0.21867

Table 8.9: Numerical values of the parameter $c(U_{ref}, \alpha)$.

c	$U_{ref} = 1 \text{ m s}^{-1}$	$U_{ref} = 2.5 \text{ m s}^{-1}$	$U_{ref} = 5 \text{ m s}^{-1}$	$U_{ref} = 7.5 \text{ m s}^{-1}$	$U_{ref} = 10 \text{ m s}^{-1}$	$U_{ref} = 15 \text{ m s}^{-1}$	$U_{ref} = 20 \text{ m s}^{-1}$
$\alpha = 0^\circ$	0.12429	0.06939	0.00221	0.00085	0.00051	0.00024	0.00015
$\alpha = 30^\circ$	0.00922	0.00134	0.00100	0.00065	0.00044	0.00025	0.00015
$\alpha = 60^\circ$	0.00503	0.00146	0.00090	0.00059	0.00043	0.00024	0.00015

Table 8.10: Numerical values of the parameter $d(U_{ref}, \alpha)$.

d	$U_{ref} = 1 \text{ m s}^{-1}$	$U_{ref} = 2.5 \text{ m s}^{-1}$	$U_{ref} = 5 \text{ m s}^{-1}$	$U_{ref} = 7.5 \text{ m s}^{-1}$	$U_{ref} = 10 \text{ m s}^{-1}$	$U_{ref} = 15 \text{ m s}^{-1}$	$U_{ref} = 20 \text{ m s}^{-1}$
$\alpha = 0^\circ$	-0.86927	-2.57305	-0.20669	-0.24994	-0.27320	-0.27138	-0.30387
$\alpha = 30^\circ$	-0.61663	-0.22921	-0.20558	-0.24974	-0.27209	-0.27058	-0.30411
$\alpha = 60^\circ$	-0.76808	-0.15782	-0.20184	-0.24875	-0.26965	-0.27077	-0.30320

9 IMPACT ON PRECIPITATION MEASUREMENTS

In this chapter, the impact of wind is evaluated for common NCGs output or derived variables, such as precipitation intensity, PSVD and radar reflectivity, based on the previously computed CRs. Although CRs are independent on the site climatology, an assumption regarding the shape of the DSD is necessary here to quantify the wind-induced bias on integral precipitation characteristics. In this chapter, for the sake of conciseness, an exponential shape of the natural DSD is assumed, however correction curves can be easily tailored to the specific installation site of the instrument in hand by including any specific DSD formulation (gamma function).

9.1 WIND INDUCED BIAS ON THE PSVD

The primary goal of NCGs is the in-situ measurement of the microphysical characteristics of precipitation. In the previous chapter wind was shown to have a strong impact on the number of hydrometeors that effectively reach the instrument sensing area, also affecting their fall velocity close to the gauge body. Some amount of bias in the PSVD matrix provided in output by the gauge under windy conditions is therefore expected.

9.1.1 Fall velocity

As discussed in chapter 2.3, hydrometeors approach the ground at their terminal velocity. Before the instrument has a chance to detect them, however, they may encounter wind-induced updraft or downdraft components that modify their fall velocity, hence introducing inaccuracies in the measurements. This was highlighted in chapter 8.2, where the trajectories of smaller and lighter hydrometeors were shown to significantly change their fall velocity when approaching the instrument.

From the LPT model results, the vertical velocity of each hydrometeor as it reaches the instrument sensing area is known for every combination of wind speed and direction. Results are further made non-dimensional by dividing the fall velocity of each particle by their terminal velocity for ease of comparison.

9.1.1.1 Fall velocity bias for the Thies LPM

Figure 9.1 presents the computed changes in the hydrometeor fall velocity when they cross the sensing area of the instrument at low wind speed (2 m s^{-1}) for various wind directions. Figures 9.1a and 9.1b show that, at $\alpha = 0^\circ$ and $\alpha = 90^\circ$ respectively, the fall velocity of small hydrometeors up to 1 mm in diameter is reduced when they cross the instrument sensing area. Hydrometeors having a small diameter show a reduction of almost 15% on average (Figure 9.1a). Larger size hydrometeors are instead unaffected, since their Stoke number for this particular case is much higher (see chapter 5.3.2). The wind-induced bias on the fall velocity furthermore increases with increasing wind speed, however, in most cases, small-size hydrometeors tend to stop reaching the instrument sensing area altogether before their fall velocity can be reduced further.

Figures 9.1c and 9.1d show the case of the worst performing wind directions. At $\alpha = 157.5^\circ$ (Figure 9.1c) the fall velocity of small size hydrometeors is overestimated, up to 20% on average for the smallest diameter

considered. At $\alpha = 180^\circ$, instead, a strong reduction in the hydrometeor fall velocity is observed, up to 40% on average, more pronounced than in the previous two cases.

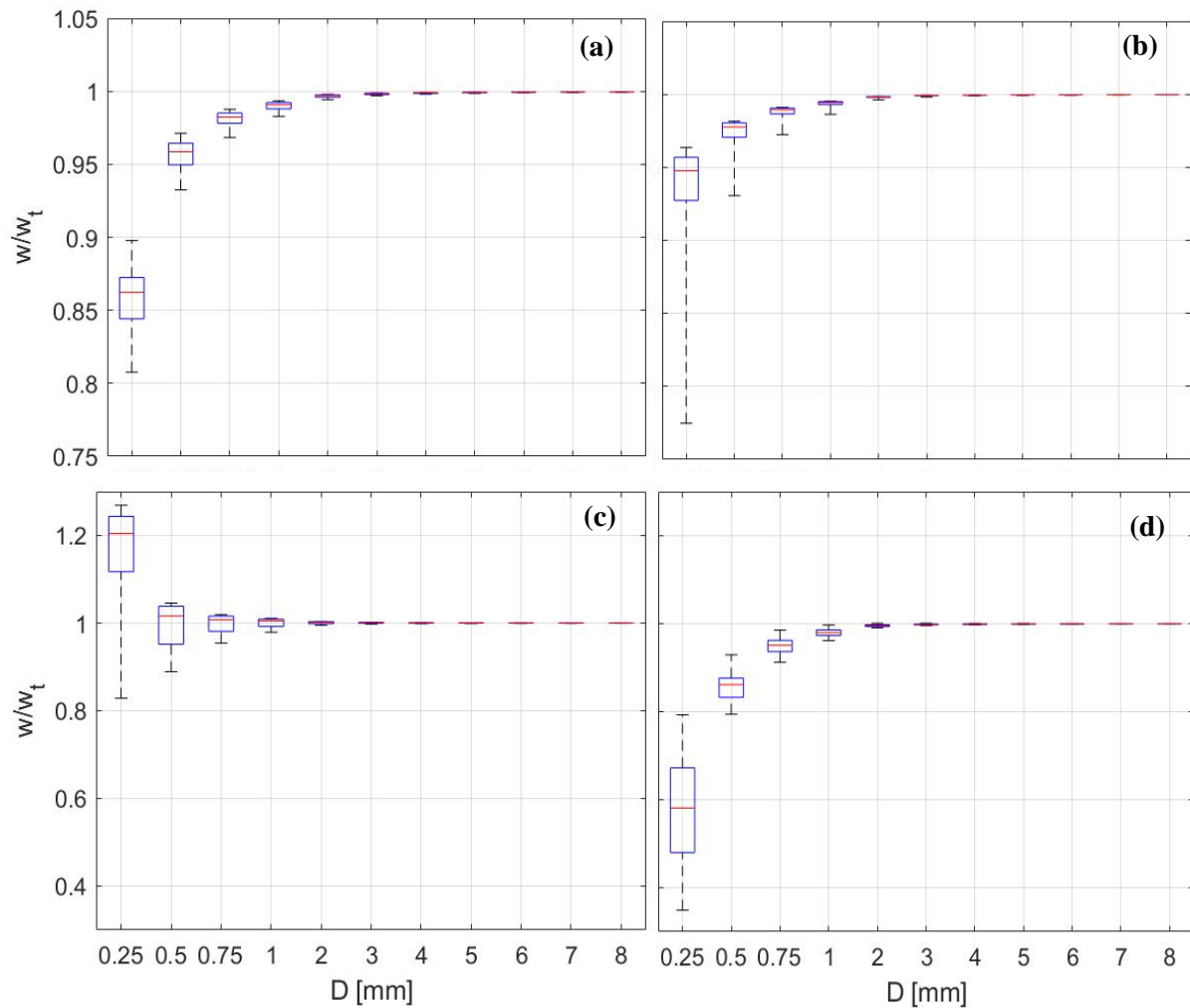


Figure 9.1: Non-parametric (box plot) representation of the non-dimensional fall velocity of hydrometeors when crossing the sensing area of the Thies LPM at $U_{ref} = 2 \text{ m s}^{-1}$ and $\alpha = 0^\circ$ (a), $\alpha = 90^\circ$ (b), $\alpha = 157.5^\circ$ (c) and $\alpha = 180^\circ$ (d). Fall velocity values are made non-dimensional by dividing them by the terminal velocity of drops of the same size. The red line indicates the median values, limits of the box represent the 25th and 75th percentiles, while whiskers indicate the 10th and 90th percentile.

The variability of the fall velocity of drops of the same size is in general limited – except for the smallest diameter hydrometeors – and quickly reduces to negligible values for larger hydrometeor sizes. It is also worth noting that a significant amount of bias in the hydrometeor fall velocity is nevertheless present for the configuration that produces the least amount of flow disturbance near the instrument sensing area ($\alpha = 90^\circ$).

9.1.1.2 Fall velocity bias for the OTT Parsivel²

Changes in the hydrometeor fall velocity for the OTT Parsivel² are presented in Figure 9.2 for low wind speed (2.5 m s^{-1}) and varying wind directions. The configuration at $\alpha = 0^\circ$ shows a quite different behaviour

with respect to other wind directions. In Figure 9.2a ($\alpha = 0^\circ$), indeed, the fall velocity is unaffected except for the smallest diameter hydrometeors, which show some overestimation. This can be easily explained by the small downdraft observed in these conditions, that is also responsible for the higher catch ratio reported in chapter 8.3.2. In Figure 9.2b ($\alpha = 22.5^\circ$), instead, the fall velocity of smaller hydrometeors is considerably underestimated for diameters up to 1 mm. The larger hydrometeors are nearly unaffected, like in the case of the Thies LPM. Likewise, the wind-induced bias on the fall velocity increases with increasing wind speed, up to a point when smaller diameter hydrometeors tend to stop reaching the instrument sensing area altogether.

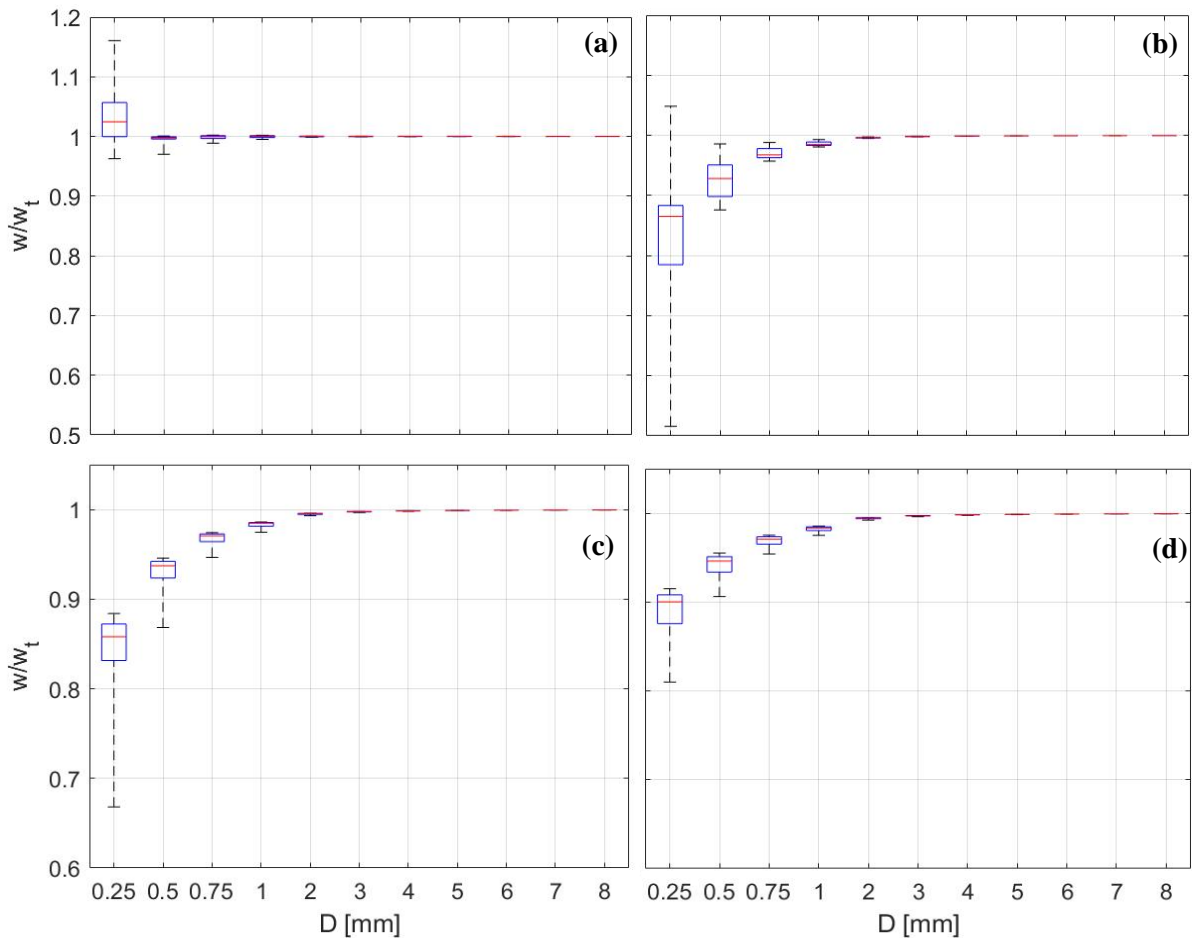


Figure 9.2: Non-parametric (box plot) representation of the non-dimensional fall velocity of hydrometeors when crossing the sensing area of the OTT Parsivel² at $U_{ref} = 2.5 \text{ m s}^{-1}$ and $\alpha = 0^\circ$ (a), $\alpha = 22.5^\circ$ (b), $\alpha = 45^\circ$ (c) and $\alpha = 90^\circ$ (d). Fall velocity values are made non-dimensional by dividing them by the terminal velocity of drops of the same size. The red line indicates the median values, limits of the box represent the 25th and 75th percentiles while whiskers indicate the 10th and 90th percentile.

Figures 9.2c and 9.2d show the cases at $\alpha = 45^\circ$ and $\alpha = 90^\circ$ respectively. They show quite a similar behaviour, however the first case presents a higher fall velocity underestimation and increased variability for drops of the same size. Overall, small size hydrometeors present underestimation up to about 15% on average.

A significant amount of bias in the measurement of the hydrometeors fall velocity is observed even for the configuration that produces the least amount of flow disturbance near its sensing area ($\alpha = 90^\circ$). The variability of the fall velocity of drops of the same size is in general lower than in the case of the Thies LPM.

9.1.1.3 Fall velocity bias for the Vaisala WXT-520

The reduction of the fall velocity induced by wind shows a very limited dependency on the wind direction. In Figure 9.3, results are presented for the three wind directions simulated and a low wind speed (2.5 m s^{-1}). Figures 9.3a ($\alpha = 0^\circ$), 9.3b ($\alpha = 30^\circ$) and 9.3c ($\alpha = 60^\circ$) show a significant reduction of the fall velocity of small size hydrometeors. This is due to the non negligible updraft observed close to the instrument sensing plate that was shown in chapter 7.4.4. Reduction in the hydrometeors fall velocity of about 40% are obtained for the smallest diameters considered. Larger hydrometeors are instead unaffected, like in the previous investigated instruments. Likewise, the wind-induced bias on fall velocity increases with increasing the wind speed.

It is worth noting that, even if the reduction in fall velocity produced by the updraft near the instrument sensing area is significant for small size drops, the reduction in their total kinetic energy is still negligible for all except the lowest wind speeds.

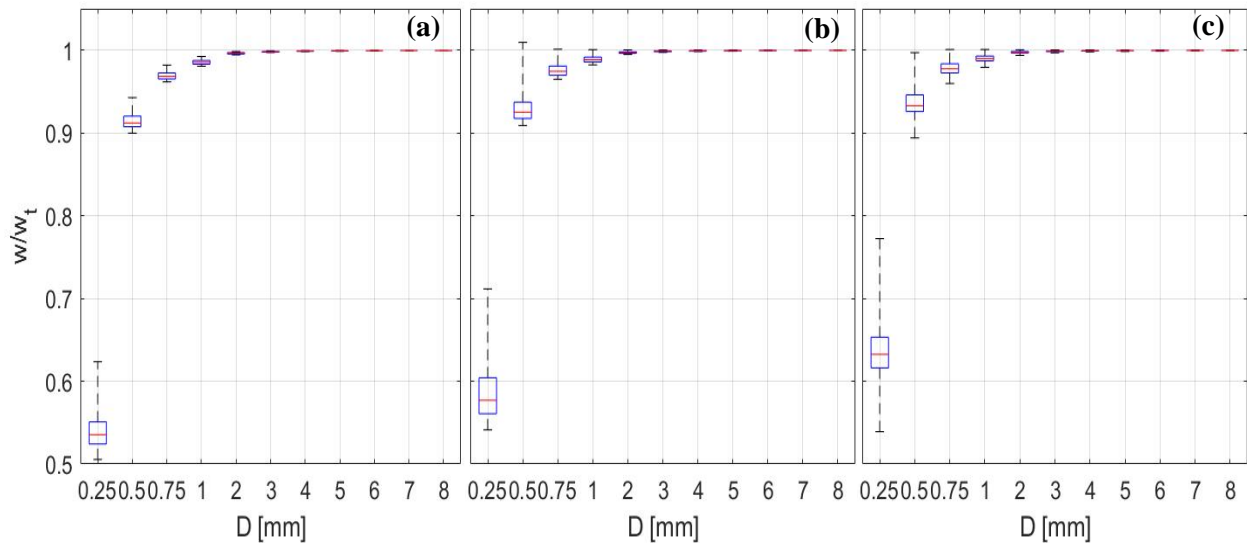


Figure 9.3: Non-parametric (box plot) representation of the non-dimensional fall velocity of hydrometeors when impacting on the sensing area of the Vaisala WXT-520 at $U_{ref} = 2.5 \text{ m s}^{-1}$ and $\alpha = 0^\circ$ (a), $\alpha = 30^\circ$ (b) and $\alpha = 60^\circ$ (c). Fall velocity values are made non-dimensional by dividing them by the terminal velocity of drops of the same size. The red line indicates the median values, limits of the box represent the 25th and 75th percentiles while whiskers indicate the 10th and 90th percentile.

9.1.2 Drop size distribution

The DSD is most often the primary metrics that is sought from NCG measurements. It is necessary for evaluating, for example, visibility or radar reflectivity and in general for computing the integral characteristics of precipitation. Local climatology is the primary factor influencing the DSD and several

formulations exist (see chapter 2.1), mostly obtained from in-situ measurements from NCGs, being themselves affected by wind induced biases.

Chapter 8.3 showed that the exposure effect varies considerably depending on the hydrometeor size, wind speed and direction. It was shown that a significant number of small size hydrometeors fail to reach the instrument sensing area altogether, while the number of larger ones may decrease with increasing the wind speed. This reduced counting of hydrometeors introduces a bias in the reported DSD.

Changes in the reported DSD under windy conditions are evaluated by multiplying the undisturbed DSD by the previously computed CRs. In this chapter, as an example, CRs are applied to the Marshall Palmer formulation of the DSD, already reported in Equation 4.1, that, due to its simplicity, better highlights the wind induced bias. Since the CRs are site-independent the procedure can be easily applied to any measured or site-specific DSD.

9.1.3.1 DSD bias for the Thies LPM

Chapter 8.3.1.1 reported a strong dependency of the CRs measured by the Thies LPM on the wind direction. The same dependency propagates to the wind-induced bias on the reported DSD. Figure 9.4 shows examples of the wind-induced changes of the DSD for two sample wind directions.

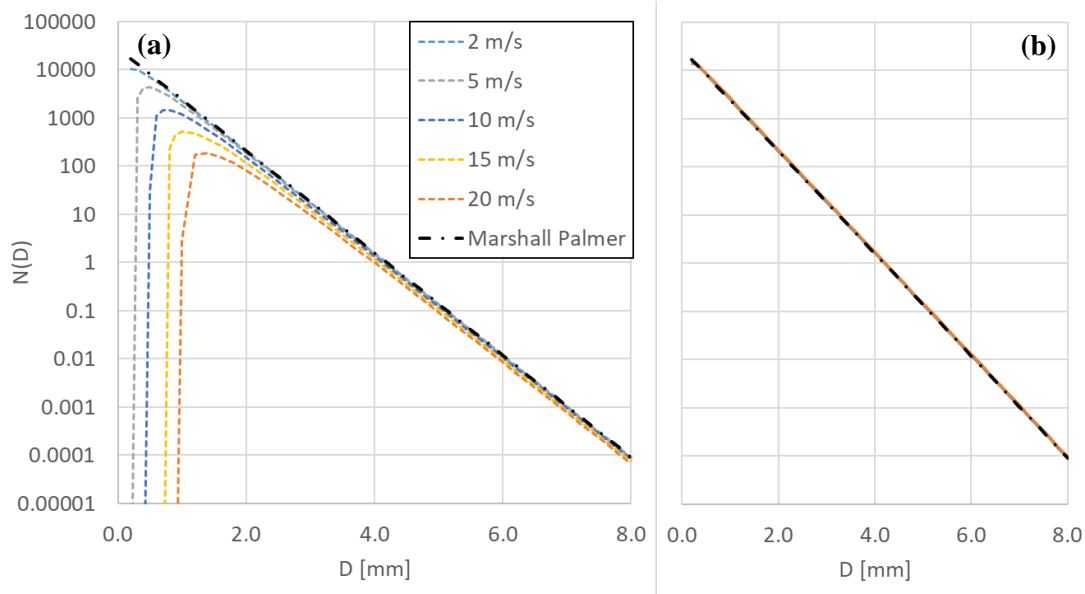


Figure 9.4: Example of wind-induced bias on the measured DSD for the Thies LPM, assuming a reference Marshall-Palmer distribution, as a function of the wind speed and at $\alpha = 0^\circ$ (a) and $\alpha = 90^\circ$ (b). Parameters of the reference distribution are computed for $RI = 10 \text{ mm h}^{-1}$.

For $\alpha = 0^\circ$ (Figure 9.4a), wind has a clear effect on the reported DSD, with a significant underestimation of the number of small size hydrometeors. This bias is already present at low wind speed and significantly increases with increasing the wind speed. Underestimation is also observed for hydrometeors of a larger diameter, even if reduced in magnitude. This would explain, at least in some cases, the fact that disdrometers in the field generally report a very low number of small hydrometeors if compared against the Marshall-

Palmer distribution, leading to the necessity to introduce a formulation based on the gamma function, although less theoretically grounded.

In the case of $\alpha = 90^\circ$ (Figure 9.4b), the wind direction is that of minimum blockage, with CRs values close to unity. The instrument therefore manages to detect the correct number of hydrometeors of various sizes, even at a high wind speed, without any significant change in the reported DSD.

9.1.3.2 DSD bias for the OTT Parsivel²

Results for the OTT Parsivel² show a similar dependency on the wind direction as for the Thies LPM. Figure 9.5 shows examples for two sample wind directions.

In the case of $\alpha = 0^\circ$ (Figure 9.5a), a clear effect on the reported DSD is evident. As in the case of the Thies LPM, the number of small size hydrometeors is severely underestimated, introducing an error that increases with increasing the wind speed. The underestimation is slightly higher than in the previous case and corroborates the hypothesis that the lower number of small hydrometeors reported by in-field measurements may be due to wind induced biases.

Likewise, for $\alpha = 90^\circ$ (Figure 9.5b), due to the minimal flow obstruction offered, no significant loss of hydrometeors is visible, even at high wind speed, and small changes occur in the reported DSD.

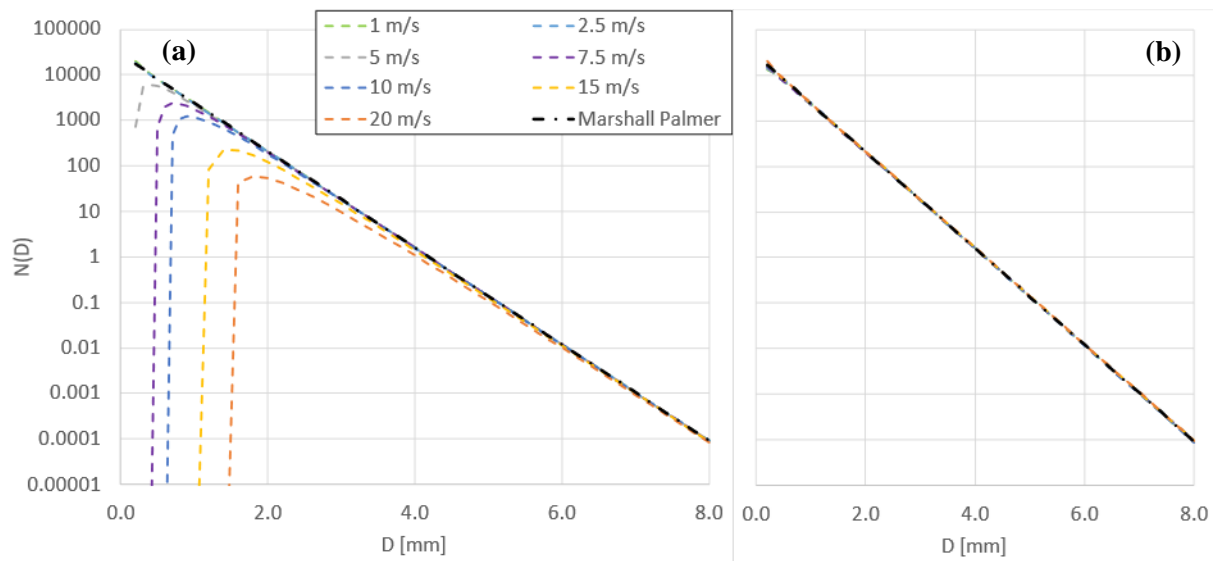


Figure 9.5: Example of the wind-induced bias on the measured DSD for the OTT Parsivel² assuming a reference Marshall-Palmer distribution, as a function of the wind speed and at $\alpha = 0^\circ$ (a) and $\alpha = 90^\circ$ (b). Parameters of the reference distribution are computed for $RI = 10 \text{ mm h}^{-1}$.

9.1.3.3 DSD bias for the Vaisala WXT-520

Since the Vaisala WXT-520 is an impact disdrometer, changes in the reported DSD cannot be obtained by simply multiplying a reference DSD for the computed KCR values. Instead, the kinetic energy associated with each drop diameter from the chosen DSD is computed, then KCRs are applied to it. From the corrected kinetic energy values, the diameter of the equivalent drop possessing such kinetic energy when falling vertically at terminal velocity is obtained after inverting the drop size-terminal velocity relationship.

Figure 9.6 shows an almost identical behaviour between the configurations at $\alpha = 0^\circ$ (a) and $\alpha = 60^\circ$ (b). This is expected since low dependence on the wind direction was already shown for KCRs in chapter 8.3.3. Results show that, with increasing the wind speed, the DSD shifts towards the larger sizes, since the increase in the drop kinetic energy means that the instrument tends to associate their impact to drops having a larger diameter. This has a clear effect on the reported DSD and can produce overestimation for all drop diameters and a lack of the smallest drops (that are instead sensed as larger ones) in the reported DSD. Contrary to the optical disdrometers (Thies LPM and OTT Parsivel²), in the case of the Vaisala WXT-520 at no wind direction a bias-free detection of the DSD is observed.

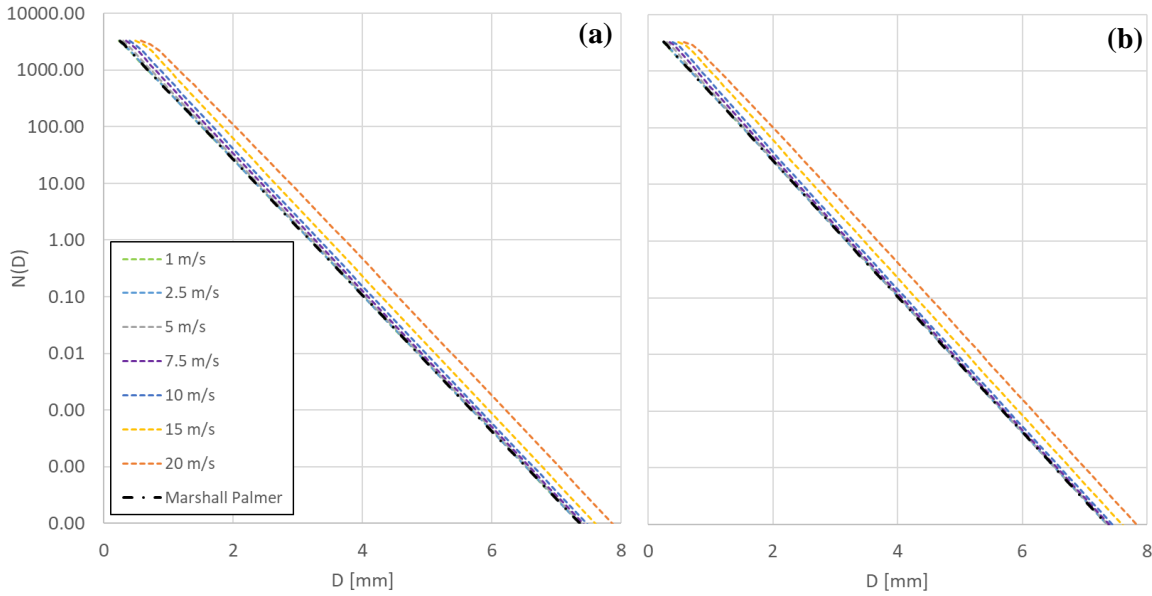


Figure 9.6: Example of the wind-induced bias on the measured DSD for the Vaisala WXT-520, assuming a reference Marshall-Palmer distribution, as a function of the wind speed and at $\alpha = 0^\circ$ (a) and $\alpha = 60^\circ$ (b). Parameters of the reference distribution are computed for $RI = 10 \text{ mm h}^{-1}$.

9.2 THE COLLECTION EFFICIENCY

The Collection Efficiency (CE) is defined as the ratio between the total amount of precipitation that effectively cross the sensing area of the instrument and the ideal amount that would have crossed it if no wind-induced disturbance was present (as defined in Equation 5.1). It can also be numerically computed from the CRs, once a precipitation climatology, and therefore the DSD as a function of precipitation intensity, is assumed. For liquid precipitation, the DSD proposed by Cauteruccio et al. (2020) based on disdrometer data measured by Caracciolo et al. (2008) is used here as an example. It is computed using Equation 2.2 where values of N_0 and Λ are presented in Tables 9.1 and 9.2, respectively.

Table 9.1: Values of the DSD coefficient N_0 for different ranges of RI , used in equation 2.4, following the parametrization proposed by Cauteruccio et al. (2020) based on disdrometer data measured by Caracciolo et al. (2008).

	$RI \leq 1$ [mm h ⁻¹]	$1 < RI \leq 2$ [mm h ⁻¹]	$2 < RI \leq 5$ [mm h ⁻¹]	$5 < RI \leq 10$ [mm h ⁻¹]	$10 < RI \leq 20$ [mm h ⁻¹]	$RI > 20$ [mm h ⁻¹]
N_0	365.1	1692.8	2775.0	4459.0	6989.4	18370.0

Table 9.2: Values of the exponent Λ for different ranges of RI , used in equation 2.4, following the parametrization proposed by Cauteruccio et al. (2020) based on disdrometer data measured by Caracciolo et al. (2008).

	$RI \leq 1$ [mm h ⁻¹]	$1 < RI \leq 2$ [mm h ⁻¹]	$2 < RI \leq 5$ [mm h ⁻¹]	$5 < RI \leq 10$ [mm h ⁻¹]	$10 < RI \leq 20$ [mm h ⁻¹]	$RI > 20$ [mm h ⁻¹]
Λ	3.561	3.134	2.914	2.771	2.723	2.609

Once $N(D, RI)$ is known, the numerical collection efficiency is obtained from Equation 9.1 as:

$$CE(U, \alpha, RI) = \frac{\int_0^{d_{max}} V(D) \cdot n_{sens}(D, U, \alpha) \cdot N(D, RI) \cdot dD}{\int_0^{d_{max}} V(D) \cdot n_{ind}(D, U, \alpha) \cdot N(D, RI) \cdot dD}$$

9.1

where $V(D)$ is the volume of the generic drop of diameter D , while $n_{sens}(D, U, \alpha)$ is the number of hydrometeors that cross the instrument sensing area and $n_{ind}(D, U, \alpha)$ is the number of hydrometeors that would have crossed the sensing area if no disturbance was present. The CE, here obtained using Equation 9.1, is therefore a function of the wind velocity (U), wind direction (α) and rainfall intensity (RI).

9.2.1 The collection efficiency of the Thies LPM

The CE surface as a function of the wind speed and direction is reported in Figure 9.7 for a sample rainfall intensity of 10 mm h⁻¹. Wind direction is shown to be the primary factor influencing the instrument performance, while wind speed has a less relevant role. For wind directions equal to 0° or close to 180° the collection efficiency drops considerably, even at moderate and low wind speed. Meanwhile, for wind directions near 90° the instrument performance is very close to the ideal one, showing only a slight overcatch at higher wind speeds.

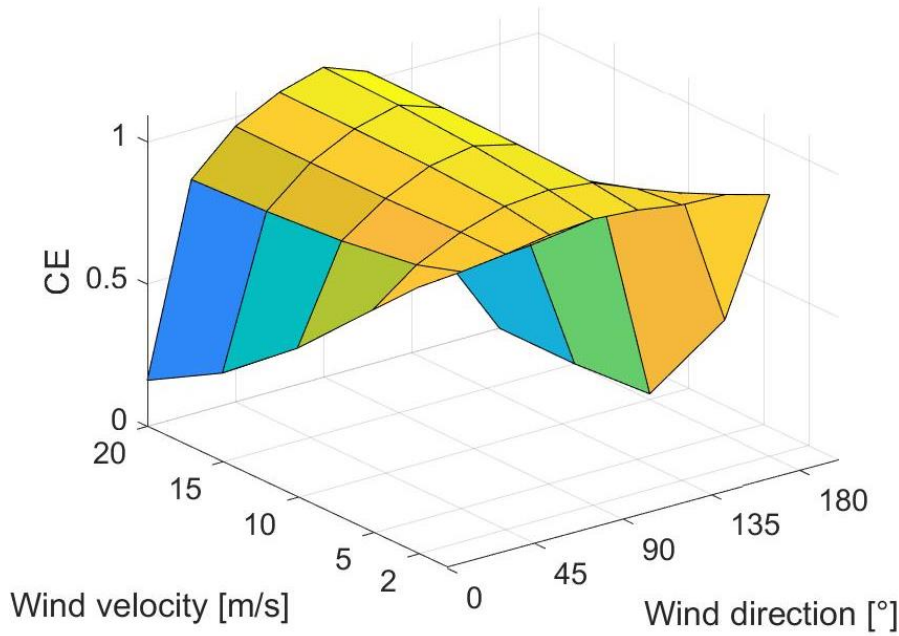


Figure 9.7: Collection efficiency surface for the Thies LPM as a function of wind speed and direction. Values are computed using Equation 9.1 considering the DSD proposed by Cauteruccio et al. (2020) based on disdrometer data measured by Caracciolo et al. (2008) for $RI = 10 \text{ mm h}^{-1}$.

By varying the RI, different CE surfaces, like the one shown in Figure 9.7, are obtained. To evaluate correction curves for the wind-induced bias over a wide RI range, best-fit functions of the CE as a function of RI are obtained, as shown in Figure 9.8, for fixed wind directions (shown in different panels) and wind speed (colour coded)

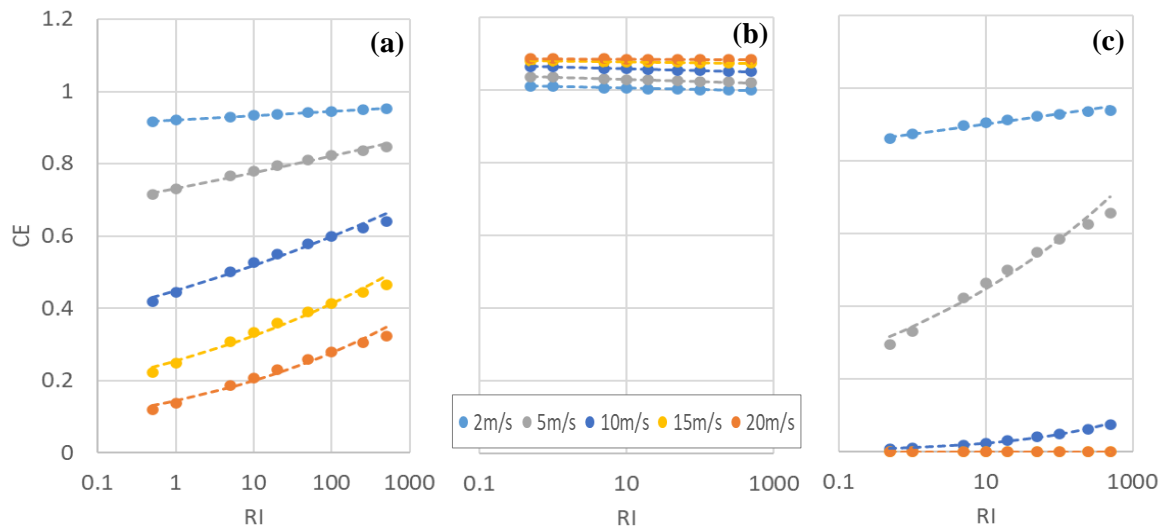


Figure 9.8: Collection efficiency for the Thies LPM as a function of wind speed (colour coded) and rainfall intensity at $\alpha = 0^\circ$ (a), $\alpha = 90^\circ$ (b) and $\alpha = 180^\circ$ (c). Values are computed using Equation 9.1 considering the DSD proposed by Cauteruccio et al. (2020) based on disdrometer data measured by Caracciolo et al. (2008) for RI between 0.5 mm h^{-1} and 500 mm h^{-1} .

Considering the rainfall intensity range between 0.5 mm h⁻¹ and 500 mm h⁻¹, all combinations of wind speed and direction are well fitted by a power law, shown in Equation 9.2:

$$CE = a \cdot RI^b$$

9.2

where a and b are the two best-fit parameters, whose values are reported in tables 9.3 and 9.4 for all wind directions and wind speeds considered.

Table 9.3: Numerical values of the best-fit parameter a of Equation 9.2 for the Thies LPM as a function of wind speed and direction.

a	$\alpha=0^\circ$	$\alpha=22.5^\circ$	$\alpha=45^\circ$	$\alpha=67.5^\circ$	$\alpha=90^\circ$	$\alpha=112.5^\circ$	$\alpha=135^\circ$	$\alpha=157.5^\circ$	$\alpha=180^\circ$
U=2 m s ⁻¹	0.9208	0.9408	0.9666	0.9938	1.0097	0.9935	0.9655	0.9583	0.8754
U=5 m s ⁻¹	0.7326	0.8879	0.9655	1.0159	1.0353	1.0075	0.9268	0.8742	0.3443
U=10 m s ⁻¹	0.4482	0.8479	0.9602	1.0303	1.0631	1.0155	0.8362	0.6006	0.0121
U=15 m s ⁻¹	0.2539	0.8301	0.9622	1.0357	1.0794	1.0184	0.8043	0.3736	0.0000
U=20 m s ⁻¹	0.1447	0.8191	0.9648	1.0388	1.0866	1.0196	0.7680	0.2173	0.0000

Table 9.4: Numerical values of the best-fit parameter b of Equation 9.2 for the Thies LPM as a function of wind speed and direction.

b	$\alpha=0^\circ$	$\alpha=22.5^\circ$	$\alpha=45^\circ$	$\alpha=67.5^\circ$	$\alpha=90^\circ$	$\alpha=112.5^\circ$	$\alpha=135^\circ$	$\alpha=157.5^\circ$	$\alpha=180^\circ$
U=2 m s ⁻¹	0.0059	0.0037	0.0021	-0.0002	-0.0018	0.0000	0.0023	0.0019	0.0131
U=5 m s ⁻¹	0.0252	0.0061	0.0033	-0.0004	-0.0023	0.0010	0.0092	0.0088	0.1148
U=10 m s ⁻¹	0.0628	0.0059	0.0032	0.0012	-0.0019	0.0030	0.0188	0.0488	0.3032
U=15 m s ⁻¹	0.1060	0.0055	0.0029	0.0013	-0.0007	0.0033	0.0187	0.0972	-0.4780
U=20 m s ⁻¹	0.1412	0.0043	0.0025	0.0016	-0.0001	0.0036	0.0134	0.1371	-0.4780

From these results and considering the definition of CE (equation 5.1), the actual rainfall intensity can then be obtained from the rainfall measured by the instrument using Equation 9.3, as:

$$RI_r = \left(\frac{RI_m}{a} \right)^{\frac{1}{b+1}}$$

9.3

where RI_r is the actual rainfall intensity that reaches the instrument in the field and RI_m is the measured rainfall intensity. This simple approach, however, cannot be used for high wind speed and $\alpha = 180^\circ$ since the instrument may fail to report precipitation altogether. This condition should be therefore avoided in field measurements.

9.2.2 The collection efficiency of the OTT Parsivel²

The resulting CE surface for the OTT Parsivel² is illustrated in Figure 9.9 and shows that, like in the previous case, wind direction is the primary factor controlling the instrument performance. Note that only the range 0-90° is illustrated in the picture, since the instrument geometry is here also symmetrical with respect to the Y direction, and a specular behaviour is expected in the range 90-180°. For the configuration at $\alpha = 0^\circ$, the CE drops considerably with increasing the wind speed although, even at the highest wind speed, some precipitation is still sensed by the instrument. The trend is reversed for the configuration at $\alpha = 45^\circ$, where the CE increases with increasing the wind speed. This was already noted in the CRs and is due to the specific shape of the instrument heads, that allow some hydrometeors approaching with a shallow trajectory to cross the laser beam in positions that would be normally unreachable for vertically falling drops. Finally for the configuration at $\alpha = 90^\circ$, the CE is almost constant, and only slightly depends on the wind speed. This is the best performing configuration and, as already noted before, can provide almost unbiased measurements.

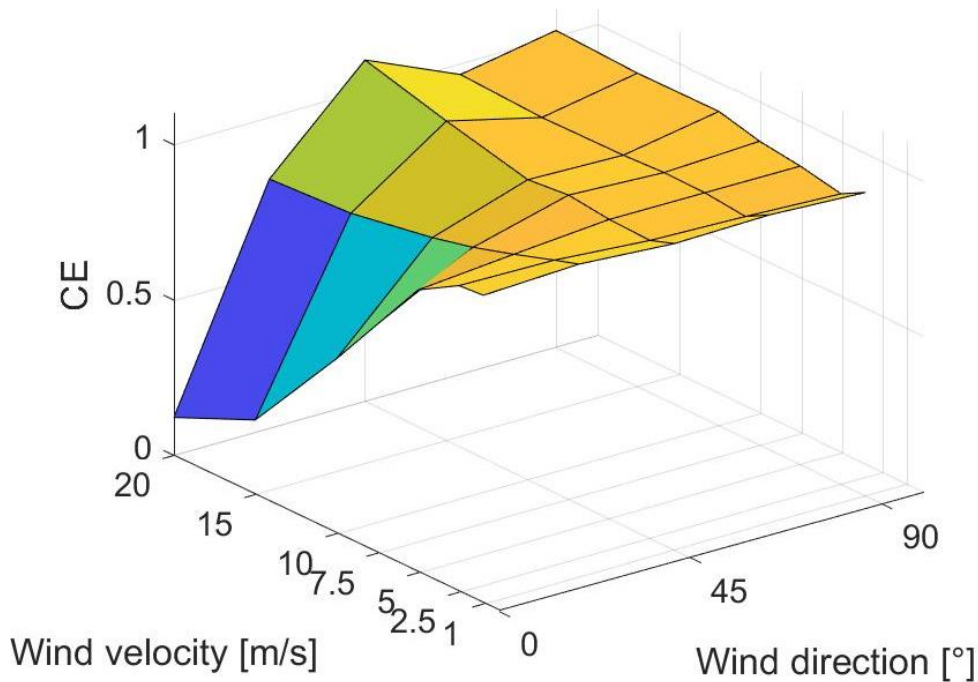


Figure 9.9: Collection efficiency surface for the OTT Parsivel² as a function of wind speed and direction. Values are computed using Equation 9.1 considering the DSD proposed by Cauteruccio et al. (2020) based on disdrometer data measured by Caracciolo et al. (2008) for $RI = 10 \text{ mm h}^{-1}$.

After computing the CE for different RI values, the best-fit functions of the CE variation with the wind direction (different panels) and the wind speed (colour coded) are obtained as shown in Figure 9.10.

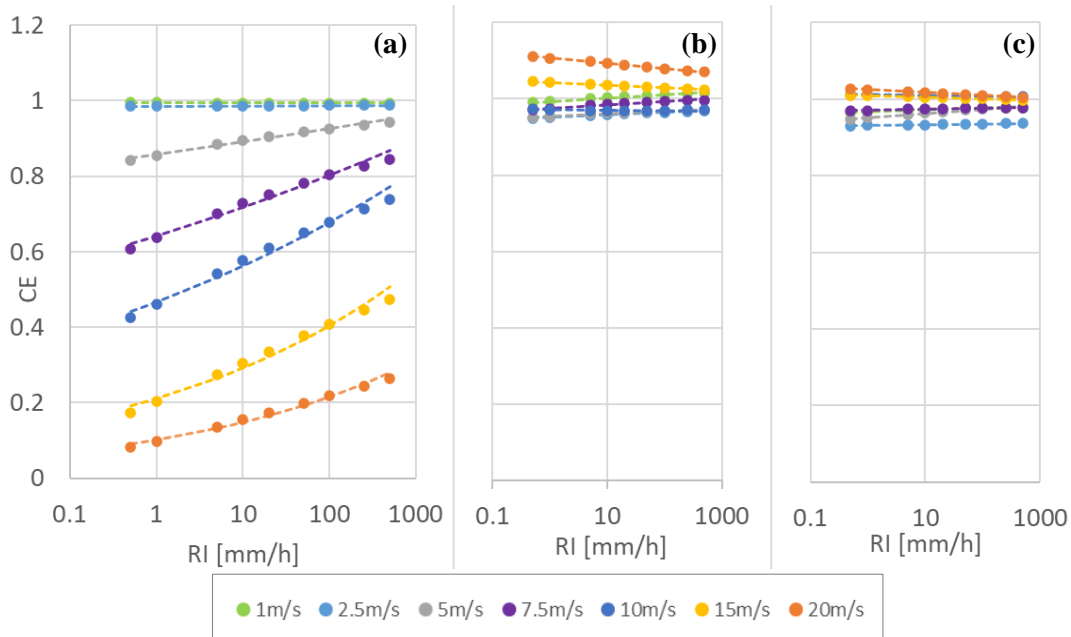


Figure 9.10: Collection efficiency for the OTT Parsivel² as a function of wind speed (colour coded) and rainfall intensity at $\alpha = 0^\circ$ (a), $\alpha = 45^\circ$ (b) and $\alpha = 90^\circ$ (c). Values are computed using Equation 9.1 considering the DSD proposed by Cauteruccio et al. (2020) based on disdrometer data measured by Caracciolo et al. (2008) for RI between 0.5 mm h^{-1} and 500 mm h^{-1} .

Considering the rainfall intensity range $0.5 - 500 \text{ mm h}^{-1}$, as in the previous case, all combinations of wind speeds and directions are well fitted by the same functional form (power law) that is shown in Equation 9.2. The values of the two fitting parameters a and b are reported in tables 9.5 and 9.6 for all wind directions and wind speeds considered.

Table 9.5: Numerical values of the best-fit parameter a of Equation 9.2 for the OTT Parsivel² as a function of wind speed and direction.

a	$\alpha=0^\circ$	$\alpha=22.5^\circ$	$\alpha=45^\circ$	$\alpha=67.5^\circ$	$\alpha=90^\circ$
$U=1 \text{ m s}^{-1}$	0.9942	1.0029	0.9938	0.9816	0.9680
$U=2.5 \text{ m s}^{-1}$	0.9861	0.9723	0.9514	0.9409	0.9317
$U=5 \text{ m s}^{-1}$	0.8572	0.9113	0.9552	0.9525	0.9524
$U=7.5 \text{ m s}^{-1}$	0.6420	0.8638	0.9749	0.9562	0.9709
$U=10 \text{ m s}^{-1}$	0.4682	0.8393	0.9710	0.9491	1.0122
$U=15 \text{ m s}^{-1}$	0.2123	0.8062	1.0431	0.9487	1.0094
$U=20 \text{ m s}^{-1}$	0.1035	0.8040	1.1072	0.9620	1.0256

Table 9.6: Numerical values of the best-fit parameter b of Equation 9.2 for the OTT Parsivel² as a function of wind speed and direction.

b	$\alpha=0^\circ$	$\alpha=22.5^\circ$	$\alpha=45^\circ$	$\alpha=67.5^\circ$	$\alpha=90^\circ$
$U=1 \text{ m s}^{-1}$	0.0000	0.0022	0.0038	0.0031	0.0020
$U=2 \text{ m s}^{-1}$	0.0002	0.0060	0.0031	0.0028	0.0010
$U=5 \text{ m s}^{-1}$	0.0169	0.0069	0.0031	0.0058	0.0049
$U=7.5 \text{ m s}^{-1}$	0.0488	0.0119	0.0043	0.0052	0.0014
$U=10 \text{ m s}^{-1}$	0.0808	0.0159	-0.0005	0.0018	-0.0008
$U=15 \text{ m s}^{-1}$	0.1406	0.0114	-0.0030	0.0020	-0.0018
$U=20 \text{ m s}^{-1}$	0.1605	0.0041	-0.0054	0.0021	-0.0033

The actual rainfall intensity that reaches the instrument in the field, RI_r , can be computed from the measured rainfall intensity, RI_m , by using Equation 9.3, already formulated for the Thies LPM. Furthermore, in the case of the OTT Parsivel², this simple approach, is viable even for high wind speed and $\alpha = 0^\circ$ since the instrument is still able to report some amount of precipitation in those cases. However, this condition is still not ideal and should be therefore avoided in field measurements.

9.2.3 The kinetic collection efficiency of the Vaisala WXT-520

Since the Vaisala WXT-520 is an impact disdrometer, it is useful to define for this instrument, in perfect analogy with the CE, the Kinetic Collection Efficiency (KCE). The KCE is still defined as the ratio between the total volume of hydrometeors that are effectively sensed by the instrument and the ideal volume that would have been sensed if no wind-induced disturbance was present. However, since an impact disdrometer measures the kinetic energy of drops, the volume of hydrometeors effectively sensed by the instrument is a derived measurement.

Calculation of the volume sensed by the gauge is not straightforward in this case and is performed as follows. First, the kinetic energy flux of the monodisperse reference precipitation is multiplied by the corresponding KCR value. From the kinetic energy flux, by inverting the diameter-terminal velocity relationship, the diameter of the equivalent monodisperse precipitation, that would provide the same kinetic energy flux when falling vertical at its terminal velocity, is computed. Finally, the volume effectively sensed by the instrument is obtained by integrating the volume of the corrected monodisperse precipitation over the drop size, similarly to the classic CE computation.

This process was repeated for each combination of wind speed and direction, by considering a target range of the precipitation intensity between 0.5 - 500 mm h⁻¹. The obtained KCE is, like the CE, a function of wind speed (U), wind direction (α) and rainfall intensity (RI). Results can be visualized in a two-dimensional plot once a rainfall intensity reference value is chosen.

Figure 9.11 shows that, contrary to the previous cases, wind direction is not the primary factor to affect the instrument performance, while wind speed is decisive. KCE values are close to unity in low wind speed

conditions (1 m s^{-1} and 2.5 m s^{-1}), while the instrument quickly starts to overestimate precipitation at higher wind speeds. The increase in KCE values with increasing the wind speed is almost linear and reaches values that are multiple times the reference kinetic energy.

Figure 9.12 shows that RI also strongly affect the value of the KCE, since most of the overcatch is caused by the small size drops, while larger drops are less affected. At low RI, the ratio between the number of small and large hydrometeors is high, and the wind-induced overcatch is at its maximum. However, at higher RI, the number of large drops significantly increases, therefore reducing the overall overcatch.

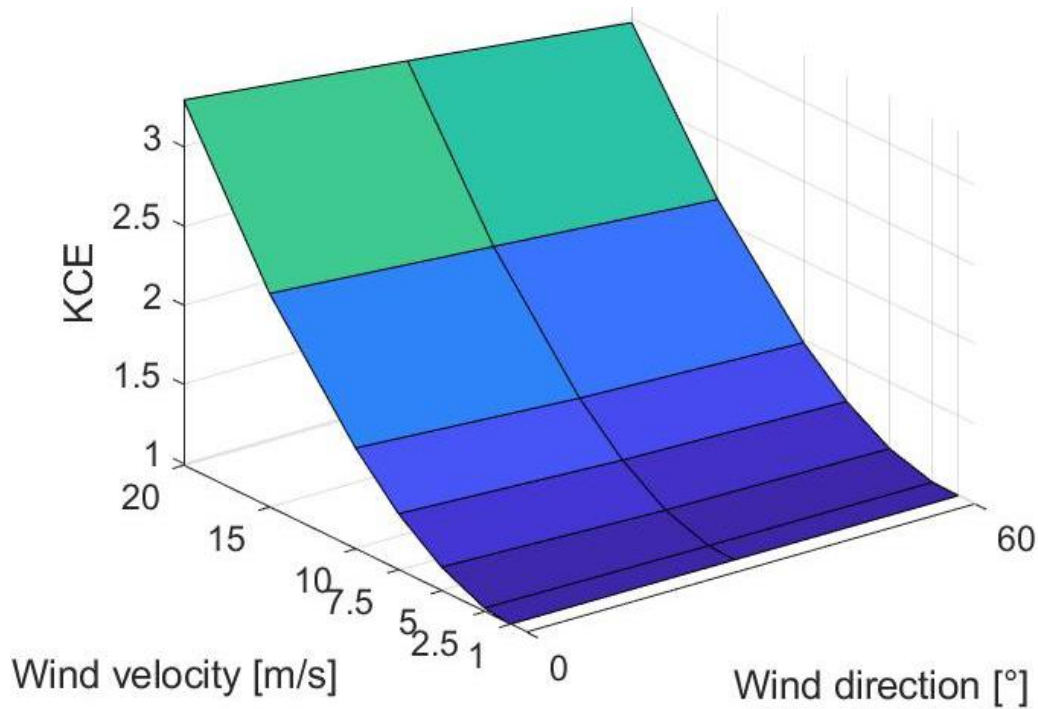


Figure 9.11: Kinetic collection efficiency surface for the Vaisala WXT-520 as a function of wind speed and direction. Values are computed using Equation 9.1 considering the DSD proposed by Cauteruccio et al. (2020) based on disdrometer data measured by Caracciolo et al. (2008) for $RI = 10 \text{ mm h}^{-1}$.

The KCE values for varying RI are fitted as shown in Figure 9.12. Throughout the considered rainfall intensity range, all combinations of wind speed and fall velocity are again well fitted by a power law function, as shown in Equation 9.4.

$$KCE = a \cdot RI^b$$

9.4

where a and b are the two best-fit parameters, that are reported in tables 9.7 and 9.8 for the considered combinations of wind speed and direction.

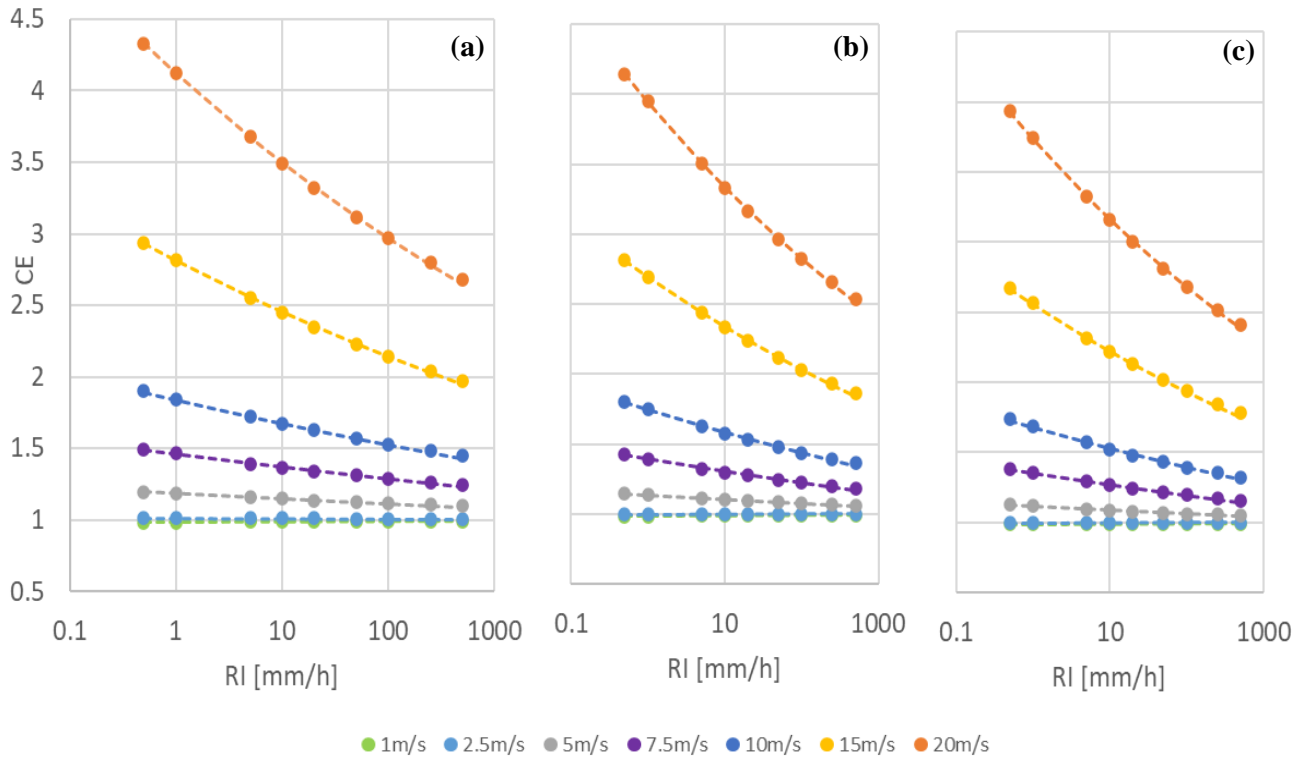


Figure 9.12: Kinetic collection efficiency for the Vaisala WXT-520 as a function of wind speed (colour coded) and rainfall intensity at $\alpha = 0^\circ$ (a), $\alpha = 30^\circ$ (b) and $\alpha = 60^\circ$ (c). Values are computed using Equation 9.1 considering the DSD proposed by Cauteruccio et al. (2020) based on disdrometer data measured by Caracciolo et al. (2008) for RI between 0.5 mm h^{-1} and 500 mm h^{-1} .

Table 9.7: Numerical values of the best-fit parameter a of Equation 9.2 for the Vaisala WXT-520 as a function of wind speed and direction.

a	$\alpha=0^\circ$	$\alpha=30^\circ$	$\alpha=60^\circ$
$U=1 \text{ m s}^{-1}$	0.9840	0.9852	0.9856
$U=2.5 \text{ m s}^{-1}$	1.0123	0.9969	0.9929
$U=5 \text{ m s}^{-1}$	1.1841	1.1357	1.1155
$U=7.5 \text{ m s}^{-1}$	1.4611	1.3923	1.3523
$U=10 \text{ m s}^{-1}$	1.8411	1.7478	1.6809
$U=15 \text{ m s}^{-1}$	2.8111	2.6911	2.5606
$U=20 \text{ m s}^{-1}$	4.1222	3.9410	3.7397

Since the KCE is defined as the ratio between the sensed and reference precipitation volume, analogously to the previous cases, the actual rainfall intensity RI_r is once again obtained from the measured rainfall intensity RI_m using Equation 9.3.

Table 9.8: Numerical values of the best-fit parameter b of Equation 9.2 for the Vaisala WXT-520 as a function of wind speed and direction.

b	$\alpha=0^\circ$	$\alpha=30^\circ$	$\alpha=60^\circ$
$U=1 \text{ m s}^{-1}$	0.0014	0.0012	0.0012
$U=2 \text{ m s}^{-1}$	-0.0008	0.0006	0.0007
$U=5 \text{ m s}^{-1}$	-0.0132	-0.0118	-0.0109
$U=7.5 \text{ m s}^{-1}$	-0.0277	-0.0282	-0.0269
$U=10 \text{ m s}^{-1}$	-0.0406	-0.0422	-0.0410
$U=15 \text{ m s}^{-1}$	-0.0592	-0.0609	-0.0608
$U=20 \text{ m s}^{-1}$	-0.0711	-0.0724	-0.0724

In the case of the Vaisala WXT-520, this simple approach is viable for any wind speed and direction since the instrument would always report a certain amount of precipitation. Special care should however be posed at analysing measurements obtained in high wind speed conditions due to the large bias noted in such cases.

9.3 RADAR REFLECTIVITY FACTOR

The radar reflectivity factor (dBZ) (see chapter 2) is an important parameter that is primarily used for the remote sensing of precipitation. Measurements are obtained from weather radar and/or satellites that employ active microwave sensors, usually with the intent of using such measure to estimate precipitation intensity. Ground-based weather radars are increasingly included into national and international networks to provide spatial measurements of precipitation. However, conversion of radar reflectivity at a certain altitude and distance into an accurate quantitative precipitation estimate is still difficult. Issues include drop size distribution evaluation, melting precipitation, low-level precipitation, attenuation, surface effects, beam blockage, or beam-filling problems (Raubert & Nesbitt, 2018), etc.

For this reason, ground based, in-situ measurement of precipitation microphysical characteristics is a necessity for calibrating and improving retrieval algorithms. As shown in chapter 2, radar reflectivity factor (dBZ) is directly derived from the PSD, that was shown to be affected by wind in chapter (9.1). For this reason, it is of interest to determine how retrieval of dBZ from in-situ measurements of NCGs is affected by wind. For each gauge investigated, the bias in the dBZ, called Radar Retrieval Efficiency (RRE), is obtained as the ratio between the radar reflectivity factor obtained using the corrected DSD presented in chapter 9.1.3 and the same values computed using a synthetic DSD (Marshall-Palmer). This procedure is DSD dependent; however, it can be easily adapted to any specific climatology by simply including any site-specific DSD.

9.3.1 Radar retrieval efficiency for the Thies LPM

Chapter 9.1.2.1 showed that, depending on the wind speed and direction, the DSD reported by the Thies LPM reports a significant bias. This is therefore also evident in the obtained RRE values, that are shown in Figure 9.13.

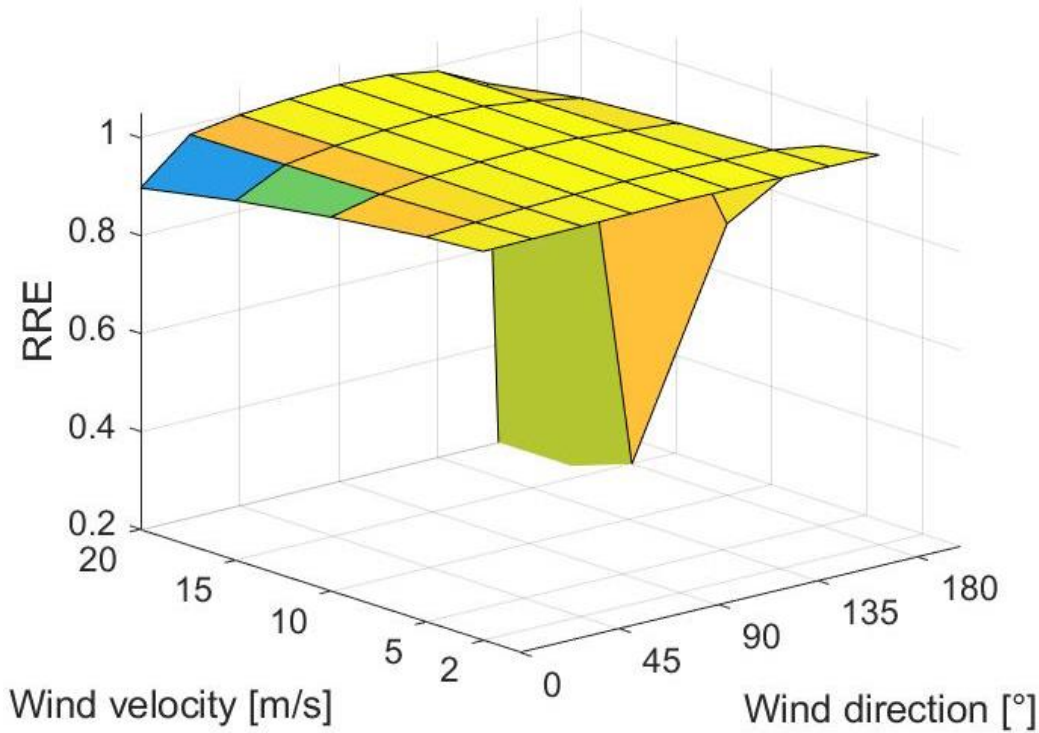


Figure 9.13: RRE values, as a function of the wind speed and direction, for the Thies LPM, computed as the ratio between the radar reflectivity factor measured by the gauge and the reference one. The reference DSD adopted is the one proposed by Marshall and Palmer (1948), evaluated for a $RI = 10 \text{ mm h}^{-1}$.

Figure 9.13 shows a behaviour that is somewhat similar to the one observed for the CE (see chapter 9.2.1), but with a much flatter RRE. Wind direction is still the primary factor in evaluating the wind induced bias. For an angle $\alpha = 0^\circ$, a limited reduction of the RRE is evident, that increases with increasing the wind speed. Angles between $\alpha = 22.5^\circ$ and $\alpha = 157.5^\circ$ show limited bias and values of the RRE close to unity. Finally, for $\alpha = 180^\circ$, some significant bias is evident for wind speed equal to 15 and 20 m s^{-1} since little to no precipitation is sensed by the gauge in these conditions.

As in the case of the CE, RRE values are a function of the precipitation intensity, as shown, as an example, in figure 9.14 for different wind directions, considering RI values between 0.5 mm h^{-1} and 500 mm h^{-1} .

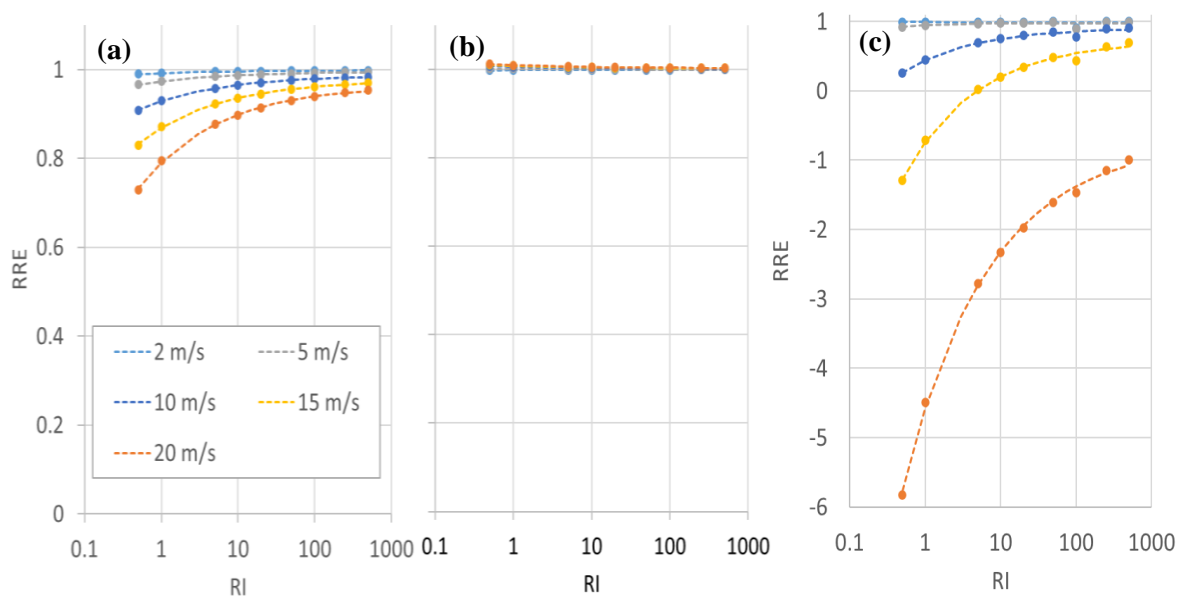


Figure 9.14: RRE for the Thies LPM as a function of the RI, in the range between 0.5 mm h^{-1} and 500 mm h^{-1} for various wind directions at $\alpha = 0^\circ$ (a), $\alpha = 90^\circ$ (b) and $\alpha = 180^\circ$ (c). Different wind speeds are colour coded as shown in the legend. Dashed lines represent the best fit curve, obtained using Equation 9.5.

Figure 9.14 shows that RRE values increases with increasing the precipitation intensity. This is expected since larger diameter hydrometeors contribute most in the dBZ computation. Results are fitted using a three parameters power law, as shown in equation 9.5:

$$RRE = a + b \cdot RI^c$$

9.5

where a , b and c are the three fitting parameters, whose values are reported in Tables 9.9, 9.10 and 9.11 for all wind directions and wind speeds considered.

Table 9.9: Numerical values of the best-fit parameter a of Equation 9.5 for the Thies LPM as a function of wind speed and direction.

a	$\alpha=0^\circ$	$\alpha=22.5^\circ$	$\alpha=45^\circ$	$\alpha=67.5^\circ$	$\alpha=90^\circ$	$\alpha=112.5^\circ$	$\alpha=135^\circ$	$\alpha=157.5^\circ$	$\alpha=180^\circ$
U=2 m s ⁻¹	0.9982	0.9987	0.9990	0.9996	1.0002	0.9996	0.9991	0.9988	0.9706
U=5 m s ⁻¹	0.9953	0.9969	0.9989	0.9999	1.0009	1.0000	0.9990	0.9971	0.9720
U=10 m s ⁻¹	0.9874	0.9944	0.9996	1.0014	1.0025	1.0014	0.9986	0.9942	0.9064
U=15 m s ⁻¹	0.9770	0.9928	0.9994	1.0026	1.0041	1.0026	0.9979	0.9909	0.7350
U=20 m s ⁻¹	0.9645	0.9920	0.9993	1.0029	1.0050	1.0029	0.9964	0.9840	-0.7172

Table 9.10: Numerical values of the best-fit parameter b of Equation 9.5 for the Thies LPM as a function of wind speed and direction.

b	$\alpha=0^\circ$	$\alpha=22.5^\circ$	$\alpha=45^\circ$	$\alpha=67.5^\circ$	$\alpha=90^\circ$	$\alpha=112.5^\circ$	$\alpha=135^\circ$	$\alpha=157.5^\circ$	$\alpha=180^\circ$
$U=2 \text{ m s}^{-1}$	-0.0064	-0.0048	-0.0029	-0.0008	0.0011	-0.0006	-0.0022	-0.0040	0.0216
$U=5 \text{ m s}^{-1}$	-0.0217	-0.0109	-0.0036	0.0015	0.0042	0.0014	-0.0047	-0.0103	-0.0236
$U=10 \text{ m s}^{-1}$	-0.0587	-0.0179	-0.0031	0.0049	0.0084	0.0045	-0.0130	-0.0246	-0.4648
$U=15 \text{ m s}^{-1}$	-0.1087	-0.0215	-0.0032	0.0064	0.0115	0.0058	-0.0157	-0.0516	-1.4779
$U=20 \text{ m s}^{-1}$	-0.1740	-0.0236	-0.0035	0.0071	0.0130	0.0064	-0.0188	-0.1263	-3.8684

Table 9.11: Numerical values of the best-fit parameter c of Equation 9.5 for the Thies LPM as a function of wind speed and direction.

c	$\alpha=0^\circ$	$\alpha=22.5^\circ$	$\alpha=45^\circ$	$\alpha=67.5^\circ$	$\alpha=90^\circ$	$\alpha=112.5^\circ$	$\alpha=135^\circ$	$\alpha=157.5^\circ$	$\alpha=180^\circ$
$U=2 \text{ m s}^{-1}$	-0.4060	-0.4060	-0.3969	-0.3592	-0.4153	-0.3134	-0.3938	-0.4049	-0.1320
$U=5 \text{ m s}^{-1}$	-0.4179	-0.4023	-0.3993	-0.3509	-0.4020	-0.3097	-0.4262	-0.4077	-1.1212
$U=10 \text{ m s}^{-1}$	-0.4167	-0.3939	-0.3719	-0.3494	-0.3897	-0.3222	-0.4211	-0.4410	-0.4755
$U=15 \text{ m s}^{-1}$	-0.4190	-0.3904	-0.3756	-0.3773	-0.3841	-0.3680	-0.4152	-0.4548	-0.4419
$U=20 \text{ m s}^{-1}$	-0.4218	-0.3844	-0.3352	-0.3764	-0.3821	-0.3675	-0.4090	-0.4604	-0.3839

From these results and analogously to chapter 9.2.1, the actual dBZ can be obtained from the dBZ measured by the instrument using Equation 9.6.

$$dBZ_r = \frac{dBZ_m}{a + b \cdot RI^c}$$

9.6

where dBZ_r is the actual radar reflectivity factor in the field and dBZ_m is the radar reflectivity factor measured by the gauge. This approach requires the knowledge of the RI, a parameter that is provided by the gauge alongside dBZ_m . However, since the RI measurement is also affected by wind, a correction should be applied (as shown in chapter 9.2.1) before using it in Equation 9.6. Under high wind speed conditions and for $\alpha = 180^\circ$, it was shown that the instrument may fail to report precipitation altogether. This condition cannot provide reliable measurements even after corrections and should be therefore avoided in the field.

9.3.2 Radar retrieval efficiency for the OTT Parsivel²

For the OTT Parsivel², a similar dependence of the DSD on wind speed and direction was shown in chapter 9.2.2. The derived RRE values for this gauge are shown, similarly to the previous case, in Figure 9.15.

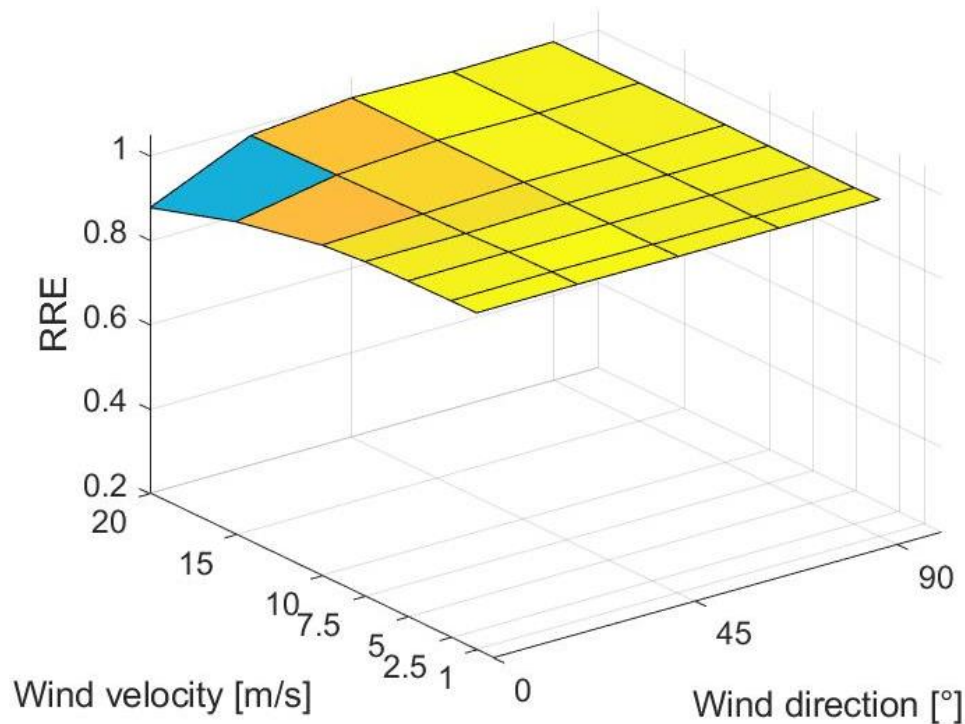


Figure 9.15: RRE values as a function of the wind speed and direction, for the OTT Parsivel², computed as the ratio between the radar reflectivity factor measured by the gauge and the reference one. The adopted reference DSD is the one proposed by Marshall and Palmer (1948), evaluated for a RI of 10 mm h⁻¹.

Figure 9.15 shows that a limited dependency on both wind speed and direction is present. The RRE surface remains quite flat, with values close to unity, only for an angle of $\alpha = 0^\circ$ and a high wind speed a significant reduction of RRE is visible. Contrary to the Thies LPM, in the case of the OTT Parsivel², all combinations of wind speed and direction are able to provide satisfactory measurements of the dBZ, especially at lower wind speeds, where the bias is negligible for all wind directions.

Analogously to the Thies LPM, RRE values as a function of the precipitation intensity are shown in figure 9.16 for different wind directions, considering RI values between 0.5 mm h⁻¹ and 500 mm h⁻¹.

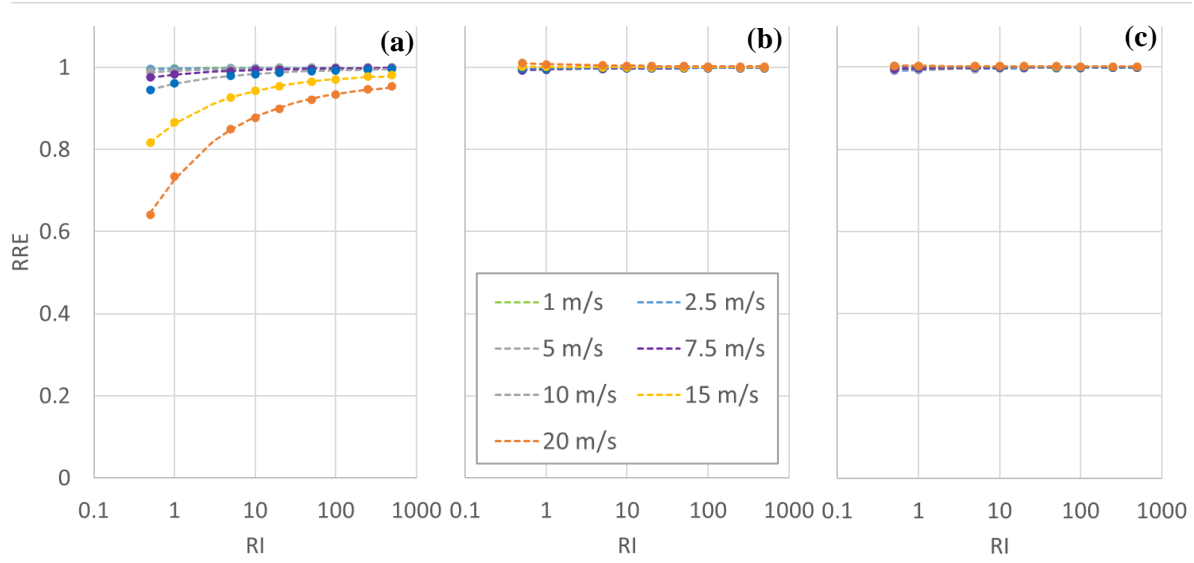


Figure 9.16: RRE for the OTT Parsivel² as a function of the RI, in the range between 0.5 mm h^{-1} and 500 mm h^{-1} for a wind direction at $\alpha = 0^\circ$ (panel a), $\alpha = 45^\circ$ (panel b) and $\alpha = 90^\circ$ (panel c). Different wind speeds are colour coded as shown in the legend. Dashed lines represent the best fit curve, obtained using in Equation 9.5.

Figure 9.16 shows that RRE values increase with increasing the precipitation intensity. This is expected since larger diameter hydrometeors contribute most in the dBZ computation. As previously shown in Figure 9.15, significant changes in the RRE values only occur for an angle $\alpha = 0^\circ$, that provides the maximum flow obstruction. Results are again fitted using a three parameters power law, as shown in equation 9.5. The fitting parameters a , b and c are reported, for the OTT Parsivel², in Tables 9.12, 9.13 and 9.14 for all wind directions and wind speeds considered.

Table 9.12: Numerical values of the bestfit parameter a of Equation 9.5 for the OTT Parsivel² as a function of wind speed and direction.

a	$\alpha=0^\circ$	$\alpha=22.5^\circ$	$\alpha=45^\circ$	$\alpha=67.5^\circ$	$\alpha=90^\circ$
U=1 m s ⁻¹	0.9994	0.9994	0.9986	0.9987	0.9994
U=2.5 m s ⁻¹	0.9992	0.9993	0.9984	0.9981	0.9988
U=5 m s ⁻¹	0.9991	0.9988	0.9992	0.9995	0.9996
U=7.5 m s ⁻¹	0.9987	0.9974	0.9990	0.9990	0.9999
U=10 m s ⁻¹	0.9966	0.9975	0.9997	0.9986	0.9991
U=15 m s ⁻¹	0.9862	0.9955	1.0000	0.9992	1.0012
U=20 m s ⁻¹	0.9666	0.9939	1.0012	0.9994	1.0013

Table 9.13: Numerical values of the best-fit parameter b of Equation 9.5 for the OTT Parsivel² as a function of wind speed and direction.

b	$\alpha=0^\circ$	$\alpha=22.5^\circ$	$\alpha=45^\circ$	$\alpha=67.5^\circ$	$\alpha=90^\circ$
$U=1 \text{ m s}^{-1}$	-0.0021	-0.0011	-0.0022	-0.0025	-0.0026
$U=2.5 \text{ m s}^{-1}$	-0.0031	0.0001	-0.0036	-0.0053	-0.0055
$U=5 \text{ m s}^{-1}$	-0.0080	-0.0038	-0.0040	-0.0041	-0.0045
$U=7.5 \text{ m s}^{-1}$	-0.0166	-0.0121	-0.0047	-0.0039	-0.0029
$U=10 \text{ m s}^{-1}$	-0.0372	-0.0173	-0.0031	-0.0040	0.0022
$U=15 \text{ m s}^{-1}$	-0.1231	-0.0243	0.0011	-0.0038	0.0015
$U=20 \text{ m s}^{-1}$	-0.2380	-0.0286	0.0064	-0.0026	0.0016

Table 9.14: Numerical values of the best-fit parameter c of Equation 9.5 for the OTT Parsivel² as a function of wind speed and direction.

c	$\alpha=0^\circ$	$\alpha=22.5^\circ$	$\alpha=45^\circ$	$\alpha=67.5^\circ$	$\alpha=90^\circ$
$U=1 \text{ m s}^{-1}$	-0.3735	-0.2938	-0.3874	-0.4126	-0.4248
$U=2.5 \text{ m s}^{-1}$	-0.3768	-0.1351	-0.4075	-0.3998	-0.4011
$U=5 \text{ m s}^{-1}$	-0.4489	-0.4665	-0.4032	-0.4150	-0.4028
$U=7.5 \text{ m s}^{-1}$	-0.4951	-0.4090	-0.3857	-0.4135	-0.3991
$U=10 \text{ m s}^{-1}$	-0.4697	-0.3980	-0.3534	-0.4097	-0.3536
$U=15 \text{ m s}^{-1}$	-0.4522	-0.3862	-0.4368	-0.3970	-0.3626
$U=20 \text{ m s}^{-1}$	-0.4347	-0.3784	-0.4168	-0.3942	-0.3691

From these results, the actual dBZ can be obtained from the dBZ measured by the instrument using Equation 9.6. Even under high wind speed conditions, the OTT Parsivel² provides good performances for all wind directions, with measurements that show low bias or can be easily corrected, making it more suitable than the Thies LPM for dBZ retrieval in windy conditions.

9.3.3 Radar retrieval efficiency for the Vaisala WXT-520

The Vaisala WXT-520 showed a limited dependency of the wind-induced bias on the wind direction, presenting instead a strong dependence on wind speed (see chapter 9.2.3). The same behaviour is therefore obtained in the RRE values, as shown in Figure 9.17.

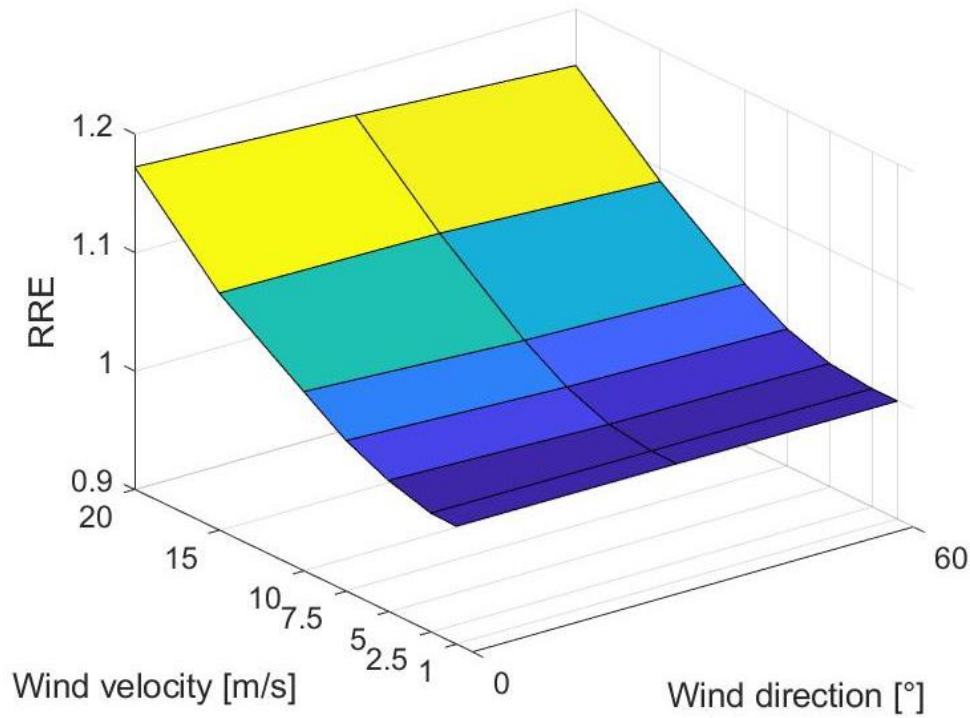


Figure 9.17: RRE values, as a function of the wind speed and direction, for the Vaisala WXT-520, computed as the ratio between the radar reflectivity factor measured by the gauge and the reference one. The adopted reference DSD is the one proposed by Marshall and Palmer (1948), calculated for a $RI = 10 \text{ mm h}^{-1}$.

Figure 9.17 shows that wind speed is the primary factor in evaluating the wind induced bias on the dBZ for the Vaisala WXT-520. Variation of the angle between $\alpha = 0^\circ$ and $\alpha = 60^\circ$ presents only a limited influence on the obtained RRE values, that instead significantly increase with increasing the wind speed. Especially at the higher wind speeds, a significant bias is evident, due to the increase in large size drops being reported in the DSD measured by the gauge.

An example of the trend of RRE values as a function of the RI is shown in figure 9.18 for different wind directions, considering RI values between 0.5 mm h^{-1} and 500 mm h^{-1} . Figure 9.18 shows that the RRE follows an opposite trend with respect to the previous gauges, with values that decrease with increasing the precipitation intensity. This is expected since larger size hydrometeors contribute most in the dBZ computation and present a lower percentual increases in their total kinetic energy due to the wind. Results are fitted using a three parameters power law, as shown in equation 9.5. The best-fit parameters a , b and c for the Vaisala WXT-520 are presented in tables 9.15, 9.16 and 9.17 for all wind speeds and directions considered.

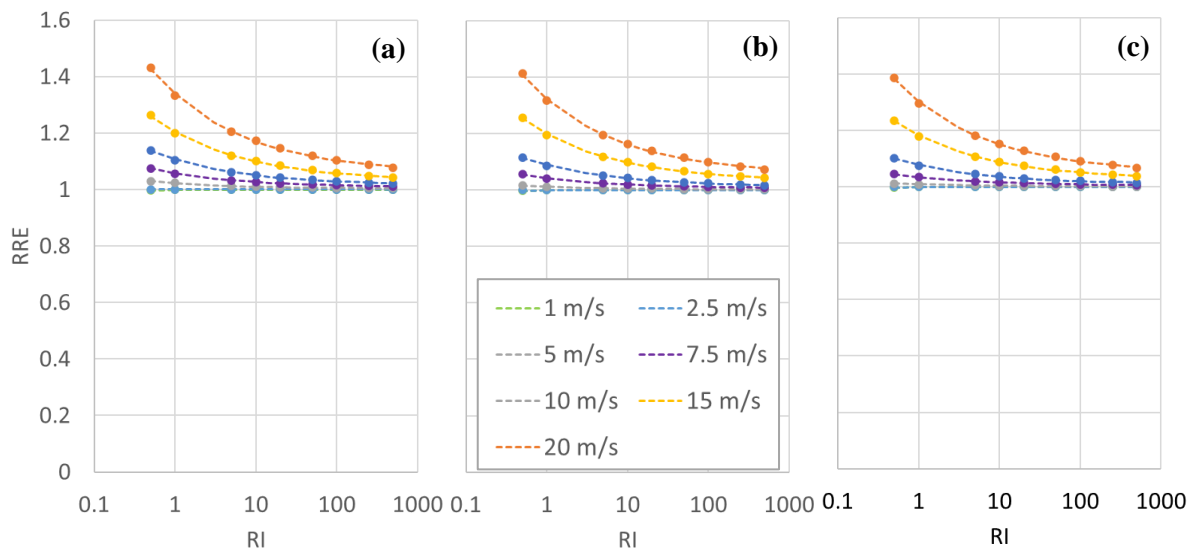


Figure 9.18: RRE for the Vaisala WXT-520 as a function of the RI, in the range between 0.5 mm h^{-1} and 500 mm h^{-1} for wind directions at $\alpha = 0^\circ$ (panel a), $\alpha = 30^\circ$ (panel b) and $\alpha = 60^\circ$ (panel c). Different wind speeds are colour coded as shown in the legend. Dashed lines represent the best fit curve, obtained using Equation 9.5.

Table 9.15: Numerical values of the bestfit parameter a of Equation 9.5 for the Vaisala WXT-520 as a function of wind speed and direction.

a	$\alpha=0^\circ$	$\alpha=22.5^\circ$	$\alpha=45^\circ$
$U=1 \text{ m s}^{-1}$	0.9999	0.9999	0.9999
$U=2.5 \text{ m s}^{-1}$	1.0001	1.0000	1.0000
$U=5 \text{ m s}^{-1}$	1.0030	1.0014	1.0010
$U=7.5 \text{ m s}^{-1}$	1.0079	1.0056	1.0045
$U=10 \text{ m s}^{-1}$	1.0154	1.0123	1.0108
$U=15 \text{ m s}^{-1}$	1.0316	1.0309	1.0279
$U=20 \text{ m s}^{-1}$	1.0582	1.0548	1.0507

The actual dBZ is obtained from the measured dBZ using Equation 9.6. While no combination of wind speed and direction fails to report precipitation, some significant bias is shown at the higher wind speeds. Under these conditions, the gauge may provide less reliable measurements, especially for light rainfall events. Results obtained under these conditions should be therefore treated with care and correction for the wind-induced bias should be applied.

Table 9.16: Numerical values of the bestfit parameter b of Equation 9.5 for the Vaisala WXT-520 as a function of wind speed and direction.

b	$\alpha=0^\circ$	$\alpha=22.5^\circ$	$\alpha=45^\circ$
$U=1 \text{ m s}^{-1}$	-0.0010	-0.0008	-0.0008
$U=2.5 \text{ m s}^{-1}$	0.0006	-0.0001	-0.0004
$U=5 \text{ m s}^{-1}$	0.0201	0.0104	0.0076
$U=7.5 \text{ m s}^{-1}$	0.0500	0.0369	0.0302
$U=10 \text{ m s}^{-1}$	0.0917	0.0760	0.0670
$U=15 \text{ m s}^{-1}$	0.1725	0.1685	0.1543
$U=20 \text{ m s}^{-1}$	0.2808	0.2677	0.2517

Table 9.17: Numerical values of the bestfit parameter c of Equation 9.5 for the Vaisala WXT-520 as a function of wind speed and direction.

c	$\alpha=0^\circ$	$\alpha=22.5^\circ$	$\alpha=45^\circ$
$U=1 \text{ m s}^{-1}$	-0.4378	-0.4423	-0.4419
$U=2.5 \text{ m s}^{-1}$	-0.4356	-0.3258	-0.4514
$U=5 \text{ m s}^{-1}$	-0.4256	-0.4403	-0.4451
$U=7.5 \text{ m s}^{-1}$	-0.4213	-0.4288	-0.4333
$U=10 \text{ m s}^{-1}$	-0.4147	-0.4200	-0.4221
$U=15 \text{ m s}^{-1}$	-0.4083	-0.4080	-0.4100
$U=20 \text{ m s}^{-1}$	-0.3985	-0.3996	-0.4010

9.4 DISCUSSION

Results presented in this chapter show that for both microphysical and integral precipitation characteristics, the impact of wind generally introduces a significant amount of bias.

For all three gauges, the fall velocity of small size hydrometeors tends to decrease with increasing the wind speed. An increase in the fall velocity is also possible for some specific combinations of wind speed and direction. This fact may explain, at least partially, the presence of non-terminal hydrometeors in NCGs measurements, especially since non negligible bias is produced even for the most favourable conditions. However, super terminal hydrometeors were observed in the field (see e.g. Montero et al. 2009, Larsen et al. 2014 and Chatterjee et al. 2022), that are not compatible with the wind-induced bias observed in chapter 9.1.1, since they present significantly higher fall velocities. This suggests that other factors (like in-flight breakage or impacts on the gauge body) may also play a significant role in explaining their presence.

DSD is another microphysical property of precipitation that is affected by wind. Chapter 9.1.2 shows that depending on the combination of wind speed and direction the number of smaller drops sensed by the gauge can decrease significantly (in the case of optical disdrometer) or their diameter may be overestimated (in the case of impact disdrometer). Results obtained by applying the computed CRs on a simple Marshall-Palmer distribution shows that the DSD reported by the gauge tends to assume the form of a gamma distribution. This may raise some questions on the DSD formulations obtained from measurements in the field. However, it was also shown that, at least for some combinations of the wind speed and direction, all gauges can provide almost bias free DSD measurements.

In terms of CE, optical disdrometers have shown to be sensitive to the wind direction, with a strong impact on the total amount of precipitation collected. Depending on the gauge, some wind directions provide poor performances even at moderate wind speed and should be therefore avoided in the field. Impact gauges, instead, are more sensitive to wind speed and tend to considerably overestimate the precipitation volume at medium to high wind speed.

Another integral precipitation characteristic considered in this chapter is the radar reflectivity factor. This was shown to be less influenced by wind than the CE, since larger diameter hydrometeors are its primary constituent. However, for some wind directions (in the case of optical gauges) and high wind velocity a significant bias is present that should be taken into considerations when analysing such measurements.

In conclusion, it was shown that wind has an even more relevant impact on precipitation measurements from NCGs than traditional CGs. Wind effects should be mitigated in the field by a proper selection of the installation site, by installing wind shields and/or orienting the gauge so that the prevalent wind at the site impacts the gauges from the least impacting direction. If not present, anemometers should be installed near the precipitation gauge, possibly at the same height of its sensing area, to allow for real-time or post-processing correction of the wind-induced bias.

10 CONCLUSIONS

The attention currently gathered by NCGs is quite notable, even though representing a small fraction of the total number of deployed precipitation gauges. Their use in the field is bound to continuously grow in time, due to several advantages, discussed in this work, over more traditional instruments. However, the major disadvantage of NCGs is their technological complexity, which requires the manufacturer's intervention for maintenance and often provide only the post-processed data in their output telegram. The effects of this increased complexity are highlighted in the literature through evidence of calibration and correction issues, as discussed in chapter 1.3.

The goal of this work is to investigate two main sources of error, producing the largest impact on precipitation measurements. The first is wind, a well-established source of environmental error for traditional CGs but also affecting NCGs. The wind-induced bias is evaluated in this work by means of numerical simulation models, validated by means of WT measurements, and shown to be a viable tool for investigating such bias for the complex external geometry of typical NCGs. The second source investigated is the instrumental bias, due to calibration issues, evaluated using the ad-hoc developed CRG.

It is shown that NCGs are more influenced by wind than traditional CGs. The measurement bias induced by wind can result in both strong precipitation underestimation, up to 100%, or strong overestimation of more than 300%, depending on the investigated instrument.

In the case of optical gauges, the lack of axial symmetry makes wind direction the primary factor in determining the wind-induced bias. For the investigated instruments it was shown that the maximum bias is experienced when wind is parallel to the laser beam while the best performances are obtained when wind is perpendicular to the laser beam. Such gauges however, according to the manufacturers' instructions and due to optical constraints, cannot be orientated with the prevailing wind at the installation site.

Wind speed is instead the primary factor in determining the wind-induced bias for impact disdrometers. This is due to their quasi radially symmetric shape and their measuring principle. In fact, hydrometeors carried by wind have increase their kinetic energy with increasing the wind speed, producing larger errors than the undercatch due to the aerodynamic effect.

It is also shown that the DSD reported by NCGs is strongly affected by wind. Optical disdrometers tend to underestimate the number of small hydrometeors (below 1 mm in diameter) even at moderate wind speed, when the wind flow is parallel to the laser beam. Meanwhile, impact disdrometers tend to overestimate the number of small or even larger hydrometeors due to the increase in kinetic energy induced at wind speed above 5 m s^{-1} . This suggests that some of the differences in the shape of the DSD reported by different instruments installed in the field may be due to the wind.

The instrumental performance of NCGs can be assessed by means of laboratory testing using the developed CRG and the proposed calibration procedure. Results from two optical gauges show a tendency to underestimate both the drop size and fall velocity of single water drops. This is especially true for small size drops, representing the larger proportion of precipitation events, for which the percentage error was high. Furthermore, this underestimation propagates to integral variables provided by the gauge, like the rainfall intensity, that is therefore also strongly underestimated. The measured drop size and fall velocity

showed considerable dispersion, larger than the dispersion of generated drops, especially for the smaller ones, suggesting low accuracy of single drop measurements.

Laboratory tests also showed that the functioning of optical gauges is affected by light flashes, which either produce false readings or inhibits the ability of the gauge to detect hydrometeors. This increases the complexity of calibrating such instruments but also raises the question of the bias that may be introduced by lightings on such gauges when installed in the field.

Together with the calibration procedure, a classification of NCGs in terms of percentage error was proposed, in analogy to the one already existing for CGs. However, the instruments tested showed significant errors, largely exceeding the proposed limits for all quantity of interest considered. This means that both instruments cannot be classified according to the guidelines proposed in this work and would not be suitable for employment in precipitation monitoring networks or as ground reference for areal measurement techniques.

Results of this work for both the wind-induced and instrumental biases, corroborated by field intercomparison results from the literature, prove that the performance of NCGs are significantly below the measurement quality standards of traditional CGs. Before they can effectively replace CGs in precipitation measurement networks, a common and widely agreed calibration procedure must be adopted by both manufacturers and end-users. Furthermore, users would need to apply correction curves for the wind-induced bias and consider the wind climatology of the installation site. It would also be necessary for the manufacturers to include the possibility to retrieve the raw data from the instrument and document the correction algorithms installed on board the instruments.

To further expand the knowledge about the wind-induced bias of NCGs, the results of this work need to be compared against field measurements performed at suitable test sites where shielded reference instruments are available. This will not only allow validating the numerical results but also evaluating the applicability of such corrections in the field and compute the residual bias after correction.

The effect of the fall velocity reached by water drops during calibration with the CRG on the instrumental results should also be further investigated. In fact, due to height limitations of the CRG, drops larger than about 1 mm fall far from their terminal velocity. This may have an impact on the results, even if larger diameters were among the best performing (in term of percentage error) during testing. For this reason, future improvements will be needed to increase the release height of the CRG or to accelerate the drops before they reach the instrument sensing area.

11 REFERENCES

- Adolf Thies GmbH & Co. KG Instruction for Use; Adolf Thies GmbH & Co.: Göttingen, Germany, 2011*
- Alfonsi, G. (2009). *Reynolds-averaged Navier–Stokes equations for turbulence modelling. Applied Mechanics Reviews*, 62(4).
- Alter, J. C. (1937). *Shielded storage precipitation gages. Monthly Weather Review*, 65(7), 262-265.
- Aqilah, F., Islam, M., Juretic, F., Guerrero, J., Wood, D., & Ani, F. N. (2018). *Study of Mesh Quality Improvement for CFD Analysis of an Airfoil. IIUM Engineering Journal*, 19(2), 203-212.
- Atlas, D., Srivastava, R. C., & Sekhon, R. S. (1973). *Doppler radar characteristics of precipitation at vertical incidence. Reviews of Geophysics*, 11(1), 1-35.
- Atlas, D., & Ulbrich, C. W. (1977). *Path-and area-integrated rainfall measurement by microwave attenuation in the 1–3 cm band. Journal of Applied Meteorology and Climatology*, 16(12), 1322-1331.
- Baire, Q., Dobre, M., Piette, A. S., Lanza, L., Cauteruccio, A., Chinchella, E., ... & Garcia Izquierdo, C. (2022). *Calibration Uncertainty of Non-Catching Precipitation Gauges. Sensors*, 22(17), 6413.
- Baker, T. J. (2005). *Mesh generation: Art or science?. Progress in Aerospace Sciences*, 41(1), 29-63.
- Barros, A. P. (2014). *NASA GPM-Ground Validation: Integrated Precipitation and Hydrology Experiment 2014 Science Plan*.
- Baumgardner, D., Kok, G., Dawson, W., O'Connor, D., & Newton, R. (2002). *A new ground-based precipitation spectrometer: The Meteorological Particle Sensor (MPS). In Proceedings of the 11th Conference on Cloud Physics, Ogden, UT, USA (pp. 3-7)*.
- Beard, K. V. (1976). *Terminal velocity and shape of cloud and precipitation drops aloft. Journal of Atmospheric Sciences*, 33(5), 851-864.
- Beard, K. V., and Chuang, C. (1987). *A New Model for the Equilibrium Shape of Raindrops, Journal of the Atmospheric Sciences*, 44(11), pp 1509–1524
- Beguería, S., Buisán Sanz, S. T., Collado Aceituno, J. L., & Alastrué Tierra, J. J. (2018). *Impact of wind and temperature on snowfall measurements by Thies LPM and OTT Parsivel2 optical disdrometers compared with DFAR (Double Fence Automated Reference) measurements at WMO. SPICE Formigal-Sarrios site*.
- Bernauer, F., Hürkamp, K., Rühm, W. and J. Tschiersch (2015). *On the consistency of 2-D video disdrometers in measuring microphysical parameters of solid precipitation. Atmospheric Measurement Techniques*, 8 (8), 3251-3261.
- BIRAL, *User manual, installation – operation -maintenance; Bristol Industrial and Research Associates Limited.: Bristol, UK, 2022*.

- Blanchard, D. C. (1953). Raindrop size-distribution in Hawaiian rains. *Journal of the Atmospheric Sciences*, 10(6), 457-473.
- Bringi, V., Thurai, M., & Baumgardner, D. (2018). Raindrop fall velocities from an optical array probe and 2-D video disdrometer. *Atmospheric Measurement Techniques*, 11(3), 1377-1384.
- Bringi, V. N., Chandrasekar, V., & Xiao, R. (1998). Raindrop axis ratios and size distributions in Florida rainshafts: An assessment of multiparameter radar algorithms. *IEEE transactions on geoscience and remote sensing*, 36(3), 703-715.
- Buisán, S., Monteagudo, L., Arilla, B., Collado, J. L., Alastrué, J., & Earle, M. E. (2018). An assessment of the impact of a single-Alter windshield on snowfall accumulation reported by a heated tipping bucket gauge.
- Capozzi, V., Annella, C., Montopoli, M., Adirosi, E., Fusco, G., & Budillon, G. (2021). Influence of wind-induced effects on laser disdrometer measurements: Analysis and compensation strategies. *Remote Sensing*, 13(15), 3028.
- Caracciolo, C., Prodi, F., & Uijlenhoet, R. (2006). Comparison between Pludix and impact/optical disdrometers during rainfall measurement campaigns. *Atmospheric research*, 82(1-2), 137-163.
- Caracciolo, C., Porcù, F., & Prodi, F. (2008). Precipitation classification at mid-latitudes in terms of drop size distribution parameters. *Advances in Geosciences*, 16, 11-17.
- Caretto, L.S., Gosman, A.D., Patankar, S.V. und Spalding, D.B. (1972) Two Calculation Procedures for steady, three-dimensional Flows with Recirculation. *Proceedings of third International Conference Numerical Methods in Fluid Dynamics, Paris*.
- Caton, P. G. F. (1966). A study of raindrop-size distributions in the free atmosphere. *Quarterly Journal of the Royal Meteorological Society*, 92(391), 15-30.
- Cauteruccio, A. (2020). The role of turbulence in particle-fluid interaction as induced by the outer geometry of catching-type precipitation gauges. PhD Thesis, https://doi.org/10.15167/cauteruccio-arianna_phd2020-04-06.
- Cauteruccio, A., & Lanza, L. G. (2020). Parameterization of the collection efficiency of a cylindrical catching-type rain gauge based on rainfall intensity. *Water*, 12(12), 3431.
- Cauteruccio, A., Brambilla, E., Stagnaro, M., Lanza, L. G., & Rocchi, D. (2021a). Experimental evidence of the wind-induced bias of precipitation gauges using particle image velocimetry and particle tracking in the wind tunnel. *Journal of Hydrology*, 600, 126690.
- Cauteruccio, A., Colli, M., Stagnaro, M., Lanza, L.G. and E. Vuerich (2021b). In situ precipitation measurements in T. Foken (editor): *Springer Handbook of Atmospheric Measurements, Part B: In-situ Measurement Techniques* (in press), Springer Nature, pp. 35.

- Cauteruccio, A., Chinchella, E., Stagnaro, M., & Lanza, L. G. (2021c). Snow particle collection efficiency and adjustment curves for the hotplate precipitation gauge. *Journal of Hydrometeorology*, 22(4), 941-954.
- Cauteruccio, A., Brambilla, E., Stagnaro, M., Lanza, L. G., & Rocchi, D. (2021d). Wind Tunnel Validation of a Particle Tracking Model to Evaluate the Wind-Induced Bias of Precipitation Measurements. *Water Resources Research*, 57(7), e2020WR028766.
- Chandrasekar, V., Cooper, W. A., & Bringi, V. N. (1988). Axis ratios and oscillations of raindrops. *Journal of Atmospheric Sciences*, 45(8), 1323-1333.
- Chatterjee, C., Porcù, F., Das, S., & Bracci, A. (2022). An Investigation on Super-and Sub-Terminal Drops in Two Different Rain Categories and Climate Regimes. *Remote Sensing*, 14(11), 2515.
- Chen, G., Xiong, Q., Morris, P. J., Paterson, E. G., Sergeev, A., & Wang, Y. (2014). OpenFOAM for computational fluid dynamics. *Notices of the AMS*, 61(4), 354-363.
- Chubb, T., Manton, M. J., Siems, S. T., Peace, A. D., & Bilish, S. P. (2015). Estimation of wind-induced losses from a precipitation gauge network in the Australian Snowy Mountains. *Journal of Hydrometeorology*, 16(6), 2619-2638.
- Colli, M., Lanza, L. G., La Barbera, P., & Chan, P. W. (2014). Measurement accuracy of weighing and tipping-bucket rainfall intensity gauges under dynamic laboratory testing. *Atmospheric research*, 144, 186-194.
- Colli, M., Rasmussen, R., Thériault, J. M., Lanza, L. G., Baker, C. B., & Kochendorfer, J. (2015). An improved trajectory model to evaluate the collection performance of snow gauges. *Journal of Applied Meteorology and Climatology*, 54(8), 1826-1836.
- Colli, M., Lanza, L. G., Rasmussen, R., & Thériault, J. M. (2016a). The collection efficiency of shielded and unshielded precipitation gauges. Part I: CFD airflow modeling. *Journal of Hydrometeorology*, 17(1), 231-243.
- Colli, M., Lanza, L. G., Rasmussen, R., & Thériault, J. M. (2016b). The collection efficiency of shielded and unshielded precipitation gauges. Part II: Modeling particle trajectories. *Journal of Hydrometeorology*, 17(1), 245-255.
- Colli, M., Pollock, M., Stagnaro, M., Lanza, L. G., Dutton, M., & O'Connell, E. (2018). A Computational Fluid-Dynamics assessment of the improved performance of aerodynamic rain gauges. *Water Resources Research*, 54(2), 779-796.
- de Moraes Frasson, R. P., Da Cunha, L. K., & Krajewski, W. F. (2011). Assessment of the Thies optical disdrometer performance. *Atmospheric Research*, 101(1-2), 237-255.
- Delahaye, J. Y., Barthès, L., Golé, P., Lavergnat, J., & Vinson, J. P. (2006). A dual-beam

- spectropluviometer concept. *Journal of Hydrology*, 328(1-2), 110-120.
- Duchon, C. E., & Essenberg, G. R. (2001). Comparative rainfall observations from pit and aboveground rain gauges with and without wind shields. *Water Resources Research*, 37(12), 3253-3263.
- Fehlmann, M., Rohrer, M., von Lerber, A., & Stoffel, M. (2020). Automated precipitation monitoring with the Thies disdrometer: biases and ways for improvement. *Atmospheric Measurement Techniques*, 13(9), 4683-4698.
- Förster, J., Gust, G., & Stolte, S. (2004). A piezoelectrical rain gauge for application on buoys. *Journal of Atmospheric and Oceanic Technology*, 21(2), 179-193.
- Friedrich, K., Higgins, S., Masters, F. J., & Lopez, C. R. (2013). Articulating and stationary PARSIVEL disdrometer measurements in conditions with strong winds and heavy rainfall. *Journal of Atmospheric and Oceanic Technology*, 30(9), 2063-2080.
- Garg, K., & Nayar, S. K. (2005). When does a camera see rain?. In *Tenth IEEE International Conference on Computer Vision (ICCV'05) Volume 1* (Vol. 2, pp. 1067-1074). IEEE.
- Garrett, T. J., Fallgatter, C., Shkurko, K., & Howlett, D. (2012). Fall speed measurement and high-resolution multi-angle photography of hydrometeors in free fall. *Atmospheric Measurement Techniques*, 5(11), 2625-2633.
- Giannetti, F., & Reggiannini, R. (2021). Opportunistic rain rate estimation from measurements of satellite downlink attenuation: A survey. *Sensors*, 21(17), 5872.
- Green, M.J. and P. R. Helliwell, 1972: The effect of wind on the rainfall catch. *Distribution of precipitation in mountainous areas*. World Meteorological Organization, Rep. 326, Vol. 2, 27-46.
- Green, A. W. (1975). An approximation for the shapes of large raindrops. *Journal of Applied Meteorology and Climatology*, 14(8), 1578-1583.
- Greenberg, S. (2001). *Ground Based Rainfall Measurements at the NASA Wallops Flight Facility*. Pennsylvania State University, 15.
- Grossklaus, M., Uhlig, K., & Hasse, L. (1998). An optical disdrometer for use in high wind speeds. *Journal of Atmospheric and Oceanic Technology*, 15(4), 1051-1059.
- Gunn, R., & Kinzer, G. D. (1949). The terminal velocity of fall for water droplets in stagnant air. *Journal of Atmospheric Sciences*, 6(4), 243-248.
- Guo, B., Han, Q., Chen, H., Shangguan, L., Zhou, Z., & Yu, Z. (2017). The emergence of visual crowdsensing: Challenges and opportunities. *IEEE Communications Surveys & Tutorials*, 19(4), 2526-2543.
- Haberlandt, U., & Sester, M. (2010). Areal rainfall estimation using moving cars as rain gauges—a modelling study. *Hydrology and Earth System Sciences*, 14(7), 1139-1151.

- Hösch, H., Tokay, A., & Simmer, C. (2013). *Characteristics of Falling Snow and its Variability during GCPEX*. In *EGU General Assembly Conference Abstracts* (pp. EGU2013-2485).
- Houze Jr, R. A., McMurdie, L. A., Petersen, W. A., Schwaller, M. R., Baccus, W., Lundquist, J. D., ... & Chandrasekar, V. (2017). *The olympic mountains experiment (OLYMPEX)*. *Bulletin of the American Meteorological Society*, 98(10), 2167-2188.
- Hunt, J. C., Wray, A. A., & Moin, P. (1988). *Eddies, streams, and convergence zones in turbulent flows. Studying turbulence using numerical simulation databases, 2. Proceedings of the 1988 summer program*.
- Issa, R. I. (1986). *Solution of the implicitly discretised fluid flow equations by operator-splitting*. *Journal of computational physics*, 62(1), 40-65.
- Jeanmasson, G., Mary, I., & Mieussens, L. (2019). *On some explicit local time stepping finite volume schemes for CFD*. *Journal of Computational Physics*, 397, 108818.
- Jevons, W. S. (1861). LIV. *On the deficiency of rain in an elevated rain-gauge, as caused by wind*. *The London, Edinburgh, and Dublin Philosophical Magazine and Journal of Science*, 22(149), 421-433.
- Jiang, S., Babovic, V., Zheng, Y., & Xiong, J. (2019). *Advancing opportunistic sensing in hydrology: A novel approach to measuring rainfall with ordinary surveillance cameras*. *Water Resources Research*, 55(4), 3004-3027.
- Kathiravelu, G., Lucke, T., & Nichols, P. (2016). *Rain drop measurement techniques: A review*. *Water*, 8(1), 29.
- Kikuchi, K., Kameda, T., Higuchi, K., & Yamashita, A. (2013). *A global classification of snow crystals, ice crystals, and solid precipitation based on observations from middle latitudes to polar regions*. *Atmospheric research*, 132, 460-472.
- Kim, B. S., Kim, Y. G., & Lee, S. H. (2017). *Development of rainfall information production technology using the optical signal of windshield rain sensors*. *International Information Institute (Tokyo). Information*, 20(6B), 4521-4533.
- Kinnell, P. I. A. (1972). *The acoustic measurement of water-drop impacts*. *Journal of Applied Meteorology and Climatology*, 11(4), 691-694.
- Kochendorfer, J., Nitu, R., Wolff, M., Mekis, E., Rasmussen, R., Baker, B., ... & Jachcik, A. (2018). *Testing and development of transfer functions for weighing precipitation gauges in WMO-SPICE*. *Hydrology and Earth System Sciences*, 22(2), 1437-1452.
- Kochendorfer, J., Earle, M., Rasmussen, R., Smith, C., Yang, D., Morin, S., ... & Meyers, T. (2021). *How well are we measuring snow post-SPICE?*. *Bulletin of the American Meteorological Society*, 1-49.
- Kourtellis, A. G., Kasparis, T., Jones, L., & Lane, J. (2005, September). *Disdrometer calibration using an*

- adaptive signal processing algorithm. In Proceedings of OCEANS 2005 MTS/IEEE (pp. 2572-2577). IEEE.*
- Krajewski, W. F., Kruger, A., Caracciolo, C., Golé, P., Barthes, L., Creutin, J. D., ... & Vinson, J. P. (2006). *DEVEX-disdrometer evaluation experiment: Basic results and implications for hydrologic studies. Advances in Water Resources, 29*(2), 311-325.
- Kruger, A., & Krajewski, W. F. (2002). *Two-dimensional video disdrometer: A description. Journal of Atmospheric and Oceanic Technology, 19*(5), 602-617.
- La Barbera P., Lanza L. G., “Metodo per la determinazione della intensita' di precipitazione da un veicolo/natante in movimento, e sistema per la caratterizzazione spazio-temporale di un campo di precipitazione su aree estese del territorio.”, IT patent no. ITRM20130469A1, issued February 10, 2015.
- Lanza L.G., Leroy M., Alexadropoulos C., Stagi L., Wauben W. (2005). *WMO Laboratory Intercomparison of Rainfall Intensity Gauges — Final Report IOM Report No. 84, WMO/TD No. 1304*
- Lanza, L.G. and L. Stagi (2008). *Certified accuracy of rainfall data as a standard requirement in scientific investigations. Advances in Geosciences, 16*, 43-48.
- Lanza, L. G., & Vuerich, E. (2009). *The WMO field intercomparison of rain intensity gauges. Atmospheric Research, 94*(4), 534-543.
- Lanza, L. G., Merlone, A., Cauteruccio, A., Chinchella, E., Stagnaro, M., Dobre, M., ... & Parrondo, M. (2021). *Calibration of non-catching precipitation measurement instruments: A review. Meteorological Applications, 28*(3), e2002.
- Lanzinger, E., Theel, M., & Windolph, H. (2006). *Rainfall amount and intensity measured by the Thies laser precipitation monitor. TECO-2006, Geneva, Switzerland, 4-6.*
- Larsen, M. L., Kostinski, A. B., & Jameson, A. R. (2014). *Further evidence for superterminal raindrops. Geophysical Research Letters, 41*(19), 6914-6918.
- Larsen, M. L., & Schönhuber, M. (2018). *Identification and characterization of an anomaly in two-dimensional video disdrometer data. Atmosphere, 9*(8), 315.
- Larsen, M. L., & Blouin, C. K. (2020). *Refinements to Data Acquired by 2-Dimensional Video Disdrometers. Atmosphere, 11*(8), 855.
- Leijnse, H., Uijlenhoet, R., & Stricker, J. N. M. (2008). *Microwave link rainfall estimation: Effects of link length and frequency, temporal sampling, power resolution, and wet antenna attenuation. Advances in Water Resources, 31*(11), 1481-1493.
- Licznar P., Łomotowski J., Błoński S. and G.J. Ciach (2008). *Microprocessor field impactometer calibration: Do we measure drops' momentum or their kinetic energy? Journal of Atmospheric and*

- Oceanic Technology* 25 (5), 742-753.
- Liu, F. (2016). A thorough description of how wall functions are implemented in OpenFOAM. *Proceedings of CFD with OpenSource Software*, 34.
- Löffler-Mang, M., Kunz, M., & Schmid, W. (1999). On the performance of a low-cost K-band Doppler radar for quantitative rain measurements. *Journal of Atmospheric and Oceanic Technology*, 16(3), 379-387.
- Löffler-Mang, M., & Joss, J. (2000). An optical disdrometer for measuring size and velocity of hydrometeors. *Journal of Atmospheric and Oceanic Technology*, 17(2), 130-139.
- Löffler-Mang, M., Schön, D., & Landry, M. (2011). Characteristics of a new automatic hail recorder. *Atmospheric research*, 100(4), 439-446.
- Magono, C., & Lee, C. W. (1966). Meteorological classification of natural snow crystals. *Journal of the Faculty of Science, Hokkaido University. Series 7, Geophysics*, 2(4), 321-335.
- Marshall, J. S., & Palmer, W. M. K (1948). The distribution of raindrops with size. *Journal of Meteorology*, 5(4), 165-166.
- Masahiro Adachi, "Automatic wiper apparatus", JP patent no. JPS59100034A, issued June 9, 1984.
- Masuda, M., Yatagai, A., Kamiguchi, K., & Tanaka, K. (2019). Daily adjustment for wind-induced precipitation undercatch of daily gridded precipitation in Japan. *Earth and Space Science*, 6(8), 1469-1479.
- Menter, F. R. (1994). Two-equation eddy-viscosity turbulence models for engineering applications. *AIAA journal*, 32(8), 1598-1605.
- Menter, F. R., Kuntz, M., & Langtry, R. (2003). Ten years of industrial experience with the SST turbulence model. *Turbulence, heat and mass transfer*, 4(1), 625-632.
- Merlone, A., Coppa, G., Musacchio, C., Lanza, L.G., Cauteruccio, A., Stagnaro, M., et al. (2022) The INCIPIT project: calibration and accuracy of non-catching instruments to measure liquid/solid atmospheric precipitation. In: *WMO/CIMO Technical Conference on Meteorological and Environmental Instruments and Methods of Observation (CIMO TECO-2022)*. Paris, France, 21–24 September 2022.
- Messer, H., Zinevich, A., & Alpert, P. (2006). Environmental monitoring by wireless communication networks. *Science*, 312(5774), 713-713.
- Montero-Martínez, G., Kostinski, A. B., Shaw, R. A., & García-García, F. (2009). Do all raindrops fall at terminal speed?. *Geophysical Research Letters*, 36(11).
- Muchan, K., & Dixon, H. (2019). Insights into rainfall undercatch for differing raingauge rim heights. *Hydrology Research*, 50(6), 1564-1576.

- Mueller, E. (1965). *Radar rainfall studies* (Doctoral dissertation, Ph. D. dissertation, University of Illinois).
- Mueller, C. C., & Kidder, E. H. (1972). Rain gage catch variation due to airflow disturbances around a standard rain gage. *Water Resources Research*, 8(4), 1077-1082.
- Nešpor, V., Krajewski, W. F., & Kruger, A. (2000). Wind-induced error of raindrop size distribution measurement using a two-dimensional video disdrometer. *Journal of Atmospheric and Oceanic Technology*, 17(11), 1483-1492.
- Nešpor, V., & Sevruk, B. (1999). Estimation of wind-induced error of rainfall gauge measurements using a numerical simulation. *Journal of atmospheric and oceanic technology*, 16(4), 450-464.
- Nicoud, F., & Ducros, F. (1999). Subgrid-scale stress modelling based on the square of the velocity gradient tensor. *Flow, turbulence and Combustion*, 62(3), 183-200.
- Nipher, F. E. (1878). *On the determination of the true rainfall, by elevated gauges*. Salem Press.
- Nitu, R., Roulet, Y.-A., Wolff, M., Earle, M., Reverdin, A., Smith, C., Kochendorfer, J., Morin, S., Rasmussen, R., Wong, K., Alastrué, J., Arnold, L., Baker, B., Buisán, S., Collado, J. L., Colli, M., Collins, B., Gaydos, A., Hannula, H.-R., Hoover, J., Joe, P., Kontu, A., Laine, T., Lanza, L., Lanzinger, E., Lee, G. W., Lejeune, Y., Leppänen, L., Mekis, E., Panel, J.-M., Poikonen, A., Ryu, S., Sabatini, F., Theriault, J., Yang, D., Genthon, C., van den Heuvel, F., Hirasawa, N., Konishi, H., Nishimura, K., and Senese, A. (2018). *WMO Solid Precipitation Intercomparison Experiment (SPICE) (2012–2015), Instruments and Observing Methods Report No. 131*, World Meteorological Organization, Geneva.
- Notarangelo, N. M., Hirano, K., Albano, R., & Sole, A. (2021). Transfer learning with convolutional neural networks for rainfall detection in single images. *Water*, 13(5), 588.
- Notaroš, B. M., Bringi, V. N., Kleinkort, C., Kennedy, P., Huang, G. J., Thurai, M., ... & Lee, G. (2016). Accurate characterization of winter precipitation using multi-angle snowflake camera, visual hull, advanced scattering methods and polarimetric radar. *Atmosphere*, 7(6), 81.
- OTT (2016). *Present Weather Sensor OTT Parsivel2, operating instructions*; OTT Hydromet GmbH, Kempten, Germany.
- Patankar, S.V. and Spalding, D.B. (1972) A Calculation Procedure for Heat Mass and Momentum Transfer in Three Dimensional Parabolic Flows, *Int. J. Heat Mass Transfer*, 15(1972), pp. 1787-1806.
- Puppenbenutzer (user). (2009). Rain sensor scheme. Retrieved Genuart 06, 2022, from https://en.wikipedia.org/wiki/File:Rain_sensor_en.svg
- Pollock, M. D., O'Donnell, G., Quinn, P., Dutton, M., Black, A., Wilkinson, M. E., ... & O'Connell, P. E. (2018). Quantifying and mitigating wind-induced undercatch in rainfall measurements. *Water Resources Research*, 54(6), 3863-3875.
- Pope, S. B., & Pope, S. B. (2000). *Turbulent flows*. Cambridge university press. pp. 182–263.

- Prodi, F., Tagliavini, A., & Medini, R. (2000). Time variability in rainfall events observed by Pludix. *Physics and Chemistry of the Earth, Part B: Hydrology, Oceans and Atmosphere*, 25(10-12), 959-963.
- Pruppacher, H. R., & Beard, K. V. (1970). A wind tunnel investigation of the internal circulation and shape of water drops falling at terminal velocity in air. *Quarterly Journal of the Royal Meteorological Society*, 96(408), 247-256.
- Pruppacher, H. R., & Pitter, R. L. (1971). A semi-empirical determination of the shape of cloud and rain drops. *Journal of Atmospheric Sciences*, 28(1), 86-94.
- Rabiei, E., Haberlandt, U., Sester, M., & Fitzner, D. (2013). Rainfall estimation using moving cars as rain gauges—laboratory experiments. *Hydrology and Earth System Sciences*, 17(11), 4701-4712.
- Rasmussen, R. M., Vivekanandan, J., Cole, J., Myers, B., & Masters, C. (1999). The estimation of snowfall rate using visibility. *Journal of Applied Meteorology*, 38(10), 1542-1563.
- Rasmussen, R. M., Hallett, J., Purcell, R., Landolt, S. D., & Cole, J. (2011). The hotplate precipitation gauge. *Journal of Atmospheric and Oceanic Technology*, 28(2), 148-164.
- Rasmussen, R., Baker, B., Kochendorfer, J., Meyers, T., Landolt, S., Fischer, A. P., ... & Gutmann, E. (2012). How well are we measuring snow: The NOAA/FAA/NCAR winter precipitation test bed. *Bulletin of the American Meteorological Society*, 93(6), 811-829.
- Rauber, R. M., & Nesbitt, S. W. (2018). *Radar meteorology: A first course*. John Wiley & Sons.
- Reynolds, O. (1995). On the Dynamical Theory of Incompressible Viscous Fluids and the Determination of the Criterion. In *Proceedings of the Royal Society-Mathematical and Physical Sciences* (Vol. 451, No. 1941, pp. 5-47).
- Robinson, A. C., & Rodda, J. C. (1969). Rain wind and aerodynamic characteristics of rain-gauges. *Meteorological Magazine*, 98(1161), 113.
- Rodda, J. C., & Smith, S. W. (1986). The significance of the systematic error in rainfall measurement for assessing wet deposition. *Atmospheric Environment* (1967), 20(5), 1059-1064.
- Ryde, J. W. (1946). The attenuation and radar echoes produced at centimeter wavelengths by various meteorological phenomena. *Meteorological Factors in Radio Wave Propagation*, London, 169-189.
- Ryu, S., Lee, G., Nitu, R., Smith, C., Lim, E., & Kin, H. L. (2012). Automatic double fence reference (DFAR) for measuring solid precipitation: Gauge based characterization. *Second session of the international organization committee for the WMO solid precipitation intercomparison experiment*, World Meteorological Organization, Boulder, CO.
- Salmi, A., Ikonen, J., & Oyj, V. (2005, May). Piezoelectric precipitation sensor from Vaisala. In *WMO Technical Conference on Instruments and Methods of Observation (TECO-2005)*, Bucharest, Romania (pp. 4-7).

- Salmi, A., Elomaa, L., Kopsala, P., Laukkanen, E., & Oyj, V. (2011). Piezoelectric Vaisala raincap® rain sensor applied to drop size distribution monitoring. In *Technical Conference on Meteorological and Environmental Instruments and Methods of Observation* (pp. 1-7). Geneva: World Meteorological Organization.
- Sarkar, T., Das, S., & Maitra, A. (2015). Assessment of different raindrop size measuring techniques: Inter-comparison of Doppler radar, impact and optical disdrometer. *Atmospheric Research*, 160, 15-27.
- Sevruk, B. (1982). *Methods of correction for systematic error in point precipitation measurement for operational use*. World Meteorological Organization, Rep. 21, 106 pp.
- Sevruk, B., & Zahlavova, L. (1994). Classification system of precipitation gauge site exposure: evaluation and application. *International journal of climatology*, 14(6), 681-689.
- Sevruk, B., Ondrás, M., & Chvíla, B. (2009). The WMO precipitation measurement intercomparisons. *Atmospheric Research*, 92(3), 376-380.
- Sheppard, B. E. (1990). Measurement of raindrop size distributions using a small Doppler radar. *Journal of Atmospheric and Oceanic Technology*, 7(2), 255-268.
- Skofronick-Jackson, G., Hudak, D., Petersen, W., Nesbitt, S. W., Chandrasekar, V., Durden, S., ... & Wolde, M. (2015). Global precipitation measurement cold season precipitation experiment (GCPEX): For measurement's sake, let it snow. *Bulletin of the American Meteorological Society*, 96(10), 1719-1741.
- Smith, C., Hoover, J., Kochendorfer, J., & Nitu, R. (2012). Specifications for the WMO-SPICE single alter shield configuration. WMO-SPICE Tech. Doc., WMO, 6.
- Smith, C. D., Ross, A., Kochendorfer, J., Earle, M. E., Wolff, M., Buisán, S., ... & Laine, T. (2020). Evaluation of the WMO Solid Precipitation Intercomparison Experiment (SPICE) transfer functions for adjusting the wind bias in solid precipitation measurements. *Hydrology and Earth System Sciences*, 24(8), 4025-4043.
- Smith, C. D., Mekis, E., Hartwell, M., & Ross, A. (2022). The hourly wind-bias-adjusted precipitation data set from the Environment and Climate Change Canada automated surface observation network (2001–2019). *Earth System Science Data*, 14(12), 5253-5265.
- Strangeways, I. (2006). *Precipitation: theory, measurement and distribution*. Cambridge University Press.
- Szakall, M., Diehl, K., Mitra, S. K., & Borrmann, S. (2009). A wind tunnel study on the shape, oscillation, and internal circulation of large raindrops with sizes between 2.5 and 7.5 mm. *Journal of the Atmospheric Sciences*, 66(3), 755-765.
- Tagliavini, G., McCorquodale, M., Westbrook, C., Corso, P., Krol, Q., & Holzner, M. (2021). Drag coefficient prediction of complex-shaped snow particles falling in air beyond the Stokes regime. *International Journal of Multiphase Flow*, 140, 103652.

- Telionis, D., Yang, Y., & Rediniotis, O. (2009). *Recent developments in multi-hole probe (MHP) technology. In 20th international congress of mechanical engineering (Vol. 21).*
- Testik, F. Y., & Rahman, M. K. (2016). High-speed optical disdrometer for rainfall microphysical observations. *Journal of Atmospheric and Oceanic Technology*, 33(2), 231-243.
- Testik, F. Y., & Pei, B. (2017). Wind effects on the shape of raindrop size distribution. *Journal of Hydrometeorology*, 18(5), 1285-1303.
- Thériault, J. M., Rasmussen, R., Ikeda, K., & Landolt, S. (2012). Dependence of snow gauge collection efficiency on snowflake characteristics. *Journal of Applied Meteorology and Climatology*, 51(4), 745-762.
- Thériault, J. M., Rasmussen, R., Petro, E., Trépanier, J. Y., Colli, M., & Lanza, L. G. (2015). Impact of wind direction, wind speed, and particle characteristics on the collection efficiency of the double fence intercomparison reference. *Journal of Applied Meteorology and Climatology*, 54(9), 1918-1930.
- Thies A. GmbH & Co. KG. (2011). *Instruction for Use; Adolf Thies GmbH & Co.: Göttingen, Germany.*
- Thurai, M., Bringi, V., Gatlin, P. N., Petersen, W. A., & Wingo, M. T. (2019). Measurements and modeling of the full rain drop size distribution. *Atmosphere*, 10(1), 39.
- Thurai, M., Bringi, V. N., Wolff, D. B., Marks, D. A., & Pabla, C. S. (2020). Drop size distribution measurements in outer rainbands of hurricane dorian at the NASA wallops precipitation-research facility. *Atmosphere*, 11(6), 578.
- Tokay, A., Petersen, W. A., Gatlin, P., & Wingo, M. (2013). Comparison of raindrop size distribution measurements by collocated disdrometers. *Journal of Atmospheric and Oceanic Technology*, 30(8), 1672-1690.
- Tokay, A., Wolff, D. B., & Petersen, W. A. (2014). Evaluation of the new version of the laser-optical disdrometer, OTT Parsivel 2. *Journal of Atmospheric and Oceanic Technology*, 31(6), 1276-1288
- Turbulent Flow Instrumentation Pty Ltd. (2011). *Cobra Pressure Probe; TFI Ltd.: Tallangatta, Victoria, Australia.*
- Tuukka, P. (2015). Calibration of non-catching precipitation sensors (Vaisala). In *MeteoMet2 workshop. Genova University. March 11th-12th 2015.*
- Uijlenhoet, R., & Torres, D. S. (2006). Measurement and parameterization of rainfall microstructure. *Journal of hydrology*, 328(1-2), 1-7.
- Uijlenhoet, R., Overeem, A., & Leijnse, H. (2018). Opportunistic remote sensing of rainfall using microwave links from cellular communication networks. *Wiley Interdisciplinary Reviews: Water*, 5(4), e1289.
- Ulbrich, C. W. (1983). Natural variations in the analytical form of the raindrop size distribution. *Journal*

- of climate and applied meteorology, 1764-1775.*
- Upton, G., & Brawn, D. (2008). *An investigation of factors affecting the accuracy of Thies disdrometers. In WMO Technical Conference on Instruments and Methods of Observation (TECO-2008), St. Petersburg, Russian Federation (pp. 27-29).*
- Utsumi, N., Kanae, S., Kim, H., Seto, S., Oki, T., Nitta, T., & Hirabayashi, Y. (2008). *Importance of wind-induced undercatch adjustment in a gauge-based analysis of daily precipitation over Japan. Hydrological Research Letters, 2, 47-51.*
- Vaisala (2012). *Vaisala Weather Transmitter WXT520, users' guide; Vaisala Oyj: Helsinki, Finland.*
- Vuerich, E., Monesi, C., Lanza, L.G., Stagi, L. and E. Lanzinger (2009). *WMO Field Intercomparison of Rainfall Intensity Gauges. World Meteorological Organisation – Instruments and Observing Methods Rep. No. 99, WMO/TD No. 1504, pp. 286.*
- Waldvogel, A. (1974). *The N0 jump of raindrop spectra. Journal of the Atmospheric Sciences, 31(4), 1067-1078.*
- Wang, P. K. (2013). *Physics and dynamics of clouds and precipitation. Cambridge University Press.*
- Wauben, W., Mathijssen, T., & Oudshoorn, C. (2016, September). *Field evaluation of sensors for precipitation type discrimination. In Proceedings of the WMO Technical Conference on Meteorological and Environmental Instruments and Methods of Observation (CIMO TECO 2016), Madrid, Spain (pp. 27-30).*
- Wilcox, D. C. (1988). *Reassessment of the scale-determining equation for advanced turbulence models. AIAA journal, 26(11), 1299-1310.*
- Willert, C., & Kompenhans, J. (2010). *PIV analysis of Ludwig Prandtl's historic flow visualization films. arXiv preprint arXiv:1010.3149.*
- WMO – World Meteorological Organization, (2021): *Guide to Instruments and Methods of Observation. WMO-N. 8, ISBN 978-92-63-10008-5.*
- Wolff, M. A., Isaksen, K., Petersen-Øverleir, A., Ødemark, K., Reitan, T., & Brækkan, R. (2015). *Derivation of a new continuous adjustment function for correcting wind-induced loss of solid precipitation: results of a Norwegian field study. Hydrology and Earth System Sciences, 19(2), 951-967.*
- Jones, W. P., & Launder, B. E. (1972). *The prediction of laminarization with a two-equation model of turbulence. International journal of heat and mass transfer, 15(2), 301-314.*
- Yang, D., Elomaa, E., Tuominen, A., Aaltonen, A., Goodison, B., Gunther, T., ... & Milkovic, J. (1999). *Wind-induced precipitation undercatch of the Hellmann gauges. Hydrology Research, 30(1), 57-80.*
- Yang, D. (2014). *Double fence intercomparison reference (DFIR) vs. bush gauge for “true” snowfall measurement. Journal of Hydrology, 509, 94-100.*